Università Degli Studi di Padova

Dipartimento di Fisica e Astronomia "G. Galilei"
SCUOLA DI DOTTORATO DI RICERCA IN ASTRONOMIA
CICLO XXVI

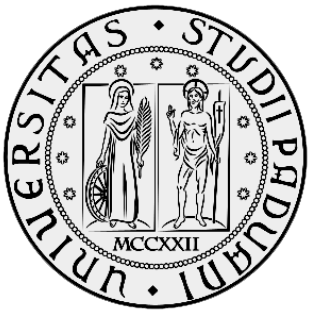

Doctoral Thesis

Tidal Effects on the Oort Cloud Comets and Dynamics of the Sun in the Spiral Arms of the Galaxy

PhD School Director: Ch. mo Prof Giampaolo Piotto
Supervisor: Ch. mo Prof. Luigi Secco

PhD student: Alice De Biasi

"If one does not know to which port one is sailing, no wind is favorable.."

Lucio Anneo Seneca

UNIVERSITÀ DEGLI STUDI DI PADOVA
Dipartimento di Fisica e Astronomia "G. Galilei"
SCUOLA DI DOTTORATO DI RICERCA IN ASTRONOMIA
CICLO XXVI

Abstract

Tidal Effects on the Oort Cloud Comets and Dynamics of the Sun in the Spiral Arms of the Galaxy

The Solar System presents a complex dynamical structure and is not isolated from the Galaxy. In particular the comet reservoir of our planetary system, the Oort cloud, is extremely sensitive to the the galactic environment due to its peripheral collocation inside the Solar System. In this framework, the growing evidences about a possible migration of the Sun open new research scenarios relative to the effects that such kind of migration might induce on the cometary motion. Following several previous studied, we identified the spiral arm structure as the main perturbation that is able to produce an efficient solar migration through the disk. Widening the classical model for the spiral arms, provided by Lin& Shu to a 3D formalism, we verified the compatibility between the presence of the spiral perturbation and a significant solar motion for an inner Galactic position to the current one, in agreement with the constrains in position, velocity and metallicity due to the present conditions of our star. The main perturbers of the Oort cloud, the close stellar passages and the tidal field of the Galaxy, might be both affected by the variation of Galactic environment that the solar migration entails. Despite that, in order to isolate the effects to the two different perturbators, we decided to focus our attention only on the Galactic tide. The perturbation due to the spiral structure was included in the study on the cometary motion, introducing the solar migration and adding the direct presence of the non-axisymmetric component in the Galactic potential of the tidal field. The results show a significant influence of the spiral arm in particular on cometary objects belonged to the outer shell of the Oort cloud, for which provides an injection rate three times bigger than the integration performed without the spiral arms. The introduction of the spiral perturbation seems to bolster the planar component of the tide, indeed it produces the most significant variation of the perihelion distance for moderate inclination orbits with respect to the plane. The peak for the cometary injections has been registered between 6 and 7 kpc. If this evidence will be confirmed by more realistic cometary sample, it might involve a redefinition of the habitability edges in the Galaxy (GHZ). In particular regions not precluded to the formation of life, may compromise the development of the life with a high cometary impact risk.

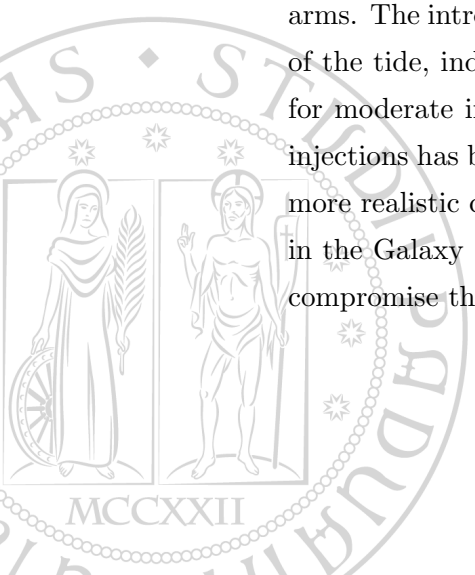

UNIVERSITÀ DEGLI STUDI DI PADOVA
Dipartimento di Fisica e Astronomia "G. Galilei"
SCUOLA DI DOTTORATO DI RICERCA IN ASTRONOMIA
CICLO XXVI

Riassunto

Tidal Effects on the Oort Cloud Comets and Dynamics of the Sun in the Spiral Arms of the Galaxy

Il Sistema Solare è una struttura con una dinamica complessa e non isolata da quella galattica. In particolare la riserva cometaria del nostro sistema planetario, la nube di Oort, a causa della sua periferica collocazione all'interno del Sistema Solare, risulta estremamente sensibile all'ambiente galattico circostante. In questo contesto, le crescenti evidenze di una possibile migrazione del Sole, aprono un nuovo scenario di indagine relativo ai cambiamenti che tale migrazione potrebbe indurre sul moto cometario. Seguendo un filone di ricerca già tracciato, abbiamo identificato nella struttura a spirale la principale perturbazione in grado di produrre un efficace effetto migratorio per il Sole. Ampliando il classico modello di Lin & Shu con una modellizzazione 3D per i bracci a spirale considerati in regime transiente, siamo stati in grado di verificare la compatibilità tra tale perturbazione e un moto solare attraverso il disco, in accordo con i vincoli di posizione, velocità e metallicità imposti dalla attuale condizione della nostra stella. Malgrado i maggiori perturbatori della nube di Oort, i passaggi stellari ravvicinati e il campo mareale della Galassia, siano entrambi potenzialmente sensibili alla variazione di ambiente galattico che una migrazione solare comporta, abbiamo concentrato il nostro studio unicamente sulla marea galattica. La perturbazione dovuta alla spirale, è stata incorporata nello studio dei moti cometari, sia attraverso l'introduzione della migrazione solare, che come effetto diretto sulle comete grazie alla presenza della componente non-assisimmetrica nel campo mareale. I risultati mostrano un'influenza significativa della spirale, in particolar modo sulla popolazione cometaria del guscio più esterno della nube, per la quale si sono registrati tassi di immissione cometaria 3 volte maggiori rispetto al caso senza tale perturbazione. La spirale sembra rinforzare l'azione della componente piana della marea, producendo infatti le maggiori variazioni sui perieli cometari in corrispondenza di orbite con inclinazioni moderate rispetto al piano galattico. Si è inoltre rilevato che il picco di immissione cometaria si trova in corrispondenza di distanze galattiche per il Sole comprese tra 6 e 7 kpc. Se tale evidenza fosse confermata anche da campioni cometari più realistici, potrebbe comportare un vincolo ulteriore alla definizione della zona di abitabilità galattica (GHZ). In particolare, regioni del disco

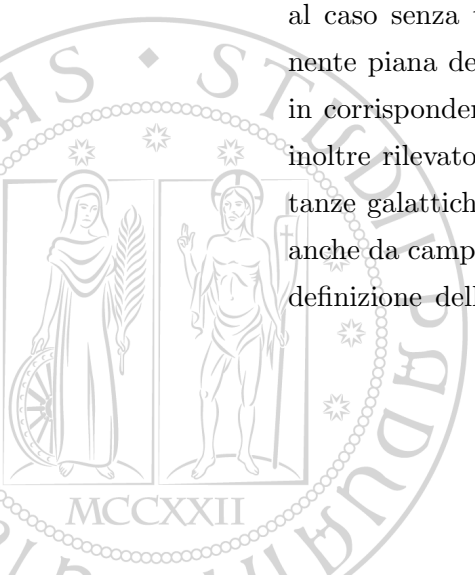

non attualmente precluse alla formazione della vita, potrebbero risultare inadatte allo sviluppo della stessa per un rischio di impatto cometario troppo elevato.

Contents

List of Figures

List of Tables

Abbreviations

AMR	**A**ge-**M**etallicity **R**elationship
CMD	**C**old **D**ark **M**atter
DH	**D**ark **H**alo
JFC	**J**upiter **F**amily **C**omet
DM	**D**ark **M**atter
GHZ	**G**alactic **H**abitable **Z**one
HTC	**H**alley-**T**ype **C**omet
LPC	**L**ong **P**eriod **C**omet
MDF	**M**etallicity **D**istribution **F**unction
MPI	**M**odified **P**seudo - **I**sotherm
NFW	**N**avarro **F**rank and **W**hite
RS	**R**andom **S**ample
SP	**S**piral **P**erturbation
SPC	**S**hort **P**eriod **C**omet
TSE	**T**aylor **S**eries **E**xpansion

Introduction

Comets are the celestial bodies that had deeply fascinated the human mind in every time: their motion, apparently unpredictable with respect the fixed stars, produced an halo of mystery around these objects, impeding their complete comprehension for a long time. Man fears everything is not able to explain, for this reason comets became the messanger of bad luck and divine fury. This vision lasted up to 17th-century, when the astronomer Edmond Halley demonstrated the true nature of comets: bodies belonging to our Solar System with periodic orbits. After Halley the next fundamental step in the comet science was made by the American astronomer Fred Whipper that in 1950 formulated the theory that will become famous under the name of "dirty snowballs": according with his model a comet is not a diffused aggregate of particles but a solid core of few kilometers radius, composed by ice mixed with solid particles. Finally the Estonian astronomer Ernest Öpik and the Dutch astronomer Jan Oort postulated, independently, a theory concerning the origins of comets in our Solar System in 1932 and 1950 respectively: comets represent the remnants of the planetary formation and are stored in a spherical cloud, in a very peripheral zone of our planetary system, now well-known as Oort cloud.

It is interesting to notice how one of the most ancient phenomena detected by men (recorded observations stretch back more than 2000 years, with a comet noted in Chinese records in the years 240 B.C,) has takes thousands years to find a full explanation. Presently comets are considered to be the key to understand the Solar System formation and evolution. Indeed they are probably the most primitive objects of the Solar System, because they formed and stored in distant regions where the cold temperature preserved the pristine chemical conditions. The orbital structure of the main comet reservoir, the Oort cloud, is the more ancient fossil about the dynamical processes that occurred at the beginning of the Solar System formation. Building a good model for these dynamical processes is a way to reconstruct the framework in which our planetary system formed

and evolved.
The growing evidences about the possibility of a migration of our Sun through the disk, from an inner position to the current one, may change the point of view about one of the main perturbed of Oort cloud: the tidal field of the Galaxy. If the Sun may experienced a different Galactic environment, that could also modify the evolution of the main cometary reservoir of our planetary system. It results particularly relevant remembering that comets are also strictly linked with the theme of the Life, playing a twofold role into the processed of life formation and development. On one side cometary impacts might brought the fundamental bricks of the living organisms, like water and prebiotic organic compounds, but on the other side a heavy comets bombardment could compromise the planetary environment, making it unable to host the life. In this prospective, the mechanisms that injected the comets in the inner region of our planetary system, might also establish some constrains for the Galactic habitability.

The thesis is divide in 5 main parts, each of them dedicated to the dissertation of a fundamental aspect of the subject of the study:

- **Chapter 1**: is devoted to a brief overview about the cometary objects. We listed the different cometary family, analyzing the difference in their origin and dynamical behaviors. We also dedicated wide paragraphs to the formation and the evolution of the Oort cloud, looking to the conditions that may make the formation of this kind of structure possible in a more general Galactic environment, following theoretical dissertation presented in the literature.

- **Chapter 2**: in this second chapter the axisymmetric model for the Galaxy potential is provided. It represents the start point of our study and that will be used to compare the results that will obtain with the addition of a spiral arms perturbation.

- **Chapter 3**: is completely dedicated to the structure that we have identified as a possible responsible of the solar migration: the spiral arms. This, partially still unknown, non-axisymmetric structure belonging to the Milky Way, may produce the motion of the Sun breaking the cylindrical symmetric of the Galactic potential. We will probe this possibility and provide a statistical study about the main parameters that may influence the structure and the action of the spiral arms on the Solar System.

- **Chapter 4**: in this chapter we introduce the concept of Galactic Habitable Zone (GHZ), producing a small summary about the main approaches to this idea present in the literature, and as different authors tried to define the edges and requirements to encompass the Galactic area with the most suitable conditions for the arise

of Life. We will compare our results about the solar migration, verifying the agreement with the constrains fixed by the canonical model of Lineweaver et al. (2004).

- **Chapter 5**: finally we devoted the last chapter to the investigation about the Galactic tide. First we performed a calculation for the cometary orbits in the usual axisymmetric potential with a Sun nearly fixed around its birth position, model the tidal effects due only to bulge, disk and dark matter halo of the Galaxy. In a second moment we made a comparison with cometary samples integrated in a Galactic potential with the presence of a spiral structure, following a Sun with a migration through the disk, probing the strong effects on the Oort cloud due to the additional perturbation of the spiral arms.

The work that we are going to present tried to find a place in this very complex framework, in which the Galactic dynamics is strongly tied to the planetary one, and a very fine balance between different factors is required in order to preserve life as we know it.

1

Comets: a brief overview

When we speak about comets, we involve different categories of objects with a wide range of dynamical features and different type of evolution. In this chapter we try to summarize the differences among the cometary families. We start distinguishing different classes of objects inside the huge whole called trans-Neptunian population and after we will look to each particular cometary family. Few paragraphs are also devoted to the description of the formation and evolution of the Oort cloud also in Galactic environment different from the solar one.

1.1 Comets in general: the trans-Neptunian population

The trans-Neptunian population is a population of numerous small bodies that orbit the Sun at greater average distance than Neptune. That population is usually subdivided in two sub-populations: the *scattered disk* and the *Kuiper Belt*. The definition of these sub-populations is not unique and various authors often using slightly different criteria. Here we follow Morbidelli (2005), that proposed a partition based on the dynamics of the objects and their relevance for the reconstruction of the primordial evolution of the outer part of our planetary system, reminding that all bodies in the Solar System must have been formed on orbits typical of an accretion disk (with very small eccentricities and inclinations).

The *scattered disk* is the region of the orbital space that can be visited by bodies that have encountered Neptune within a Hill radius[1], at least once during the age of the Solar System, assuming that planetary orbits did not suffer significant modification. The bodies do not provide us any relevant information about the primordial structure of the Solar System. Indeed their current eccentric orbits might have been the transformation of quasi-circular ones in Neptune's zone by pure dynamical evolution, in the framework

[1] see Eq. (A.32) in § A

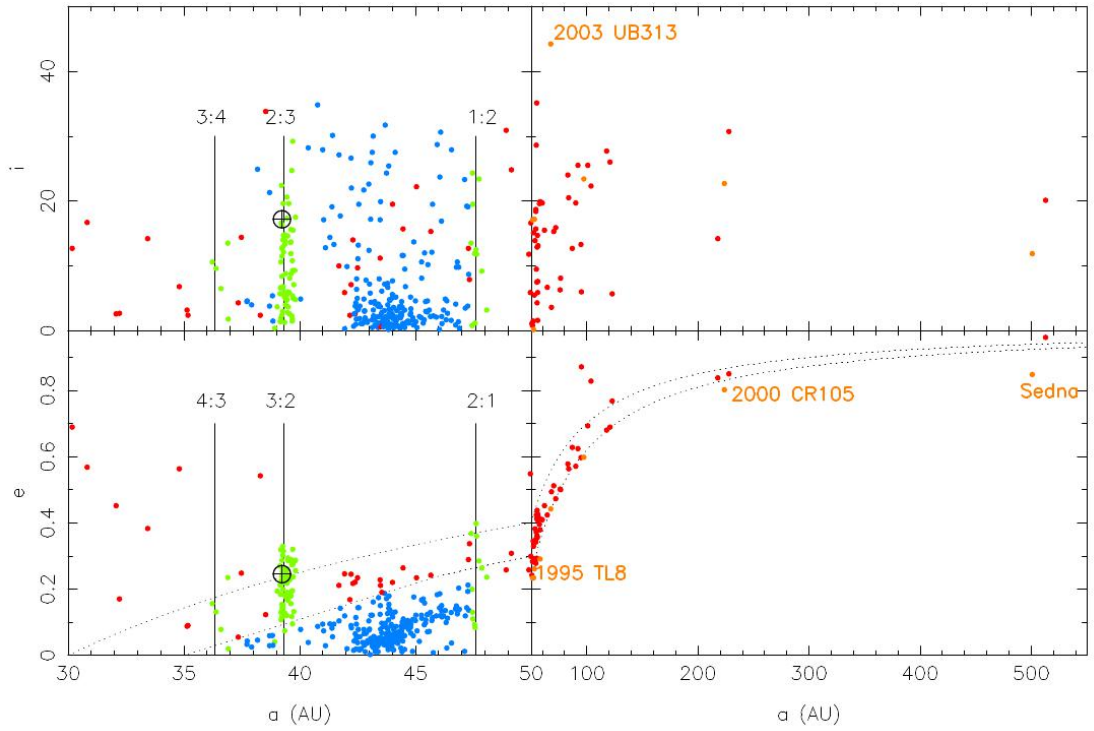

FIGURE 1.1: *The orbital distribution of multi-opposition trans-Neptunian bodies, as of Aug. 26, 2005 (top panel: inclination i in deg vs semimajor axis a, bottom panel: eccentricity e vs semimajor axis a). Scattered-disk bodies are represented in red, extended scattered-disk bodies in orange, classical Kuiper Belt bodies in blue and resonant bodies in green. The dotted curves in the bottom left panel denote $q = 30$ AU and $q = 35$ AU; those in the bottom right panel $q = 30$ AU and $q = 38$ AU. The vertical solid lines mark the locations of the 3:4, 2:3 and 1:2 mean motion resonance with Neptune. The orbit of Pluto is represented by a crossed circle Morbidelli (2005).*

of the current architecture of the planetary system.

The *Kuiper belt* is the trans-Neptunian region that cannot be visited by bodies encountering Neptune. Therefore, the non-negligible eccentricities and/or inclinations of the Kuiper belt bodies cannot be explained by the scattering action of the planet on its current orbit, but they reveal that some excitation mechanism, which is no longer at work, occurred in the past.

In order to divide the observed trans-Neptunian bodies into these two different classes, we can use a dynamical criteria. For the region with semimajor axis[2] values $a < 50$ AU we can refer to the result by Duncan et al. (1995) and Kuchner et al. (2002), who numerically mapped the regions of the (a, e, i) space with $32 < a < 50$ AU, that can lead to a Neptune encountering orbit within 4 Gy. Because dynamics are reversible, these are also the regions that can be visited by a body after having encountered the planet, in other word the scattered disk. For the $a > 50$ AU region, it is possible to use the results in Levison and Duncan (1997) and Duncan and Levison (1997), where the evolution of the particles that encountered Neptune in Duncan et al. (1995) have been followed

[2]see §A.2.1 for the definition of all the orbital elements.

for another 4 Gyr. The initial conditions did not cover all possible configurations, but it is reasonably to assume that these integrations cumulatively show the regions of the orbital space that can be potentially visited by bodies transported to $a > 50$ AU by Neptune encounters: so we are again inside the scattered disk.
In Fig.(1.1) is possible to see the (a, e, i) distribution of the trans-Neptunian bodies during at least three oppositions. The bodies of the scattered disk are represented as red dots. We identified two sub-population for the Kuiper belt: the resonant population (green dots) and the classical belt (blue dots). The former is made of objects located at the major mean-motion resonances with Neptune (with perihelion distances much smaller than the classic population due to the mechanism against close encounters provided by mean-motion resonances), while the classical belt objects do not present any particular resonant configuration. According to Trujillo et al. (2001), the scattered disk and the Kuiper belt have about an equal populations, while the resonant objects, altogether, make about 10% of the classical objects.
In Fig. (1.1) with magenta dots is highlighted the existence of bodies with $a > 50$ AU, on highly eccentric orbits, which do not belong to the scattered disk according to the given definition. Among them in orange are 2000CR105 ($a = 230$ AU, perihelion distance $q = 44.17$ AU and inclination $i = 22.7°$), Sedna ($a = 495$ AU, $q = 76$ AU) and 2003 UB313 ($a = 67.7$ AU, $q = 37.7$ AU but $i = 44.2°$). Following Gladman et al. (2002), we can call these particular objects *extended scattered-disk objects* for three reasons:

(i) They are very close to the scattered-disk boundary.

(ii) They presumably formed much closer to the Sun, because to achieve their size (300-2000 km) they need an accretion timescale sufficiently short Stern (1996), implying that they have been transported in semi-major axis space (e.g. scattered), to reach their current locations.

(iii) The lack of objects with $q > 41$ AU and $50 < a < 200$ AU should not be due to observational biases, given that many classical belt objects with $q > 41$ AU and $a < 50$ AU have been discovered. This suggests that the extended scattered-disk objects are not the highest eccentricity members of an excited belt beyond 50 AU.

From these considerations it possible to argue that in the past the true scattered disk extended well beyond its present boundary in perihelion distance Morbidelli (2005).
As perihelion distance and semi-major axis increase, the observational biases grows, then the currently known extended scattered-disk objects may be the emerging representatives of a conspicuous scattered-disk population.

1.2 Comets in particular: different comet families

Comets are usually classified in categories according to their orbital period (see Morbidelli (2005) and Fig. 1.2), the first classification for the comet orbits was made by *Lardner* (1853) Dones et al. (2004) and his main categories survive still today. Comets with orbital period $P > 200$ yr are called *long period comets* (LPCs); those with shorter period are called *short period comets* (SPCs). The threshold of 200 yr has been chosen has not a scientific motivation, but mostly depends on the facts that modern instrumental astronomy is about two centuries old, so that the long period comets that we see now are unlikely to have been observed in the past.
Through a backward numerical integration it is possible to compute the orbital elements

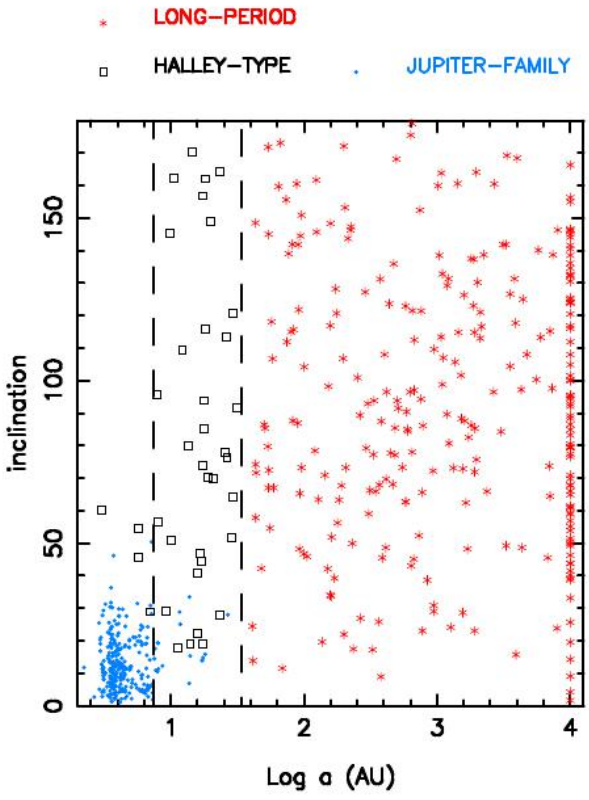

FIGURE 1.2: *The distribution of comets according to their orbital semi-major axis and inclination (in deg). The separation between Halley-types and Jupiter family comets has been made according to the value of their Tisserand parameter. The vertical dashed line correspond to orbital periods $P = 20$ yr and $P = 200$ yr.*

that the comets had when they last passed at aphelion, plotting the cometary orbital distribution a clustering of long period comets with $a \sim 10^4$ AU becomes evident(see also §1.3.1). Since these comets must pass through the giant planets system for the first time they are called *new comets*. Indeed a passage through the inner Solar System likely will modify the semi-major axis that could not longer remains of order 10^4 AU, typically decreases up to 10^3 AU or the orbit becomes hyperbolic. The reason is that the binding

energy of a new comet is $E = -GM_\odot/2a \sim 10^{-4}$, but typically, during a close perihelion passage, the energy suffers a change of order of the mass of Jupiter relative to the Sun: 10^{-3}. This change is due to the fact that the comet has a barycentric motion when it is far away, an heliocentric motion when it is close, and the distance of the barycenter from the Sun is of the order of the relative mass of Jupiter.

The short period comets are also subdivided in *Halley-type* (HTCs) and *Jupiter family* (JFCs). In the past, the edge between the two classes was the orbital period respectively longer or shorter than 20 yr. This threshold has been chosen because of the significant change in the inclination distribution at the corresponding value of semi-major axis (see Fig. 1.2). The continuous change of comets semi-major axis, due to the encounters with the planets, forces modification of this criteria. In particular, all short period comets had to have a larger semi-major axis in the past, given that they come from the trans-planetary region. Adopting the partition based on orbital period, the possibility that some objects will change their classification during their lifetime is not negligible.

For this reason *Levison* Levison (1996) decided to classify short period comets according to their *Tisserand parameter* relative to Jupiter, that we can express as

$$T_J = \frac{a_J}{a} + 2\sqrt{\frac{a}{a_J}(1-e^2)}\cos i. \tag{1.1}$$

The robustness of this classification is established by the quasi-conservation of the Tisserand parameter during the comet's evolution. In Levison's classification, Halley-type and Jupiter family comets have T_J respectively smaller and larger than 2.

It could be useful, in order to understand the importance of the Tisserand's parameter, to derive its expression and discuss its properties.

The Tisserand parameter is an approximation of the Jacobi constant that is an invariant of the dynamics of a small body in the restricted circular three-body problem expressed as follow[3]

$$C_J = -(\dot{x}^2 + \dot{y}^2 + \dot{z}^2) + 2\left(\frac{1}{r} + \frac{m_p}{\Delta}\right) + 2H_z, \tag{1.2}$$

where $GM_\oplus = a_p = 1$ are assumed, and a_p, m_p are the semi-major axis and mass of the perturbing planet, H_z is the z-component of the small body's angular momentum and Δ the distance between the small body and the planet.

The kinetic energy of the small body can be expressed as a function of its semi-major axis and heliocentric distance:

$$\frac{1}{2}(\dot{x}^2 + \dot{y}^2 + \dot{z}^2) = -\frac{1}{2a} + \frac{1}{r}, \tag{1.3}$$

[3] see §A.3. We can rewrite and rename Eq. (A.27.)

while the z-component of the angular momentum can be written:

$$H_z = \sqrt{a(1-e^2)}\cos i. \tag{1.4}$$

Substituting Eq. 1.3 and 1.4 into Eq. 1.2 and neglecting the term m_p/Δ one obtains

$$C_J \sim T_J \equiv \frac{1}{2} + 2\sqrt{a(1-e^2)}\cos i, \tag{1.5}$$

where the right hand side coincides with Eq. 1.1, if a is expressed in units of the planet's semi-major axis. This derivation shows that the Tisserand parameter is constant as long as the Jacobi constant is preserved, and m_p/Δ is small, condition equivalent to impose that the comet is not in a close encounter with the planet. The Tisserand parameter change abruptly during a close encounter, but it returns to the value that it had before the encounter, once the distance to the planet increases back to large values. The conservation of the Jacobi constant, conversely, requires that the conditions of the restricted three-body problem are fulfilled, it means that the comet's motion has to be dominated by one planet almost on a circular orbit and then the comet can not be in a region where encounters with two planets is possible, otherwise the one-planet approximation does not hold. Also, it requires that the comet is not in a secular resonance with the planet, otherwise the effects of the planet's small eccentricity are enhanced. It is possible to demonstrate that, if a comet intersects the orbit of a planet, the Tisserand parameter T_J is related to the unperturbed relative velocity U at which it encounters the planet:

$$U = \sqrt{3 - T_J} \tag{1.6}$$

where U is expressed in units of the planet's orbital velocity. It is easy to see that the formula is not defined for $T_J > 3$, which implies that comets with such values of Tisserand parameter cannot intersect the orbit of the planet. Note however that comets non-intersecting the orbit of the planet can have $T_J < 3$. Only objects with $T_J < 2\sqrt{2} \sim 2.83$ can be ejected on hyperbolic orbit in a single encounter with a planet.

1.2.1 Short period comets

In the following paragraphs we give a brief description about the two short period comets families, in particular we will focus on the origin and dynamical properties of each categories.

The long period comets will analyzed in details in the next chapter, since they are the central object of the research of this thesis.

1.2.1.1 Jupiter family comets

The JFCs have a Tisserand parameter with respect to Jupier that is distinct from the others cometary families, it suggests that they are not the small semi-major axis end of the distribution of HTCs and LPCs Morbidelli (2005). Some clues about the origin of these objects are provided by the average low inclination of this particular comet family, and the absence of retrograde comets in the JFC population that suggests as source of this bodies a disk-like structure. The Kuiper Belt (see §1.1), a comet belt beyond Neptune suggested in 1980 by Fernandez (1980a), was indicated as the source of JFCs. Today we know that there are two distinct disk-like structures in the trans-Neptunian region: the Kuiper belt and the scattered disk. The scattered disk is too populated to be sustained in steady state by the objects leaking out of the Kuiper belt; it means that the number of objects that leave the scattered disk is larger than the number of objects entering the scattered disk from the Kuiper belt. Thus, JFC production is dominated by the scattered disk over the Kuiper belt. A detailed study, with a large number of numerical simulations, about the dynamical evolution of objects from the scattered disk to the JFC region has been done by in Levison and Duncan (1997). The simulations show that to evolve from the scattered disk to the JFC region, a comet has the need to pass from a Neptune-dominated dynamics to a Jupiter-dominated dynamics (see Fig. 1.3).

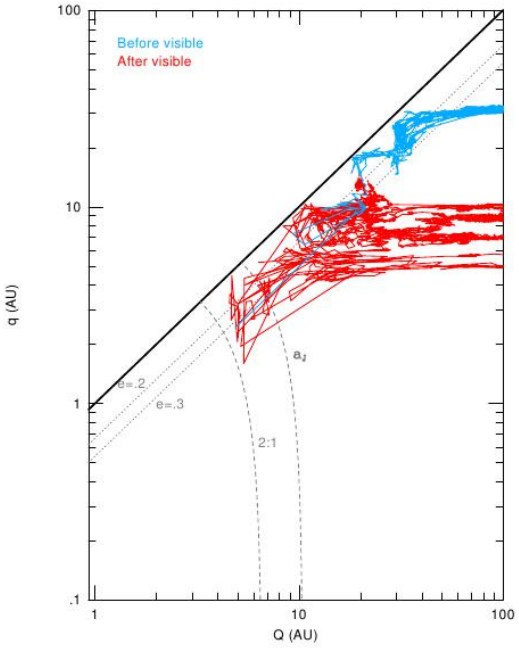

FIGURE 1.3: *The evolution of an object from the scattered disk up to its ultimate ejection, projected over the plane representing perihelion vs. aphelion distance. Blue lines denote the evolution before that the object becomes a visible JFC, red lines afters (see Levison and Duncan (1997)).*

Since the transfer process involving different planets, in principle the Tisserand parameter is not preserved. However, the particular structure of the planetary system makes possible that each piece of the transfer chain from Neptune to Jupiter is dominated by one single planet (see Fig. 1.3), and the values of the Tisserand parameters relative to the dominating planets remain almost the same. In others words the body never spends much time in a region where it can encounter two planets and entails that Tisserand parameter is therefore piece-wise conserved, and the final Tisserand parameter (with respect to Jupiter) is very close to the initial one (with respect to Neptune). The majority of the observed population in the scattered disk has $2 < T_N < 3$. The bodies coming from the scattered disk, at the end of the transfer chain, will have the Tisserand parameter encompass in the same range ($2 < T_J < 3$), namely they will be JFCs.

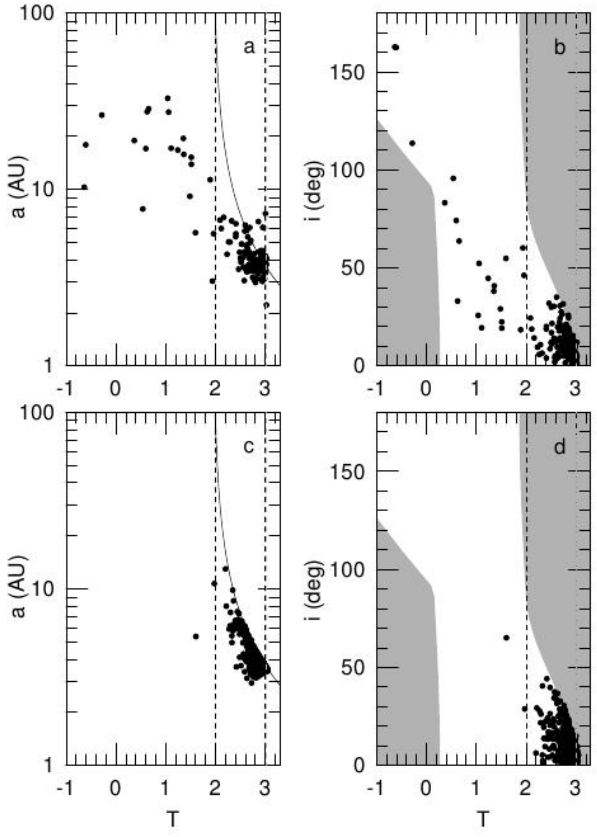

FIGURE 1.4: *The distribution of short period comets projected over the (T_J, a) and (T_J, i) planes. In the top panels: the observed distribution. In the bottom panels: the distribution of the objects coming from the scattered disk, when they are visible ($q < 2.5$ AU) for the first time (see Levison and Duncan (1997)).*

Because the Tisserand parameter remains close to 3, the inclination cannot achieve a large values (since the growth of i would decrease T_J, as it is possible to see in Eq. 1.1). In this way the final inclination distribution is mostly confined within moderate inclinations and comparable to the inclination distribution in the scattered disk (30 degrees).

In Fig. 1.4 is shown the comparison between the (a, i, T_J) distribution of the observed short period comets (top panels) with the one obtained in the numerical simulations for the objects coming from the scattered disk, when their perihelion distance fist decreases makes the comet visible (i. e. below 2.5 AU). We can underline that the objects with $T_J < 2$ (HTCs) are not reproduced, while the observed JFCs population is in good agreement with the simulations. We can conclude that the scattered disk origin for the JFCs is well confirmed also by the numerical simulations.

1.2.1.2 Halley-type comets

The similarity between distribution of the Halley-type comets and the returning LPCs (see 1.2, apart from the semi-major axis range that they cover, was usually interpreted as an indication that the HTCs are the low semi-major axis end of the returning LPC distribution Morbidelli (2005).

Some returning comets can have their semi-major axis decreased to less than 34.2 AU, due the action of close encounters with Jupiter and Saturn, with orbital period that becomes shorter than 200 yr, so that they are classified as short period comets. Their Tisserand parameter relative to Jupiter is typically smaller than 2, it means that these objects are predominantly HTCs, and not JFCs. Indeed new comets from the Oort cloud, having $q < 3$, $a \sim \infty$, $e \sim 1$ must have $T_J < 2.15$, and the Tisserand parameter remains roughly conserved during the evolution down to the SPC region, since that the scattering action is mainly dominated by Jupiter. The transfer of comets from the Oort spike (see §1.3.1) to the HTC region typically requires a large number of revolutions. Thus, the HTCs should belong to the small fraction ($\sim 4\%$) of new comets that do not fade away rapidly.

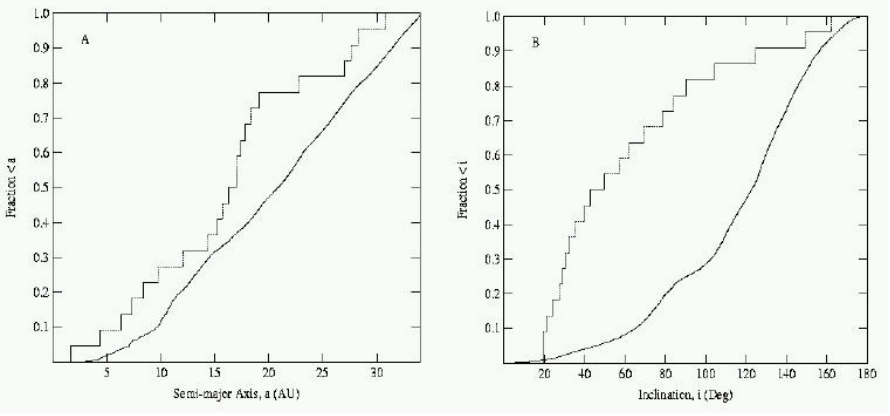

FIGURE 1.5: *Comparison between the cumulative orbital element distribution of the observed HTCs(dotted line) and those produced in the integrations of Levison et al. (2001). Only comets with $q < 1.3$ AU are considered.*

Actually this transfer process from the Oort cloud to the HTC region is not completely understood. The work Levison et al. (2001) has revised that problem with the contribution of numerical simulations. The results show a semi-major axis distribution of the HTCs obtained in the simulations in good agreement with the observed distribution, but with a deep difference in the inclination distributions (Fig. 1.5). In particular, the median inclination distribution of the observed HTCs is 45 degrees with an high percentage of 80% for prograde orbits over the total; whereas the median inclination of the HTCs obtained in the simulation is 120 degrees and only 25% of them have prograde orbit. The simulated distribution is skewed towards retrograde objects because of the latter have a longer dynamical lifetime (100,000 yr, as opposed to 60,000 yr for prograde HTCs).
Different solutions to solve this mismatch have been proposed Levison et al. (2001, 2004), but in conclusion, the problem about the origin of HTCs is currently unsolved and a quantitative model of their distribution remains to be done.

1.3 The Oort cloud: the long period comets reservoir

1.3.1 Origin and evolution of Long period comets

In 1950 Oort in his historical paper Oort (1950), finding a spike in the distribution of $1/a$ of the LPCs (see Fig. 1.6) for $a > 10^4$ AU, suggested the existence of a reservoir of objects in that distant region. The essentially isotropic n distribution of new comets not only in cos$i$ (from -1 to 1, i.e. including also retrograde orbits), but also in ω and Ω (see §A.2.1), suggested that this reservoir must have a quasi-spherical symmetry: a spherical cloud surrounding the Solar System. This cloud is now well-known as the *Oort cloud* with a population estimated between $5 \times 10^{11} - 10^{12}$ objects Dones et al. (2004), a total mass (strongly dependent from the model population) between $3.3 M_\oplus$ Heisler (1990) and $38 M_\oplus$ Weissman (1996).
Oort argued that all long period comets come from this cloud. The LPCs with $a < 10^4$ AU are returning comets, which originally belonged to the new comet group when they first entered into the inner Solar System, but subsequently under the gravitational influence of external bodies effects their orbit are perturbed and acquired a more negative binding energy (smaller semi-major axis). This view remains essentially valid even today. The Oort cloud then is the natural reservoir for long period comets of our Solar System: it is an outer shell structure roughly placed between 10000 AU and 100000 AU. The characteristic size of the Oort cloud is set by the condition that the timescale for changes in the cometary semi-major axis is comparable to the timescale for changes in perihelion

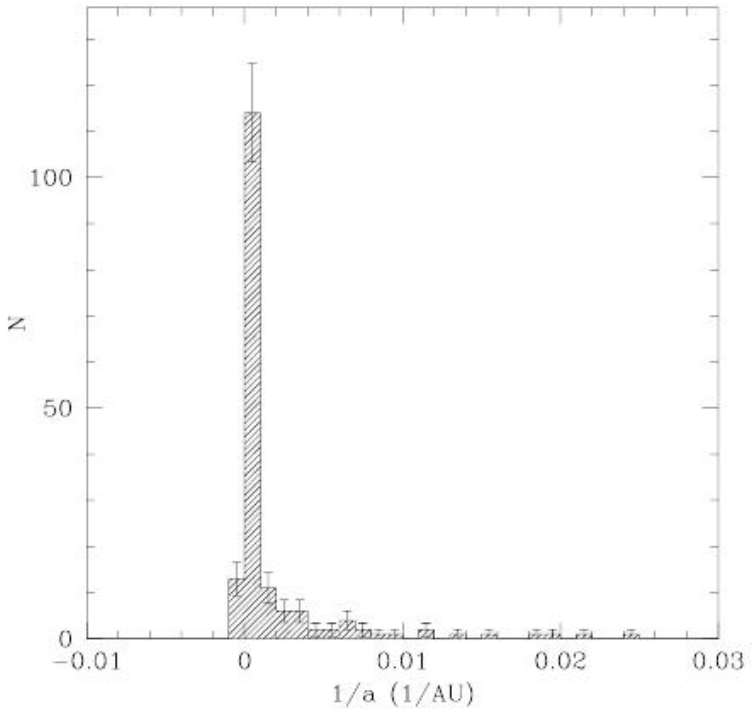

FIGURE 1.6: *The differential distribution of LPCs as a function of the inverse semi-major axis. It is possible to see the big spike at* $1/a < 10^{-4}$ *AU due to the new comets and usually called the Oort spike. Oort (1950).*

distance due to passing stars. In others words the comet must be perturbed to a semi-major axis large enough that the orbit is significantly perturbed by the passing stars, but not so large that the orbit is too weakly bound to the Solar System and the comet escapes (Dones et al. (2004), Tremaine (1993)), we will see this type of constraints in details in §1.5.1.

1.3.2 Perturbers of the Oort cloud

When Oort, Oort (1950), introduced the concept of the Oort cloud, he was aware of the need for an efficient mechanism to bring the perihelia of comets from an extremely peripheral region of our Solar System into the observable range. If this does not happen during just one orbit, likely the planetary perturbations eject it from the Solar System or capture it into a much more tightly bound orbit. Oort identified the impulses imparted to comets by *passing stars* as the only mechanism that was able to prodeuce an injection in the inner region of our planetary system. Later,Hills (1981) confirmed the Oort's hypothesis, pointing out that the Oort cloud could be perturbed by close stellar encounters, that could produce an episodic very large increase in the flux of new comets: the *comet showers*.

In the mid-1980's, it was realized that the *Galactic tidal force* also plays an important

role in the framework of the comet injection, and may in fact represent the predominant effect Duncan et al. (1987). In particular, Heisler and Tremaine (1986) showed that the "vertical" disk tide is an efficient perturber, causing regular q oscillations in the range of a of about $30000 - 40000$ AU.

The galactic tide perturbation is a smooth long term effects that causes cometary perihelion distance to cycle outward from the planetary region and back inward again on the timescale as long as billion of years. Assuming that the Galaxy has a disk-like structure and considering that the Sun is not at the center, the galactic tide has both "disk" and "radial" force components. In order to describe the galactic tidal perturbation, we consider a coordinate system centered on the Sun, with x-axis pointing away from the galactic center, y-axis in the direction of the galactic rotation and z-axis towards the south galactic pole. The radial component of the galactic tide is well expressed with forces along the x and y directions:

$$F_x = \Omega_0^2 x; \qquad F_y = \Omega_0^2 y, \tag{1.7}$$

where Ω_0 is the frequency of revolution of the Sun around the Galaxy, if the solar motion is supposed along a circular orbit. The disk component of the tide is due to a force along the z direction:

$$F_z = -4\pi G \rho_0 z, \tag{1.8}$$

where ρ_0 is the mass density in the solar neighborhood (see Heisler and Tremaine (1986) for the full galactic tide expressions). The disk component is stronger than the radial one by a factor 8-10 at solar distance, so in the past typically only the disk components was considered. Nowadays different works have pointed out the importance to include the radial components of the tide Masi et al. (2009) and also the real solar motion Gardner et al. (2011) (the radial motion and the motion across the galactic plane) and not just its circular approximation, to model a more realistic galactic perturbation on the Oort cloud.

In addition rare, but large perturbers are the giant molecular clouds (GMCs), that may be important for the long-term stability of the Oort cloud (Dones et al. (2004)), but their behavior is difficult to figure out.

Then we can summarize the perturbations acting on the Oort cloud in the following way:

- **The Stellar Perturbations**: is a perturbation that occurs at random and then may be treated as a stochastic process. A close or penetrating stellar passage through Oort cloud may deflect a large number of comets that enter in the planetary region forming a strong temporary enhancement of the flux of observable comets called "comet shower".

- **The Galactic Tidal Force**: is a quasi-integrable perturbation which acts continuously, changing the cometary orbital elements and in particular the perihelion distance. The galactic tidal produces a constant cometary flux in the inner part of Solar System.

- **The Giant Molecular Clouds**: a penetrating encounter of the Solar System with a GMC is a rare event, but it may have considerable effects, in particular a double action of erosion and mass increase that may change the dynamics of comets. However, due to the rarity (occurring with a mean interval of perhaps $3-4\times10^8$ yr Dones et al. (2004)) and the poor knowledge of the circumstances of such encounters, they are generally omitted from studies of Oort cloud dynamics.

The relative importance of these three different perturbations in the injection of new comets in the inner part of our planetary system was debated for long time. As we have seen in the first moment, the Galactic tidal perturbation was completed unknown, while in a second time became the most important one obscurating the stellar contribution. Lastly we can also add the GMCs' action, but its contribution is not completely understood . In recent work Fouchard et al. (2011) argued that the final solution could be that the injection process is dominated by a synergy between the major perturbers (stellar passages and galactic tide). While it may be that this synergy is largely due to the stars filling the "tidally active zone", from where the disk tide may bring the comets into observable orbits. In the frame of this synergy five different injection scenarios were identified in Fouchard et al. (2011). These processes are summarized in Fig. 1.7 in which they represent the generally decreasing trend of perihelion distance associated with injections by arrows directed toward the center.
The yellow region highlights the observable orbits, and the white, surrounding one represents the Jupiter-Saturn barrier[4]. The red and blue arrows show the evolution (increasing in time) due to the stellar impulses and the galactic tides, respectively. Dashed blue arrows are used to indicated how the tidal perturbation would have continued to act in the absence of the stellar impulse. The green arrows show the backward evolution starting from the time of the stellar perturbation, if only the tides are allowed to act. It was assumed, in order to simplify the model, that there is only one significant stellar impulse during the last revolution of the comet. The majority of all injections are encompassed in the cases numbered 1-4, but it could be useful to give a brief description of each case:

[4]New comets must have decreased their perihelion from $q > 10$ AU to $q < 5-3$ in less than an orbital period, otherwise, they would have encountered Jupiter and Saturn during an earlier evolution, and most likely they would have been ejected from the Solar System.

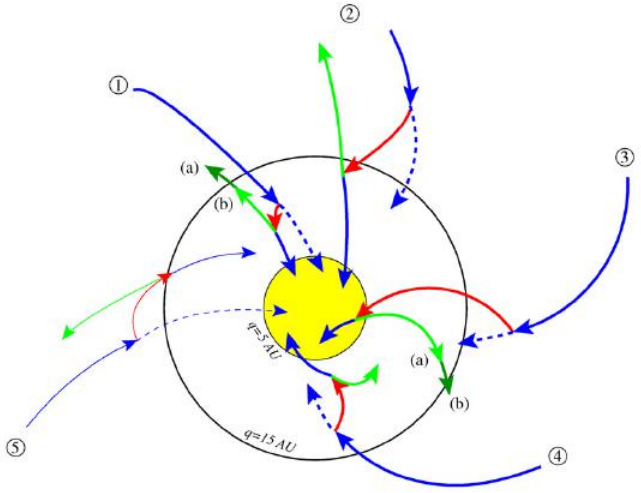

FIGURE 1.7: *Schematic representation of the variation in the angular momentum for different injection scenarios. The distance to the center in this diagram represents the angular momentum of the comets, i.e., the perihelion distance in the present case of quasi-parabolic orbits Fouchard et al. (2011).*

- **Case 1** refers to tidal injections, where the role of stellar perturbation is insignificant role. They may perturb the comets, thus affecting somewhat the post-injection orbits, but their effects in not crucial for the injection that occurred, even in their absence, because of the tides. It is possible to distinguish two subclasses called a and b, depending on the outcome of a backward integration with only tides. In case 1a, the comets cross the barrier into orbits with $q > 15$ AU, while in case 1b they do not.

- **Case 2** the injection would have failed in the absence of the stellar impulse. However, the stellar perturbation is not able to inject the comet by itself, it is only a helper to the tides.

- **Case 3** the star performs the injection with a insignificant tidal action. Also in this case is possible to distinguish two subclasses. The rare case $3b$ in which comets that get injected by a stellar impulse, would appear to have been tidally injected as judged from a purely tidal backward integration. Case $3a$ is the more common one, where the injected comets bear no clues of tidal injection.

- **Case 4** the perfect real-time synergy between the stars and tides where an injection is achieved, but it is impossible to ascribe it to either stars or tides: two mechanisms interact in a constructive way to ensure that the comets are injected.

- **Case 5** it must also happen that an injection, which the tides alone would have achieved, fails because of a stellar impulse.

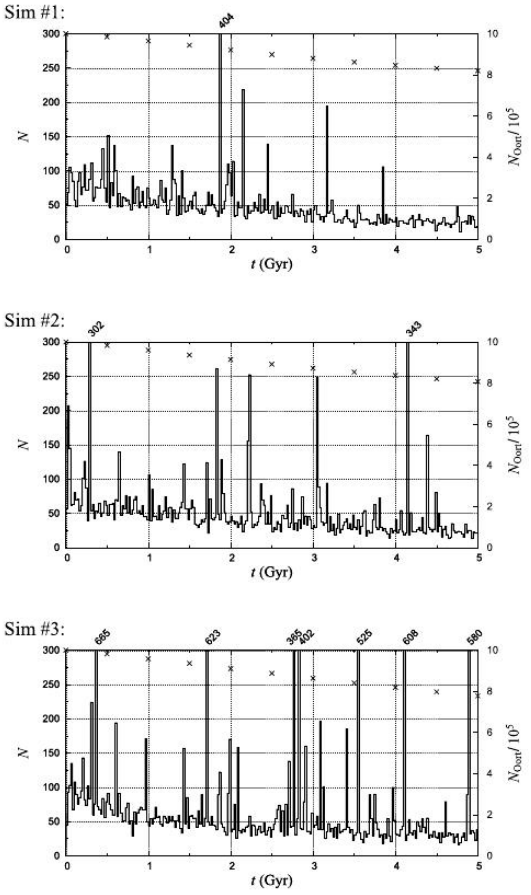

FIGURE 1.8: *Number of observable comets per interval of 20 Myr versus time for the three simulations. When the number exceeds 300, it is written above the respective graph. The crosses give the number of comets in the Oort cloud as counted every 500 Myr Fouchard et al. (2011).*

In Fouchard et al. (2011) was performed a simulation for the evolution of the Oort cloud over 5 Gyr for three different Oort clouds with 10^6 fictitious comets under the effect of the galactic tidal and of three different sample of 197906 stellar encounters occurring at random time, in order to understand the cooperation between the stellar and the tidal perturbation. The number of injected for each "Oort cloud" analogs comets is shown in Fig. 1.8, in which the threshold for the cometary injection is $q < 15$ AU. The large number of high peaks corresponding to the comet showers, while the background flux is the result of the tidal perturbation. From the simulation the authors were able to conclude that the number of injected comets peaks at semi-major axis $a \sim 33000$ AU, but the comets spread over a wide range around this value. The galactic tide is unable to inject any comets at $a < 23000$ AU but would be able to inject almost all of them at $a > 50000$ AU. The synergy between two perturbers are indentified to extend between $a \sim 15000$ AU and $a \sim 45000$ AU and to be the main contributor at $a \sim 25000$ AU.

1.3.2.1 Cometary Fading and Destruction

Oort pointed out in his 1950 paper Oort (1950) that the number of returning comets in the low continuous distribution decayed at larger values of E. That is, as comets random-walked away from the Oort cloud spike (see Fig. 1.6), the height of the low continuous distribution decline more rapidly than could be explained by a purely dynamical model using planetary and stellar perturbations. This problem is commonly referred to as *cometary fading*.
At the present moment it is still not clear what the exact mechanism for fading is. Three physical explanations have been proposed to figure out the failure to observed as many returning comets as are expected. These include:

1. random disruption or splitting due to, e.g., thermal stresses, rotational bursting, impacts by other small bodies, or tidal disruption Boehnhardt (2004);
2. loss of all volatiles;
3. formation of a nonvolatile crust or mantle on the nucleus surface Whipple (1950).

In these three cases the comet is referred to as, respectively, *disrupted*, *extinct* or *dormant*. In any case the "fading" mechanism must be a physical one: the missing comets cannot be removed by currently known dynamical process alone Wiegert and Tremaine (1999).

1.4 The formation of the Oort cloud

Comets have been driven into the Oort cloud through a scattering process induced by proto-planets combined with a Galactic tidal torque effect at the beginning of the history of the Solar System Tremaine (1993). Following Morbidelli (2005), in order to figure out this formation process we can imagine an early time when the Oort cloud was still empty and the giant planets' neighborhoods were full of icy planetesimals. The planets perturb with a scattering action the planetesimals, causing a dispersion throughout the Solar System. Some planetesimals were moved onto eccentric orbits with large semi-major axis, but with perihelion distance still in the planetary region. Those of them which reached a semi-major axis of $\sim$ 10000 AU achieved a position susceptible to a galactic tide strong enough to modify their orbit on a timescale of an orbital period. We denote the inclination of the comet relative to the galactic plane by $\widetilde{i}$ and the argument of perihelion by $\widetilde{\omega}$[5]. During the scattering process, these planetesimals remained relatively

[5] not to be confused with the inclination i and the argument of perihelion ω relative to the Solar System plane; the two planes are inclined at 120 degrees relative to each other.

close to the ecliptic plane, with an inclination relative to the galactic plane $\widetilde{i}$ of about $\sim 120°$. Due to their large e and $\widetilde{i}$ the effect of the tide dominated the evolution of e and $\widetilde{i}$. The planetesimals with $\widetilde{\omega}$ between 90° and 180° (or, symmetrically, between 270° and 360°) had their eccentricity decreased. In this way their perihelion achieved a distances beyond the planets' reach, so that they could not be scattered any more: they became Oort cloud objects. The precession of $\widetilde{\Omega}$ and the random passage of stars randomized the planetesimals' distribution, giving to the Oort cloud the spherical symmetry that is inferred from the observations.

This scenario, proposed for the first time in Kuiper (1951), was simulated in Fernandez (1978), Fernandez (1980b) using a Monte Carlo method to obtain the effects of repeated, uncorrelated encounters of the planetesimals with the giant planets and passing stars (the role of the galactic tide was not yet taken into account since its importance in this process was still unknown).

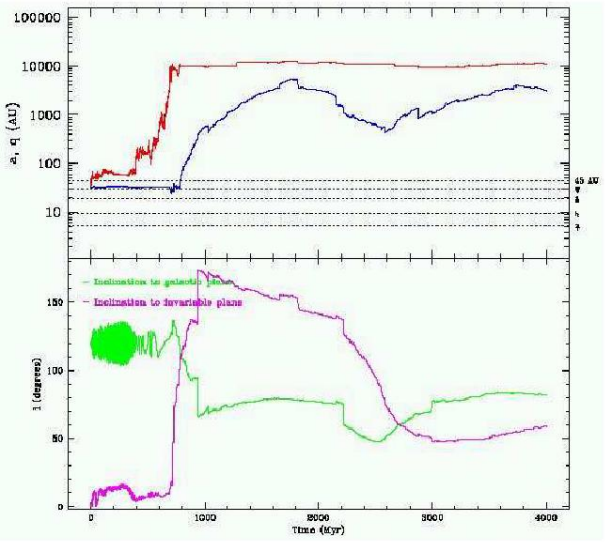

FIGURE 1.9: *Evolution of a comet from the vicinity of Neptune into the Oort cloud, from Dones et al. (2004). The top panel shows the evolution of the object's semi-major axis (red) and perihelion distance (blue). The bottom panel shows the inclinations relative to the galactic plane (green) and Solar System invariable plane (the plane orthogonal to the total angular momentum of the planetary system; in magenta).*

The extension to the galactic tide contribution during the formation of Oort cloud formation using direct numerical simulations was done in Duncan et al. (1987). In order to minimize the computing time, the simulations were started with comets already on low inclination, high eccentricity orbits: initial $a = 2000$ AU and q uniformly distributed between 5 and 35 AU. The integration scheme adopted was a generalization of that proposed by Stiefel and Scheifele (1971) for the restricted three-body problem with an additional conservative, perturbing potential Dybczyński et al. (2008). It was found that the density profile between 3000 and 50000 AU is roughly proportional to $r^{-3.5}$ (where

r is the heliocentric distance) and about 20% of comets, which survive inside the cloud after 4.5 Gyr, reside in the classical Oort cloud (semi-major axes, $a > 20000$ AU). The directional distribution of the orbits appeared completely randomized after about 1 Gyr of orbital evolution, apart from the most-inner part of the cloud.

A more recent simulation for the Oort cloud formation was performed by Dones et al. (2004), using more modern numerical simulation techniques. The initial conditions are more realistic, assuming planetesimals initially distributed in the 4-40 AU zone with small eccentricities and inclination. The giant planets were assumed to be on their current orbits, and the migration of planets was not taken into account. They also assumed that the Solar System was situated in a galactic environment identical to that presently observed, with the current frequency value of stellar passages around the Solar System and present density of galactic matter in the solar neighborhood. The evolution of the planetesimals was followed for 4 Gyr, under the gravitational influence of the 4 giant planets, the two components of the Galactic tide, and passing stars. A stellar density of $0.041 M_{\odot} pc^{-3}$ was setted at the beginning, with stellar masses distributed in the range $0.11 - 18.24 M_{\odot}$ and relative velocities between 1. 7 and 158 km/s (with a median value of 46 km/s). A total number of $\sim$ 50000 stellar encounters within 1 pc from the Sun occurred during the integration time of 4 Gyr in Dones et al. (2004). In order to understand the main processes that probably occurred during the formation of the Oort cloud, we can analyze the results of this work.

In Fig. 1.9 is possible to see an example of the evolution of a comet from the neighborhood of Neptune to the Oort cloud. With consecutive encounters, the object is first scattered by Neptune to larger semi-major axis, with a perihelion distance slightly beyond 30 AU, as typical of scattered-disk bodies. After about 700 My, the random walk in semi-major axis increases the body's semi-major axis up to $\sim$ 10000 AU. At this point the galactic tide action becomes significant, and the perihelion distance is rapidly lifted above 45 AU. Neptune's scattering action ceases to modify the orbit and the further changes in semi-major axis are due to the effects of distant stellar encounters. When the body starts to feel the galactic tide, its inclination relative to the galactic plane is 120 degrees. As the perihelion distance is lifted, the inclination decreases towards 90 degrees. A stellar passage causes a sudden variation of $\widetilde{i}$ down to 65° just before $t = 1$ Gy. This allows the galactic tide to act on the body, bringing the perihelion distance beyond 1000 AU and the inclination $\widetilde{i}$ up to 80° at $t = 1.7$ Gy, when $\widetilde{\omega}$ is 0 or 180 degrees. From this time onwards the galactic tide reverses its action, decreasing q and $\widetilde{i}$. In principle the action of the galactic tide is periodic, so that the object's perihelion should be decreased back to planetary distances. This reversibility is broken by the jumps in $a, q, \widetilde{i}$ due to the stellar encounters: the oscillation of q becomes more shallow and the return of the object into the planetary region is impeded within the age of the Solar System. During this evolution, a strong change occurs in the inclination relative to the invariable plane.

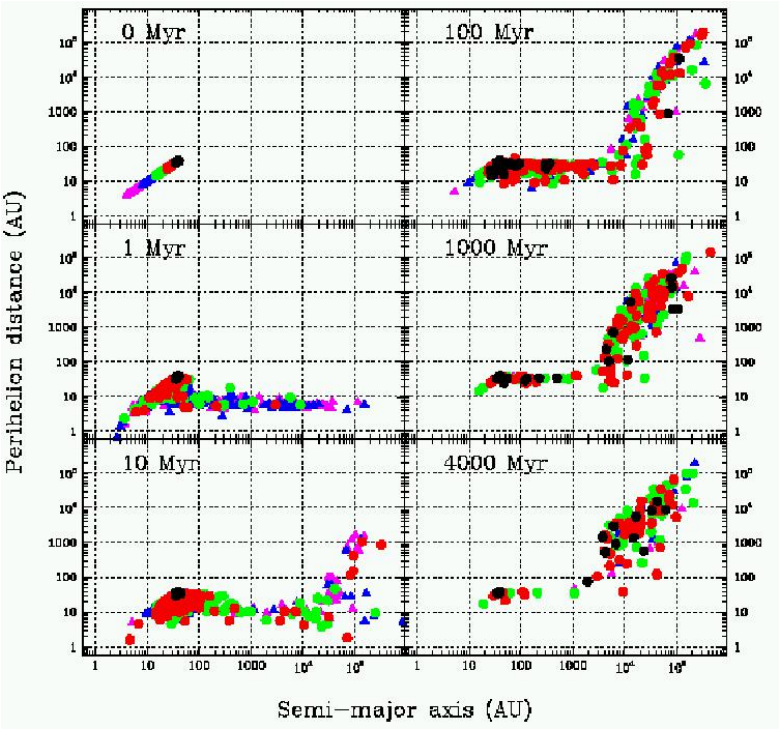

FIGURE 1.10: *Scatter plot of osculating barycentric pericenter distance vs. osculating barycentric semi-major axis, at various times in the Oort cloud formation simulations of Dones et al. (2004), see text..*

It is turned to retrograde, and then back to prograde values, as the longitude of galactic node $\widetilde{\Omega}$ precesses.

Not all particles follow this evolution previously described. It was found that if the objects have a close interaction with Jupiter and Saturn, they are mostly ejected from the Solar System. Particles that experienced a distant encounters with Saturn are transported more rapidly and further out in semi-major axis with respect to the evolution shown in Fig. 1.9. The perturber action of the galactic tide increases with a; thus, for the comets that are scattered to $a \sim 20000$ AU or beyond, the oscillation period of q and $\widetilde{i}$ is shorter than for the particle in Fig. 1.9.

Figures 1.10 and 1.11 are snapshots of the (a, q) and (a, i) distributions of all planetesimals from the beginning to the end of the simulation, with planetesimals color-coded according to their initial position: Jupiter region objects are magenta; Saturn region objects are blue; Uranus region objects are green; Neptune region objects are red and trans-Neptunian objects are black. In Fig. 1.10 is possible to see the formation of a scattered disk after only 1 Myr, operated by Jupiter and Saturn, out of particles initially in the Jupiter-Uranus region, while particles originally in Neptune's region or beyond have not been scattered out yet. This scattered disk differs from the current one because most of its objects have $q < 10$ AU. At 10 Myr the action of the galactic tide starts to be visible: particles with $a > 30000$ AU, mostly from Jupiter-Saturn region, have

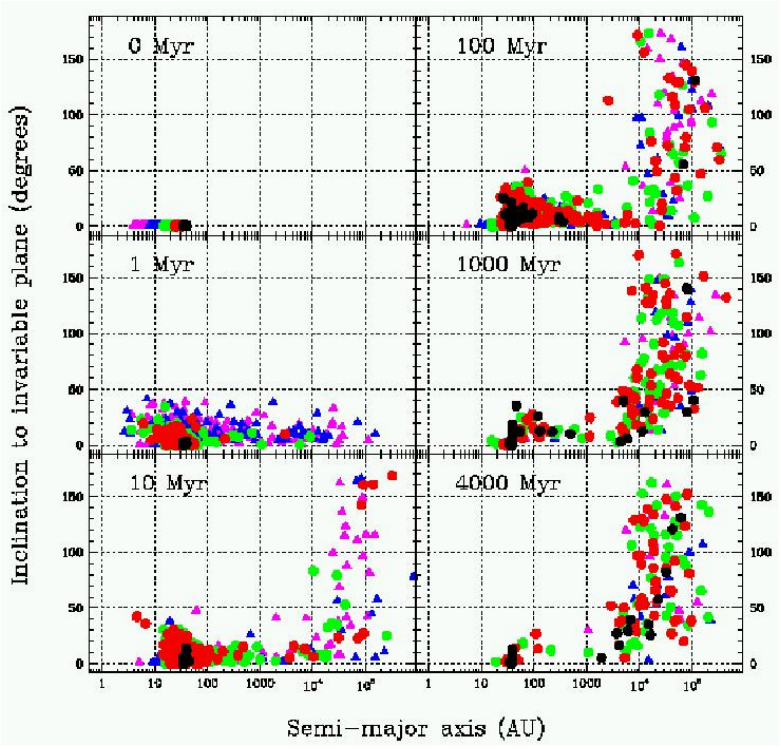

FIGURE 1.11: *Scatter plot of osculating barycentric inclination relative to the Solar System mid-plane vs. osculating barycentric semi-major axis, at various times in the Oort cloud formation simulations of Dones et al. (2004), see text..*

their perihelia lifted beyond the orbits of the planets and Neptune's particles start to populate the scattered disk. From 100 Myr to 1 Gyr, a continuous flux of particles enters in the Oort cloud from the scattered disk. The population of the Oort cloud achieves its maximum at 840 Myr, when 7.55% of the initial particles occupy the cloud. Objects from the Uranus-Neptune region gradually replace those from Jupiter-Saturn zone. The latter have been lost during stellar encounters, as they predominantly occupied the very outer part of the Oort cloud ($a > 30000$ AU). The *inner Oort cloud* usually corresponds to semimajor-axis values $a < 20000$ AU. The distribution in Fig. 1.10 at 4 Gy, should correspond to the current structure of the Oort cloud. The distribution does not differ very much from that we have at 1 Gyr, but the Oort cloud population has declined slightly in number.

Another point of view to look at the Oort cloud formation processes is represented in Fig. 1.11 by evolution of the particles inclinations. After 1 Myr the planets have scattered the comets into moderately inclined orbits. After 10 Myr is clear the participation of the galactic tide and the passing stars to the evolution of the particles with $a > 30000$ AU, that have been perturbed into a nearly isotropic distribution of inclinations. As time continues, tides affect the inclinations of particles closer to the Sun, so that at 4 Gyr inclinations are clearly isotropic for $a > 20000$ AU.

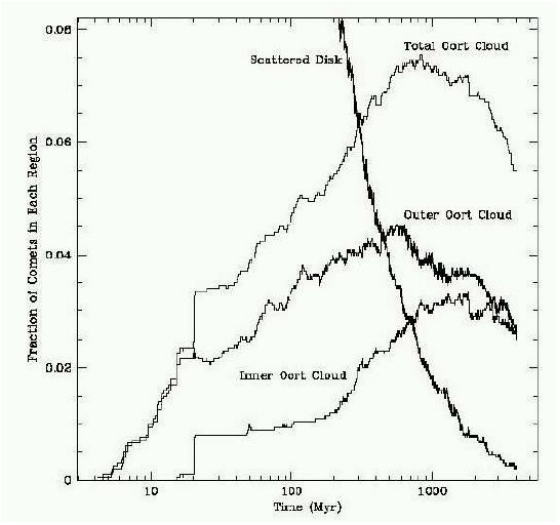

FIGURE 1.12: *Fraction of the initial planetesimal population that is in the Oort cloud, in its inner and outer parts and in the scattered disk, as a function of time Dones et al. (2004).*

The final Oort cloud's population is almost equally divided in the inner and outer parts, with radial distribution $N(r)/\mathrm{d}r \propto 1/r^3$. About 5% to 9% of the planetesimals initially in the Uranus-Neptune-transneptunian region remain in the Oort cloud at the end of the simulation. Conversely, only 2% of the planetesimals originally in the Jupiter-Saturn region are collected in the cometary cloud, due to the too strong scattering action of these planets, that pushes the particles directly from a scattered-disk orbit to unbound orbit, without passing through the Oort cloud. These result are slightly revisited by the more recent work Dybczyński et al. (2008), in which the authors point out the possibility that the Jupiter-Saturn region should have given a stronger contribution to populate the Oort cloud, so it could be possible that not all (or almost all) the Oort cloud comets formed in a cool region of the solar nebula, as it believes nowadays

Figure 1.12 shows the evolution of the mass in the Oort cloud as a function of time, highlighting that formation and erosion are not separate processes in the Oort cloud. Throughout the Solar System history, in parallel with new planetesimals entering the Oort cloud from the scattered disk, other comets left the cloud, because the galactic tide pushed their perihelion back into the planetary region or passing stars put them on hyperbolic orbits. The mass in the cloud peaks at about 800 Myr, before this maximum the formation process dominated over the erosion process. Then, because the mass of the scattered disk dropped, the erosion process became predominant, and the total mass in the cloud decayed to $\sim 5.5\%$ of the mass originally in the planetesimals' disk. The outer Oort cloud formed faster then the inner cloud, because of the contribution of planetesimals from Jupiter-Saturn region, but then it eroded faster, because its objects are less gravitationally bound to the Sun.

In disagreement with observations, in the simulation Dones et al. (2004) obtained a far

larger simulated population in the scattered disk, with respect to the population of the Oort cloud and an original mass in planetesimals, between 4 to 40 AU, that exceed between 2 and 8 times the mass of solids in the minimum-mass solar nebula.
Also for the formation and evolution of our cometary cloud a full agreement between the different performed simulations and the observed data has not been completely achieved. Furthermore a new and important feature could play a crucial role in the shape and evolution of the Oort cloud: the solar migration through the Galaxy. The motion of the Sun inside the galactic disk should completely change the environment in which the Oort cloud formed, with significant repercussions on this structure. A first tentative step to include the solar migration has been done by Kaib et al. (2011) as we see in §3.1.

1.5 Exo Oort cloud

1.5.1 "Oort-type comet Cloud" structure around different stars

Comets represent the remnants of the formation of our planetary system, for this reason a comet cloud similar to the Oort cloud is probably a common feature around extra solar planetary systems spread out inside the Galaxy. The existence of other comet clouds in different planetary systems is suggested by recent evidences of dusty excess on debris disks in exoplanetary systems observed by Spitzer at 70 μm Greaves and Wyatt (2010). From this point of view it could be interesting to apply our understanding of the formation of the Oort cloud to deduce the properties of Oort-type comet clouds around other stars, that kind of analysis was made by Tremaine (1993).
As we have already seen, comets remaining in the disk after planet formation have two possible dynamical fates: comets on near-circular orbits that are well separated from the planets will survive on these orbits with little or no dynamical evolution, while comets on orbits that approach too close to a planets are chaotic and could became planet-crossing orbits.
In Tremaine (1993) an Oort-type cloud is defined to be a roughly spherical distribution of bound comets with typical semi-major axis a_f, formed by ejection of comets from a planetary system with characteristic size $a_p << a_f$.

1.5.2 Constraints for the formation of Oort-type comet clouds

Following Tremaine (1993), we consider a system containing a central star of mass M_*, a single planet of mass M_p on a circular orbit of radius a_p, and a number of comets in planet-crossing orbits.
Usually, ejection occurs by a gradual random walk or diffusion of the comet orbit towards

escape energy. This process leads to highly eccentric orbits, since the semi-major axis of the comet a becomes large while its perihelion q remains comparable to a_p. The comet receives a kick from the planet' s gravity each time it passes through perihelion; the orbit is chaotic because the kick depends on the phase of the planet in its orbit.
As usual it is possible to describe the cometary energy as $x \equiv 1/a$, and we can also introduce the *diffusion coefficient* $D_x = \langle(\Delta x)^2\rangle^{1/2}$ be the root mean square change in x per perihelion passage arising from planetary perturbations. Numerical integrations of highly eccentric, low-inclination, planet crossing orbit yield Duncan et al. (1987)

$$D_x \simeq \frac{10}{a_p}\frac{M_p}{M_*}. \tag{1.9}$$

The characteristic *diffusion time* is then

$$t_{diff} \equiv P\frac{x^2}{D_x^2}, \tag{1.10}$$

dove $P = 2\pi a^{3/2}/(GM_*)^{1/2}$ is the comet orbital period. Thus

$$t_{diff}(x) = 1.1 \times 10^9 \text{ yr} \left(\frac{M_*}{M_\odot}\right)^{3/2} \left(\frac{M_p}{M_\oplus}\right)^{-2} \left(\frac{x}{1 \text{ AU}^{-1}}\right)^{1/2} \left(\frac{a_p}{1 \text{ AU}}\right)^2. \tag{1.11}$$

The diffusion rate speeds up (t_{diff} decreases) as the comet energy increases (x decreases). Initially the comets are on orbits similar to the planetary one, so we have $x \approx a_p^{-1}$. It means that the orbit evolution occurs if and only if

$$t_{ev} \equiv t_{diff}(x = a_p^{-1}) \lesssim t_*, \tag{1.12}$$

where t_* is the age of the planetary system. Substituting in the previous expression the definition for t_{diff} we obtain:

$$\begin{aligned} t_* \gtrsim t_{diff}(x = a_p^{-1}) &= 1.1 \times 10^9 \text{ y} \left(\frac{M_*}{M_\odot}\right)^{3/2} \left(\frac{M_p}{M_\oplus}\right)^{-2} \left(\frac{a_p^{-1}}{1 \text{ AU}^{-1}}\right)^{1/2} \left(\frac{a_p}{1 \text{ AU}}\right)^2 \\ &= 1.1 \times 10^9 \text{ y} \left(\frac{M_*}{M_\odot}\right)^{3/2} \left(\frac{M_p}{M_\oplus}\right)^{-2} \left(\frac{a_p}{1 \text{ AU}}\right)^{3/2} \end{aligned}$$

from which we can isolate $\left(\frac{M_p}{M_\oplus}\right)$ obtaining:

$$\left(\frac{M_p}{M_\oplus}\right)^2 \gtrsim \frac{10^9}{t_*} \left(\frac{M_*}{M_\odot}\right)^{3/2} \left(\frac{a_p}{1 \text{ AU}}\right)^{3/2}. \tag{1.13}$$

From the previous expression we can find a necessary condition for the formation of an Oort-type comet cloud is:

$$\frac{M_p}{M_\oplus} \gtrsim \left(\frac{t_*}{10^9}\right)^{-1/2} \left(\frac{M_*}{M_\odot}\right)^{3/4} \left(\frac{a_p}{1\ \mathrm{AU}}\right)^{3/4}. \tag{1.14}$$

In an isolated system, most comets on planet-crossing orbits would escape in a few times t_{ev}. However in practice, once the orbit becomes large, the torque from the Galactic tide changes the orbital angular momentum and thus the perihelion distance q. Once q is a few times a_p, planetary perturbations become ineffective, and the random walk of the comet's energy ceases: planet-induced diffusion in energy at fixed angular momentum is replaced by Galaxy-induced evolution in angular momentum at fixed energy. For highly eccentric orbits, we can express the specific angular momentum:

$$L = (2GM_* q)^{1/2} \approx (2GM_* a_p)^{1/2} \tag{1.15}$$

and its torque per unit mass is:

$$\frac{\mathrm{d}L}{\mathrm{d}t} = 5\pi k G \rho a^2 \tag{1.16}$$

where ρ is the local Galactic mass density ($\rho = 0.15 M_\odot\ \mathrm{pc}^{-3}$ in Tremaine (1993) that we are following, values slightly different are possible in the literature) and k is a geometrical factor that varies between 0 and 1 depending on the orientation of the orbit Heisler and Tremaine (1986). The time required for the Galactic tide to change the angular momentum by of order itself if then Duncan et al. (1987)

$$t_{tide} = 1 \times 10^{15}\ \mathrm{yr} \left(\frac{M_*}{M_\odot}\right)^{1/2} \left(\frac{\rho}{0.15 M_\odot\ \mathrm{pc}^{-3}}\right)^{-1} \left(\frac{q}{1\ \mathrm{AU}}\right)^{1/2} \left(\frac{x}{1\ \mathrm{AU}^{-1}}\right)^{2}. \tag{1.17}$$

Tidal torques freeze the comet out of the random walk in energy at the semi-major axis a_f where $t_{tide}(q = a_p) = t_{diff}$, that is

$$a_f = 10^4\ \mathrm{AU} \left(\frac{M_*}{M_\odot}\right)^{-2/3} \left(\frac{\rho}{0.15 M_\odot\ \mathrm{pc}^{-3}}\right)^{-2/3} \left(\frac{M_p}{M_\oplus}\right)^{4/3} \left(\frac{a_p}{1\ \mathrm{AU}}\right)^{-1}. \tag{1.18}$$

Many comets escape on their next orbit if $x = 1/a \lesssim D_x$. Thus freezing is an effective barrier to the escape process only if

$$\frac{1}{a_f} \gtrsim D_x; \tag{1.19}$$

or in other words if there is a significant amount of energy at the end of that process. This condition implies that many of the comets escape unless

$$\frac{M_p}{M_\oplus} \lesssim 1.7 \left(\frac{M_*}{M_\odot}\right)^{5/7} \left(\frac{\rho}{0.15 M_\odot \text{ pc}^{-3}}\right)^{2/7} \left(\frac{a_p}{1 \text{ AU}}\right)^{6/7}. \tag{1.20}$$

The frozen comets form an extended disk in the plane of the planets, which is steadily thickened by perturbations from passing stars and the Galactic tide. The timescale to convert the disk into a roughly spherical cloud is simply t_{tide}, evaluated at $q = a = a_f$. The requirement that this timescale be less than the age t_* yields the condition expressed by Eq. 1.14. Thus comet clouds formed by this process should be approximately spherical.

The cloud can not extend beyond the Roche surface of the star, set by the tidal field of the Galaxy. The size of the Roche surface can be roughly estimated by comparing the tidal force between two points separated by a vertical distance z, $4\pi G\rho z$, to the star's gravitational force at that distance, GM_*/z^2. If we denote the distance at which these forces are equal as the Roche or tidal radius a_t, we have

$$a_t = 1.7 \times 10^5 \text{ AU} \left(\frac{M_*}{M_\odot}\right)^{1/3} \left(\frac{\rho}{0.15 M_\odot \text{ pc}^{-3}}\right)^{-1/3}. \tag{1.21}$$

Planets cannot survive outside the tidal radius, so

$$a_p \lesssim a_t. \tag{1.22}$$

A comet cloud can only form if the freezing semi-major axis is less than the tidal radius, $a_f \lesssim a_t$, substituting in the corresponding expressions we obtain

$$\frac{M_p}{M_\oplus} \lesssim 8 \left(\frac{M_*}{M_\odot}\right)^{3/4} \left(\frac{\rho}{0.15 M_\odot \text{ pc}^{-3}}\right)^{1/4} \left(\frac{a_p}{1 \text{ AU}}\right)^{3/4}, \tag{1.23}$$

If the previous condition is not satisfied, the value of a_f is so high to unbound the comet to the cloud.

In addition the formation process as described here only applies if the freezing semi-major axis exceeds the planet's semi-major axis $a_f \gtrsim a_p$, which implies

$$\frac{M_p}{M_\oplus} \gtrsim 10^{-3} \left(\frac{M_*}{M_\odot}\right)^{1/2} \left(\frac{\rho}{0.15 M_\odot \text{ pc}^{-3}}\right)^{1/2} \left(\frac{a_p}{1 \text{ AU}}\right)^{3/2}. \tag{1.24}$$

An additional constraint is that the comets must not impact the planet before they diffuse to the cloud. Comets initially on orbits with $a \approx a_p$ make roughly $N = (x_p/D_x)^2$ orbits before reaching the cloud. If their typical inclination is $\Delta\theta$ and the escape speed from the planets is less that the orbital speed so that the gravitational focusing is

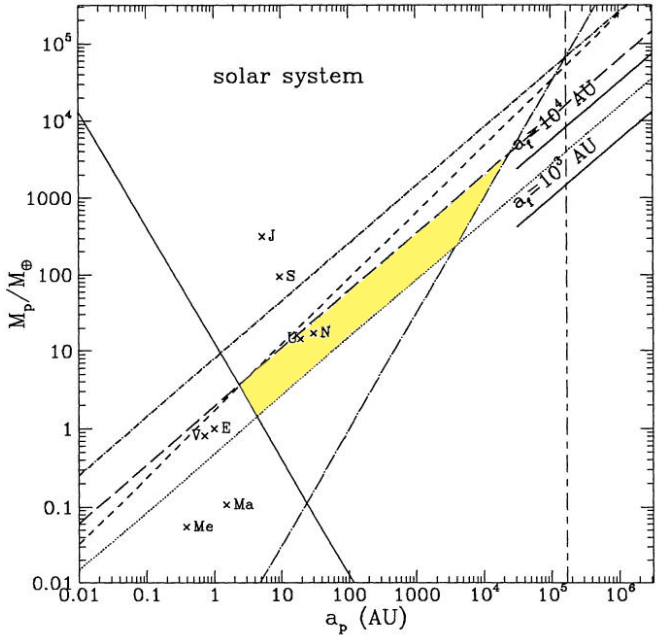

FIGURE 1.13: *A plot of planet mass against semi-major axis showing the region that are able to create an Oort-type cloud efficiently for the Solar System (yellow region), see text. The constraints plotted are: Eq. 1.14 (dotted line); Eq. 1.20 (short-dashed line); Eq. 1.22 (vertical short dash-long dashed line); Eq. 1.23 (dot-short dashed line); Eq. 1.24 (dot-long dashed line); 1.26 (solid line); Eq. 1.28 (long-dashed line) Tremaine (1993).*

negligible, the impact probability on each perihelion passage is

$$p = \frac{\left(\frac{R_p}{a_p}\right)^2}{\Delta\theta}, \tag{1.25}$$

where R_p id the planetary radius. In order that most of the comets do not strike the planet we must have $N_p \lesssim 1$ or

$$\frac{M_p}{M_\oplus} \gtrsim 13 \left(\frac{M_*}{M_\odot}\right)^{3/2} \left(\frac{a_p}{1\text{ AU}}\right)^{-3/2} \left(\frac{\rho_p}{3\text{ g cm}^{-3}}\right)^{-1/2} \left(\frac{\Delta\theta}{0.1\text{ rad}}\right)^{-3/4}, \tag{1.26}$$

where ρ_p is the planet density.

Comets are ejected from the cloud by gravitational perturbations from passing stars and other objects. The half-life of a comet orbiting a star in a region with kinematics similar to the solar neighborhood is Weinberg et al. (1987)

$$t_{1/2} = 10^{10}\text{ yr} \left(\frac{M_*}{M_\odot}\right) \left(\frac{10^4\text{ AU}}{a}\right) \left(\frac{\rho}{0.15 M_\odot\text{ pc}^{-3}}\right)^{-1}. \tag{1.27}$$

This result neglects the uncertain contribution from the molecular clouds, and is strictly valid only $a << a_t$. Replacing a by the cloud radius a_f and requiring that $t_{1/2}$ exceed

the age of the system t_* we obtain the last constraint

$$\frac{M_p}{M_\oplus} \lesssim 6 \left(\frac{M_*}{M_\odot}\right)^{5/4} \left(\frac{t_*}{10^9 \text{ y}}\right)^{-3/4} \left(\frac{\rho}{0.15 M_\odot \text{ pc}^{-3}}\right)^{-1/4} \left(\frac{a_p}{1 \text{ AU}}\right)^{3/4}. \tag{1.28}$$

Then we found the range $\frac{M_p}{M_\oplus}$ for which the formation of an Oort-type cloud is possible. That range is given by the intersection of all the constraints for the birth of the cloud itself.

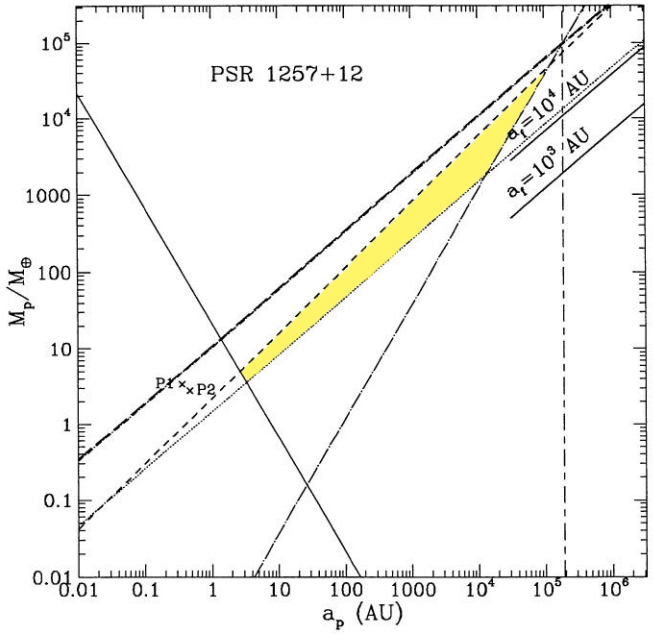

FIGURE 1.14: *The same constraints plotted in Fig. 1.13, except the parameters are chosen to match those of the pulsar: a* $1.4 M_\odot$ *star of age* 0.8×10^9 *yr, located in solar neighborhood Tremaine (1993).*

1.5.3 Applications

In Fig. 1.13, obtained by Tremaine (1993), are showed the constraints discussed in the previous paragraph for parameters appropriate for the Solar System: $M_* = 1 M_\odot$, $t_* = 4.5 \times 10^9$ yr and $\rho = 0.15 M_\odot pc^{-3}$. The positions of the eight planets are also plotted and the region of parameter space allowed by the constraints is highlight. We can summarize the results as follow:

- Comets crossing the orbit of Jupiter and Saturn can not create an Oort-type cloud: the planet are so massive that most comets are ejected. The consequence is that Oort cloud comets must come from the Uranus-Neptune region.
- The typical semi-major axis of the comet cloud formed by Uranus or Neptune is $a_f \approx 10^4$ AU, close to the semi-major axes of new comets.

- Venus and Earth could not efficiently form an Oort-type cloud, even if the massive outer planets were not present: most comets on Venus- or Earth-crossing orbits collide with these planets before reaching the cloud.

- At any planetary semi-major axis a_p there is only a narrow range (less than a factor 5) of planetary masses that are large enough to create a cometary cloud within the Solar System age, yet small enough not to eject most comets.Within this allowed range, the typical size of the comet cloud, a_f, is almost independent of a_p. Outside this range, cloud formation can still occur, but with low efficiency.

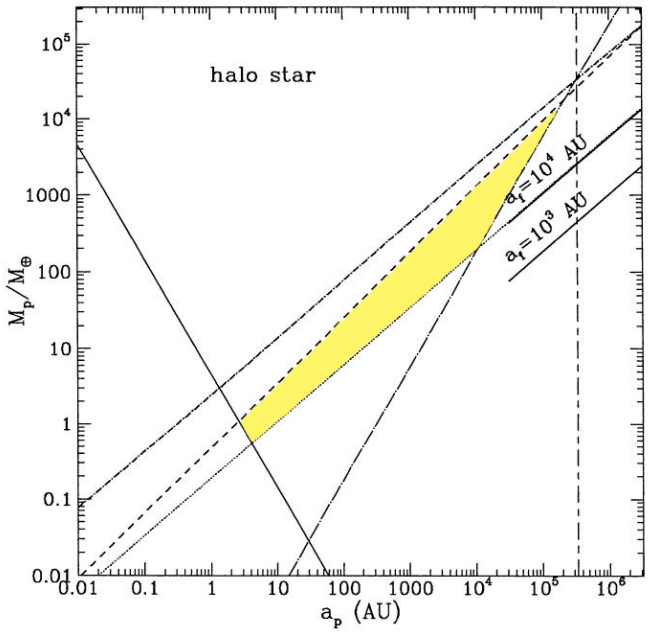

FIGURE 1.15: *The same constraints plotted in Fig. 1.13 but with parameters chosen to represent those of halo stars than the Solar System: a* $0.5M_\odot$ *star with an age of* 10^{10} *yr, and a local density of* $0.01M_\odot$ pc^{-3}. *The constraint that comets are not ejected by passing stars or other objects is not plotted, since the effects of such stars are weak Tremaine (1993).*

Exploring different possible planetary environment, Tremaine (1993) also analyzed the constraints for a planetary system around a pulsar (in particular PSR1257+12) and a typical halo star.

Fig. 1.14 plots the same previous constraints for PSR1257+12 $M_* = 1.4M_\odot$, $t_* = 8\times10^8$ yr, and a planetary semi-major axes and massed: $a_{p1} = 0.36$ AU, $a_{p2} = 0.47$ AU, $M_{p1} = 3.4M_\oplus$, $M_{p2} = 2.8M_\oplus$. The conditions on the planets that can efficiently form an Oort-type cloud are similar to those in the Solar System. However, the allowed range of parameter space is even smaller, mainly because more massive planets are needed to create a cloud within the shorter age of the system. Comets crossing the orbits of the planets would mostly be ejected or collide with the planets. Those that did manage to reach the cloud would be found at semi-major axes of a few times 10^4 AU.

Finally Fig. 1.15 shows the case of the formation of Oort cloud around a typical halo star ($M_* = 0.5, t_* = 10^{10}$ yr, $\rho = 0.01 M_\odot$ pc^{-3}). The constraints are qualitatively similar to those for the Solar System, but the planets that are most effective in producing a cloud are about a factor three smaller at a given semi-major axis.

This theoretical analysis could be very useful in order to understand which are the physical processes that drive the formation of a cometary cloud like our Oort cloud. On the other hand is also important to underline that the previous treatment is based on many assumptions and does not consider the perturbations due to a multiple planetary system.

2

The Galactic Environment

The starting point for the study of the dynamical behavior of a comet cloud in the Galactic potential is to build a realistic matter distribution for the most important dynamical components of the Milky Way. In the next paragraphs the description and the values for the main parameters for bulge, disk and dark matter halo will be provided in details.

2.1 The model for the Milky Way

A standard method in many dynamical problems is to build the galactic potential as a simple azimutally symmetric Galactic model, and decompose the total mass distribution in its different symmetric components, i.e. the bulge, the disk and the dark matter (DM) halo. This approach does not take into account of irregularities and asymmetries in the mass distribution (like the spiral structure, the bulge triaxial form), that may be have an non-neglected importance for the dynamics inside the Galaxy. Moreover the axisymmetric model is the first step on the way to build a more sophisticated pattern for our Galaxy as we will consider in the next chapter. The following sections are then dedicate to a brief description of this basic axisymmetric model.
We define a the total Galactic potential $\Phi(R, z)$, in which R is the Galactocentric radius and z the distance above the plane of the disk. The complete dynamical effect of the Galaxy could be expressed by the sum of the potentials due to bulge (Φ_{BG}), disk (Φ_D) and DM halo (Φ_{DH}):

$$\Phi_G = \Phi_{BG} + \Phi_D + \Phi_{DH} \tag{2.1}$$

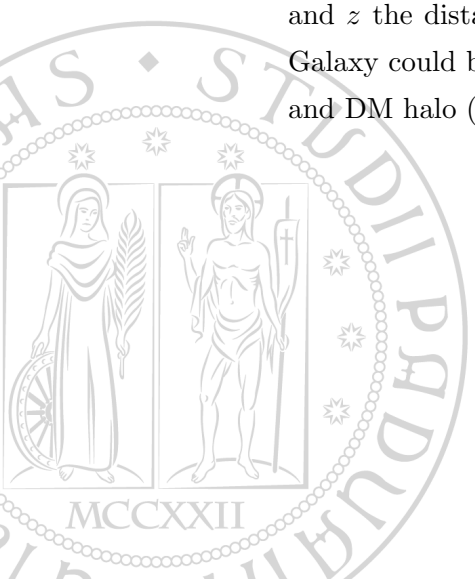

2.1.1 The Bulge

The bulge is one of the less extended components of our Galaxy: its maximum radius is evaluated between 2.5 - 3.5 kpc. For our aims its triaxial structure may be neglected considering as a good approximation the spherical model of the *Plummer sphere*, see Binney and Tremaine (2008), that has the following analytical expression for its gravitational potential:

$$\Phi_{BG}(r) = -\frac{GM_{BG}}{\sqrt{r^2 + r_c^2}} \tag{2.2}$$

where $M_{BG} = 1.6 \times 10^{10}$ $M_\odot$ is the bulge total mass and $r_c = 0.42$ kpc is the *core radius* Flynn et al. (1996).

2.1.2 The Disk

The disk presents a mixed composition in age, metallicity, velocity and velocity dispersion of its stars that complicates the disk modeling based on radial and vertical mass-luminosity distributions. A wide range of options is available in the literature, as shown by Binney and Tremaine (2008), to model a three-dimensional axisymmetric disk distinguishing the two main contributions due to the *thin* and the *thick* disk as discovered by Burstein (1979). Because the existence of the thich disk as a distinct component appears to be uncertain Bovy et al. (2012) and owing to its contribution to the total surface density is only of about 5% at solar distance Dehnen and Binney (1998), as first approximation we limit ourselves only to consider the *thin* disk.
Our starting point is the infinitely thin Freeman model Freeman (1970), having an exponential radial surface mass density distribution:

$$\Sigma(R) = \Sigma_0 e^{-R/R_d}, \tag{2.3}$$

where $\Sigma_0 \simeq 359$ $M_\odot$ pc^{-2} is the central disk surface mass density and $R_d = 4.1$ kpc is the disk scale length in agreement with the observations provided by Lewis and Freeman (1989) and with the surface density at the solar distance $\Sigma_0(R_\odot) \simeq 50$ $M_\odot$ pc^{-2} (see Kuijken and Gilmore, 1991).

The corresponding potential for the mass distribution (2.3) is:

$$\Phi_D(R) = -\pi G \Sigma_0 R \left[I_0(R/2R_d) K_1(R/2R_d) - I_1(R/2R_d) K_0(R/2R_d) \right], \tag{2.4}$$

where I_n and K_n are modified Bessel functions of order n. Even when using Hankel transform and the cylindrical Bessel function of order zero, J_0, obtaining a two-dimensional

gravitational potential $\Phi_D(R,z)$, this kind of modeling is affected by two difficulties: the typical vertical extension of our comet orbits turns to be less than the scale height observed for the Galaxy disk which is about 200 pc, with the consequence that only a fraction of the whole disk mass is involved in the tide; moreover this parametrization of the disk potential is slow to integrate. We may overcome both the problems combining three Miyamoto-Nagai disks Miyamoto and Nagai (1975) of differing scale lengths and masses:

$$\Phi_{MN}(R,z) = -\sum_{n=1}^{3} \frac{GM_n}{\sqrt{R^2 + \left[a_n + \sqrt{b^2+z^2}\right]^2}}. \tag{2.5}$$

The parameter b is related to the disk scale height, a_n to the disk scale lengths and M_n are the masses of the three disk combined components. We list the values of the constants a_n, b, M_n, according with Flynn et al. (1996), in Tab. 2.1. It is to be noticed that the potential trend given by (2.4) results in fair agreement with that provided by Eq. (2.5) at the mid-plane ($z = 0$).

Component	**Parameter**	**Value**
Bulge	M_{BG}	$1.6 \times 10^{10} M_\odot$
	r_c	0.42 kpc
Disk	a_1	5.81 kpc
	a_2	17.43 kpc
	a_3	34.86 kpc
	b	0.3 kpc
	M_1	$6.6 \times 10^{10} M_\odot$
	M_2	$-2.9 \times 10^{10} M_\odot$
	M_3	$3.3 \times 10^{9} M_\odot$
Dark Halo (NFW)	r_H	12.36 kpc
	$\rho_{1/2}$	$0.02166 M_\odot$ pc^{-3}
	$V_{Tot}(R_\odot)$	233.805 km s^{-1}
	R_{vir}/r_H	17
Dark Halo (MPI)	r_H	12.36 kpc
	ρ_0	$0.01566 M_\odot$ pc^{-3}
	$V_{Tot}(R_\odot)$	196.003 km s^{-1}
	R_{vir}/r_H	20

TABLE 2.1: Parameter values for each galactic components.

2.1.3 The DM Halo

The Galactic mass distribution of the DM halo is still uncertain and there are several models in the literature. The general representation of the DM spherical distribution is given by the *Zhao's radial density profiles* Zhao (1996):

$$\rho(r) = \frac{\rho_S}{\left(\frac{r}{r_H}\right)^{\gamma}\left[1+\left(\frac{r}{r_H}\right)^{\alpha}\right]^{\frac{\beta-\gamma}{\alpha}}} \tag{2.6}$$

where α, β and γ are three slope parameters, while r_H and ρ_S are two scale parameters. This pattern models the density as a double power law with a limit slope $-\gamma$ toward the center of the halo ($r \to 0$) and $-\beta$ to the infinity ($r \to \infty$).
Inside this general class of mass profiles we consider two alternative formulations: the first coming from the numerical simulations and the second one from the observations. We refer firstly to the Navarro-Frank-White (NFW) Navarro et al. (1997) density profile. It was obtained by N-body simulations in an hierarchical clustering cosmological scenario (CDM) and it could be reproduced by (2.6) with $(\alpha, \beta, \gamma) = (1, 3, 1)$, and scale density[1]: $\rho_S = \rho(\frac{1}{2}r_H) = \rho_{crit} \cdot \delta_c$, where ρ_{crit} and δ_c are respectively the critical density and the overdensity on the mass scale of DM halo scaled from formation epoch to $z = 0$. Introducing the virial radius R_{vir}, the NFW gravitational potential turns to be:

$$\Phi_{DH}^{NFW}(r) = -4\pi G\rho_S r_H^2 \left(\frac{\ln(1+r/r_H)}{r/r_H} - \frac{1}{1+R_{vir}/r_H}\right), \tag{2.7}$$

The second profile is a modified pseudo-isotherm (MPI) Spano et al. (2008) that has been introduced to obtain the best fits of rotation curves in spiral galaxies, taking into (2.6), $(\alpha, \beta, \gamma) = (2, 3, 0)$).
The corresponding gravitational potential is given by:

$$\Phi_{DH}^{MPI}(r) = -4\pi G\rho_0 r_H^2 \left(\frac{\ln\left(r/r_H + \sqrt{1+\left(\frac{r}{r_H}\right)^2}\right)}{r/r_H} - \frac{1}{\sqrt{1+\left(\frac{R_{vir}}{r_H}\right)^2}}\right). \tag{2.8}$$

with ρ_0 the central dark halo density. The two profiles are characterized by different limits for the inner slopes: the NFW model has a slope limit equal to -1, while the MPI presents an inner slope limit equal to 0. The choice between the two previous models for the DM halo opens the wide cusp/core chapter. Whithout entering the complex, still open problem, we may summarize it as a deep mismatch between the DM

[1] Introducing the normalization of the general profile (2.6) at r_H, the scale density becomes: $\rho_S = \rho(r_H) \cdot 2^{\chi}; \chi = (\beta - \gamma)/\alpha$.

model provided by the collisionless simulations and by the observational data. Strictly speaking, if the radial density profile for DM halo toward the center follows an universal trend $\rho(r) \propto r^{-\gamma}$, we have a *cuspy profile* for $\gamma \geq 1$ (e.g., NFW profile) and a *cored profile* for $\gamma < 1$ (e.g., MPI profile). At this time a definitive answer does not exist, even if there are some lines of evidence that suggest 0.4 could be the best observed value, see Binney and Evans (2001), Merrifield (2004).

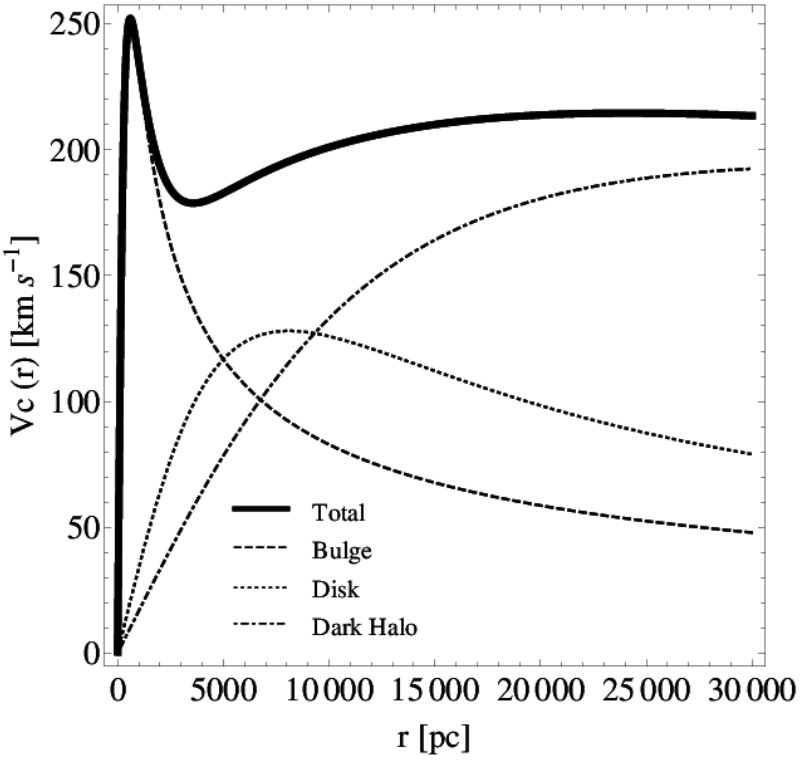

FIGURE 2.1: Contributions to the circular velocity plotted vs. r from the different Galaxy components. DM halo has a MPI profile (see text).

In order to choose suitable values for the parameters that appear within the two presented DM halo models, we follow the pattern proposed by Klypin et al. (2002), in particular the model A1 (with no exchange of angular momentum), bounded to the cosmological constraint of the collapse (or formation) redshift, z_F. In a CDM cosmology, with $H_0 = 75$ kms^{-1}Mpc^{-1} and $\Omega_0 = 1$, the virial mass of the DM halo has been set at: $M_{vir} = 10^{12} M_\odot$. Using the subroutine of Navarro et al. (1997), in which z_F is precisely defined as the redshift z at which half of final mass is in progenitors more massive than 1% of the final mass itself, we obtain: $z_F = 2.68$, the corresponding value for the overdensity $\delta_c = 1.179 \cdot 10^5$ (in units of critical density at z= 0) and then the value $\rho_{1/2}$ in the NFW density profile and that of $\rho_o = \rho(0)$ for the MPI profile, assuming both profiles reach the same density value at their corresponding scale radius r_H.

To conclude our Galaxy modeling we have to verify if the trend for the total circular velocity obtained turns to be in agreement with that observed next to the Sun. The values provided for the total circular velocity next to the solar system by the two different

halos considered are reported in Tab.2.1. The values are respectively below and above the mean observed value of $V_{tot}(R_\odot) = 220$ km s^{-1}, however they are both inside the measured error bar for these distances, see Klypin et al. (2002).
From all the previous considerations, it follows that both the NFW and MPI profiles have in principle to be considered as able to describe a DM halo, but according to the conclusions on cusp/core problem, we think the MPI profile, with its better agreement with the observations, is more suitable to contribute in the right way to the total Galaxy potential. The contributions to the total circular velocity trend vs. r for the different Galaxy components are plotted in Fig.2.1.

2.1.4 The Galactic mass distributions

Finally we can compose the total trend of the Galactic mass distribution as function of the distance r from the Galactic center. In Fig. 2.2, where the single mass distribution relative to bulge, disk and DM halo (MPI) are also shown. The Galactic mass is dominated by the bulge contribution until about 4 kpc from the center, and beyond this threshold, approaching the solar neighborhood, the contribution of the disk becomes the strongest one. The DM halo, though not negligible, has always a lower weight for distances smaller than the solar ones.

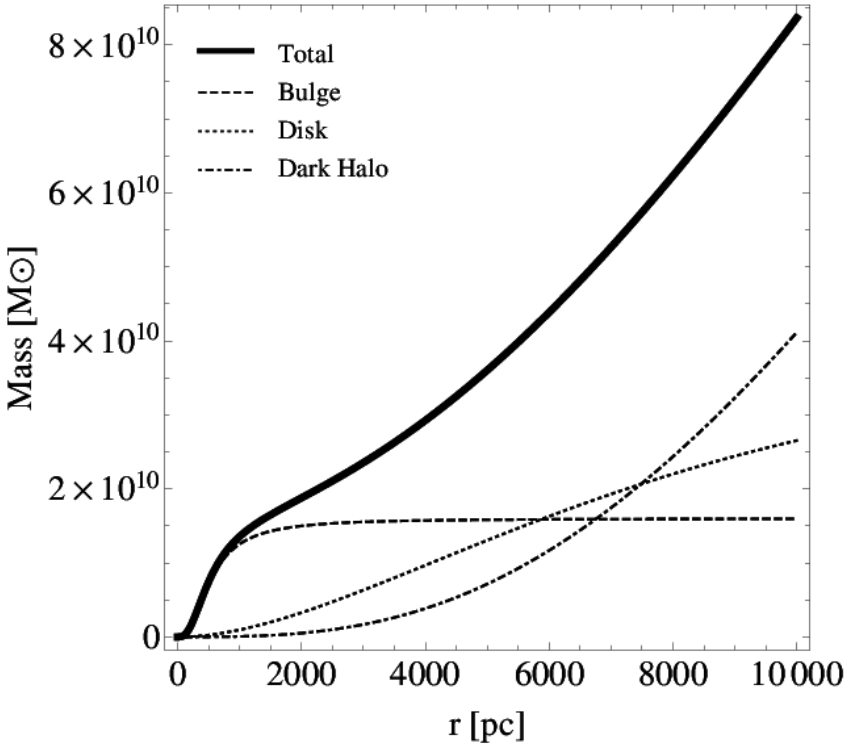

FIGURE 2.2: Contributions to the mass distribution plotted vs.r from the different Galaxy components. DM halo has a MPI profile (see text).

2.2 The solar motion in an axisymmetric potential

As seen, the galactic potential formed by the contribution of bulge, disk and dark halo is essentially axisymmetric, in other words in a cylindrical coordinate system (R, θ, z), we can express the total potential as:

$$\Phi_G = \Phi_B(R,z) + \Phi_D(R,z) + \Phi_{DH}(R,z) = \Phi(R,z). \tag{2.9}$$

Solving Newton's equation of motion in cylindrical coordinates for this axisymmetric potential yields:

$$\begin{cases} \ddot{R} - R\dot{\theta}^2 = -\dfrac{\partial \Phi}{\partial R} \\ \dfrac{\mathrm{d}}{\mathrm{d}t}(R^2\dot{\theta}) = 0 \\ \ddot{z} = -\dfrac{\partial \Phi}{\partial z} \end{cases} \tag{2.10}$$

The second of the previous ones expresses the conservation of the angular momentum component about the z-axis: $L_z = R^2\dot{\theta}$, while the other two equations describe the coupled oscillation in R and z-direction. For the previous galactic potential we also find another integral of motion: the energy

$$E = \frac{1}{2}[\dot{R}^2 + (R\dot{\theta})^2 + \dot{z}^2] + \Phi(R,z). \tag{2.11}$$

If we integrate the equations of motion Eq. 2.10, taking into account the solar peculiar velocity components, $U_\odot = 11.1 \pm 0.74$ km/s, $V_\odot = 12.24 \pm 0.47$ km/s, $W_\odot = 7.25 \pm 0.37$ km/s, Schönrich et al. (2010), the results is a rosette orbits with an oscillation in the radial direction of about 1 kpc around a galactocentric distance of 8 kpc and a smaller oscillation ($\pm$100 pc) above and below the galactic plane, as we will explicitly see in the next chapter.

3

The Spiral Arms Effects on the Solar Path

The spiral arm structure is the main candidate as the perturbation able to induced an efficient stellar migration. We will explored the effects of this non-axisymmetric component of the Galaxy on the solar path, starting from the spiral parameters associated with the solar environment.

3.1 The solar migration: a new framework of research

The small value for the solar peculiar velocity suggested for a long time that the Sun has not experienced many orbital perturbations in the past. The Sun, as all the galactic disk stars, has been assumed to remain near its birth radii. Indeed when the solar path is integrated in an analytical axisymmetric potential (as the potential modeled by the sum of bulge, dark halo and disk) it is found a nearly fixed galactocentric distance (between 8-9 kpc) and a small vertical oscillation (within$\sim$ 100 pc) Matese et al. (2005).
Despite that, the assumption of a time-invariant axisymmetric potential may not be a good approximation for our Milky Way, since the structure of the galactic disk contains irregular non-axisymmetric components such the bar and the spiral arms. The latter in particular may play a crucial role for the understanding of the solar dynamics inside the Galaxy. It was found by Sellwood and Binney (2002) and more recently by Roškar et al. (2008a), that stars orbiting near the corotation resonance of the spiral arms could experience significant changes in their angular momentum. As a result, many stars had their mean orbital distances significantly changed, yet their peculiar velocities were not substantially increased in many cases and in particular stars on nearly circular orbits (with low peculiar velocities as our Sun) were particularly sensitive to this type of dynamical evolution since their angular orbital velocities remain nearly fixed, allowing them to undergo resonant interaction with the spiral arms for longer period. Then the solar dynamical history may be more complex than that suggested by its low peculiar

velocity, and the Sun's evolution could has been driven and modified by the presence of non-axisymmetric components in the Galaxy's potential.
The idea of a stellar migration in the disk actually is present from many years, already in Yuan (1969a) pointed out that the perturbation due to the spiral structure may entail a variation for the birth radii for the stars in galactic disk. Despite that, only recent numerical simulations focused the migration on the Sun and our planetary system. Kaib et al. (2011) in particular have demonstrated that the Sun may have radially migrated through the galactic disk by up to 5-6 kpc. The hypothesis of a solar migration could also explain why the solar metallicity is about 0.14 dex Nordström et al. (2004), Wielen et al. (1996), larger than the mean value of the nearby solar-age stars. Indeed if the Sun formed closer to the galactic center it may have been in a more metal rich environment. In order to understand if this type of solar migration could be possible, Kaib et al. (2011) perform a N-body simulation for an integration time of 4 Gyr, in which the tidal field is built directly from the accelerations calculated by galactic simulation code and reloaded for each time step. In their sample they identified some solar analogs, i.e. particles chosen based on the stellar age, position, and kinematics almost compatible with the solar current one at the end of the simulation. They found 31 stars in a simulated galaxy of 2.5 $\times 10^6$ star particles, that met all of the fixed criteria and display a diverse variety of orbital histories. The dynamical evolution of some solar analogs points out that a closer solar position to the galactic center in the beginning of the Sun's history it is compatible with the current one. Indeed a large fraction of the solar analogs in their simulation spent at least a few hundred Myr orbiting within 5 kpc or less of the galactic center (See Fig.3.1). They then draw a new framework for the solar dynamical evolution in which the Sun may have been born a smaller galactocentric distances and it could have encountered much higher disk densities, entailing that also the stellar encounters and galactic tides that imprinted the structure of the Oort cloud would likely have been stronger in the past.
The non-axisymmetric components of the galactic potential, in particular the spiral arms, may be crucial in order to obtain a full description of the solar path inside the disk and of the Oort cloud formation and evolution, then they could not be neglected.

3.1.1 Metallicity gradient

To build up the metallicity gradient of our Galaxy's thin disk is not an easy task. Also the simplest model has indeed to be consistent with:

i) the story of a disk galaxy formation inside the cosmological environment,

ii) the disk dynamical evolution,

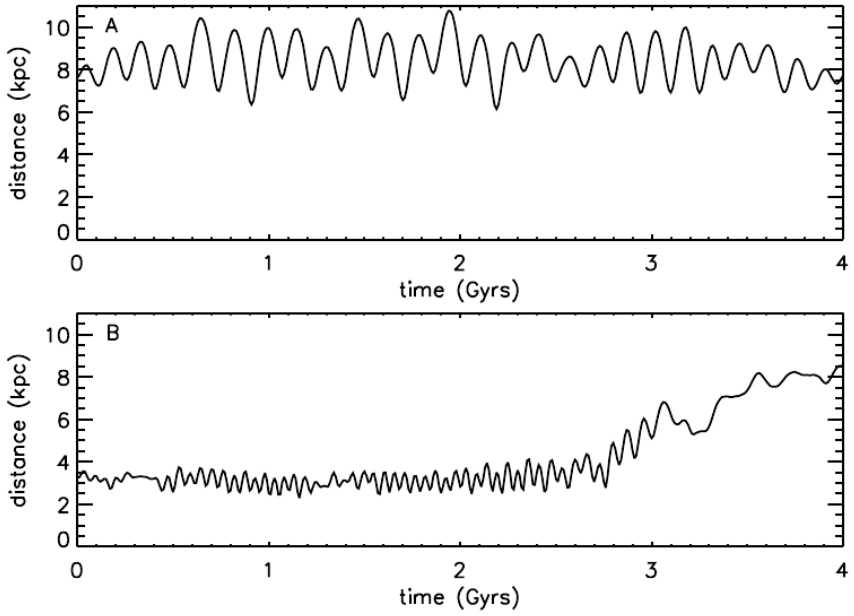

FIGURE 3.1: Galactocentric distance vs time for two solar analogs in the simulation performed by Kaib et al. (2011). Both simulations show a change for the solar position during the history of the Solar System: one oscillating between 6 and 10 kpc (A), while the other exhibits a stronger variation from a very close position (3 kpc) at the beginning of the Sun's history up to the current solar position (B)

iii) the local star formation prescription

iv) the standard chemical evolution once assumed a given initial mass function and a model for spectral evolution of stellar populations

Moreover, from one side the description of so many physical processes composing the whole picture needs the introduction of many parameters, from the other side the observational comparison to match them has to deal with a very large spread. So if there are many good models considering the cosmological, dynamical and chemical evolution Chiappini et al. (2001), Fenner and Gibson (2003), Lineweaver et al. (2004), Naab and Ostriker (2006), Pagel (1997), Piovan et al. (2011), Portinari and Chiosi (1999), Prantzos and Silk (1998) which are able to reproduce in a consistent way the mean metallicity distribution function (MDF) and the age-metallicity relationship (AMR), however evidence suggests that a large amount of scatter is present in the AMR of field stars and open clusters probably due to the superposition of stellar migration across significant galactocentric distances, in turn a result of scattering with transient spiral arms Roškar et al. (2008a,b).

3.1.1.1 Starting Sun's position

If also the Sun has undergone migration, how may one to re-build its path on the basis of metallicity distribution on the disk? The overall observational uncertainties, which enormously increase considering the different chemical species (see, e.g., Table 1, in Portinari and Chiosi (1999), Fig. 3.2), give the impression that reference to one experimental mean metallicity gradient could be meaningless. In spite of that the different models considered lead to an intrinsic self-consistency, i.e., they are able to point out a mean value for the metallicity gradient on the disk without so large a spread among the models. As a good reference we take the paper of Naab and Ostriker (2006) by comparing their results with the other relevant contributions, in particular that of Lineweaver et al. (2004).
Naab and Ostriker (2006) obtain, at the present time, a mean metallicity gradient as:

$$\frac{dlogZ}{dR} = -0.05/dex \cdot \mathrm{kpc}^{-1}$$

not too much different from:

$$\frac{dlogZ}{dR} = -0.06/dex \cdot \mathrm{kpc}^{-1},$$

given by Lineweaver et al. (2004)(interpolation of their Fig. 1). In both papers the gradient becomes significantly steeper in the past:
$\frac{dlogZ}{dR} = -0.07/dex \cdot \mathrm{kpc}^{-1}$ Naab and Ostriker (2006)
and:
$\frac{dlogZ}{dR} = -0.08/dex \cdot \mathrm{kpc}^{-1}$ Lineweaver et al. (2004)
at epoch of solar system formation.

tracer	reference	Δr	$\frac{d[O/H]}{dr}$	$\frac{d[N/H]}{dr}$	$\frac{d[S/H]}{dr}$
HII regions	Shaver et al. (1983)[(1)]	4–13	-0.07±0.015	-0.09±0.015	-0.01±0.02
(optical)	Fich & Silkey (1991)	12–18	—	~ 0	—
	Vilchez & Esteban (1996)	12–18	-0.036±0.02	-0.009±0.020	-0.041±0.020
HII regions	Rudolph et al. (1997)[(2)]	0–17	-0.079±0.009	-0.111±0.012	-0.079±-0.009
(FIR)	Afflerbach et al. (1997)	0–12	-0.064±0.009	-0.072±0.006	-0.063±0.006
OB stars	Smartt & Rolleston (1997)	6–18	-0.07±0.01	—	—
	Gummersbach et al. (1998)	5–14	-0.07±0.02	-0.08±0.02	—
Type II PNæ	Maciel & Köppen (1994)	4–14	-0.06±0.01	—	-0.07±0.01

[(1)] Rescaled to $r_\odot = 8.5$ kpc.
[(2)] Includes the data of Simpson et al. (1995).

FIGURE 3.2: Observed abundance gradients of various elements by Portinari and Chiosi (1999). Δr is the galactocentric radial range covered by each respective study (in kpc). Gradients are expressed in dex/kpc.

If we assume that Sun has a mean over-metallicity of about $0.1dex$ (about 20%) in respect to its nearby stars and the local ISM at its present position Lineweaver et al. (2004), Naab and Ostriker (2006), Pagel (1997), possible values for galactic distance R_i corresponding to the metallicity at its formation, may be:
$R_i = 5.8 - 6.3$ kpc
considering the two limits of the present gradient given by Naab and Ostriker (2006) and Lineweaver et al. (2004) respectively.
Taking into account the values of the past gradients in both cases, we would obtain, respectively:
$R_i = 6.6 - 6.7$ kpc
Summarizing the results, we may take the two limits for the mean metallicity gradient and Sun's starting position, respectively as:

$$\frac{dlogZ}{dR} = (-0.05) - (-0.08)/dex \cdot \text{kpc}^{-1} \tag{3.1}$$

$$R_i = 5.8 - 6.7 \text{ kpc} \tag{3.2}$$

It should be noted that also the observed mean logarithmic gradient of oxygen over H for Galactic HII regions, is believed by Pagel (1997) to be: $-0.07/dex \cdot \text{kpc}^{-1}$, which falls in the range of (3.1). The same value (which corresponds to about the mean between the limit values of (3.1)) with error of $0.01/\text{dex} \cdot \text{kpc}^{-1}$, is also given by Mo et al. (2010) to characterize the Milky Way.

3.2 Spiral arms theory

The main features of the Milky Way's spiral arms are known over the last 40 years, however theory and observation still do not agree. Indeed questions about their nature (transient or quasi-stationary), about their structure (e.g. the number of arms) and dynamics such as their amplitude and pattern speed are still open.
The present knowledge about the structure and the behavior of spiral arms relies both on:

- the gas (observed longitude-velocity diagram)
  Binney et al. (1991), Bissantz et al. (2003)
- maser in high mass stars forming region
  Reid et al. (2009)
- the stars
  e.g. Binney et al. (1997), Georgelin and Georgelin (1976b), Lépine et al. (2011)

In a recent study by Vallée (2008), all the spiral arms constraints are taken into account in order to obtain an average cartographic model for the location in space and velocity for the spiral arms (see Fig. 3.3).

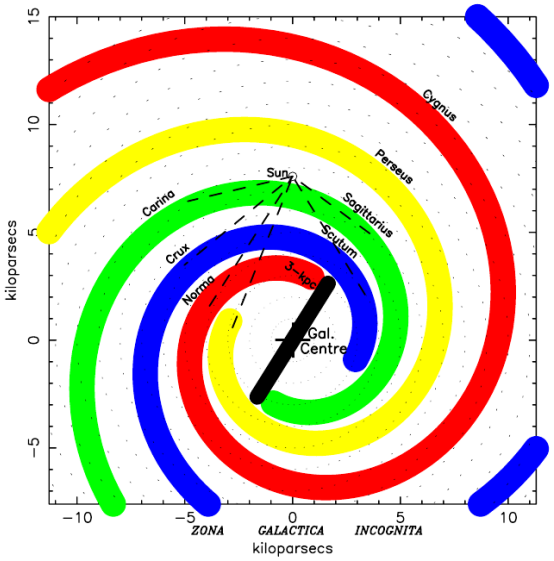

FIGURE 3.3: Spiral arms 2D cartographic model performed by Vallée (2008). The actual arm tangents obtained from observations of gas, dust and stars are underlined by the dashed line.

3.2.1 The long-live density waves model

In addition to many constraints for the structure of the spiral arms, often not in agreement among them, also the real nature of this non-axisymmetric component of our Galaxy is still an intricate riddle. The classical description for the spiral arms as long-live density waves was proposed by Lin and Shu (1964). From a theoretical point of view the correspondence with this theory seems strictly linked with the presence and the features of a bar in the disk (see 3.2.1.2). Despite that also the relation between the spiral arms life and the presence of a bar is a problem not completely clarified. Indeed it seems that the radial velocity dispersion profile support the Lin & Shu theory in a barless disks but in the same time it may be strongly unstable. On the other side the presence of center bar, without nonlinear mode coupling with the spiral arms structure, could support a long-lived spiral pattern, but also a transient spiral arms structure was found even in presence of a bar. Another result, favourable to the Lin & Shu model, comes from the recent simulation performed by D'Onghia et al. (2013). They obtained locally long-lived self-perpetuating spiral arms (as response of a modest overdensity corotating with the galactic disk) which could be locally consistent with density waves, but fluctuating in amplitude with time. In addition also a flyby galaxy encounter could develop a long-lived spiral arms sustained by the coherent oscillation Struck et al. (2011). Finally

it is useful to underline that also the coexistence of both transient and long-lived spiral arms is equally possible Siebert et al. (2012).
Nothing changes on the observational side, also in this case evidence seems to exist for both transient and long-lived spiral arms. Indeed if some galaxies, as M81, show features in agreement with the classical density wave theory Kendall et al. (2008), Lowe et al. (1994), other objects, e.g. M51, presents mass fluxes inconsistent with a steady flow Shetty et al. (2007)
In despite of the difficulties to circumscribe the behavior for the spiral arms perturbation in an unique framework in agreement both with the observative and theoretical evidences, the description provided by Lin and Shu (1964) remains a solid way to approach the perturbation due to the main non-axisymmetric component of our Galaxy. The long-lived density wave theory is a self-consistent formulation that predicts the formation of a spiral arms structure as consequence of the disk instability. It will allow us to mimic the spiral action within the Galaxy potential. The following paragraphs provide more detail regarding the theory.

3.2.1.1 Instabilities on the disk

The disk instability has a crucial role during the genesis of the spiral arms in the Lin& Shu theory. We have to distinguish between *local instability* and *global instability*. The former controls whether or not perturbations much smaller than the size of the disk can grow. Since star formation requires the fragmentation and collapse of gas clouds, local instability is likely to be a necessary condition for star formation in the galaxy disks. The *global instability* can cause a significant transformation of the overall disk structure. Its analysis is related to perturbations with wavelengths that are comparable to the disk size. Even if there does not exist an unique explanation for the spiral arms formation, Lin and Shu (1964) hypothesis seems to be related with this global kind of instability.

The disk instability analysis is based on first-order perturbation theory. The same strategy is adopted for the gravitational Jeans' instability, as the mechanism able to increase the initial density perturbations in Cosmology. A set of fundamental hydrodynamical equations, like continuity, Euler and Poisson equations are introduced the solution of which are the unperturbed values of density, pressure and eulerian velocity Mo et al. (2010). Then each quantity is written as a sum of its static value plus a small perturbation. A new set of linear equations is obtained keeping only terms that are first order in the small perturbations. Expanding the perturbations in terms of eigenmodes (e.g. Fourier expansion) a dispersion relation is achieved in order to investigate the unstable modes.
Following Mo et al. (2010), we consider a thin, self-gravitating gaseous disk which is

axisymmetric so that it is convenient to work with cylindrical coordinates (R, ϕ, z), (v_R, v_ϕ, v_z) being the respective velocities and $z = 0$ corresponds to the disk plane. Neglecting the thickness of the disk, the continuity equation reads as:

$$\frac{\partial \Sigma}{\partial t} + \frac{1}{R}\frac{\partial}{\partial R}(\Sigma R v_R) + \frac{1}{R}\frac{\partial}{\partial \phi}(\Sigma v_\phi) = 0 \tag{3.3}$$

where Σ is the disk surface density. The Euler equations in these coordinates becomes:

$$\frac{\partial v_R}{\partial t} + v_R\frac{\partial v_R}{\partial R} + \frac{v_\phi}{R}\frac{\partial v_R}{\partial \phi} - \frac{v_\phi^2}{R} = -\frac{\partial}{\partial R}(\Phi + h) \tag{3.4}$$

$$\frac{\partial v_\phi}{\partial t} + v_R\frac{\partial v_\phi}{\partial R} + \frac{v_\phi}{R}\frac{\partial v_\phi}{\partial \phi} + \frac{v_\phi v_R}{R} = -\frac{1}{R}\frac{\partial}{\partial \phi}(\Phi + h) \tag{3.5}$$

where Φ is the gravitational potential at $z = 0$ and Σ is related to it by Poisson equation:

$$\Delta\Phi = 4\pi G\Sigma\delta(z) \tag{3.6}$$

the $\delta(z)$ being the Dirac delta function. The quantity h represents the pressure force.[1]

- **Local Instability**

  Setting:

  1) $\Sigma = \Sigma_0 + \Sigma_1$
  2) $v_R = v_{R_0} + v_{R_1}$
  3) $v_\phi = v_{\phi_0} + v_{\phi_1}$
  4) $\Phi = \Phi_0 + \Phi_1$
  5) $h = h_0 + h_1$

  where the subscripts "0" and "1" refer to unperturbed and perturbed quantities, respectively, a new set of linear equations is obtained (see Mo et al. (2010)).

  In general, we may expand a perturbation in the form:

$$Q_1 = \Sigma Q_a(R) e^{-i(\omega t - m\phi)} \tag{3.7}$$

  where Q_1 means the perturbation quantity and the summation is over all modes a with ω its angular frequency and m its azimuthal wavenumber. In the case of a perturbation on a scale much smaller than the size of the disk, the analysis is simplified. In particular under the tight-winding approximation (see next subsect.5.3), in which the variations with angle ϕ are negligible with respect to the

[1] Since we do not care about the vertical structure of the disk, we may assume the disk to be uniform in the z direction. It follows that: $dh = c_s^2 dln\Sigma$, c_s being the sound velocity

radial ones, the following *dispersion* relation for axisymmetric perturbations (i.e. m=0) may be achieved:

$$\omega^2 = \kappa^2 - 2\pi G\Sigma_o |k| + k^2 c_s^2 \tag{3.8}$$

taking into account that the mechanism which resists the growth of perturbations is due to the damping of a sound wave with velocity c_s, κ being the epicyclic frequency of the unperturbed disk at the radius considered. It should be noted that Eq. (3.8) corresponds, without the term κ^2, to the Jeans' criterion for gravitational instability. The κ term is owing to the Coriolis force which acts with pressure against the increasing perturbations. Modes with $\omega^2 < 0$ grow exponentially with time and so are unstable, while those with $\omega^2 > 0$ are stable.

So a gaseous disk becomes locally stable against all local perturbations if the following condition for the quantity Q, holds:

$$Q \equiv \frac{c_s \kappa}{\pi G \Sigma_o} > 1 \tag{3.9}$$

In the case of a stellar disk in which the "effective pressure" is due to the random motions of the stars, the stability criterion becomes:

$$Q \equiv \frac{\sigma_R \kappa}{3.36 G \Sigma_o} > 1 \tag{3.10}$$

The two inequalities are known as Toomre's stability criterion Toomre (1964), derived for axisymmetric perturbations with wavelengths that are much smaller than the size of the disk.

- **Global Instability**

  In this case is not possible to write down an universal dispersion relation or stability criterion. In few simple cases is possible work analytically in order to get insight to the problem. For example in the case of McLaurin disk the perturbation can be expanded in the following modes:

  $$P_l^m(\xi) e^{im\phi}, \xi \equiv (1 - R^2/a^2)^{1/2}$$

  with a the disk radius and P_l^m an associated Legendre function with $0 \leq m \leq l$.

  The first modes corresponding to real perturbations of the disk are : $l = 2, m = 0$ or $m = 2$:

  a) $l = 2, m = 0$, corresponds to an axisymmetric pulsation (expansion and contraction);

b) $l = 2, m = 2$, corresponds to a rotating, elliptical deformation of the disk, called *bar mode* corresponding to the bar instability.

This bar is a highly flattened triaxial structure whose figure rotates as a solid body with an angular frequency Ω_p, called *the pattern speed*.

3.2.1.2 Formation of Spiral Arms

The formation of the main non-axisymmetric structure of our Galaxy is a very complex phenomenon. Here we'll sketch only some of the main current ideas, (for more detail see Binney and Tremaine (2008), Mo et al. (2010)) The mathematical form $f(R)$, which gives a reasonable description of the shapes of observed spirals, is the logarithmic spiral $f(R) = f_o ln(R) + \phi_o$, where the constant f_o describes how tightly the spiral pattern is wound.

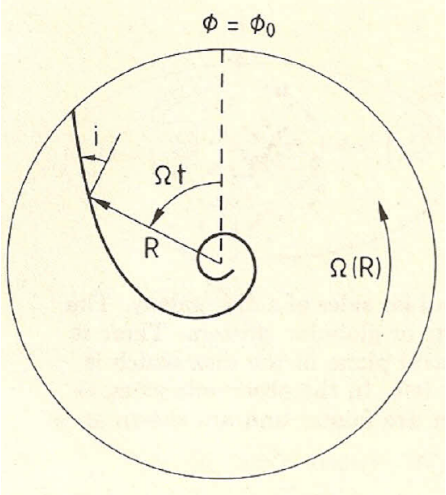

FIGURE 3.4: Geometrical feature of a spiral arm in a differentially rotating disk with $\Omega(R) \propto R^{-1}$. i_p is the pitch angle Binney and Tremaine (2008).

That may be better described by the *pitch* angle , i_p, which at any given point (R, ϕ) along the spiral is defined as the angle between the local tangent of the spiral and the circle of radius R (see Fig. 3.4):

$$\tan i_p = m \left| R \frac{\partial f}{\partial R} \right|^{-1} \tag{3.11}$$

where m is the arm number. The logarithmic spiral is special in having a constant pitch angle.

Spiral arms can be classified by their orientation relative to the direction of rotation of the galaxy. A *trailing* arm is one whose outer tip points in the direction opposite to

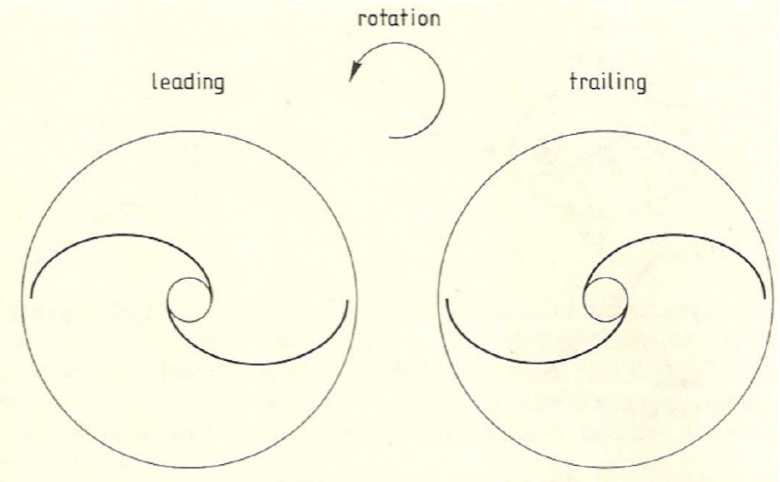

FIGURE 3.5: Leading and trailing arms Binney and Tremaine (2008).

galactic rotation. On the contrary, the outer tip of a *leading* arm points in the direction of rotation (see, Fig. 3.5).

The most basic reason for the formation of spiral arms is the differential rotation of disks. In a disk with constant rotational velocity $V_{rot} = V$ and angular velocity $\Omega = V/R$ a circular patch is sheared into a spiral arm due to the differential rotation (Fig. 3.6). The differential rotation of the galaxy winds up the arm in a time short compared with the age of the galaxy. For a typical galaxy with a flat rotation curve, $V = 220Kms^{-1}$, at $R = 10kpc$ after the time $t = 10^{10}yr$, the pitch angle would be $i_p = 0.25^o$, and the inter-arm separation would be $\Delta R = 0.28kpc$, implying that the spiral is much too tightly wound to be observed Binney and Tremaine (2008). To overcome this problem, well-known as **the winding problem**, the Lin-Shu hypothesis may help according to which the spiral structure is a *stationary density wave* in the stellar density and gravitational potential of the disk and hence not subject to the winding problem. Coming back to the global instability, and taking into account the case previously underlined, i.e., the mode: $l = 2, m = 2$, two different instabilities may arise. One is the bar-like, with a limit pattern speed $\Omega_p = \Omega$ which produces a deformation in the circular orbits into elliptical ones simply aligned along the bar (Fig. 3.7, case (a)). The other one corresponds to a spiral-like perturbation.

The circular orbits are deformed again in elliptical orbits but their orientations tend to align in such a way to cause a *crowding* of the orbits along a two-armed spiral pattern (Fig. 3.7 case (b) or (c)) with a pattern speed $\Omega_p \neq \Omega$. The challenge is to demonstrate that a self-consistent model can be constructed. It means finding a set of orbits in the perturbed potential that, once stacked together, can reproduce the density distribution of the perturbed disk. That appears really occur as it appears in the Fig. 3.7 according to the development of Lin and Shu (1964) idea, when the disk material is compressed

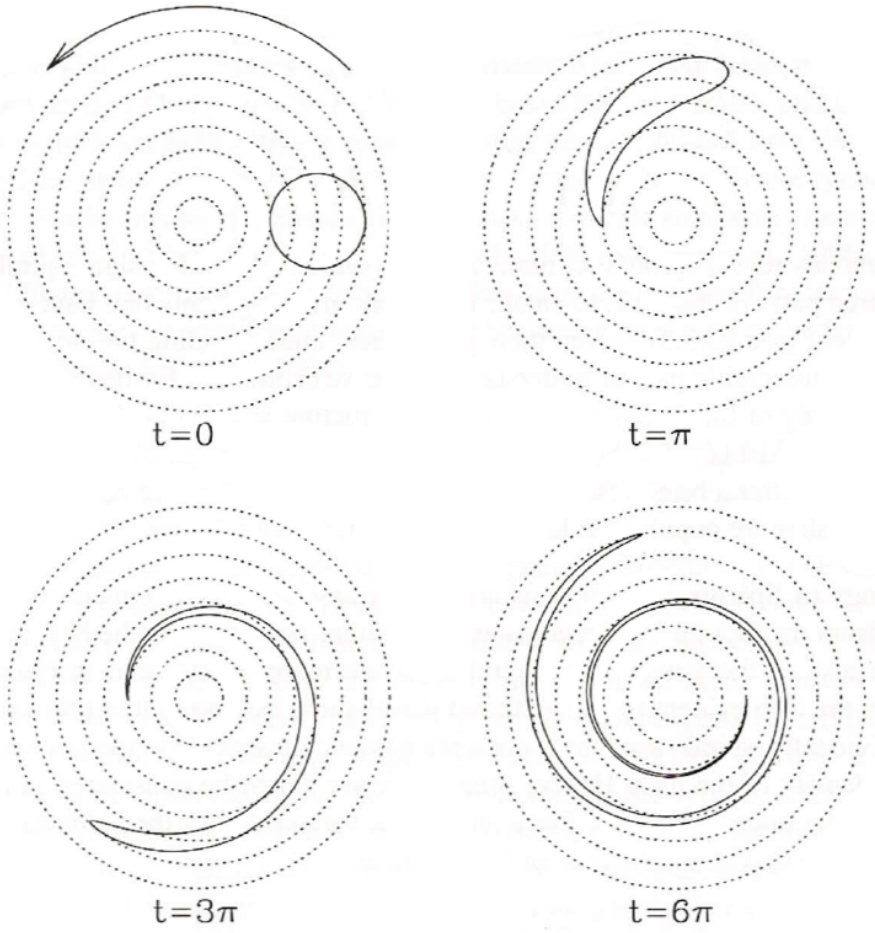

FIGURE 3.6: A circular patch at $t = 0$ is sheared into a spiral arm due to the differential rotation in the direction indicated by the arrow Mo et al. (2010).

and swepts by a spiral density wave. If the stellar gas is cold enough, its reaction to a spiral wave produces narrow gaseous arms with enhanced density, where young stars may form. Hence, spiral density waves can naturally explain why star formation occurs along the spiral arms in a dominant way. One of the most important predictions of the Lin-Shu hypothesis is that spirals are *trailing* because unstable modes are usually trailing.

3.2.2 Spiral arms associated with the solar environment

The determination of the true nature and detailed structure of the spiral arms are challenging problems, but new spectroscopic and astrometric surveys provided six-dimensional phase-space information for a large volume of stars around the Sun, allowing Siebert et al. (2012) to set a new dynamical constraint on the spiral arms structure inside our galactic potential: the galactocentric radial velocity gradient of $\sim$ 4 km s^{-1}kpc^{-1} by Siebert et al. (2011a), obtained using more than 200.000 stars from the RAVE survey

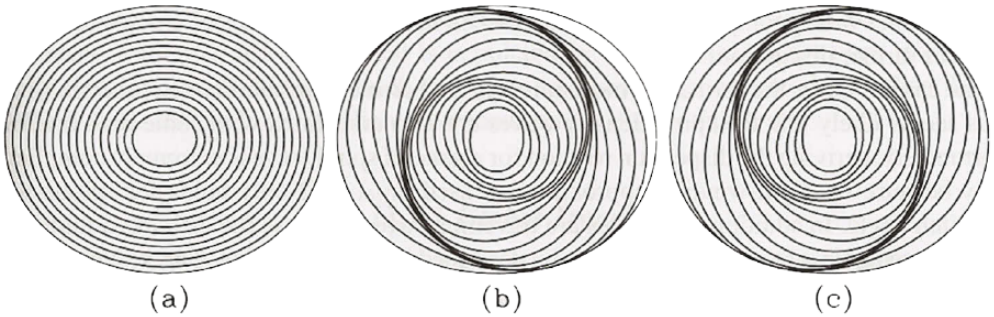

FIGURE 3.7: Self-consistent construction of density perturbations in a disk. In the case of a bar-like perturbation with $\Omega = \Omega_p$ (case (a)), the deformed orbits align along the bar. In the case of spiral-like perturbation (cases (b) and (c)), the orbit orientation changes as function of radius. The crowding of the orbits gives rise to a self-consistent reproduction of the induced spiral pattern Mo et al. (2010).

(see B). They linked the observed radial velocity gradient for the solar neighborhood (up to a distance of 2 kpc from the Sun) with the presence of a relatively long-lived spiral arm structure. Assuming, to first order, that the behavior above the plane is a reflection of what would happen in the whole razor-disk, they were able to constrain the spiral arms structure using the densities wave description Lin and Shu (1964), valid only in the regime of weak, long- lived and tightly wound spirals (small pitch angle). As in Minchev (2008), the spiral structures may be treated like a small deviation to the axisymmetric model of the Galaxy by expressing them as a quasi-steady density waves following the Lin-Shu hypothesis Lin et al. (1969). The gravitational potential of each spiral wave could be expanded in Fourier series and expressed as a function of the radial distance from the galactic center R, the solar angular position θ and the time t:

$$\Phi_{SA}(R,\theta,z) = \sum_m A_m \exp[i(\omega t - m\theta_m + \Phi(R))] \tag{3.12}$$

with corresponding surface density:

$$\Sigma_{SA}(R,\theta,z) = \sum_m \Sigma_m \exp[i(\omega t - m\theta_m + \Phi(R))] \tag{3.13}$$

with A_m and Σ_m amplitudes of the corresponding spiral perturbations. In particular the potential for the single spiral pattern takes the form:

$$\Phi_{SA}(R,\theta,t) = A(R)\ \exp[i(\omega t - m\theta + \Phi(R))] \tag{3.14}$$

where $A(R)$ is the amplitude of the perturbation that may be expressed as a fraction of the galactic background potential, m the number of arms and $\Phi(R)$ a monotonic

function which, in case of logarithmic spiral, can be expressed as:

$$\Phi(R) = \omega \ \mathrm{cotg} i_p \ \ln R, \tag{3.15}$$

with i_p pitch angle and $\Omega_p = \omega/m$ angular frequency of the perturbation (i.e. the pattern speed).
As we have already seen, there is not a single accepted pattern of the the spiral arms structure of our Galaxy. The same uncertainty comprises also the values of the parameters involved in the expression of the spiral arm perturbation. We find models that differ in the value of the pitch angle i_p and the pattern speed Ω_p, and there is not an agreement also with the number of arms m. Even if form the literature is not possible to outline an univocal framework for the major non-axisymmetric perturbation of the Galaxy, previous works may give some indications about the range of these parameters, that was summarized by García-Sánchez et al. (2001):

- the pitch angle i_p results to be ranging from $\sim 5°$ to $\sim 27°$ (see Elmegreen (1985) for more details)
- for the value of m the different studies provide essentially two possibility. The first one is a four arms model (see for example Henderson (1977) and Blitz et al. (1983) that obtained a four-armed spiral structure from HI and CO data; Simonson (1976) that provided a two-armed inner pattern with two additional more peripheral arms; or Georgelin and Georgelin (1976a) that indicated a four arm structure using optical HII regions). On the other side we can find a two-armed spiral (suggested by the density-wave spiral arms for the study of young objects in the solar neighborhood or by Bash (1981) also using the HII regions).
- the results about the pattern speed mainly cluster around two different range of values, depends on the techniques used during the estimation of this parameter: $\Omega_p \sim 11 - 14 \mathrm{km\ s^{-1} kpc^{-1}}$ (see Lin et al. (1969); Yuan (1969a,b); Gordon (1978)) and $\Omega_p \sim 20 - 28 \mathrm{km\ s^{-1} kpc^{-1}}$ (provide for example by Creze and Mennessier (1973); Nelson and Matsuda (1977); Avedisova (1989); Amaral and Lepine (1997); Mishurov and Zenina (1999)).

In particular the different values of Ω_p entails a change in the behavior of spiral arm perturbation. Indeed with largest values for pattern speed imply that the spiral waves travel outwards from the center of the Galaxy, the opposite propagation direction provides lower values for Ω_p. Following the theory of Lin et al. (1969), the density wave pattern propagates around the Galaxy with a pattern speed Ω_p that can extend over

part of the disk delimited by the inner and the outer Lindblad resonances as follow:

$$\Omega - \frac{\kappa}{m} < \Omega_p < \Omega + \frac{\kappa}{m} \tag{3.16}$$

where Ω is the angular velocity of rotation at a distance R, m the number of spiral arms and κ the epicyclic frequency[2] at this distance. At resonance locations energy is dissipated and can lead to damping of spiral structure. In addition to the outer and the inner resonance, a corotation resonance can occur when $\Omega_p = \Omega$ where the wave can start to grow through over-reflection as obtain by Lin and Bertin (1985). The Lindblad resonances determine the edges of the region within the spiral structure can exist, but we can constrained the zone between the inner and the corotation resonance, as the area in which the density wave theory works well according to García-Sánchez et al. (2001).

Taking into account the previous indications about the spiral arm parameters, we

Mass model	m	$\langle V_R \rangle_{R_0}$ km s^{-1}	Ω_p km s^{-1} kpc^{-1}	A % (total, disc)	i deg	χ_0 deg	χ^2	
I	2	$0.9^{+0.1}_{-0.1}$	$18.9^{+0.3}_{-0.2}$	$(0.50^{+0.02}_{-0.02}, 2.27^{+0.08}_{-0.07})$	$-10.0^{+0.4}_{-0.4}$	$76.9^{+1.1}_{-1.2}$	1829.00	
I	2	-5	$16.1^{+0.1}_{-0.1}$	$(0.78^{+0.01}_{-0.01}, 3.50^{+0.07}_{-0.06})$	$-23.2^{+0.3}_{-0.5}$	$57.3^{+0.6}_{-0.5}$	1943.14	(*)
I	2	0	$18.8^{+0.2}_{-0.3}$	$(0.49^{+0.02}_{-0.02}, 2.21^{+0.08}_{-0.09})$	$-9.1^{+0.3}_{-0.4}$	$65.8^{+1.5}_{-1.0}$	1831.99	
I	2	5	$19.3^{+0.1}_{-0.2}$	$(0.69^{+0.02}_{-0.01}, 3.12^{+0.09}_{-0.05})$	$-15.6^{+0.7}_{-0.6}$	$112.1^{+1.0}_{-0.9}$	1853.04	
II	2	$0.9^{+0.3}_{-0.2}$	$18.6^{+0.3}_{-0.2}$	$(0.55^{+0.02}_{-0.02}, 3.09^{+0.10}_{-0.13})$	$-10.0^{+0.4}_{-0.4}$	$76.0^{+1.3}_{-1.0}$	1828.46	
II	2	-5	$15.1^{+0.1}_{-0.1}$	$(0.71^{+0.01}_{-0.01}, 3.93^{+0.06}_{-0.07})$	$-22.3^{+0.3}_{-0.6}$	$55.7^{+0.7}_{-0.4}$	1940.75	(*)
II	2	0	$18.5^{+0.3}_{-0.2}$	$(0.54^{+0.02}_{-0.03}, 3.03^{+0.09}_{-0.15})$	$-9.3^{+0.4}_{-0.3}$	$66.6^{+1.3}_{-1.1}$	1830.17	
II	2	5	$16.2^{+0.1}_{-0.1}$	$(0.51^{+0.01}_{-0.01}, 2.84^{+0.07}_{-0.05})$	$-16.3^{+0.7}_{-0.6}$	$111.3^{+0.9}_{-0.8}$	1859.98	
I	4	$4.9^{+0.1}_{-0.1}$	$25.8^{+0.1}_{-0.1}$	$(0.71^{+0.02}_{-0.01}, 3.22^{+0.08}_{-0.06})$	$-26.0^{+0.6}_{-0.5}$	$132.8^{+1.8}_{-1.7}$	1833.52	(*)
II	4	$4.9^{+0.1}_{-0.1}$	$25.9^{+0.1}_{-0.1}$	$(0.91^{+0.03}_{-0.02}, 5.09^{+0.16}_{-0.09})$	$-26.7^{+1.0}_{-0.4}$	$135.0^{+2.3}_{-1.7}$	1829.55	(*)

FIGURE 3.8: Table of different set of spiral arms parameters that reproduce the current radial velocity gradient in the solar neighborhood, provided by Siebert et al. (2012). The best fit solution is highlighted by the color yellow.

want also anchor our study on some observative results in agreement to the solar local environment, since we are interested into recreate the solar path. For this reason, the start point of our investigation has been the spiral arm parameters chosen according to the best fit model provided by Siebert et al. (2012) using the RAVE survey data. They analyzed a wide range of possible sets of parameters (amplitude, pattern speed, pitch angle and number of arms) in order to characterize the spiral arms structure and reproduce the observed radial velocity for the solar environment. In Fig. 3.8 are quoted all the solutions in agreement with the observed velocity field. The analysis favors a two-armed spiral ($m = 2$), since for the $m = 4$ solution with a comparable value of chi-square, the predicted pitch angle is too large. The best fit solution presents an amplitude $A = 0.55^{0.02}_{-0.02}\%$ of the background potential (equivalent to 14% of the background density), a pattern speed $\Omega_p = 18.6$ km s^{-1}kpc^{-1} and a pitch and angle

[2] $\kappa^2 = \Omega^2 \left(1 + \frac{R}{2\Omega}\frac{\mathrm{d}}{\mathrm{d}R}\right)$

$i_p = -10.0^{+0.4}_{-0.4}$ deg. A useful visualization may be seen in Fig 3.10.

Remembering the constrains due to the Lindblad resonance we can check if the value

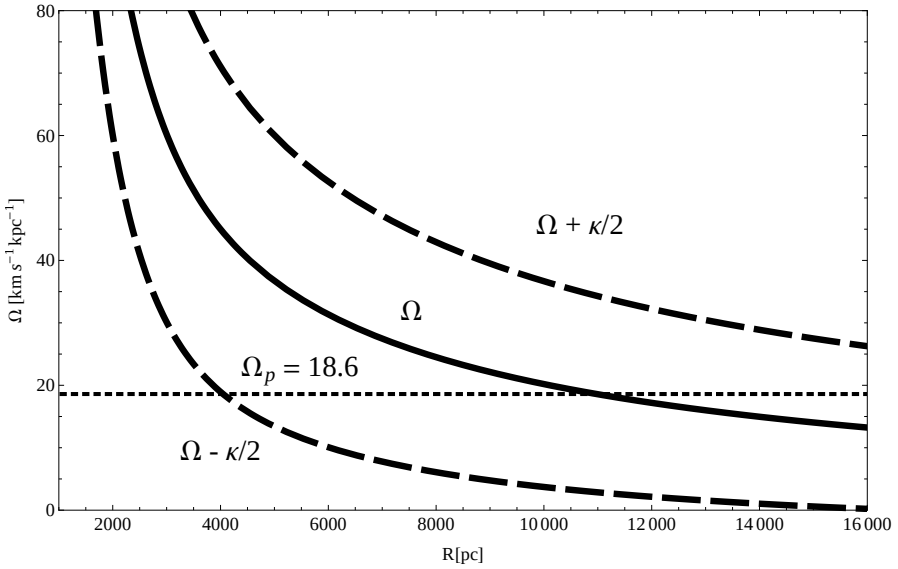

FIGURE 3.9: Resonances in rotation curve of the Galaxy. Rotation curve of the Galaxy Ω (heavy line), that corresponds to the corotation resonance and inner and outer Lindblad (dashed line) in correspondence of $\Omega \pm \kappa/m$ for a two-armed spiral arms ($m = 2$). The pattern speed $\Omega_p = 18.6$ km s^{-1} kpc^{-1} (horizontal dotted line) encloses the region in which the spiral perturbation is well described by the density-wave

for Ω_p allows to obtain a spiral structure enough extended in our model for the Galaxy. As we can see in Fig. 3.9, the pattern speed $\Omega_p = 18.6$ km s^{-1} kpc^{-1} (horizontal dotted line) encloses the region in which the spiral perturbation is well described by the density-wave theory between 4 and 11 kpc, that is in agreement with the range of galactic distance for a possible solar migration. Using the best fit model provided by Siebert et al. (2012) we can define the set of parameters which referring from now on as the "standard spiral arms" (summarized in Tab. 3.1). It represents the start point of our study: we will investigate the effects of spiral arms varying the parameters around the central value indicated by the standard case. It very important to stress the fact

Parameter	**Standard value**
Pattern Speed Ω_p	18.6 km s^{-1} kpc^{-1}
Amplitude A	0.55 % Φ_{back}
Scale height h_s	200.0 pc
Pitch angle i_p	-10.0 deg

TABLE 3.1: Spiral arm parameters for the standard case, defined using the best fit in Siebert et al. (2012)

that Siebert et al. (2012) restricted the study on the radial velocity field $\langle V_R \rangle$, building

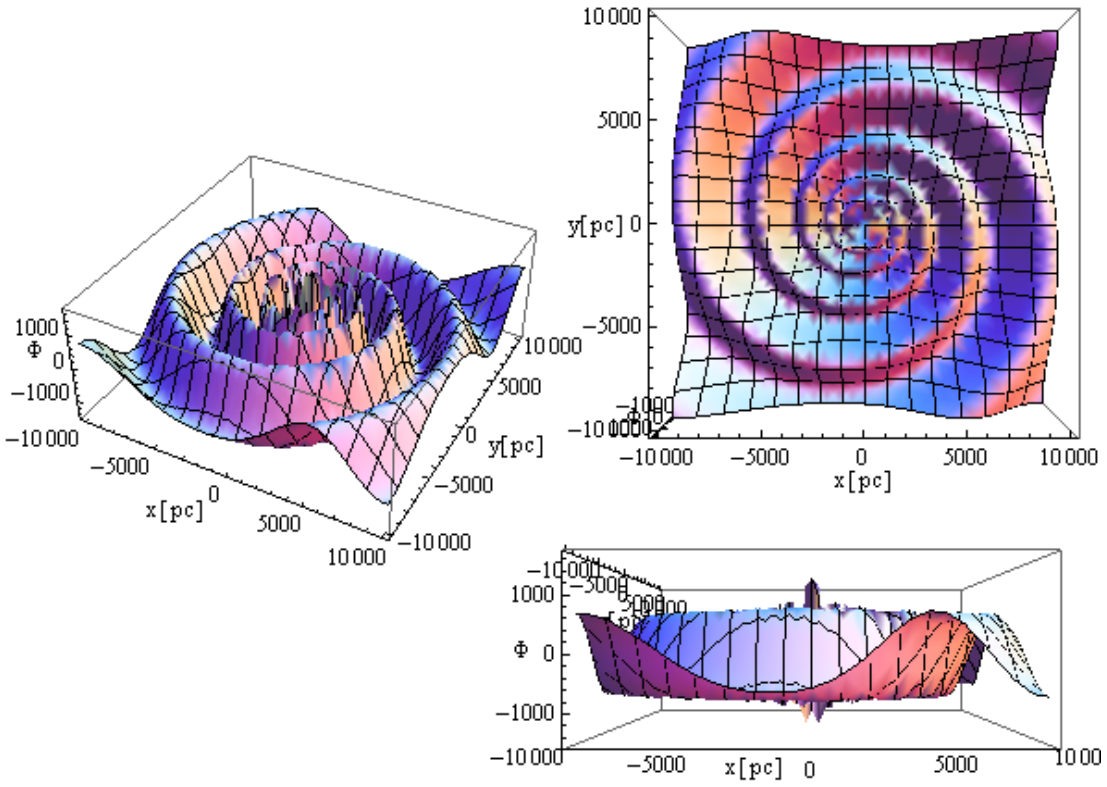

FIGURE 3.10: Visualization of spiral arms 2D perturbation potential Φ_{SA} obtained using the best fit parameters values reported in Fig. 3.8.

only a bidimensional model for the spiral arms. This choice arose from the difficulty to estimate the contribution of the asymmetric drift that enters the calculation of the transverse velocity field $\langle V_\theta \rangle$. It means that the factor $A(R)$ involves only a flat galactic potential; despite this, we used this 2D spiral arm potential description in order to go beyond the classical potential for the Galaxy and add an non-axisymmetric component, breaking its cylindrical symmetry.

3.2.3 Results for a 2D fixed spiral arms

The bidimensional spiral arms perturbation, obtained from the Lin & Shu theory and the physical constrains due to the radial velocity gradient in the solar neighborhood, may be used to modify the Galactic potential. As we have seen in the section §2.2, the solar motion in the axisymmetric potential is a rosette orbits, oscillating close to the current solar position. Such type of small perturbation along the motion around the Galaxy justified the circular approximation for solar motion in many simulations focused on the Oort Cloud dynamics. But this type of approximation could no longer be valid when a non-axisymmetric perturbation, like a spiral arms structure, is acting.

The presence of the spiral arm breaks the cylindrical symmetry of potential, indeed

$$\Phi_{TOT} = \Phi_{BG}(R,z) + \Phi_D(R,z) + \Phi_{DH}(R,z) + \Phi_{SA}(R,\theta,t) = \Phi(R,\theta,z,t) \tag{3.17}$$

The equation system (2.10) may be rewritten as follow

$$\begin{cases} \ddot{R} - R\dot{\theta}^2 = -\dfrac{\partial \Phi}{\partial R} \\ \dfrac{\mathrm{d}}{\mathrm{d}t}(R^2\dot{\theta}) = -\dfrac{\partial \Phi}{\partial \theta} \\ \ddot{z} = -\dfrac{\partial \Phi}{\partial z} \end{cases} \tag{3.18}$$

It is clear that in presence of a non-axisymmetric potential the conservation of the angular momentum and the total energy is not possible.

Integrating the solar path for 4 Gyr, using the perturbation potential shown in Fig. 3.10, we obtained a stronger variation of the solar position in the radial direction (between 5.5-9.5 kpc) and a trend for the radial position less periodic with respect to the motion under the axisymmetric potential (see Fig. 3.11). This result is in agreement with the initial position provided in the simulation performed by Kaib et al. (2011) to probe the possibility of a migration of our Sun within the galactic disk at the beginning of the Solar System history. The perturbation affects also the z-axis component of the solar motion, changing the oscillation phase, but it has not an important effect on the amplitude, as expected given the 2D nature of the spiral arms model.

The strong variation for the solar position with respect to the galactic center also entails a strong variation in the solar angular velocity around the Milky Way (see Fig. 3.12). The circular approximation for the solar orbit could no longer be a good one in the study on cometary dynamics, and the real solar path may have important repercussions in the total perturbation effect due to the galactic tidal field. It is important to stress that the model assumed for the spiral arms is constrained by observations for the current solar position. The coefficients involved in that formulation could present a modulation with respect to the radial position of the Sun, which we are at the moment not able to take into account during the integration.

The bidimensional approach for the spiral arms perturbation may overestimate the effect along the radial direction for the solar path, indeed all the strength of the perturbation is concentrated in the disk plane, while a particle that present a z-position$\neq 0$ but very close to the disk, is completely insensitive to the spiral arms action: the change in the perturbation power could be too abrupt. Also the assumption of a constant spiral arm action, without any variation in time, could be a description far from the real physical framework. For these reasons the first aim of this work has been the extension of the

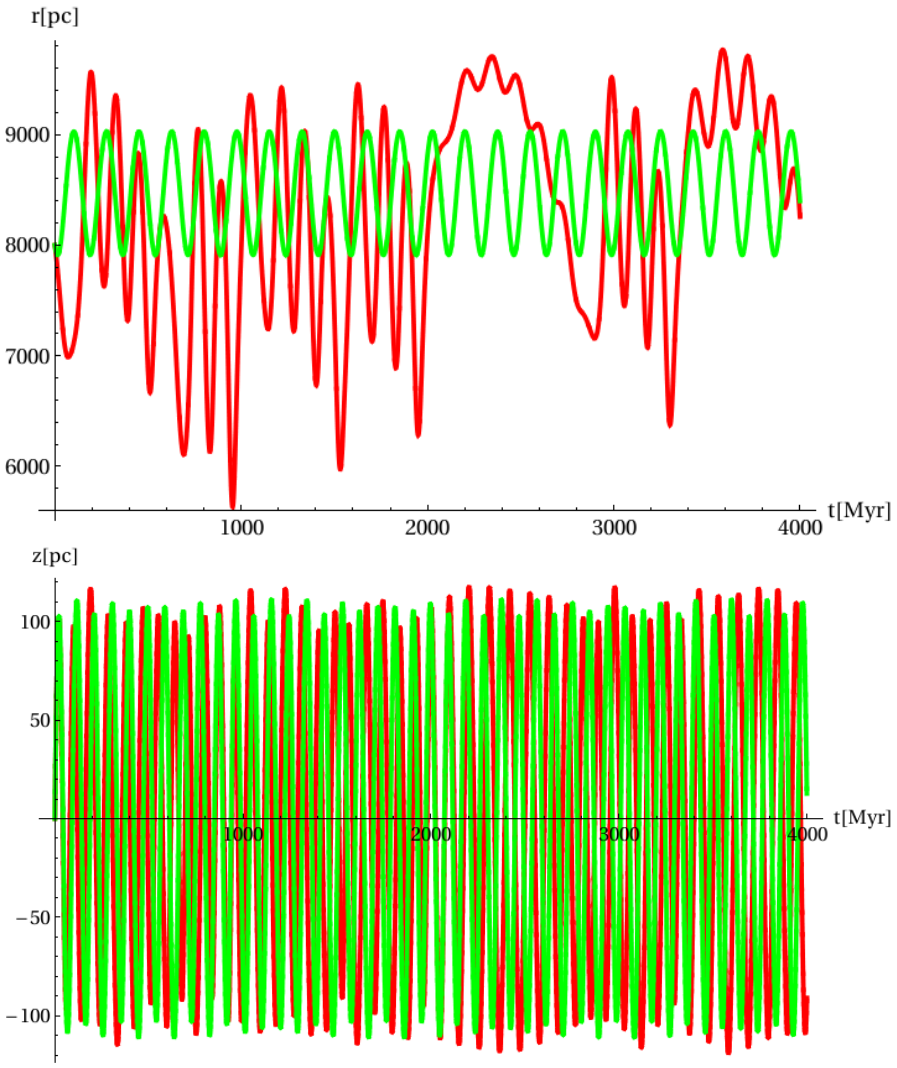

FIGURE 3.11: Solar path with (red) and without (green) the action of the bidimensional spiral arms perturbation of Fig. 3.10 on an integration time of 4 Gyr

spiral arms potential formulation to a 3D time dependent expression.

3.3 3D extension for the spiral arms

The starting point for a 3D extension for the spiral arms perturbation is its description in a flat disk. The spiral arm properties are assumed to be slowly varying functions of radius $H(R,t)$, multiplied by more rapidly varying, periodic (mod 2π) function $F(\Psi)$ of $\Psi = m\phi + f(R,t)$, where

- m is the number of spiral arms;
- ϕ is the azimuthal angle in the inertial Galactic coordinate system;
- R is the radius;

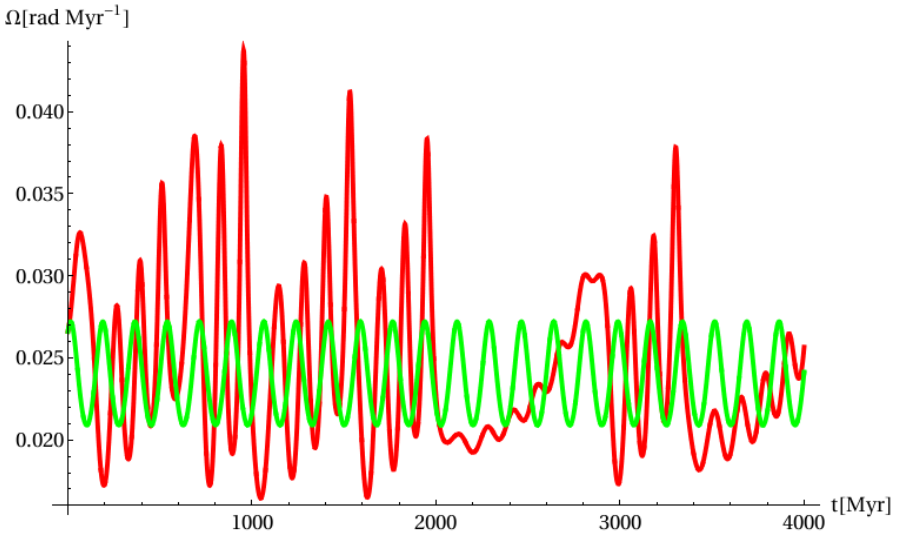

FIGURE 3.12: Solar angular velocity with (red) and without (green) the bidimensional spiral arms perturbation of Fig. 3.10 on an integration time of 4 Gyr.

- f is the *shape function* $f(R,T) \equiv mg(R,t)$ see Binney and Tremaine (2008).

This description entails that any physical function Q (density, velocity, etc.) in the 2D disk which nominally depends upon all the separate independent variables, i.e. $Q = Q(R,\phi,t)$, actually has the simpler form $Q = H(R,t)F(\Psi)$. Moreover, since H varies slowly, $\mathrm{d}Q \approx H\mathrm{d}F$ with $\mathrm{d}F = F'\mathrm{d}\Psi = F'(m\mathrm{d}\phi + f_R\mathrm{d}R + f_t\mathrm{d}t)$, where $f_* = \partial f(R,t)/\partial *$. Likewise, F repeats when $\kappa \mathrm{d}R = 2\pi$ at fixed t, where we write the spiral density wave as *radial wavenumber* $\kappa = f_R$. In addition, F is unchanged at fixed t when we contemplate small changes that satisfy $(m\mathrm{d}\phi + f_R\mathrm{d}R) = 0$ or equivalently $|f_R| = |m\mathrm{d}\phi/\mathrm{d}R|$.
Consider the locus of the maximum of F in the plane. The tangent of the pitch angle of the locus is $\tan\alpha = |\Delta x/\Delta y|$ where

- Δx is the change along the radial direction;
- Δy is the change in the azimuthal direction;

the angle is taken to lie between $0 \leq \alpha \leq 2\pi$ and k can be either positive or negative ($k < 0$ for the leading spiral arms and $k > 0$ for the trailing spiral arms) . In the same way we can write $\cot\alpha = |R\mathrm{d}\phi/\mathrm{d}R| = |Rf_R/m| = |Rk/m|$.
At this point we consider a 2D (surface-density) perturbation in the $z = 0$ plane, see Binney and Tremaine (2008). The superficial density of an infinitely thin disk may be represented from a mathematical point of view as the sum of a unperturbed superficial density $\Sigma_0(R)$ plus a perturbed one $\Sigma_1(R,\phi,t)$. We can write Σ_1 separating the fast variation part, due to the passage through the spiral arms, from the slower variation

linked to motion along the spiral arms, in the following form

$$\Sigma_1(R,\phi,t) = H(R,t)e^{i[m\phi+f(R,t)]} = H(R,t)e^{i\Psi} \tag{3.19}$$

where $\Psi = \Psi(R,\phi,t)$ as above. The next step is determine the gravitational potential due to the perturbation Σ_1. Since the perturbation of the superficial density oscillates quickly around the average zero value, there is an almost full cancellation of the contribution due to the far components of the structure on the local potential; in other words the perturbed potential of a certain position would be completely determined by the structure properties within few wavelengths from that particular position. In order to determine the potential in close to the point (R_0,ϕ_0), we can replace the shape function $f(R,t)$ with the first two terms of the Taylor's series

$$f(R_0,t) + f_R(R_0,t)(R-R_0) = f(R_0,t) + k(R_0,t)(R-R_0) \tag{3.20}$$

then we obtain

$$\Sigma_1(R,\phi,t) \simeq \Sigma_a e^{ik(R_0,t)(R-R_0)} \text{ where } \Sigma_a = H(R_0,t)e^{i[m\phi+f(R,t)]}. \tag{3.21}$$

The variations with the angle ϕ are not taken into account since they are much slower than the ones in the radial direction when the density waves are tightly wrapped as in our case.
The potential expression for a bidimensional wave on a infinitely thin disk is

$$\Phi_1(x,y,z,t) = -\frac{2\pi G\Sigma_a}{|k|}e^{i(kx-mt)-|kz|} \tag{3.22}$$

that we can rewrite as

$$\Phi_1(R,\phi,z,t) \simeq \Phi_a e^{ik(R_0,t)(R-R_0)-|k(R_0,t)z|} \text{ where } \Phi_a = -\frac{2\pi G\Sigma_a}{|k|} \tag{3.23}$$

Considering $R = R_0$ and $\phi = \phi_0$, we can obtain the 3D potential expression due to the density in Eq. 3.21, using the relation obtained, as follows:

$$\begin{aligned}
\Phi_1(R,\phi,z,t) &= \Phi_a e^{\cancel{ik(R,t)(R-R)}-|k(R,t)z|} \\
&= -\frac{2\pi G}{|k|}\Sigma_a e^{-|k(R,t)z|} \\
&= -\frac{2\pi G}{|k|}H(R,t)e^{i[m\phi+f(R,t)]-|k(R,t)z|} \\
&= -\frac{2\pi G}{|k|}H(R,t)e^{i\Psi-|k(R,t)z|} + (O|kR|^{-1} \\
&= \Phi_s(R,\phi,z,t).
\end{aligned} \tag{3.24}$$

The 2D form that Siebert et al. (2012) quote is

$$\Phi_s(R,\phi,0,t) = A\Phi_{back}(R)e^{i\Psi}, \tag{3.25}$$

comparing the last expression of Eq. 5.12 with the previous one and noting that $A\Phi_{back}$ is equivalent to the factors that multiply the oscillatory piece in the former[3], we can obtain the 3D generalization for the 2D potential provided by Siebert et al. (2012)

$$\Phi_s(R,\phi,z,t) = A\Phi_{back}(R)e^{i\Psi-|kz|} \tag{3.26}$$

This implies that the characteristic scale height above and below the plane is $1/|k|$ which is quite large[4]. Our initial problem was about how the potential varied as $|z|$ increased. This shows that the potential is almost constant, i.e. the 2D Siebert form is going to be "close" to right answer as long as the Sun does not lie at $kz > 1$. On the other hand, it is also possible to see that the potential has a discontinuity in slope that occurs at $z = 0$. It's equivalent to the force changing sign as one crosses the plane. This is unphysical and comes from the assumption that the surface density is all at $z = 0$. In fact, the material that makes up the spiral arm has a scale height that is at least 100 pc. Not only is the jump unphysical but it is also fatal as far as a smooth numerical integration is concerned.

In order to fix up the problem we started with a volume density instead of a surface density. Assume that the density has a Gaussian form

$$\rho(z) = \frac{\Sigma(R)}{\sqrt{2\pi}h}e^{-z^2/(2h^2)}, \tag{3.27}$$

where h is the scale height. Integrating over all z we obtain the surface density as

$$\Sigma(R) = \int_{-\infty}^{+\infty}\rho(z')\mathrm{d}z' \tag{3.28}$$

We will evaluate the contribution to the potential generated at each level z' by the infinitesimal surface density $\mathrm{d}\Sigma = \rho(z')\mathrm{d}z'$ and then sum the results to find the full potential. The key is that $z \to z - z'$ in the solution from 3.22. The logical steps are:

$$\begin{aligned}\Phi_s(R,\phi,z,t) &= -\frac{2\pi G}{|k|}\int \mathrm{d}\Sigma e^{i\Psi-|k(z-z')|} \\ &= -\frac{2\pi G}{|k|}e^{i\Psi}\int \mathrm{d}z'\rho(z')e^{-|k(z-z')|} \\ &= A\Phi_{back}e^{i\Psi}\int \mathrm{d}z'\rho(z')e^{-|k(z-z')|}\end{aligned} \tag{3.29}$$

[3] $A\Phi_{back} = -\frac{2\pi G}{|k|}H(R,t)$

[4] Since we have $e^{-|kz|} = e^{-1} \to |zk| = 1 \to |z| = 1/|k|$

where I've inserted the Eq. 3.25 for the planar result. So the 3d potential is

$$\Phi_s(R,\phi,z,t) = \Phi_s(R,\phi,0,t)\chi(z,h,k) \tag{3.30}$$

where χ encapsulates the changes from the pure 2D result when the sources are smeared with scale height h, explicitly

$$\begin{aligned}\chi(z,h,k) &= \int \mathrm{d}z'\rho(z')e^{-|k(z-z')|} \\ &= \int \frac{\mathrm{d}z'}{\sqrt{2\pi}h} e^{-z'^2/(2h^2)} e^{-|k(z-z')|}.\end{aligned} \tag{3.31}$$

The only remaining issue is determine the way in which we choose the scale height h. This describes the vertical extent of the distribution of the material responsible for the spiral arms' density excess. A reasonable strategy consist in to calculate h by making an assumption about the velocity dispersion of the material.
The total gravitational potential in the vicinity of the plane is $\Phi(z) = \Phi(0) + \Phi'(0)z + \Phi''(0)z^2/2$. Symmetry implies $\Phi'(0) = 0$. Consider a 1D Gaussian velocity distribution for a distribution function $\propto e^{E/\sigma^2}$ where $E = v^2/2 + \Phi(z)$. The rms vertical component of the velocity at any given z is

$$\begin{aligned}\langle v_z^2 \rangle &= \frac{\int v^2 e^{-v^2/2\sigma^2}\mathrm{d}v}{\int e^{-v^2/2\sigma^2}\mathrm{d}v} \\ &= \sigma^2\end{aligned} \tag{3.32}$$

and we can calculate the density variation with height as follow

$$\begin{aligned}\frac{\rho(z)}{\rho(0)} &= \frac{\int e^{-(\Phi(z)+v^2/2)\sigma^2}\mathrm{d}v}{\int e^{-(\Phi(0)+v^2/2)\sigma^2}\mathrm{d}v} \\ &= e^{-(\Phi(z)-\Phi(0))/\sigma^2} \\ &= e^{-(\Phi''(0)z^2)/(2\sigma^2)}\end{aligned} \tag{3.33}$$

and in the last step we have assumed that the Taylor series approximation about the plane is sufficient. So, we can make the identification with the exponential presents in Eq. 3.27 and using the Poisson equation we obtain

$$\begin{aligned}h &= \frac{\sigma}{\sqrt{\Phi''(0)}} \\ &= \frac{\sigma}{\sqrt{4\pi G\rho(0)}}\end{aligned} \tag{3.34}$$

We can choose σ arbitrarily and evaluate $\rho(0)$ from the model for the potential to infer $h \sim 100 - 200$ pc; this show that fixed h implies $\sigma \propto \sqrt{\rho(0)}$.

3.3.1 Summary for the 3D spiral arms model

It may be useful to summarize the results about the 3D spiral arms model. The general transient 3D spiral arms perturbation could be expressed, taking into account only the real part of the of the exponential, as follow:

$$\Phi_{spiral}(R,\theta,t,z) = e^{\frac{-(\Delta t)^2}{2W^2}} A\Phi_{back}\cos[\omega(\Delta t)+m(-\theta+\text{cotg}(i_p)\ \ln(R/R0))+\varphi_{max}]\cdot\chi(z,h_s,\kappa), \tag{3.35}$$

where $\Delta t = t - t_{max}$ and $R0$ the initial position for the Sun.
It could be useful to divide the different terms inside Eq. 3.35 in order to analyze the role and summarize of the different terms inside Eq. 3.35 and summarize the parameters inside of each one.

- **transient term** $e^{\frac{-(\Delta t)^2}{2W^2}}$: gaussian profile to modulate the spiral perturbation intensity from 0 to a maximum value in correspondence to the time t_{max} and then decreases it again for $t > t_{max}$. Within this term we find
  - $W = \sigma = 0.5 \cdot$ (galactic rotational period at $R0$), the time width of the perturbation, approximately identified as the life scale for the spiral arm;
  - $\Delta t = t - t_{max}$ with $t_{max} = 6\sigma$ the time for the maximum power for the spiral arm perturbation
- **3D term** $\chi(z,h_s,\kappa) = \int \frac{dz'}{\sqrt{2\pi}h_s} e^{-z'^2/(2h_s^2)} e^{-|\kappa(z-z')|}$: to introduce the third dimension for the perturbation, where
  - $h_s = 200$ pc is the scale height
  - $\kappa = -(m\text{cotg}i_p)/R0$ is the wave number with $m = 2$ the number of arms, $i_p = -10$ deg is the pich angle and $R0$ is the initial solar position with respect to the galactic center as usual.
- **amplitude term** $A\Phi_{back}$ that determines the power of the spiral arm perturbation with respect to the background galactic potential, in particular
  - $\Phi_{back} = \Phi_G = \Phi_{bulge} + \Phi_{disk} + \Phi_{halo}$ (see §2.1)
  - $A = 0.55\%$ is the amplitude following Siebert et al. (2012)
- **periodic term** $\cos[\omega(\Delta t)+m(-\theta+\text{cotg}(i_p)\text{Ln}(r/R0)+\varphi_{max}]$ expresses the period nature of the spiral arm perturbation, in which we find
  - $\omega = m\cdot\Omega_p$ with $\Omega_p = 18.6$ km s^{-1}kpc^{-1} angular frequency of the perturbation
  - φ_{max} the spiral phase at the time of maximum spiral intensity

3.4 Overlapping vs separate spiral arms perturbations

The Sun's motion is driven by *all* the spiral arms present in the disk. Some are forming, some are winding up and some are decaying away. Presumably, at any time there are just a few important ones that influence the dynamics of the Sun. The crucial point to investigate is whether the effect of multiple spiral arms on the Sun be approximated as a sequence of independent encounters. This issue is important because independent encounters bring great simplifications to modeling, for example it may allows us to take into account only the total number of encounters and not the detailed time-dependent arrival sequence. In particular we can ask how many spiral arm encounters will move the Sun from its birth position to the current position without describing exactly when the encounters occurred. Conversely, it might be possible to prove the impossibility to move the Sun from its birth position to its current position, irrespective of the specifics of when the encounters took place.

The simplest possible experiment to check the agreement between the effects due to overlapping and separate sequence of spiral arms, is the investigation on two spirals with a given separation. Starting from a fixed position and velocity for the Sun a straightforward integration gives the final dynamical state of the Sun. All times and frequencies are quoted in terms of half rotation period and frequency of the Sun at its current location.

For each calculation each spiral arm started with zero amplitude, grew to a maximum value and then diminished to zero again. The parameters of each spiral were fixed: amplitude, scale height and pattern speed. The separation of the two spirals was varied: from 0 to 4 rotation periods plus the limiting case of infinite separation. The width W of the spiral was fixed at one time scale. The plot in Fig. 3.13 illustrates the sum of the spiral amplitudes for a specific peak separation and peak width. These two spirals are almost fully separated.

A set of encounters with randomly sampled spiral pattern phase ψ_{max} provided the initial conditions for each calculation. For each final result the post-encounter epicycle guiding center radius, radial velocity amplitude and vertical velocity amplitude were calculated. The statistical distributions of the post-encounter dynamical quantities were compared.

From the results we:

- obtained the trends in the epicycle parameters (radial migration R_g, radial heating $A(v_R)$ and vertical heating $A(v_z)$, see §3.4.1) as functions of the spiral amplitude, scale height, and pattern speed for two infinitely separated spirals;

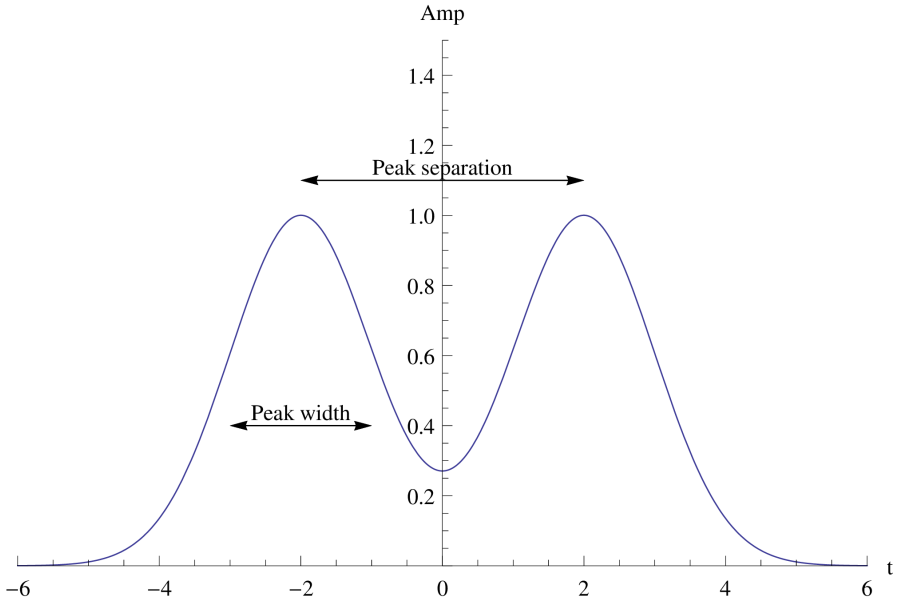

FIGURE 3.13: The sum of the amplitudes of two separate spiral patterns shows some overlap when the peak separation is 4 time scale (2 rotation periods) and the peak width is 1 time scale.

- tried to understand if these trends are modified when the spirals have a finite separation;
- investigated if the differences that are present between the infinite and finite separations are important for an experiment consisting of a limited number of spiral encounters.

3.4.1 The epicycle parameters

In order to check if two joined spiral arms versus two separate and consecutive spiral perturbation act in a different way, we performed a comparison between the epicycle parameters produced by these two different type perturbations. Before proceeding, it would be well to spend few words about the epicycle approximation itself, to understand if these quantities provide a correct description for the physical framework of our research.

For nearly circular orbit generated by an axisymmetric potential it is useful to derive an approximate solution to the equations system in Eq. 2.10, Binney and Tremaine (2008). It is possible to define

$$x \equiv R - R_g \tag{3.36}$$

where $R_g(L_z)$ is the guiding-center radius, i.e. the radius for the circular orbit of angular momentum L_z. In correspondence to $(R = R_g, z = 0)$ we find a minimum for the effective

potential defined as

$$\Phi_{eff} = \Phi + \frac{L_z^2}{2R^2} \quad \rightarrow \quad \left(\frac{\partial \Phi_{eff}}{\partial R}\right)_{(R_g,0)} = \left(\frac{\partial \Phi}{\partial R} - \frac{L_z^2}{R^2}\right)_{(R_g,0)} = 0. \tag{3.37}$$

Expanding Φ_{eff} in a Taylor series about x and neglect all terms in Φ_{eff} of order xz^2 or higher, we obtain the **epicycle approximation**. Using this approximation the equations of motions become very simple, introducing two new quantities: the epicycle or radial frequency:

$$\kappa^2 \equiv \left(\frac{\partial^2 \Phi_{eff}}{\partial R^2}\right)_{(R_g,0)} = \left(\frac{\partial^2 \Phi}{\partial R^2}\right)_{(R_g,0)} + \frac{3Lz^2}{R_g^4} \tag{3.38}$$

and the vertical frequency

$$\nu^2 \equiv \left(\frac{\partial^2 \Phi_{eff}}{\partial z^2}\right)_{(R_g,0)} = \left(\frac{\partial^2 \Phi}{\partial z^2}\right)_{(R_g,0)}. \tag{3.39}$$

The equations of motions then become

$$\begin{cases} \ddot{x} = -\kappa^2 x \\ \\ \ddot{z} = -\nu^2 z \\ \\ \dot{\theta} = \frac{L_z}{R^2} \end{cases} \tag{3.40}$$

According to these equations, x and z evolve like the displacements of two harmonic oscillations, with frenquencies κ and ν, respectively.
In the epicycle approximation the motion is then very simple

$$\begin{cases} R(t) = A\cos(\kappa t + a) + R_g \\ \\ z(t) = B\cos(\nu t + b) \\ \\ \theta(t) = \Omega_g + \theta_0 - \dfrac{2\Omega_g A}{\kappa R_g}\sin(\kappa t + a) \end{cases} \tag{3.41}$$

with A, B, a, b and θ_0 all constants. In particular from the constants A and B we can calculate the amplitude for the radial and vertical direction of the motion, we expressed A and B as

$$\begin{cases} A = \sqrt{x_0^2 + \frac{v_{x0}^2}{k^2}} \\ B = \sqrt{z_0^2 + \frac{v_{z0}^2}{\nu^2}} \end{cases} \tag{3.42}$$

Using $x_0 = (R_f - R_g)$, $v_{x0} = v_x(R_f)$, $z_0 = z_f$ and $v_{zo} = v_z(z_f)$ where the quantities with the subscript f are the final results at the end of the integration. Finally the amplitudes for v_R and v_z were obtained

$$\begin{cases} A(v_R) = k \cdot A \\ A(v_z) = \nu \cdot B \end{cases} \tag{3.43}$$

In addition the epicycle approximation has the following integrals of motion:

- the angular momentum L_z,
- the energy radial component $E_R = \frac{1}{2}(\dot{x}^2 + \kappa^2 x^2)$,
- the energy z- component $E_z = \frac{1}{2}(\dot{z}^2 + \nu^2 z^2)$
- the total energy $E = E_R + E_z + \Phi_{eff}(R_g, 0)$

Using the 3D model, presented in the previous sections, we considered a spiral perturbation with a modulation in time: the perturbation grows, achieves a peak and after decreases until it disappears. That means that very far from the peak, the galaxy potential is approximately axisymmetric and a stellar motion around the galactic center could be described by the epicycle approximation.
We considered an integration time of 12 σ, where σ is half characteristic lifetime chosen for the spiral arms structure (see §3.3.1; in this way at the beginning and at the end of the integration we are enough far from the maximum power of the spiral arms perturbation, to consider the galaxy potential axisymmetric. If the previous assumption is correct, considering only one spiral arms perturbation, in an integration time equals to 12 σ, the results provided by the full expression for the equations of motion (Eq. 2.10) and the epicycle approximation (Eq. 3.40) will be overlapping before and after the full development of the spiral arm.
This check is useful in order to understand if it is right to consider the epicycle parameters as representative for the real orbit at the end of the integration time, and if they can be used in order to simplify the comparison between the joined and separate spiral arms perturbation.

We make the comparison between the results come from the full integration and those coming from the epicycle approximation. We consider a stellar orbit that was not circular from the beginning, i.e. a stellar orbit with a peculiar motion in its initial conditions. In particular we use exactly the solar peculiar motion.
First at all we verified if the behavior for the integrals of motion is as expected. For the full integration we analyzed the trend for the total energy E and the angular momentum L_Z (see Fig. 3.14).

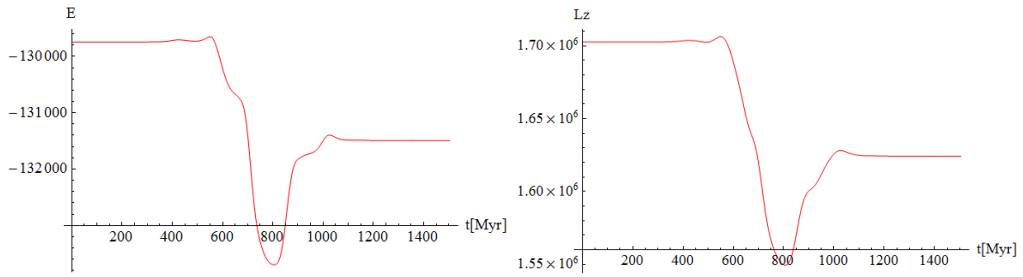

FIGURE 3.14: Trend for the energy E and the angular momentum L_z of the Sun under the spiral arms perturbation (full integration)

We underline that the conservation for E and L_z, before and after the perturbation due to the spiral arms, is verified.

The second step is to check the correspondence between the full integration (in red) and the exact (blue) for the quantities R, z, and total energy E. As you can see in Fig 3.15,

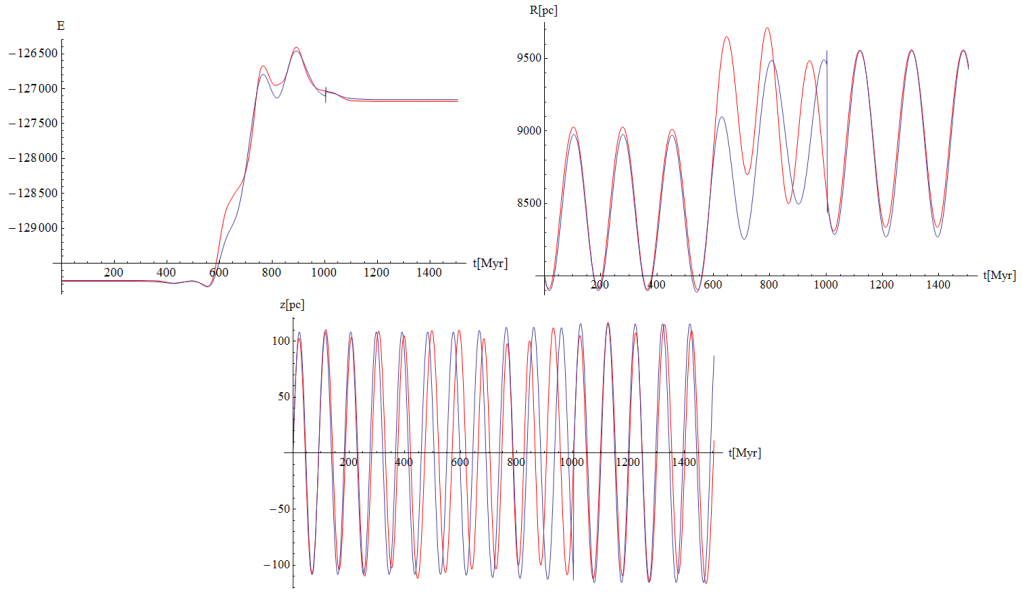

FIGURE 3.15: Comparison between the trends of E, R and z obtained integrating the equation of motion in the full (red) and in the epicycle approximation (blue) form.

the agreement between approximate and not approximate trends look like very good at the beginning of the integration time, when the spiral arms perturbation have not been born yet, and at the end when the perturbation completely disappears. The two trends drift apart in-between as it was expected, when the spiral arm perturbation works at the maximum of its power. It confirms that the epicycle parameters are powerful tools, that may be utilized to probe also the joined vs the separate spiral arms perturbation behavior.

3.4.2 Joined vs separate spiral arms code

The following paragraphs provide a brief description about the code to compare the action of two overlapping and separate spiral arms perturbations.

3.4.2.1 Joined perturbations

We have to consider a sum of two perturbations that perturb the solar path and that we can express

$$\Phi s_{tot} = \Phi s_1 + \Phi s_2; \tag{3.44}$$

where Φs_1 and Φs_2 are the perturbing potentials respectively of the first and the second spiral arm structures considered, each one expressed by Eq. 3.35. For each of these perturbations we can define a time for the maximum t_{max} perturbation and a corresponding spiral phase ψ_{max}, in particular we have:

- For Φs_1:
  - $\psi 1_{max} = \text{RandomReal}[0, 2\pi]$;
  - $t1_{max} = 6\sigma$ with $\sigma = \frac{1}{2}$ rotational period at the present position of the Sun with respect the galactic center (~ 8000 pc);
- For Φs_2:
  - $\psi 2_{max} = \text{RandomReal}[0, 2\pi]$;
  - $t2_{max} = \text{RandomReal}[t1_{max} - 3\sigma, t1_{max} + 3\sigma]$

Starting from an initial solar state

$$w_{i\odot} = \{R_{i\odot}, z_{i\odot}, \theta_{i\odot}, v_{Ri\odot}, v_{zi\odot}, v_{\theta i\odot}\} \tag{3.45}$$

we runned the integration over the integration time $[T_{min}, T_{max}]$, where

- $T_{min} = \text{Min}[t1_{max}, t2_{max}] - 6\sigma$;
- $T_{max} = \text{Max}[t1_{max}, t2_{max}] + 6\sigma$;

obtained a final solar state at the end of the integration,

$$w_{f\odot} = \{R_{f\odot}, z_{f\odot}, \theta_{f\odot}, v_{Rf\odot}, v_{zf\odot}, v_{\theta f\odot}\}. \tag{3.46}$$

We close the code relative to the overlapping perturbations, storing

- the integration time: T_{min}, T_{max};
- two times of maximum perturbation: $t1_{max}$, $t2_{max}$;
- two spiral phases for the maximum: $\psi 1_{max}$, $\psi 2_{max}$;
- two solar phases in correspondence to the two maxima ($t1_{max}$, $t2_{max}$): θ_{1max}, θ_{2max};
- vector solar state at the beginning and at the end of the integration: $w_{i\odot}$, $w_{f\odot}$.

3.4.2.2 Separate perturbations

In order to make a comparison between the results obtained by the overlapping perturbations with the effects due to two distinct spiral arm perturbations, we have to reload the initial solar conditions $w_{i\odot}$ as the new starting conditions for the integration.
If $t1_{max} < t2_{max}$ we can divide in two following steps the procedure:

- **STEP 1**
  We reloaded from the overlapping perturbation:
  - the previous initial conditions as the new ones $\rightarrow w_{i1\odot} = w_{i\odot}$;
  - the maximum spiral phase $\psi 1_{max}$
  - the time for the maximum perturbation $t1_{max}$

  We integrated the solar motion under the single perturbation potential:

$$\Phi s_1(t1_{max}, \psi 1_{max}), \tag{3.47}$$

  over an integration time $T1_{int} = [t1_{max} - 6\sigma, t1_{max} + 6\sigma] = [t1_{start}, t1_{end}]$, obtained an intermediate solar state:

$$w_{middle\odot} = \{R_{m\odot}, z_{m\odot}, \theta_{m\odot}, v_{Rm\odot}, v_{zm\odot}, v_{\theta m\odot}\}. \tag{3.48}$$

  At the end of this first step we can record
  - the intermediate solar state: $w_{middle\odot}$;
  - the integration time: $t1_{start}$, $t1_{end}$;
  - the solar phase at maximum time $t1_{max}$, θ'_{1max}.

- **STEP 2**
  We reloaded from the previous step:

– the intermediate conditions as the new starting ones $\rightarrow w_{i2\odot} = w_{middle\odot}$;

– the solar phase in correspondence to the maximum perturbation in the overlapping case: θ_{2max}

From these new initial conditions we integrated the solar motion under the single perturbation potential:

$$\Phi s_2(t'_{max}, \psi'_{max}), \tag{3.49}$$

over an integration time $T2_{int} = [t1_{end}, t1_{end} + 12\sigma] = [t1_{end}, t_{final}]$.
For this second perturbation potential we can define:

– $t'_{max} = t1_{end} + 6\sigma$ as the time in correspondence of the maximum spiral perturbation;

– $\psi'_{max} = \psi 2_{max} - \theta_{2max} + (\theta_{m\odot} + \Omega_{\odot} 6\sigma)$, where θ_{2max} is the solar angular position for the time $t2_{max}$. In this way we conserved the quantity $(\psi_{max} - \theta)$ for the second perturbation both for the overlapping and the separate case.

So we obtained the final solar state for two separate and consecutive spiral arm perturbation:

$$w_{final\odot} = \{R_{ff\odot}, z_{ff\odot}, \theta_{ff\odot}, v_{Rff\odot}, v_{zff\odot}, v_{\theta ff\odot}\}. \tag{3.50}$$

At the end of the second step we can record

– the intermediate solar state: $w_{final\odot}$;

– the integration time: $t1_{end}$, t_{final};

– the solar phase at maximum time t'_{max}, θ'_{max}.

Otherwise if $t1_{max} > t2_{max}$ we have to invert 1 with 2, inside the two previous steps.

3.4.3 Runs

A large number of runs is necessary for faithful representation of the distribution of the galactocentric radius and of the vertical and radial velocity amplitudes.
For every calculation with finite separation there was a corresponding case run with infinite separation. This allowed detailed comparison to be made to investigate how the probability distribution function (PDF) for correlated encounters compared to that for two independent encounters. The statistical approach we are considering is the most suitable to face the many unknown aspects of the problem we are dealing with. As we underline at the beginning of §3.2.1.1 and 3.4 there is not probably an unique way

Dynamics	Overlapping & separate
Initial conditions	Sun's current values
Number of cases	10,000 & 10,000
Amplitude A	0.5, 1, 2
Scale height h_s	0.5, 1, 2
Pattern speed Ω_p	0.25, 0.5, 0.75, 1, 1.5, 2, 3, 4
Peak separation	0, 1, 2, 4

TABLE 3.2: Range of parameters to check the overlapping vs separate spiral arms dynamics. The amplitude A, the scale height h_s and the pattern speed Ω_p are expressed as multiplies of the "standard case" quoted in §3.3.1

to explain the complex phenomenon of the spiral arms formation. Moreover, at any time some of them are forming, some are winding up and are decaying away. For the complexity of the framework, the statistical method allow an investigation to different possible scenarios.

3.4.3.1 Trends for two infinitely separated encounters

The more suitable framework in which we can study the effects on the solar path, due to the different choices for the spiral arm's parameters is considering two infinitely separated perturbations. Starting from the "standard case" with amplitude 1 (0.55% of the background potential) and scale height 1 (200 pc) for range of pattern speeds, it is possible to find the PDF trend of each epicycle parameter. The trends of the PDF for the guiding center position, R_{gc}, after two independent encounters for the considered values of patterns speeds, are collected in Fig. 3.16, where the lines are color-coded according to the Ω_p. The Sun lies at 8 kpc at the beginning and the figure shows that spiral arms with $\Omega_p < 1$ (where 1 means the rotation frequency obtained by the best fit in Siebert et al. (2012) provided by the current solar environment) tend to pull the Sun inward; conversely ones with $\Omega_p > 1$ tend to move it outward. For $\Omega_p \sim 1$ the distribution spreads more than it shifts (green and cyan lines for $\Omega_p = 1$ and 1.5). In other word we can conclude that advection dominates away from $\Omega_p \sim 1$ and diffusion near it and we can call these "advective" and "diffusive" encounters, respectively. Varying the other spiral arms parameters the same PDF trends for R_G are seen for all amplitudes and scale heights: larger (smaller) amplitudes yield larger (smaller) effects as one would expect. However, the effect of scale height variation is small.

We repeated the same investigation on the effect due to the variation of the spiral arms parameters for the radial and vertical velocity.

The Sun's initial radial velocity is about 11.1 km/s Schönrich et al. (2010), so we can note that the PDF for v_R (Fig. 3.17, when $\Omega_p \sim 1$ (green and cyan lines), is peaked

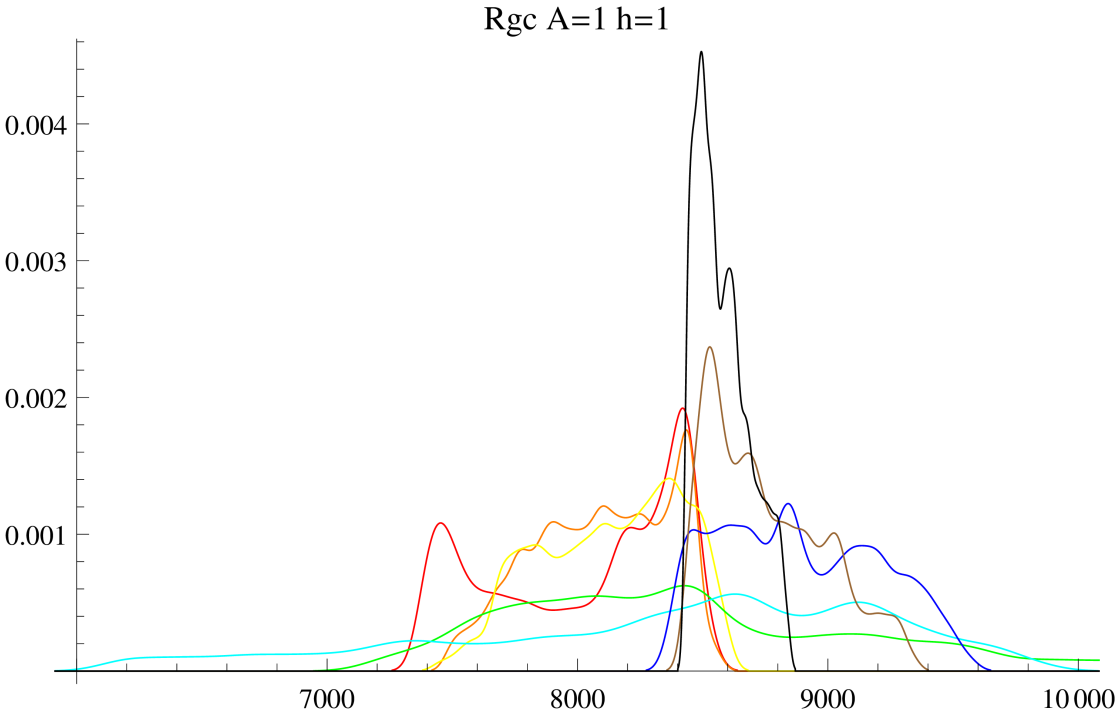

FIGURE 3.16: The PDF for R_{gc} (in pc) after two infinitely separated encounters where $\Omega_p = 0.25$ (red), 0.5 (orange), 0.75 (yellow), 1 (green), 1.5 (cyan), 2 (blue), 3 (brown), 4 (black).

near the Sun's starting conditions. The implication is that the diffusive encounters minimize radial heating, while other pattern speeds lead to more substantial heating. It is important to note, for example, the black and red lines, corresponding to maximum and minimum pattern speeds simulated respectively, that give broader and hotter distributions. These are substantially similar which implies that heating occurs whichever way the Sun is pulled. On the other hand the radial heating is *not* significantly altered by the scale height of the spiral arm disturbance. Finally we analyzed the variation of the vertical velocity depending on Ω_p, A and h_s. Recalling the Sun's initial vertical velocity of 7.25 km/s Schönrich et al. (2010), we can underline that the diffusive encounters minimize the vertical heating (see Fig. 3.18). In addition, unlike the radial case, the vertical heating is substantially reduced when the spiral arm scale height increases.
After this study on the spiral arm parameters, we can summarize the main evidence as follow

- the **pattern speed** Ω_p is the parameter most crucial for the perturbation effects of the spiral arms, in particular: the radial quantities (the guiding center radius R_g and amplitude for the radial velocities $A(v_R)$) undergo net changes far from $\Omega_p \sim \Omega_{standars} = 18.6\text{km s}^{-1}\text{ kpc}^{-1}$ and diffusion (increase in variance) near it. On the other hand, the diffusive encounters minimize the vertical heating.

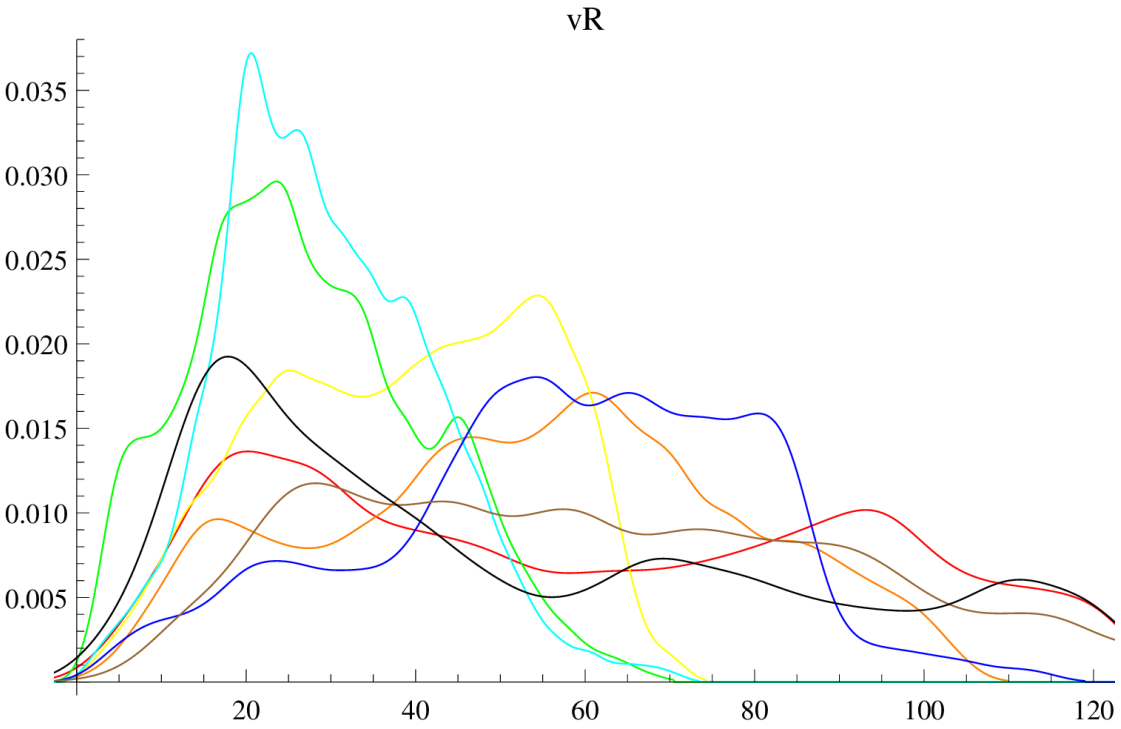

FIGURE 3.17: The PDF for v_R (in pc/Myr) after two infinitely separated encounters where $\Omega_p = 0.25$ (red), 0.5 (orange), 0.75 (yellow), 1 (green), 1.5 (cyan), 2 (blue), 3 (brown), 4 (black).

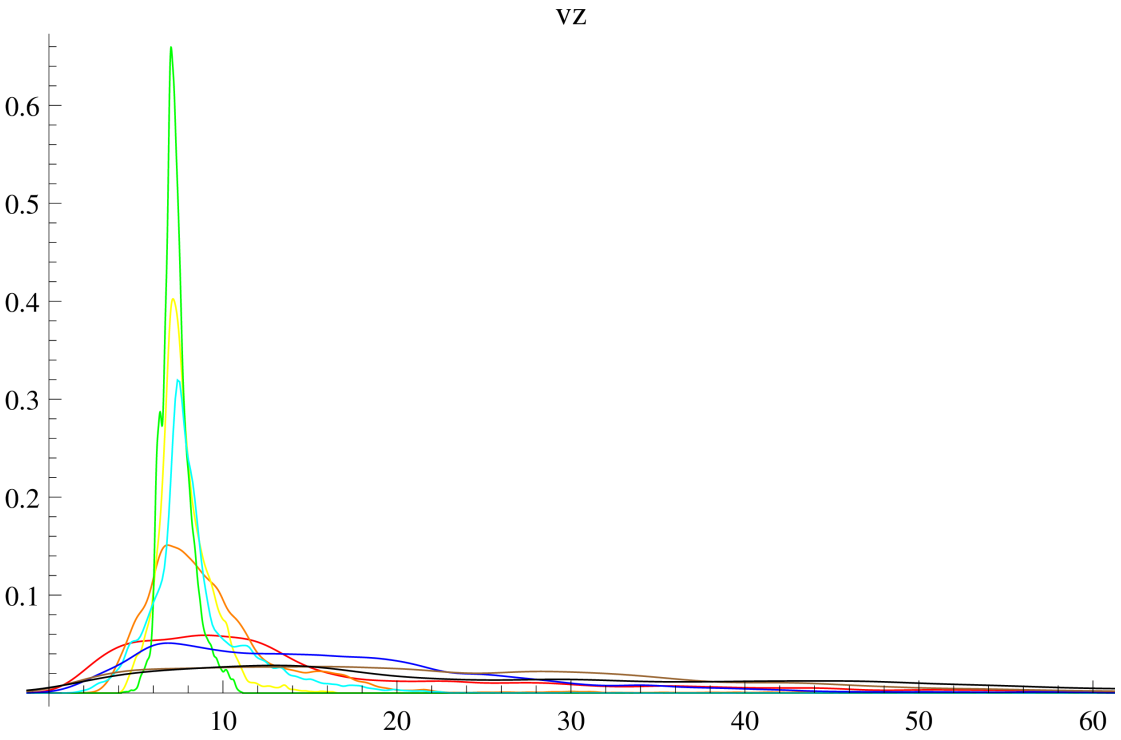

FIGURE 3.18: The PDF for v_z after two infinitely separated encounters where $\Omega_p = 0.25$ (red), 0.5 (orange), 0.75 (yellow), 1 (green), 1.5 (cyan), 2 (blue), 3 (brown), 4 (black).

- the **amplitude** A also plays an important role with the same variation trend, although in a way less significant than what produced by the changing in Ω_p.
- the variation of the **scale height** h_s involves especially the vertical motion indeed: the radius and the radial heating are not significantly altered by the scale height of the spiral arms disturbance: While the amplitude of the vertical veolocity $A(v_z)$ is substantially reduced when h_s increases.

These investigations provide a simple way to anticipate the general effect of encounters at other radii and for a range of conditions, that may be different from that considered in 3.1. In particular, we compare $\Omega(R)$ (the angular velocity in correspondence of the galactocentric position R) to Ω_p to decide whether encounters tend to advect the orbit (i.e. systematically push it in or out in galactocentric radius) or to increase its spread. Radial heating may be minimized by Ω_p with a value lying midway between the Ω's at the beginning and ending galactocentric radii. So if metallicity dictates, for example, a starting position of about 6 kpc and the current position is 8 kpc, and if Ω varies roughly linearly, then the more efficient way to influence a stellar orbit is with pattern speed with $\Omega_p \sim \Omega(R_{gc} = 7 \text{ kpc})$. In addition we have also some evidence that the vertical heating is easily controlled by altering the scale height of the spiral arms. From these results we can obtain a simple prescription for how to arrange to move the Sun without overheating in either the v_R or v_z directions.

In conclusion we can underline that the main thing that we missed in this study is an understanding of how changing the width of the spiral arm alters these results, indeed W is been fixed at half of the rotation period. This might be important since all the characteristic epicycle frequencies are of that order. The **width** W of the spiral arms perturbation may be another crucial parameter, but additional investigations are needed.

3.4.3.2 Effect of finite separation

When two spirals influence the orbit at the same time the results will differ from those obtained from two infinitely separated encounters. The PDF of final galactocentric radius after two coherent encounters with the "standard parameters" is shown in Fig 3.19. The red line corresponds to the final distribution of radii when the two spirals arm amplitudes have zero separation (though in space the arms will generally have different phases); the blue line when the encounters are infinitely separated. The sequence of colored lines shows the PDF as the separation increases. The bumps and wiggles in individual PDFs are not noise or errors. They are probably related to frequency matching between the spiral arms and specific orbital frequencies (radial, vertical, angular frequencies of the epicycle). Obviously the PDFs are not identical and the differences

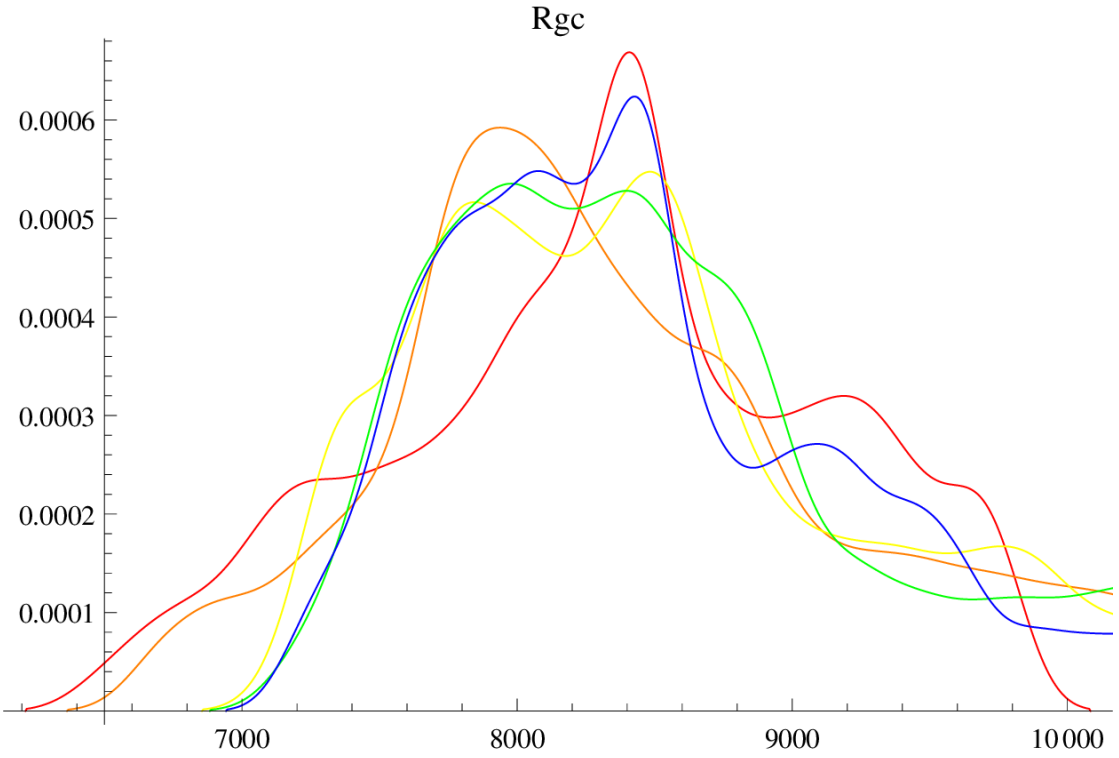

FIGURE 3.19: The final PDF's for R_{gc} for calculations with different peak separations. In rotation periods the separations are 0 (red), 1 (orange), 2 (yellow), 4 (green); and the infinitely separate calculations (blue). As the time between encounters increases the PDFs approach the PDF for independent encounters (see text).

between them diminish as the separation in time of encounter increases. Similar comparisons can be made for v_R and v_z, as is shown in Fig. 3.20 and 3.21 respectively.

Certainly more careful study could be made of the distributions but one should first average over small ranges in all the parameters that might be relevant for resonant-like behavior. This includes spiral width, spiral separation and spiral pattern speed. None of these is expected to be the same from spiral to spiral nor to have a precise relationship to the rotation frequency. It is very likely that averaging will smooth out the complicated behavior and make any trends more apparent.

In lieu of completing that study one can simply ask whether the difference between the calculated distributions is important. In order to quantify this difference we have to introduce a statistical indicator, that allow as to highlight the gap between the two considered distribution.

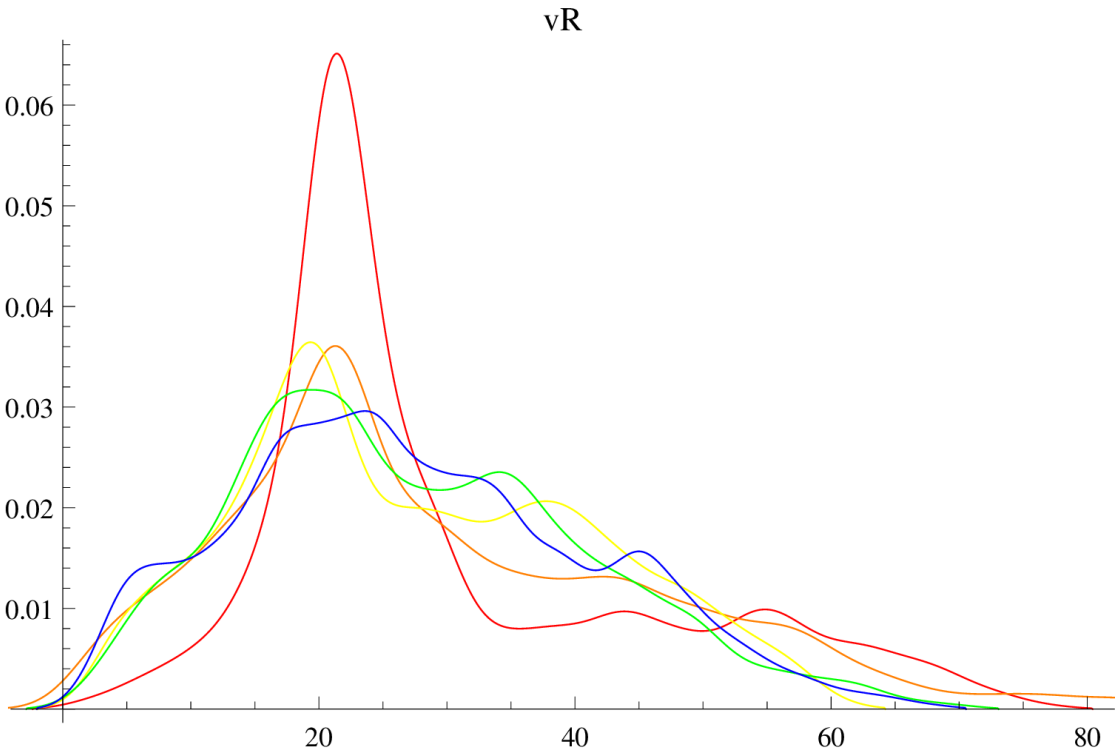

FIGURE 3.20: The PDF's for v_R for different peak separations (see Fig. 3.19).

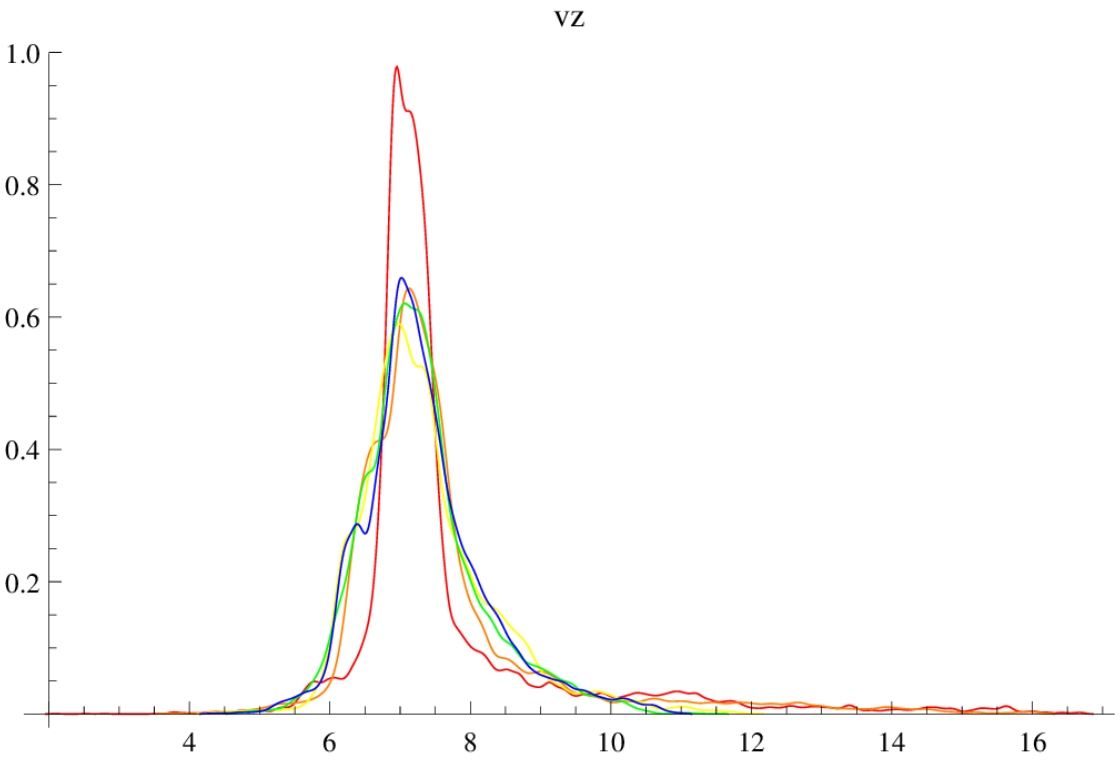

FIGURE 3.21: The PDF's for v_z for different peak separations (see Fig. 3.19).

3.4.4 A statistical measure of the difference in distributions

Discrimination in favor of a hypothesis H_2 against H_1 may be quantified in terms of the mean information per observation. The KL or Kullback-Leibler divergence of H_1 from H_2 is

$$\mathrm{KL}(2:1) = \int f_2 \log \frac{f_2}{f_1} dx \tag{3.51}$$

where $f_1 = f_1(x)$ and $f_2 = f_2(x)$ are the probability densities for H_1 and H_2 respectively. For our purpose, we can define H_2 as the "true overlapping" dynamics and H_1 as the "approximate separate" dynamics. We are interested into how many identically and independently distributed data items are needed (for f_2) before it becomes clear that this distribution is different from the approximate one.

The answer is that each unit of likelihood requires on average roughly $1/\ \mathrm{KL}(2:1)$ independently and identically distributed samples; for typical scientific conclusions one might require 3 sigma. In that case, roughly $N = 3/\ \mathrm{KL}(2:1)$ samples are needed.

There is a rather stringent limit to the number of encounters that the Sun might experience. We denote that number by N_{max}. If $\mathrm{KL}(2:1) < 3/N_{max}$ then the PDFs for the dynamical outcomes do not distinguish independent from overlapping physical encounters. In other words, if $N_{max} \leq 30$ then $\mathrm{KL}(2:1) < 0.1$ implies that the true and approximate distributions are indistinguishable at the 3 σ level. If N_{max} is less than 30 then, of course, KL could be higher and the differences between the distributions are even harder to measure.

The Sun's rotation period of ~ 200 Myr permits no more than ~ 20 full orbits in a 4 Gyr lifetime. If spiral arms grow/decay on an orbital timescale and there is only 1 arm at a time then $N_{max} = 20$ encounters, so the choice of 30 is conservative. On the other hand, the spiral arms may be short-lived and N_{max} may be larger. It then becomes essential to study cases with smaller peak widths. At present that case has not been studied.

The KL divergence is not a metric since $\mathrm{KL}(2:1) \neq \mathrm{KL}(1:2)$; it has a sense of direction since one distribution is regarded as true and the other is approximate. A symmetrized form $J(1,2) = \mathrm{KL}(1:2) + \mathrm{KL}(2:1)$ has some of the properties of a distance-like quantity. It can be regarded as a measure of the divergence between H_1 and H_2, i.e. a measure of the difficulty of discriminating between them.
Another choice to quantify the different between the two distribution may be the KS or Kolmogorov-Smirnov test. The KL divergence and KS test are quite different. KL(2:1) is a measure of the difference between f_1 and f_2 given that the data are distributed according to f_2; KS tests the null hypothesis that f_1 and f_2 are the same (small p-value

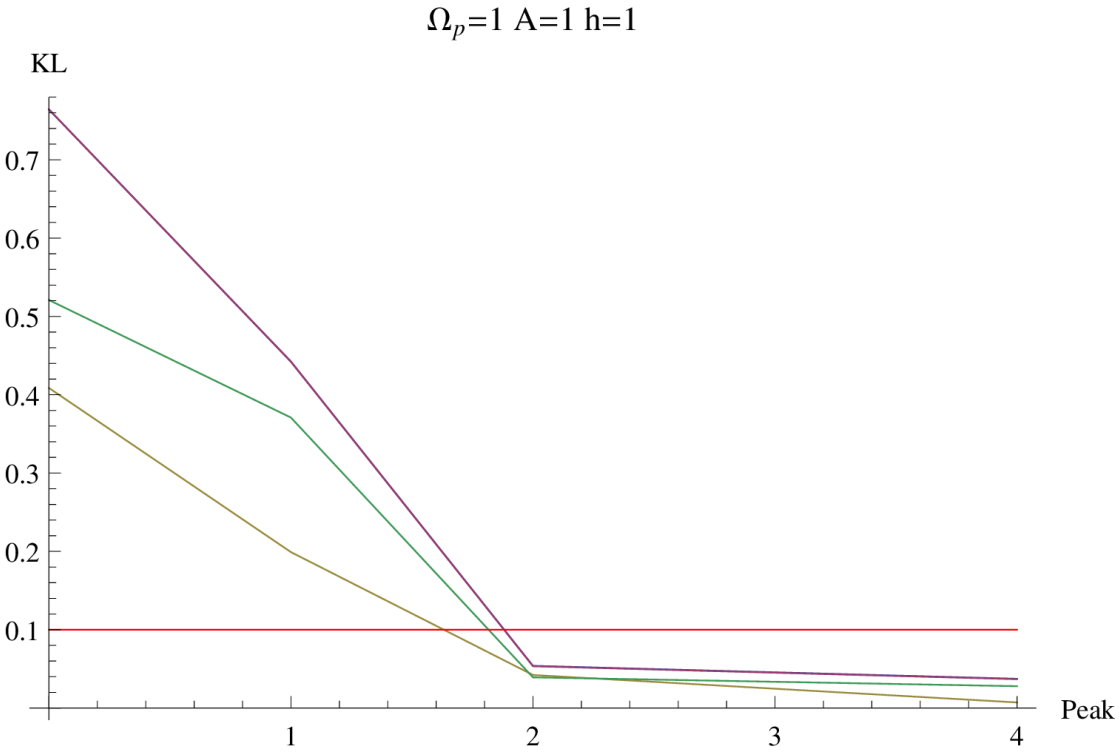

FIGURE 3.22: KL divergence (for the standard case) for distributions of guiding center radius (purple), radial velocity amplitude (brown) and vertical velocity amplitude (green). The red horizontal line is an approximate cutoff: when KL lies below the line it will be difficult to distinguish (at 3σ) true from approximate distributions within 30 encounters.

means unlikely). In a qualitative sense (and not a technical one) the KL divergence is a more powerful discriminant than the KS test and for this reason was been preferred as indicator. Finally, the dynamical distribution is multidimensional but it is difficult to work with the joint distribution. Instead, a comparison is made of individual 1D PDF's for 3 different quantities. The "standard case" is shown in Fig. 3.22.

When the separation of the two peaks is $\geq$ 2 rotation periods the distributions are indistinguishable for $\leq$ 30 samples.

The KL divergence ultimately decreases with the peak separation for all parameter sets (pattern speed, amplitude, spiral scale height) but not all cases are as clean as the standard case (Fig. 3.22). An example with $\Omega_p = 0.75$ and otherwise standard parameters shows non-monotonic behavior for v_R, the radial velocity amplitude (brown line). The KL divergence does not fall below the red horizontal line until the separation is about 4 rotation periods. The actual crossing point is likely between 2 and 4 rotation periods but the resolution in time of separation is insufficient to be more accurate.

The KL behavior for v_R may be traced back directly to the PDF. The distribution is complex, probably from exceptional resonant-like interactions. The complexity means

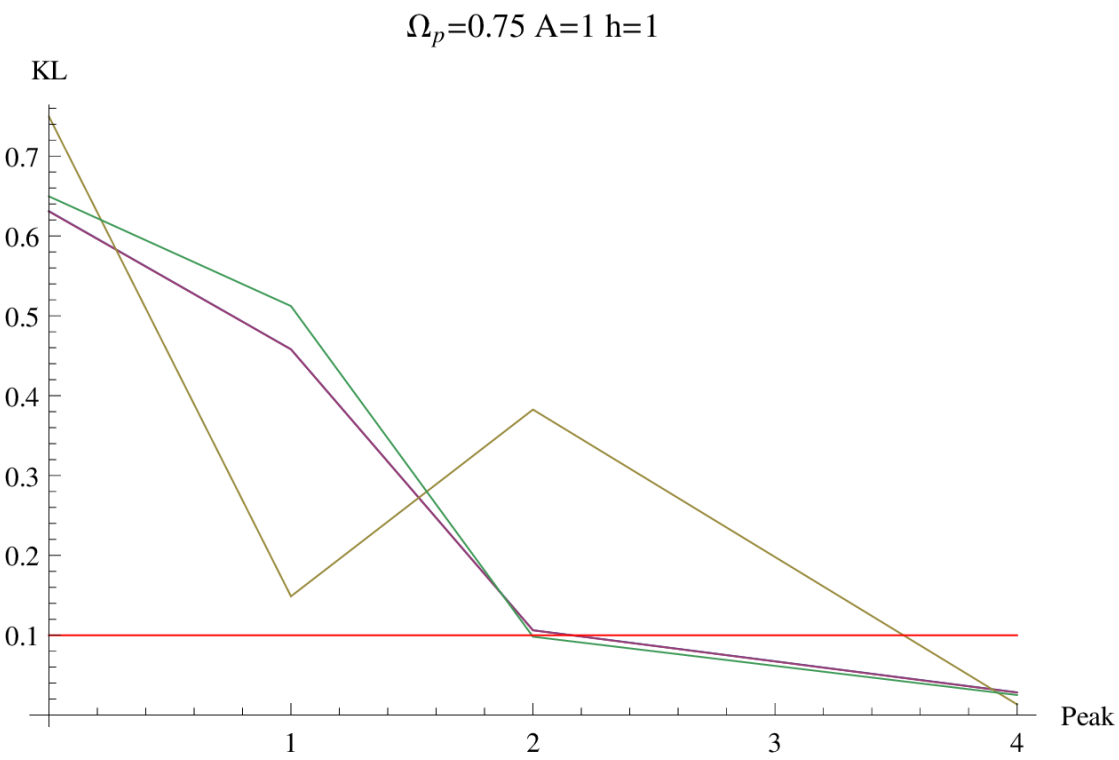

FIGURE 3.23: Same as Fig. 3.22 but for $\Omega_p = 0.75$.

that distinguishing the two distributions is somewhat easier.

It is difficult to give a definitive summary of the results for the reasons already alluded to: (1) fixed width for the peaks, (2) resonant-like interactions that need to be averaged over. Both of these could be addressed by doing more runs.

3.4.5 The spiral arms perturbation on the solar path

In the previous paragraph we have seen that the distribution originated by two joined spiral arms is almost indistinguishable with respect to one due to two separate and consecutive spiral arms perturbations. From a computation point of view the last one is the better approach in order to make less burdensome the integration for the equation of motion.

Our main aim consists now in the extrapolation of the previous results, to probe the effect due to a three-dimensional spiral arms on the sun-like stars after a multi-encounter (more than 2) perturbation, in order to verify if a non-axisymmetric component may have a crucial role in the explanation of the solar migration phenomenon. Adopting again the formulation summarized in §3.3.1 and setting the code in order to obtain 20 consecutive spiral arm encounters, we have integrated the motion for a sample of 100 sun-like particle, changing their intial positions and the parameters of the spiral arms

perturbations. This procedure allowed us to point out if the spiral arms perturbation has been able to produce a solar migration at the beginning of the history of our Solar System, underlining which feature of the spiral arm model could determine a sensitive change in the solar position.

The sample of 100 "solar analogs" for each set of spiral arms parameter (see Tab. 3.3). By solar analog we mean a star with the same mass as our Sun and the same initial peculiar velocity components ($U_\odot = 11.1 \pm 0.74$ km/s, $V_\odot = 12.24 \pm 0.47$ km/s, $W_\odot = 7.25 \pm 0.37$ km/s, Schönrich et al. (2010)). Since the solar peculiar velocity is the result of primordial events occurred during the virialization of the Galaxy, like as the violent relaxation (see, Bindoni and Secco (2008)), we can assume that it did not change even if the solar position of the Sun may be evolved during its life. Indeed, as it was already said Sellwood and Binney (2002), the spiral arms perturbation could move the stars without changing in a significant way their peculiar velocities. In the table 3.3 it is possible to see the range of initial positions and parameters of the spiral arms that were explored with the simulation. The samples for the initial positions, the pattern speed Ω_p and

Parameter	**Range of values**
Initial Position R_0	6, 6.1, 6.2, 6.3, 6.4, 6.5, 6.6, 6.7, 6.8, 6.9, 7, 8
Amplitude A	0.5, 1, 2
Pattern speed Ω_p	0.5, 0.9, 1, 1.1, 1.2, 1.3, 1.4, 1.5, 2
Scale height h_s	0.5, 1, 2
Spiral width W	0.5, 0.75, 1, 1.5, 2

TABLE 3.3: Set of parameters for each simulation with a sample of 100 particles sun-like and 20 consecutive encounters with a spiral arms perturbation. The spiral arm parameters are expressed as multiplies of the "standard case" quoted in §3.3.1

the spiral width W are not equally distributed in the considered range. This choice was determined by two requirements

- to ensure that the initial position are consistent with the over-metallicity gradient of the Sun (see §3.1.1);
- to better investigate the spiral parameters that have showed a greater importance in the determination of the solar orbit. Indeed we started with an homogeneous sample for each quantities (0.5, 1, 2 multiplies with respect to the standard case),

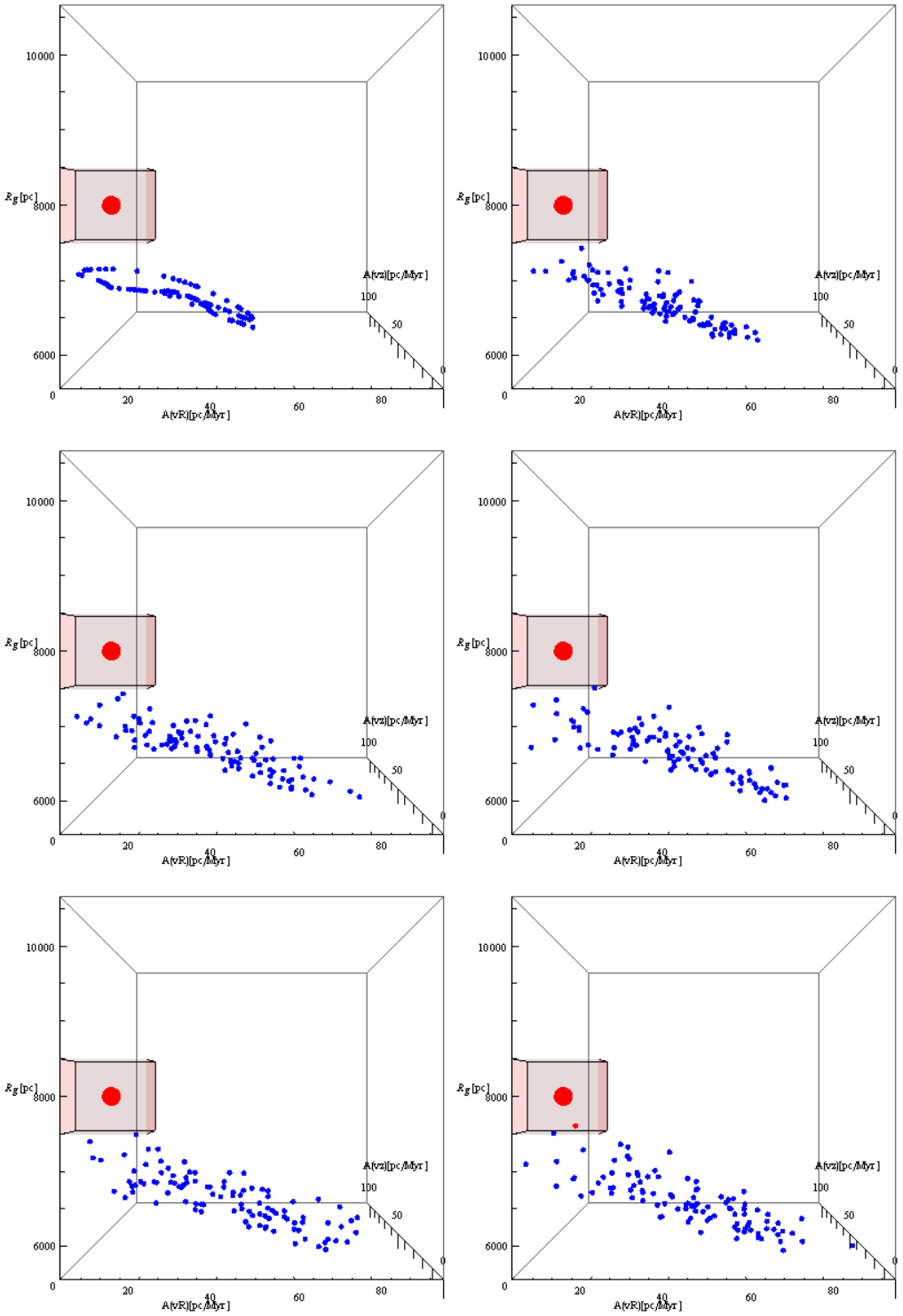

FIGURE 3.24: Evolution through 6 spiral encounters for a sample with initial position of 6.5 kpc in the standard case.The number of spiral arms encounters increases from left to right and from the top to the bottom of the figure.

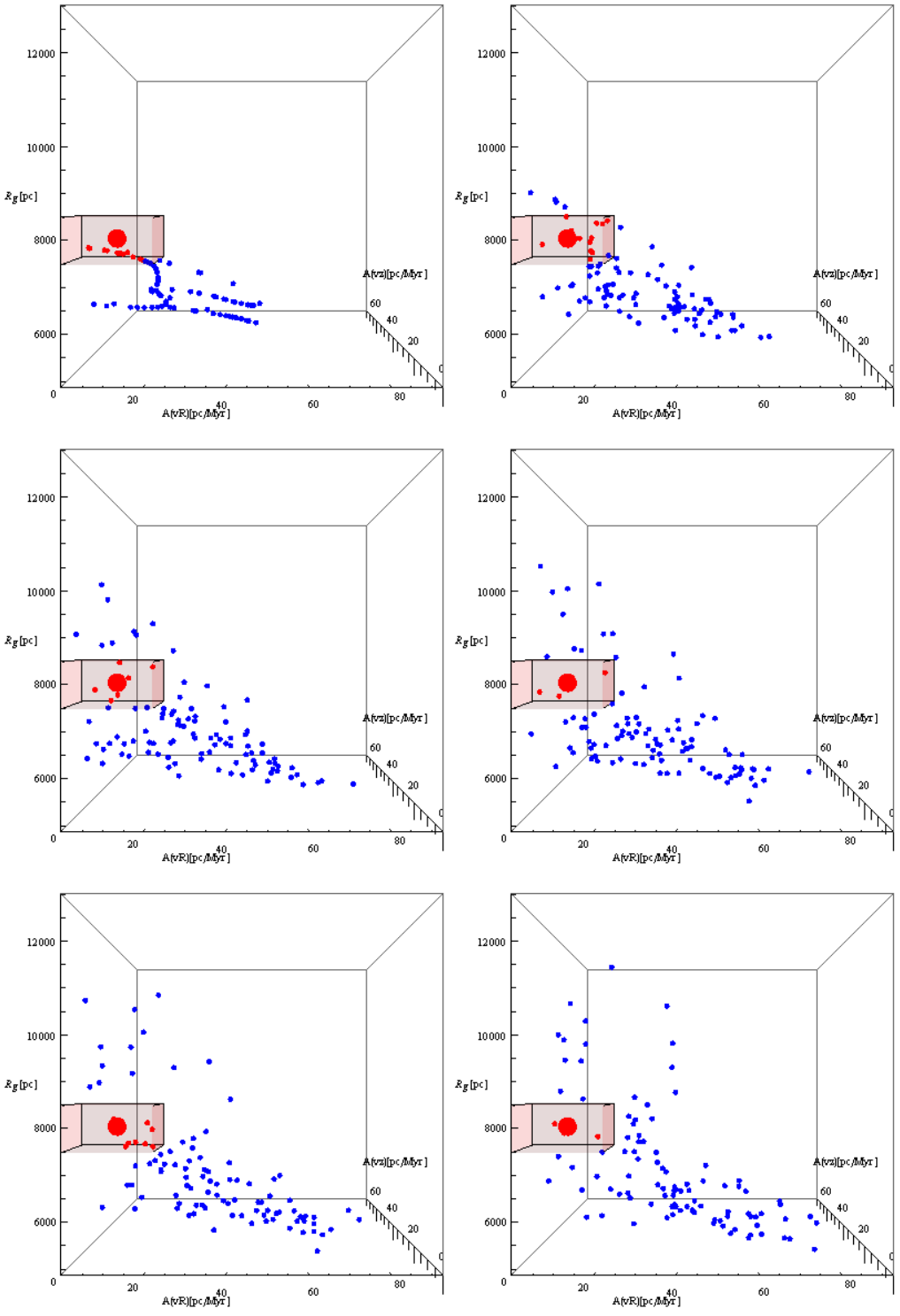

FIGURE 3.25: Evolution through 6 spiral encounters for a sample with initial position of 6.5 kpc for $\Omega_p = 1.2\Omega_{standard}$. The number of spiral arms encounters increases from left to right and from the top to the bottom of the figure.

to test the sensitivity of the solar path to each parameter. After these fist sets of simulations, we focused with more details on those quantities that induced the most significant changes in the orbits of the solar analogs.

In order to establish if a particle achieved a position compatible with that of the Sun at present after one, two or more spiral encounters, we had to impose some criteria. In particular we defined a *box of the positive suns* based on the present solar position R_g (intended as the guiding center radius), radial velocity v_R and the vertical velocity v_z. Indeed we could not consider only the agreement with the final position of the particle and the Sun, but we have also to avoid excessive heating effects, since, as we have already said, the peculiar velocities are determined by different dynamical events at the beginning of the Milky Way history and did not change in a significant way during its evolution. So the three edges are defined as follow:

- $R_g \rightarrow (R_\odot \pm 500)$pc where $R_\odot = 8000$ pc as usual;
- $A(v_R) \rightarrow (U_\odot \pm U_\odot)$ km/s
- $A(v_z) \rightarrow (W_\odot \pm W_\odot)$ km/s

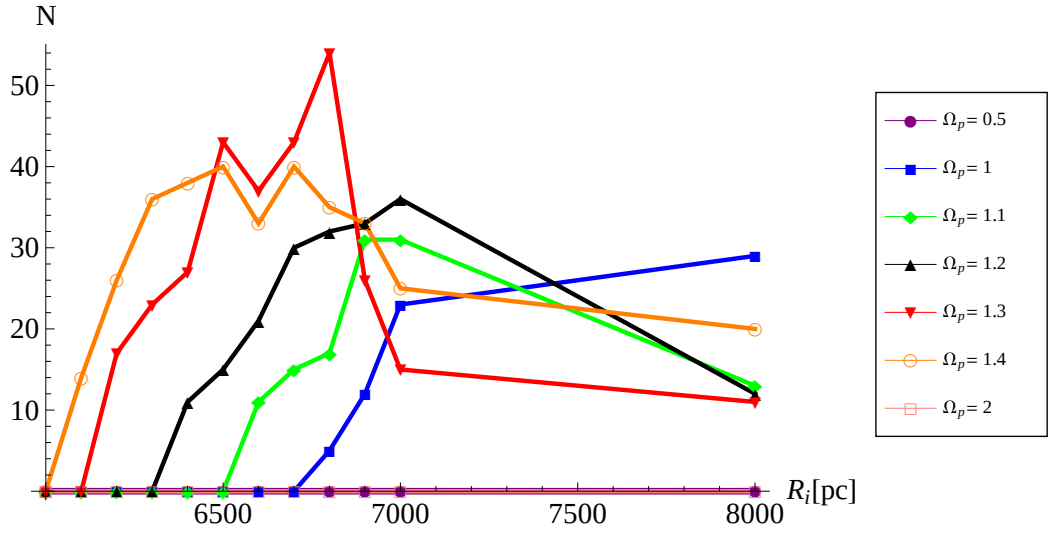

FIGURE 3.26: The number of solar analogs starting from different initial position (on the x-axis in pc) that reach the "positive box" just after one encounter with the spiral perturbation. The distribution of the results are strongly dependent from the value of Ω_p, the other parameters (the amplitude A, scale height h_s and spiral width W are set to the standard case values).

We are interested in whether a sun-like star that was located in a inner position ($\sim 6-6.5$ kpc) from the galactic center at the beginning of the Solar System, could move to the

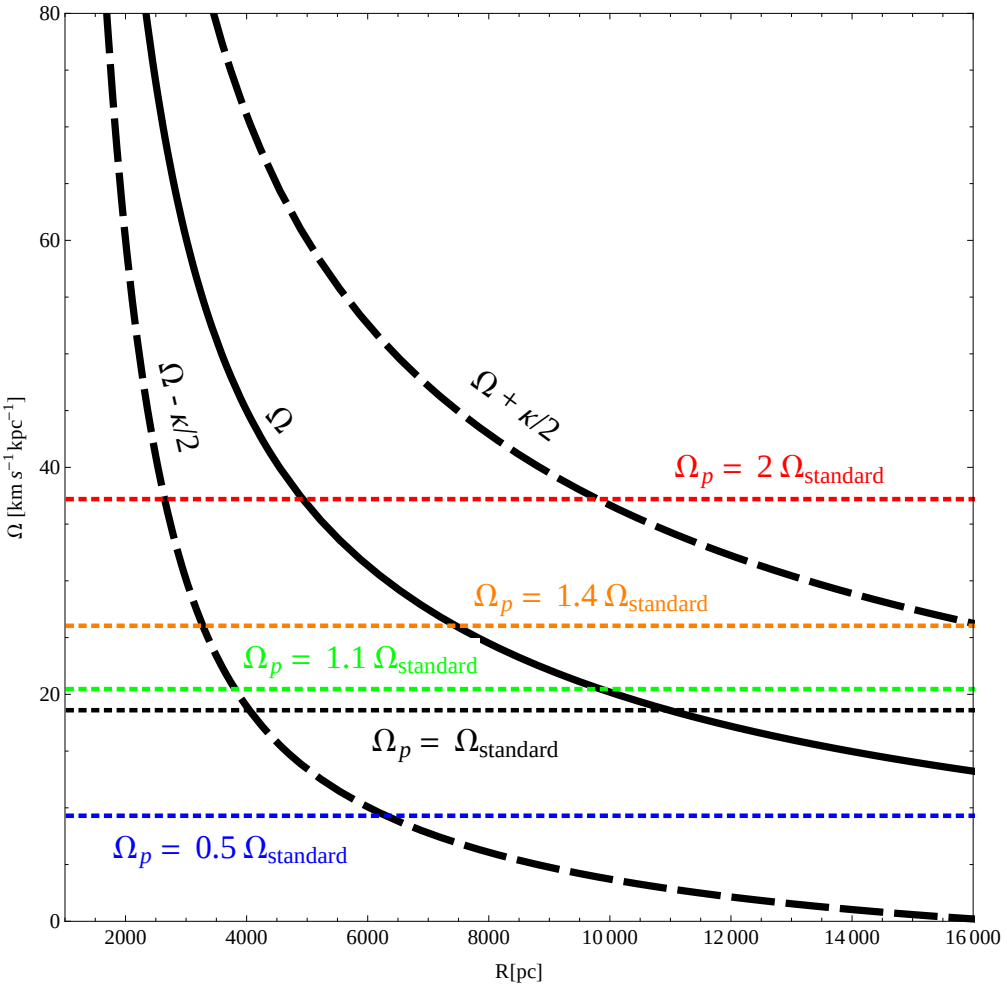

FIGURE 3.27: Collocation of the different patter speeds considered, with respect the Lindblad resonances

present solar position under the effects of one or more spiral encounters. We imposed that each spiral arms perturbation be born, grow and die in a total integration time of 12σ. In particular σ is equal to half rotation period at the initial position of the particles, then it changes as a function of R; in other words the overall duration of the perturbation depends on the initial position. However the difference between the galactic period of a particle at 6 or 8 kpc does not produce a significant difference in the final distribution of results, then we will not commit a serious mistake if we have ignored this dependence. In both cases the single spiral perturbation lasts about of the order of 1 Gyr (precisely between 1.2 and 1.5) Gyr), so it is easy to compute that after 4 or 5 spiral arm encounters we cover the total life of our Solar System.

Twenty spiral arms events is longer than the entire life of the Universe. But we know that the distribution due to two joined spiral arms is compatible with the distribution due to two separate and consecutive perturbations. Then 20 encounters allow us to consider different combinations of perturbing situations (single and consecutive spiral or multi-ovelapping perturbations), probing also some extreme cases and determining

the parameter space within which the current solar configuration can be achieved. We can follow the evolution of our sample through these spiral arm multi encounters for the standard case spiral in Fig. 3.24. The 100 particles start from an initial position of 6500 pc, the box of the positive suns is highlighted by the red rectangle, the blue points are the particles that do not satisfy the dynamical situation of the Sun today, while the red points are particles with velocities and position compatible with the current solar parameters. For the standard case, the spiral arm perturbation obtained by the snapshot of the RAVE data, it is very difficult for the particles with initial position 6.5 kpc or less to achieve a configuration in agreement with the solar one. The situation changes if we increase the pattern speed Ω_p, considering for example a Ω_p equals to 1.2 times the values provided by Siebert et al. (2012). As it is possible to see in Fig. 3.25, some particles with the same initial position (6.5 kpc) reach the solar configuration after only one encounter with the spiral arms perturbation. It confirms the importance of the parameter Ω_p in determining a significant change of the solar motion under the spiral arms action.From these results we can argue that a solar migration, from a inner galactic position to the current one, may be likely determined by a spiral arms with a pattern speed higher than the value fixed by the current solar environment ($\Omega_p = 18.6$ km s^{-1} kpc^{-1}). Despite that, we can not increase Ω_p indefinitely to produce a more efficient stellar migration, since for a double values of Ω_p in the standard case, none particle achieves the current solar area starting from an inner galactic position, also considering greater and smaller initial position. A useful summary is visible in Fig. 3.26, in which we can see the number of solar analogs starting from different initial position (on the x-axis in pc) that reach the "positive box" after one encounter with the spiral perturbation. The distribution of the results are strongly dependent from the value of Ω_p (line are color-codes with respect to the values of Ω_p), while all the other parameters are set to the standard case values.

These results are expected from the preliminary study on the spiral arm parameters (see §3.4), where it was identified that in order to produce a efficient migration outward we need $\Omega_p > \Omega_{standard}$. It is useful to highlight the previous study is referred to the current solar position (~ 8 kpc), but we can argue that the rough outline about the parameters remains valid also in other range of distance. In Fig. 3.27 is possible to see the collocation of some patter speeds considered in the study with respect to the Lindlad resonances. As was argued in the previous paragraphs, another important parameter in the spiral arm action may be the spiral width W. Performing a very preliminary investigation also for this parameter (see Tab. 3.3), we found out that the more efficient migrations are obtained for a $W = 2W_{standard}$, in other words if the temporal width of the perturbation is equal to 1 solar rotational period around the Galaxy. The physical reason as to why if varying the width makes a difference is the following: the characteristic epicycle periods are of order the rotation period. So, holding the width fixed (equal to a rotational

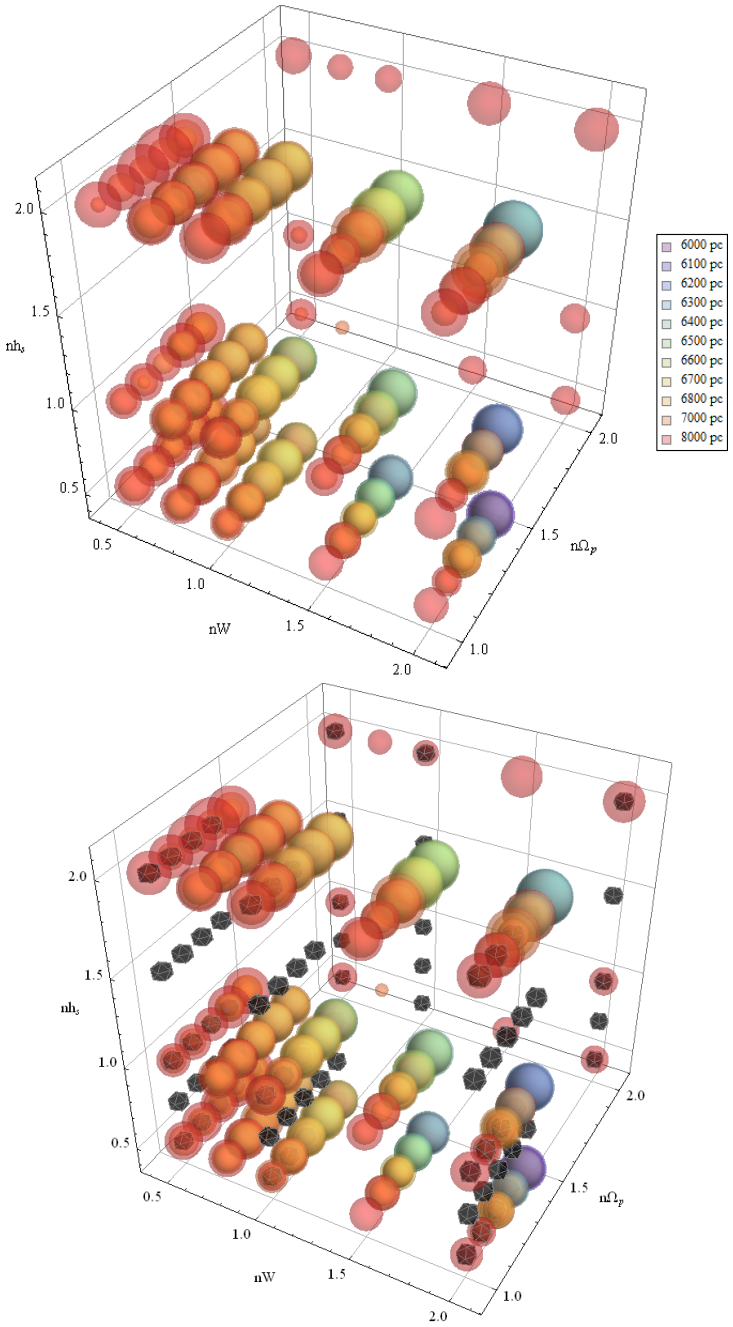

FIGURE 3.28: Bubble histogram for the particles with respect to the more important parameters for the spiral arms perturbation (amplitude, pattern speed and scale height). The dimensions of the bubble are proportional to the particles number that represent. The particles starting from different initial positions are color coded as quoted in the legend. In the top panel are quoted the numbers of particles that achieve the current solar position after one single encounter with the spiral arms perturbation. In the bottom panel we find the full set of integration, with black symbols for those combinations of parameters that did not produce any particle in the present solar position. The parameters' values are expressed as multiplies of the "standard case" (see §3.3.1)

period) it couples to a particular epicycle variation. This will be true even when one considers that all such interactions of the Sun with the spiral arm are averaged over phase.

We can collect all the information about the different spiral arms parameters in the Fig. 3.28, in which are quoted all the initial conditions and the combined effects of the different quantities that play an important role in the spiral arms perturbation.

4

Solar motion on the Galactic Habitable Zone

The position and the motion of the Sun inside the Galaxy may assume some importance when we look to the conditions that have allowed the development of life on Earth. In the following sections we will see how the idea of habitability in the Galaxy has been built and revisited during the years, traducing the habitability requirements in edges of a zone in which we meet the most suitable conditions to host complex Life. Even if we are very far to find a definite view about the challenging topic of Galactic habitability, we can use the present knowledge in order to figure out into the contest the star migration, in particular the solar one, inside the framework of the galactic habitability.

4.1 The Galactic Habitable Zone

The birth and the development of life, as we know it, are based on a very fine balance between many factors and conditions that involves different areas of study from chemistry to dynamics.
There are two main research branches on this topic:

- the **planetary** one, which is mainly connected to the presence of the liquid water on the planetary surface that depends on planetary distance, the mass of the central stars etc.;
- the **Galactic** one, that tries to figure out what would be the more suitable Galactic environment for the emergence of life.

In order to define the Galactic Habitable Zone (GHZ) we have to take into account several galactic-scale factors, they include those which are relevant to the formation of planets, such as radial disk metallicity gradient, and moreover the events that could threaten the life (nearby supernovae and gamma ray burst). Many efforts have been done in order

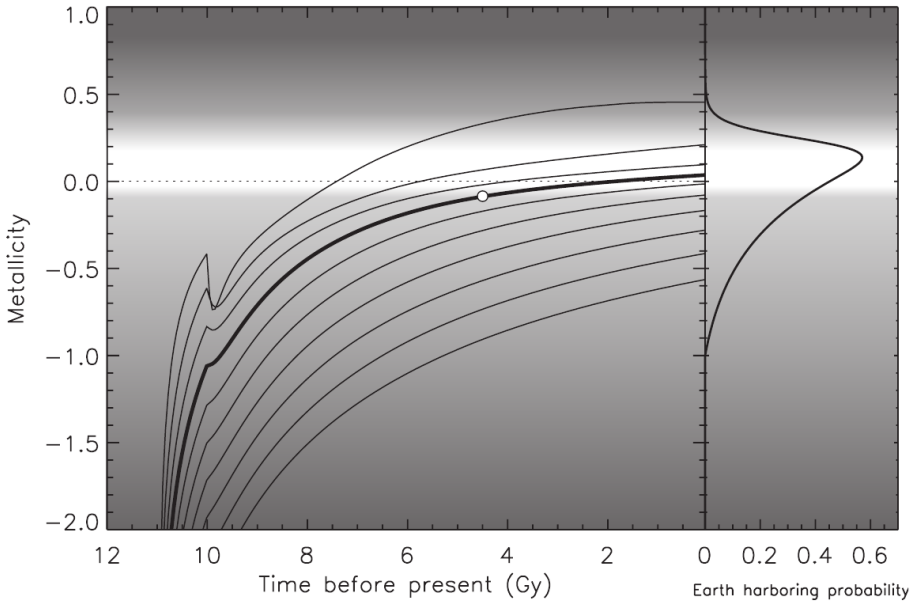

FIGURE 4.1: Space-time distribution of metals obtains by Lineweaver et al. (2004). Metallicities at different Galactocentric distances (from 2.5 kpc, upper curve, to 20.5 kpc, lower curve, with 2 kpc increments) can be compared with the probability of harboring terrestrial planets as a function of the metallicity of the host star. The solar time formation at the current galactocentric distance is highlighted by a white dot.

to identify and correlate the different factors that may influence the rise of life from a galactic point of view, see Gonzalez et al. (2001), Gowanlock et al. (2011), Lineweaver et al. (2004). The most effective summary for the life requirements inside the Galaxy was provided in the work by Lineweaver et al. (2004). In this study was combined a model of the evolution of the Galaxy Fenner and Gibson (2003) with metallicity constraints derived from extrasolar planet data (radial distributions of stars, gases and metals, the metallicity distribution of nearby stars and the solar chemical composition) Lineweaver (2001), in order to define the GHZ's size with respect to the time and distance from the galactic center. It is important to stress that the GHZ limits in metallicity the galactic area in which a star meets conditions compatible with the habitability at the moment of its birth. Indeed a star formed with the right metallicity will be able to produce Earth-like planets, no matter if it will leave the GHZ immediately after its formation.

In Lineweaver et al. (2004) four prerequisites for complex life have been identified and quantified by a probability:

1. **presence of a host star**: the most convenient way to describe the stars distribution is to use the SFR that indicates how many stars are available to host a planetary system;

2. **a sufficient amount of heavy elements to form terrestrial planets**: the metallicity to build efficiently a terrestrial planet presents an upper and a lower

limit. Indeed too little metallicity does not allow to form a Earth-mass planet, while with too much metallicity, giant planets could destroy the terrestrial ones. A metallicity-dependent probability, P_{metals}, of harboring terrestrial planets has been assigned to the space-time distribution of metals (see Fig. 4.1)

3. **enough time to allow biological evolution**: they assumed the Earth's time scale as typical and adopted 4±1 Gyr as the characteristic time for the development of complex life. This constraint is modeled as a probability $P_{evol}(t)$, defined as the cumulative integral of a normal distribution of mean 4 Gyr and dispersion 1 Gyr;

4. **an environment free of supernovae**: the high energy radiation due to a supernovae's explosion can be fatal to the rise of life. It is not easy to determine the real effect of this emission on an organism, but it surely depends sensitively on the thickness and composition of an atmosphere and on the density of dust and gas. The probability that complex life survives supernovae is defined as $P_{SN} = 0.5\xi(r,t)$ where $\xi(r,t)$ is the supernovae danger factors depending on the galactocentric distance r and the stars' formation time t.

The total probability to obtain a galactic environment favourable to complex life P_{GHZ} could be expressed as

$$P_{GHZ} = SFR \times P_{metals} \times P_{evol} \times P_{SN}. \tag{4.1}$$

The factors P_{SN} and SFR of Eq. 4.1 are not independent, but since they grow in opposite ways (with a higher SFR, the supernovae danger increase reducing P_{SN} and viceversa) finally results in a compensation between them.
$P_{GHZ}(r,t)$ expresses the number of planetary system with suitable condition for life as a function in time and space. In Lineweaver et al. (2004) the GHZ is identified as the region that includes from 68% to the 95% of these systems: a region centered at $\sim$ 8 kpc from the Galactic center broadens with time, that includes stars formed between 8 and 4 billion years ago (see Fig. 4.2). The 68% edge encompasses less than $\sim$ 10% of the stars that are born in our Galaxy and comparing the age distribution of complex life (in green on the right in Fig. 4.2) it appears that $\sim$ 75% of the stars that could host life are on average 1 Gyr older than the Sun.
In their work Lineweaver et al. (2004) did not impose that a condition life be probable, but assuming the current solar condition as a template to find similar systems, a natural consequence is that the Sun itself lies inside the GHZ defined using those constraints. A generalization for the result shown in Fig. 4.2 may be achieved looking not to the development of complex life, but to life in general; in other words they removed the 4 Gyr limit in time excluding P_{evol} from Eq. 4.1, extending the GHZ as showed in Fig. 4.3.

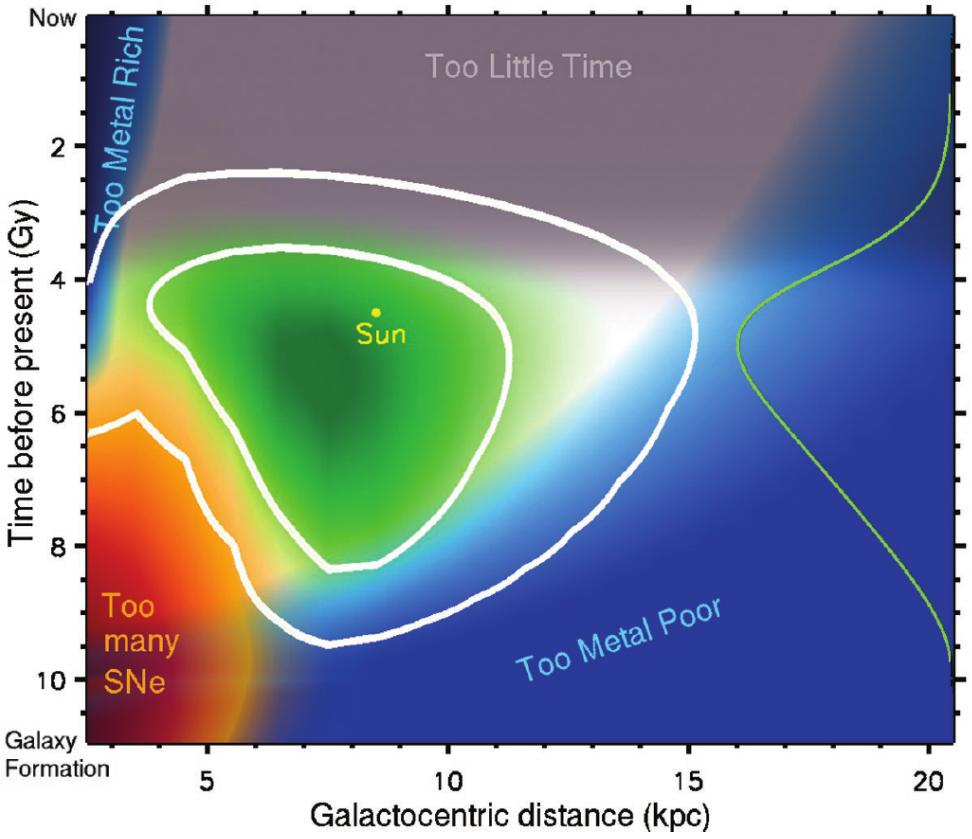

FIGURE 4.2: The GHZ in the disk of the Galaxy obtained using the requirements based on host stars presence, suitable metallicity (blue), sufficient time for evolution (gray), and freedom from life-extinguishing supernova explosions (red). The white edges encompass 68% (inner) and 95% (outer) of the origins of stars with the highest potential to be harboring complex life today. The green line on the right shows the age distribution of complex life, obtained by integrating $P_{GHZ(r,t)}$ over r, Lineweaver et al. (2004)

In this way the mean age for a star hosting life is shifted ahead in time: ~ 1 Gyr younger than the Sun.

In spite of the fact that the procedure followed in the previous study is solar-centric, the final conclusions are reasonable in the frame of our Galaxy; indeed it would be true in general that:

- the early intense star formation in the inner part of the Galaxy provided the heavy elements necessary to the formation of terrestrial planets at the beginning of the galactic history, but also produced unacceptably strong supernovae emission that did not allowed the arising of life for several billion years;
- the stellar halo and the thick disk, because of their low metallicity, unlikely host terrestrial planets;
- the bulge is not a suitable environment for life too, since it suffers from a high density of stars with intense radiation field and close encounters between stars.

The limits of the habitability in Galaxy have been revisited in few recent works, in particular by Prantzos (2008) and Gowanlock et al. (2011). The criticism of the first one is very useful. He highlights the two different approaches to the GHZ idea. One is related with the probability of complex life around one star at a given space-time location; the other one involves the volume (or surface) probability density of having complex life in a given position of the Galaxy at a given time. In other words: in the first case we are dealing with the probability for a star which arises at a given time in a given place of Galaxy to develop in one of its Earth-like planets a complex life; in the second one how many stars are able to do that at the same space-time location. The two approaches are clearly shown in Prantzos (2008). The overall probability for Earth-like planets with life is given at the bottom right of Fig.5 in Prantzos (2008), where the product of the two probabilities for Earths surviving Hot Jupiters and Earths surviving SN is considered. Substantially the calculation of P_GHZ of Lineweaver et al. (2004) has been redone after a strong critical revision on the constraints on which the definition adopted for the GHZ is based (in particular the requirements linked to the surviving supernova explosions , and the metallicity-dependent probabilities of forming Earth-like planets and Hot Jupiters).

Despite that , the study provides the GHZs size for five different epochs during the

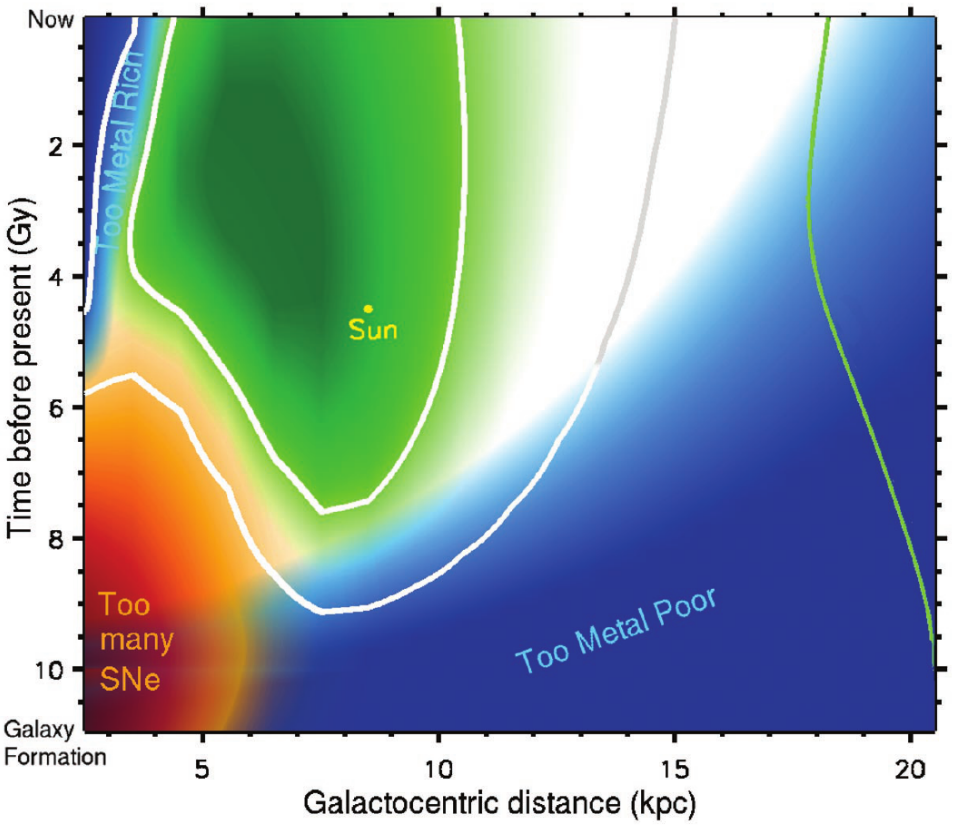

FIGURE 4.3: The GHZ in the disk of the Galaxy without the temporal requirement (4 ± 1 Gyr) for the complex life, Lineweaver et al. (2004)

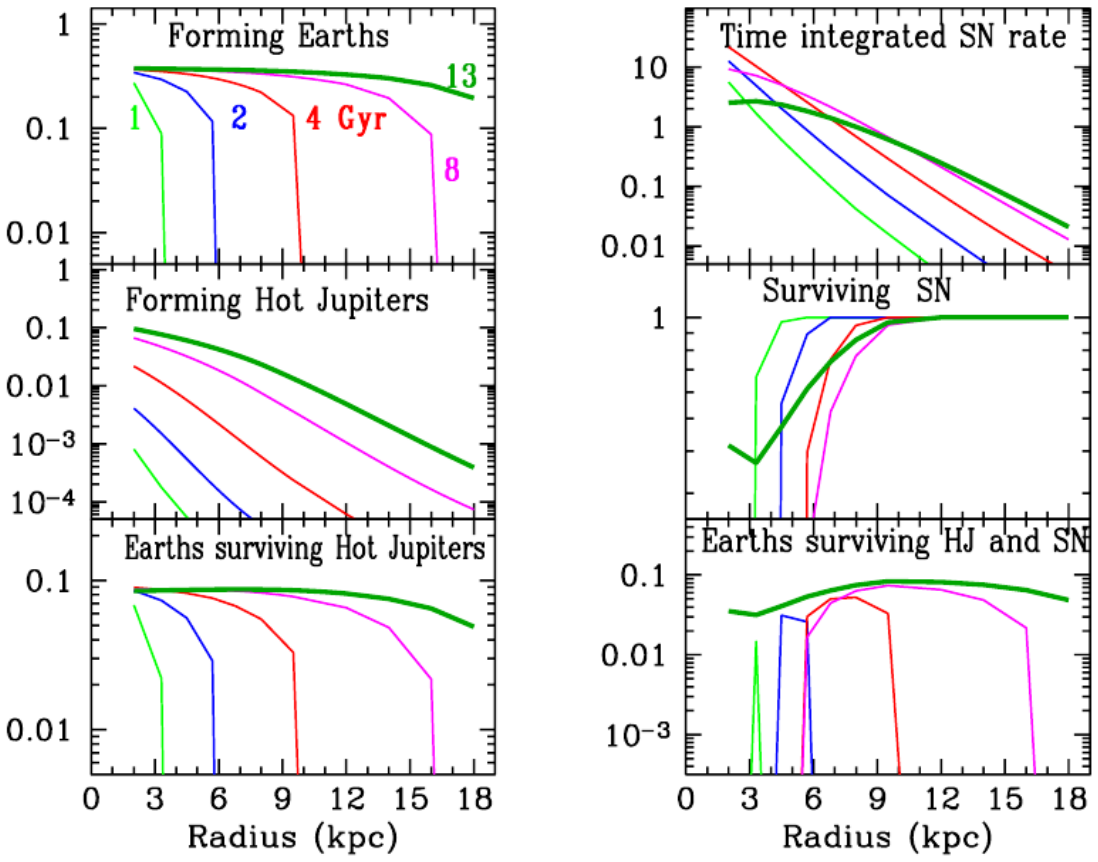

FIGURE 4.4: The probability of the events that constrain the GHZ's size provided by Prantzos (2008) for five different epochs (1, 2, 4, 8 and 13 Gyr) in the Galaxy history. The overall probability for Earth-like planets with life is shown in the bottom right panel, and defines a ring in the Milky Way disk extremely narrow at the beginning of the Galactic history, but progressively achieves the quasi-total extension of the galactic disk at present time peaking at about 10 kpc.

evolution of the Milky Way (namely 1,2,4,8 and 13 Gyr) (see Fig. 4.4). The GHZ has a ring-like shape, quite narrow at the beginning of Galaxys history (around 3 kpc), but it progressively widens, achieving the quasi total- extension of the galactic disk at present time peaking at about 10 kpc. Fig.6 (left panel) of Prantzos (2008) shows the same result as Fig.5 (bottom right) in space-time diagram, comparable with Fig. 4 of Lineweaver et al. (2004). Conversely Fig.6 (right panel) is obtained multiplying the probability distribution of the left panel with the corresponding surface density of stars which is much larger in the inner disk than in the outer one. Owing to that the main result becomes: it is the inner disk the place relatively more hospitable than the outer one and it is more interesting to seek complex life there than in the outer disk. The result is not too much different from that found by Gowanlock et al. (2011), who describe the GHZ in terms of the spatial and temporal dimensions of the Galaxy that may favor the development of complex life, it means following the second approach to the GHZ idea. The first one is strongly critical of the GHZ's edges provide in Lineweaver et al. (2004), and with

respect to the possibility to define a limit for a habitable zone in general inside the Galaxy. Indeed Prantzos (2008) pointed out that the constraints on which the definition of the GHZ is based (in particular the requirements linked to the supernovae rate, and the metallicity) depends heavily on the assumption about the evolution of the Milky Way and the probability of having stars that host terrestrial planets, which are far from be univocally defined at present. Despite that, the study provides the GHZ's size for five different epochs during the evolution of the Milky Way (namely 1, 2, 4, 8 and 13 Gyr) (see Fig. 4.4). The requirements in metallicity are represented as the probability of Earth-like planets to survive Hot Jupiter. The GHZ has a ring- like shape, quite narrow at the beginning of Galaxy's history (around 3 kpc), but it progressively widens, achieving the quasi-total extension of the galactic disk at present time peaking at about 10 kpc.

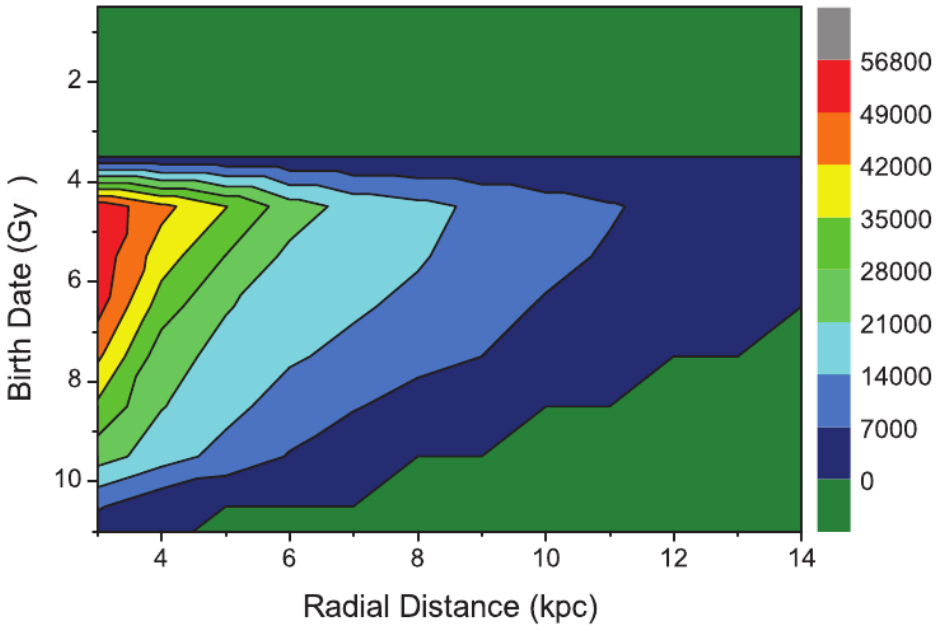

FIGURE 4.5: The GHZ in the disk provided by Gowanlock et al. (2011). The number of habitable planets per parsec (number provided by the color-coded vertical bar) is plotted as a function of radial distance and birth date. In this study the negative effects of supernovae action are reduced, obtaining in this way that the habitable planets are most prevalent in the inner part of the Galaxy.

They in fact found that our current location is not particularly favorable to host life and pointed out that the more suitable environment lies in the inner part of the Galaxy (with a peak in correspondence of 2.5 kpc, see Fig. 4.5). This extreme result is due to the reshaping of the supernovae effects in the balance between metallicity and high frequency emission: reducing the negative effects of supernovae action, the GHZ may be extended at $r \sim 2.5$ kpc from the center, thanks to the metallicity that in the inner Galaxy produces a high planet formation rate for long time scale and makes the inner

region able to support the greatest number of planets with the suitable conditions to host complex life. In addition Gowanlock et al. (2011) redefined also the morphology of the GHZ that is not longer a annular region, as in Lineweaver et al. (2004), but consists of a region near to the Galactic center, without a precise inner boundary and strongly dependent on radial distance.
After this kind of clarifications we stipulate to refer our study to the canonical model of Lineweaver et al. (2004), substantially not too much changed by the revision of Prantzos then conserving the first idea of GHZ. Our innovation will be rather to consider habitability in the context of solar migration. That is the research field in which we are moving in the present work

4.2 Sun position on the GHZ

The solar migration inside the galactic disk may become relevant also in the framework of the habitability. Indeed if the Sun is not in a fixed position from the beginning of its history, it could spend a significant fraction of its life outside the galactic region more suitable for life.
As we have already seen (§ 4.1) the GHZ was identified by Lineweaver et al. (2004) as a region centered at the current Sun's position that becomes wider with time. According to the metallicity gradient and the perturbation due to the spiral arms that we obtained, the Sun could lie at the beginning of its history closer to the galactic center, in particular around 6 kpc. We are interested to check if the perturbed solar path is compatible with the galactic conditions that allow the life to arise. Otherwise if we will find that the solar motion due the spiral perturbation entails a violation of the requisites for habitability, we should exclude this mechanism. An example of this violation is provided by the solar paths obtained by Kaib et al. (2011): in Fig. 4.6 projecting over the GHZ the solar paths of Fig. 3.1, if the motion in the left panel (A path in Fig. 3.1) is compatible with the habitability conditions, conversely the right panel (B path in Fig. 3.1) shows a motion of the Sun in totally disagreement with the possibility of life: indeed the environment of the solar formation and evolution is compromised by a too high metallicity and the destructive effects of the supernovae emissions.
So we superimposed on the GHZ few our solar paths under the effects of non-asymmetric spiral arms component, in order to understand if the variation of position for the Sun may compromise the development of life in the Solar System. In Fig. 4.7 it is possible to see the motion of a solar analog that starts this evolution closer to the galactic center ($R_{in} = 6.1$ kpc) and current solar peculiar velocities, under the effect of a multi-spiral arms perturbation with a faster rotation than the values in the current solar environment ($\Omega_p = 1.1\,\Omega_{standard}$, a reasonable assumption for the past). The sun-like star, although

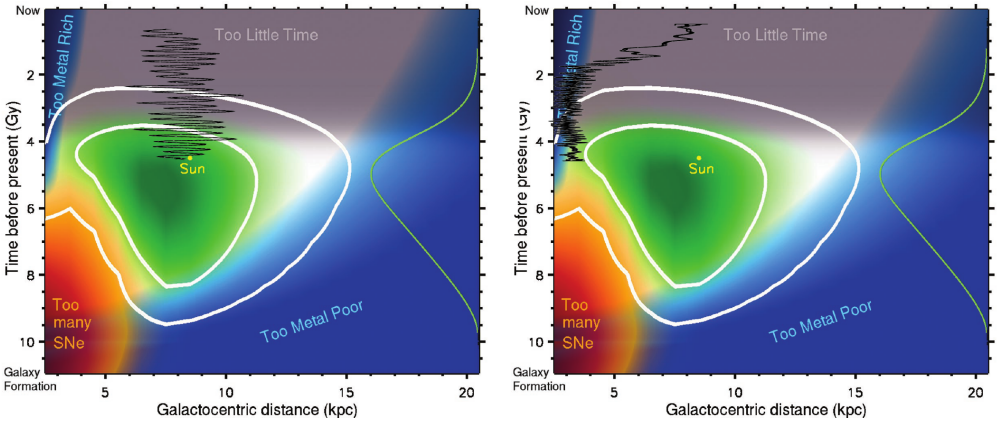

FIGURE 4.6: Solar paths by Kaib et al. (2011) superimposed on the GHZ Lineweaver et al. (2004). One the right side is shown a solar evolution in disagreement with the habitability conditions, while the solar path on the left panel is compatible with the arise of life (see text).

it starts its evolution closer to the galactic center, is still inside the GHZ. That is important, since in order to have the correct metallicity composition to form and conserve terrestrial planets, it is crucial the position at which the star was born. Indeed a later solar relocation outside the GHZ which should not have a significant relevance on the composition of the star and a its possible planet system. Conversely, an exposure to the supernovae emissions could compromise the development of life also after the formation of the central star. Indeed, it may sterilize the planetary surface, impeding the growth of complex organisms or completely destroying them.

It easy to see that this sterilization does not occur for the considered solar path, that moves outside the GHZ (left panel) only because of the request of 4 Gyr to the development of the complex life. Indeed if we remove the constrain about the complex life (right panel), looking to the formation of life in general, the solar motion lies totally inside the GHZ.

We see that the migration from a inner position due to the spiral arms action, even modified the solar motion, does not preclude to achieve the arise of life. An other point of view could be wondering if a star in the current position of the Sun at the beginning of its history may be pushed out of the GHZ, or also, if our Sun will be expelled from the GHZ in the future with negative consequence for the organisms jet present in the planetary system around the star. In Fig. 4.8 are showed two different solar paths, both with initial position of 8 kpc and the other initial conditions equal to the 6 kpc case, perturbed by a multi-encounters standard (see § 3.3.1) spiral arms perturbation, i.e. a spiral structure with features equal to those obtained in solar neighborhood Siebert et al. (2012).The difference between the two path are due to the variation for the encounters geometry (distinct value of ψ_{max}. On the left panel the solar analog suffers a strong change of its position with a maximum excursion of 3 kpc and it is pushed close the edge

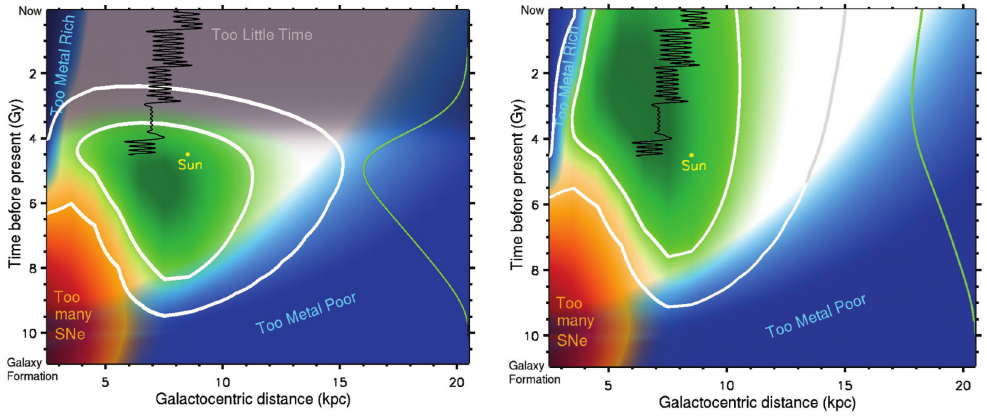

FIGURE 4.7: Solar path, with initial position of 6.1 kpc, perturbed by a multi-encounters spiral arms superimposed on the GHZ Lineweaver et al. (2004), with (left side) and without (right side) the requiring 4 ± 1 Gyr for the evolution of complex life (see text).

of the GHZ, instead on the right panel a star with the same initial conditions remains nearly fixed around the position in which the simulation started. Both these paths, although with different behaviors, show the same results: the perturbed effect produces a motion, more or less strong, but completely within the GHZ's edge.

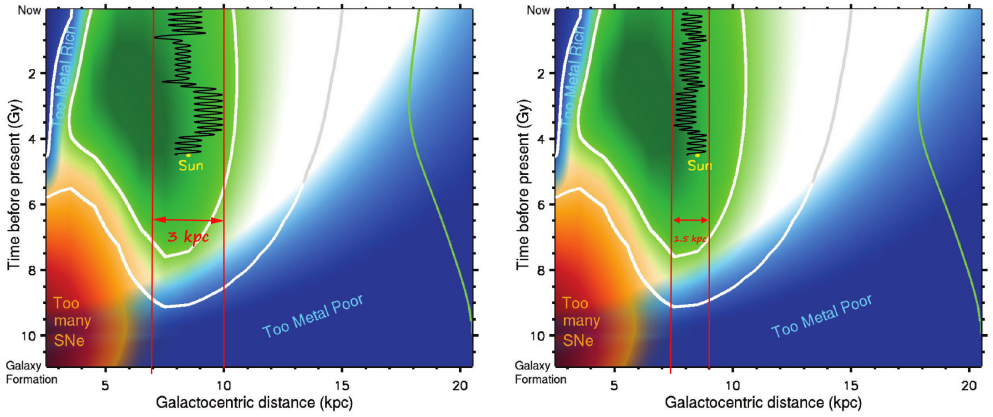

FIGURE 4.8: Two different solar paths, with initial position of 8 kpc, perturbed by a multi-encounters standard spiral arms superimposed on the GHZ Lineweaver et al. (2004) without the requiring 4 ± 1 Gyr for the evolution of complex life. The vertical red lines delimit the maximum excursion for the motion.

In conclusion the possible perturbation effects due to the spiral arms action on the solar path in relation to the GHZ's contours may open a new framework for the habitability and stellar migration research, indeed new works could be focused not only about where the single system lies at the present time, but in which galactic region it has spent the most part of its evolution time and if its path is in agreement with the development of the complex life. The GHZ may be also improved and better defined by the dynamics issues that take a role during the evolution of a star and its planetary system, taking

into account for example the consequence that a different position in the galactic environment may have on the small bodies, like comets, that could hit the planetary surface with a devastating effect for the life. As we already seen in §4.1, a deep uncertainty rules over the definition of the GHZ; then it is very important to underline that the present results are only a first attempt to introduce the problem of a possible solar migration in the framework of the requirements for the complex life in the Galaxy. It is clear that our conclusion should be completely revisited if the GHZ's edges indicated by Lineweaver et al. (2004) will be no longer valid or will be subverted. In addition our conclusion are limited by the not perfect agreement between the galactic model on which is based the GHZ and the potential that produce the solar motion, lack that also may entail some inaccuracies in our understanding of the constraints to impose for the solar path, in order to meet the most suitable conditions for the arise of Life.

5

The Spiral Arms Effects on the Oort Cloud

Several perturbers act on the main cometary reservoir of our planetary system. The main ones, the Galactic tide and the close stellar passages, might be both affected by a possible solar migration. We decide to focus our attention only on the first of these perturbations, in order to identify clearly the consequences that a change in solar position may have on the Galactic tidal field. In this chapter we will describe the cometary motion under the Galactic field with and without the spiral arms perturbation, in order to underline the main differences between the two treatments.

5.1 Cometary Orbits

It is well-know (see §1.3.2) that the quasi-integrable perturbation due to the Galactic action produces a significant change in cometary orbital elements, in particular interesting the perihelion distance q. A crucial aim of this work is tried to understand the effects of a different Galactic environment on a comet reservoir like the Oort cloud. This study may flow into several research fields:

- **a deeper understanding of our planetary system**: investigation about the solar motion inside the Galaxy and the cometary dynamics that this motion entails, that may be the key to figure out the behavior of the peripheral objects of our Solar System (for example the unexpected path of body like Sedna, see Kaib et al. (2011);
- **a redefinition of the GHZ boundaries**: since the Oort cloud is the remnant of the planetary formation, an Oort-like cometary cloud may be a commons structure around the many exoplanetary systems discovered in growing number from the first claim in 1995, see Mayor and Queloz (1995). Understanding the way in which these

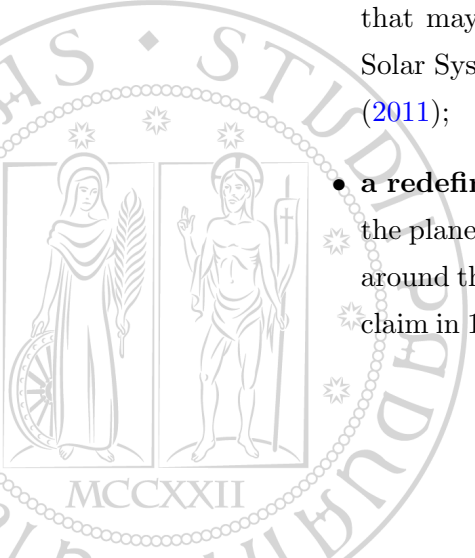

structures could have evolved, it may throw light on the ambivalent role played by the comets in arise of life, leading to a redefinition of the GHZ's edges.

As in the study about the solar path we proceeded with a gradually increasing in the perturbation of the cometary motion. First we analyzed the Galactic tidal effect on the Oort cloud in an axisymmetric potential for a nearly circular solar motion, trying to identify the contribution of each galactic component (bulge, disk and dark matter halo), in a second moment we introduced the spiral perturbation, studying cometary object that follow the solar path through its migration on the Galactic disk.

5.2 Integration in an axisymmetric potential

In a Galactic potential devoid of components that break the cylindrical symmetry, as that of bulge, disk and dark matter halo, it is possible to simplify the integration of the comet motion under some reasonable assumptions. In particular allow us to use the formalism of the *Hill' s approximation*, to make easier, from a computation point of view, the integration of the cometary motion.
The Hill's approximation adapts the formalism of the restricted three-body problem for the case in which the dimension of *satellite system* is much smaller than the distance to the center of the *host system*. The previous condition suits our problem, in which the system Sun-comet achieves the maximum size of 1 pc, while the distances from the galactic center are about three orders of magnitude larger. In this type of situation we may also assume that the variation of the gravitational potential along the cometary orbits is very smooth, making possible the application of the *distant-tide approximation* (see Binney and Tremaine (2008)). This treatment considers a spherical host system, with a gravitational potential $\Phi(R)$ at the distance R from its own center. Of course our problem does not enjoy this kind of symmetry, owing to the presence of the disk. So we have re-considered the Hill's approximation in 3D-dimensions changing the symmetry of the host system potential from a spherical to an axial one (see §C for more details). The consequence for this change in the potential symmetry, has not relevant fallout on the cometary equations if the comet orbit remains into the galactic equatorial plane. Indeed the two equations describing the comet movement on the plane, do not change with respect to the spherically symmetric 2D-dimension case. Conversely the equation along the z-axis becomes completely different, as expected, in order to take into account the cylindrical symmetry along the z-axis. We also assume that the center of mass of the satellite system (e.g. the Solar System) travels on a circular orbit with angular velocity Ω_0, at the distance R_0, the initial solar position from the center of the host system (the Galaxy). This assumption appears reasonable, due to the small variation of the radial

position for the motion of a Sun-like star under the action of an axisymmetric potential (see §3.2.3). Further we follow the analysis of the comet motion in a co-rotating Sun centered system in which the x-y plane coincides to the stellar orbital plane, $\hat{\mathbf{e}}_\mathbf{x}$ points directly away from the center of the host system and $\hat{\mathbf{e}}_\mathbf{y}$ points in direction of the orbital motion of the satellite (see Fig.5.1).

This reference system, called *synodic*, rotates with the frequency $\mathbf{\Omega}_0 \equiv \Omega_0 \hat{\mathbf{e}}_\mathbf{z}$ and in this system the acceleration of a particle is described by the following expression:

$$\frac{\mathrm{d}^2\mathbf{x}}{\mathrm{d}t^2} = -\nabla\Phi_T - 2\mathbf{\Omega}_0 \times \frac{\mathrm{d}\mathbf{x}}{\mathrm{d}t} - \mathbf{\Omega}_0 \times (\mathbf{\Omega}_0 \times \mathbf{x}), \tag{5.1}$$

where Φ_T is the total potential acting on the comet. The corresponding force may be decomposed in two different contributionss as follows:

$$\nabla\Phi_T = \nabla\Phi_s + \sum_{j,k=1}^{3} \Phi_{jk} x_k. \tag{5.2}$$

$\nabla\Phi_s$, equal to $GM_\odot/r^2$ in the solar case, represents the part of gravitational potential due to the satellite system[1], while the second term, due to the extended galactic component, comes from the *distant-tide approximation* once expanded the gravitational potential of the host system $\Phi(R)$ in Taylor series, starting from the center-of-mass of satellite system. In Eq. (5.1) it is possible to separate the effect of the Coriolis force from the centrifugal one and analyze the two contributions separately.

In our coordinate system the center of the host system lies in $\mathbf{X} = (-R_0, 0, 0)$ and the components of angular velocity are $\mathbf{\Omega}_0 = (0, 0, \Omega_0)$. Introducing the satellite system of reference $\mathbf{x} = (x, y, z)$ (see §C) it turns that: $\Phi_{xx} = \Phi''(R_0); \Phi_{yy} = \frac{\Phi'(R_0)}{R_0} \neq \Phi_{zz}$[2]; $\Phi_{xy} = \Phi_{xz} = \Phi_{yz} = 0$. Then, the motion equations may be expressed as follow:

$$\begin{cases} \ddot{x}(t) = 2\Omega_0 \dot{y}(t) + [\Omega_0^2 - \Phi''(R_0)]x(t) - \dfrac{\partial\Phi_s}{\partial x}; \\ \ddot{y}(t) = -2\Omega_0 \dot{x}(t) + \left[\Omega_0^2 - \dfrac{\Phi'(R_0)}{R_0}\right] y(t) - \dfrac{\partial\Phi_s}{\partial y}; \\ \ddot{z}(t) = -4\pi G\rho(z)z(t) - \dfrac{\partial\Phi_s}{\partial z}; \end{cases} \tag{5.3}$$

where $\rho(z) \simeq \bar{\rho} \simeq 0.1 M_\odot$ pc^{-3} is the mean density in the Sun's neighborhood, along z-direction (see Brasser et al. (2010)). Using the relation $\Phi'(R_0) = R_0\Omega_0^2$, due to the assumption of a circular motion of the star around the Galactic center and introducing

[1] Not the first order term in the Taylor development of the gravitational force due to the host system (see §C).

[2] It becomes equal only in the case of a spherically symmetric potential (see §C).

the Oort's constants in the following form:

$$\begin{aligned} A(R) &\equiv \frac{1}{2}\left(\frac{v_c}{R} - \frac{\mathrm{d}v_c}{\mathrm{d}R}\right) = -\frac{1}{2}R\frac{\mathrm{d}\Omega}{\mathrm{d}R}, \\ B(R) &\equiv -\frac{1}{2}\left(\frac{v_c}{R} + \frac{\mathrm{d}v_c}{\mathrm{d}R}\right) = -\left(\Omega + \frac{1}{2}R\frac{\mathrm{d}\Omega}{\mathrm{d}R}\right), \end{aligned} \tag{5.4}$$

where $v_c(R) = R\Omega(R)$ is the circular velocity at the radius R, we can rewrite the system (5.3) as:

$$\begin{cases} \ddot{x}(t) = 2\Omega_0\dot{y}(t) + 4\Omega_0 A_0 x(t) - \dfrac{\partial\Phi_s}{\partial x}; \\ \ddot{y}(t) = -2\Omega_0\dot{x}(t) - \dfrac{\partial\Phi_s}{\partial y}; \\ \ddot{z}(t) = -4\pi G\rho(z)z(t) - \dfrac{\partial\Phi_s}{\partial z}. \end{cases} \tag{5.5}$$

Where the equations of motion are in **Hill's approximation** form. This last formulation has many advantages: first of all it avoids the problem of the loss of significant numerical digits, that affects approaches in which the Galactic tidal term is directly integrated (as we will see in §5.3.1.1). Further we have only one system of differential equations to integrate, indeed the contribution of all the Galaxy components is inside the total angular velocity Ω_0, thanks to the additivity of the potentials and to the assumption of circular motion of the Sun. That means a significant simplification from a computational point of view. The same reasons allow us to consider an analogous set of equations for each Galactic component, in order to underline the specific contribution to the total tide due to bulge, disk and dark mater halo. The Eqs. of system (5.3) have only to be transformed taking into account Eq.s (C.20, C.21) reported in §C.
Despite that computational simplification, this treatment is an approximated one and the assumptions on which it is based could not be fulfilled in every cases of our analysis.

5.2.1 Results for the cometary integration in a 2D axisymmetric potential

We have considered the comet body like a test particle for the galactic tide and chosen a comet belonging to the outer shell of the Oort Cloud, where the solar gravitational force is lower and the galactic perturbations are then more evident. The comet has initial aphelion $Q = 140000$ AU, initial perihelion q 2000 AU, inclination i equals to zero with respect the Galactic plane and galactic longitude which $l = \frac{3\pi}{2}$ rad (see Fig.5.1), with a

direct motion direction, that has been integrate for 100 Myr. Our preliminary aim is to focus on the single contribution to the comet motion due to each Galactic components of the potential and their relative weight in to influence the comet path. The choice to restrict the cometary motion to the plane, and in fact investigating a two-dimensional orbit, finds an explanation in our purpose to provide a deepening about all the galactic perturbations that are usually neglected in cometary dynamics studies. Constraining the motion on the plane allow us to focus our attention on the planar component of the Galactic tide that, as we already seen, it is very small with respect to the orthogonal one at solar distance, see **?**. Despite that, the planar tide may play a not completely marginal role, as suggested by Masi et al. (2009), expecially in the perspective of a Galactic inner collocation for the Sun at the beginning of its history, inside the framework of a solar migration.

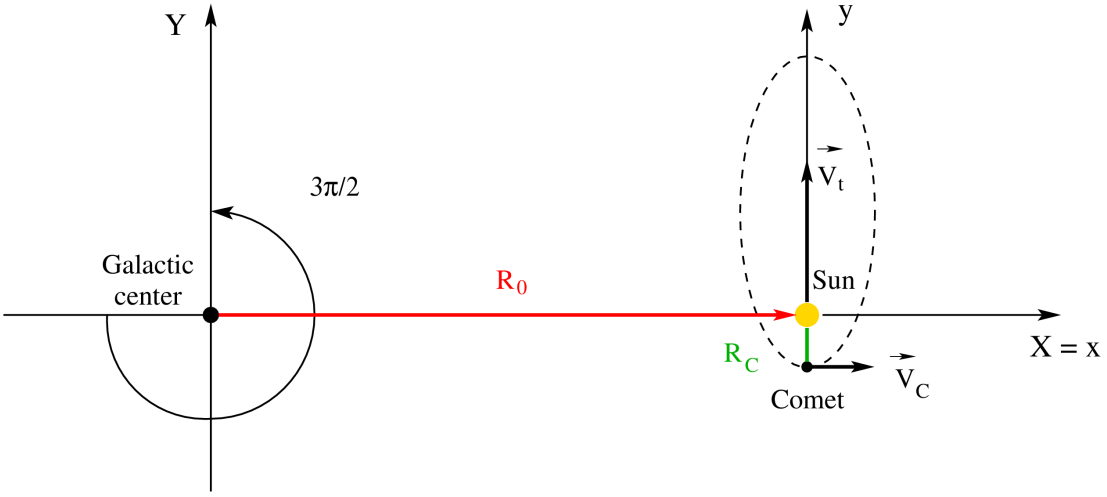

FIGURE 5.1: Picture of the initial conditions for a comet orbit with galactic longitude $\frac{3\pi}{2}$ in the reference system with the origin on the galactic center (X,Y). The heliocentric system (x,y) in Hill's approximation is also shown.

To test the influence of the position with respect the Galactic center on the comet's perihelion distance, we have integrated the cometary orbit for different distances, decomposing each time the total tidal perturbation into the contributions of the single Galactic components. To take into account that a generic central star, that hosts an analogs of Oort cloud, may have undergone a possible migration owing to the spiral arms effect stronger that in the solar case, we investigate the tides at two limit solar collocations $r = 4$, and 8 kpc, without considering shorter distances in order to preserve the spherical structure for the bulge.

As expected the integrated orbit shows that the total galactic tidal perturbation increases moving toward the center of the Galaxy (compare Fig. 5.3 with Fig. 5.2). In addition, the analysis for the single Galactic components underlines that the strongest

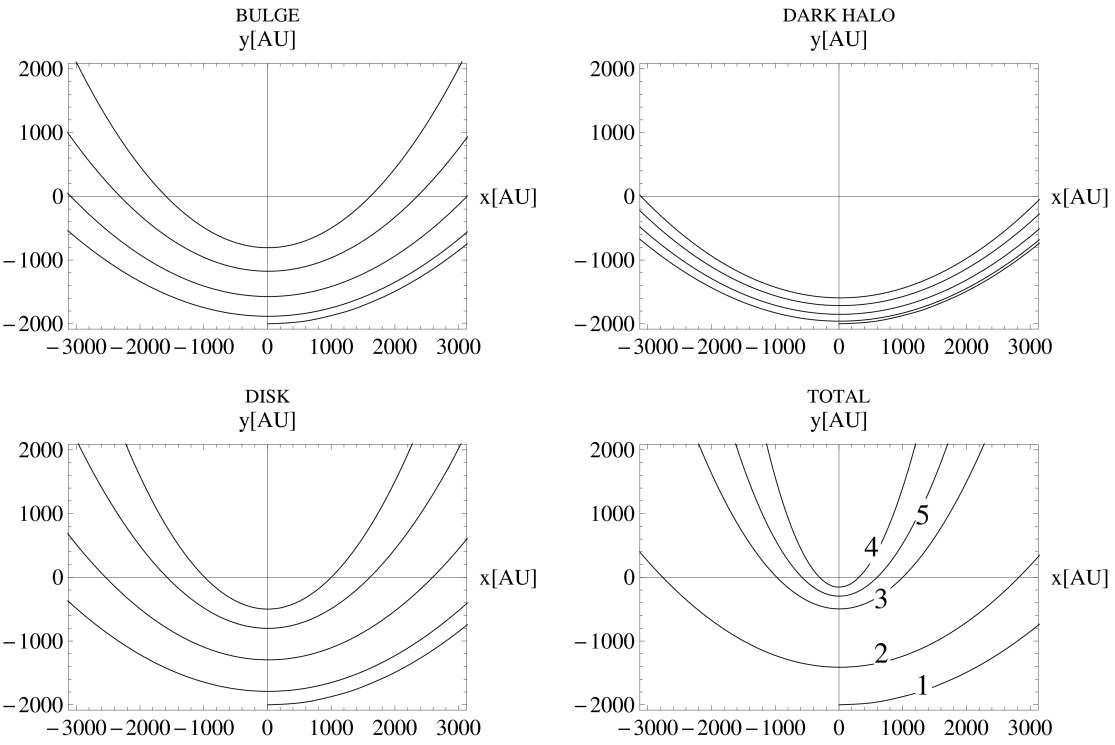

FIGURE 5.2: Zoom of the perihelion zone for the comet orbit at 8 kpc from the Galactic center (Hill's approximation). The different contributions from the Galaxy components to the perihelion variation are shown. The order of time-sequence is marked by numbers in the "'Total"' case, obtained by the sum of the contributions due to bulge, disk and dark halo.

perturbation effect is caused by the Galactic disk at 8 kpc (see Fig. 5.2). Conversely for a comet orbit closer to the Galactic center (4 kpc), the main role is played by the bulge, while the disk has only a secondary influence.

The reason may be clearly understood considering the Hill's approximation. Indeed Eqs. (C.20, C.21) tell us that the contribution of the Galaxy tide (x-component), together with the partially compensation due to the variation of centrifugal force at x-coordinate, turns out to be depending on the radial velocity contribution of each Galactic component. This contribution is factorized into two terms: one due to the trend of the radial velocity (the term in brackets at the second member of Eq.(C.21), the other one due to the amount of the corresponding square radial velocity. So at fixed distance of 8 kpc the first factor due to the disk is about equal to 1. Looking at Fig.2.1, the disk shows indeed a maximum in its circular velocity trend. The same term due to the DM halo turns to be, in absolute value < 1, due to its increasing velocity trend (less than a quadratic one). Conversely the bulge has a logarithmic derivative equal to $-\frac{1}{2}$ and then the same term reaches the value 1.5. But at fixed R the ratio between the second factors: $(v_{cD}/v_{cBG})^2 = 2.1$ is great enough in order to explain the dominance of the disk. Similar considerations allow us to predict that DM halo becomes relevant at about 15-20 kpc.

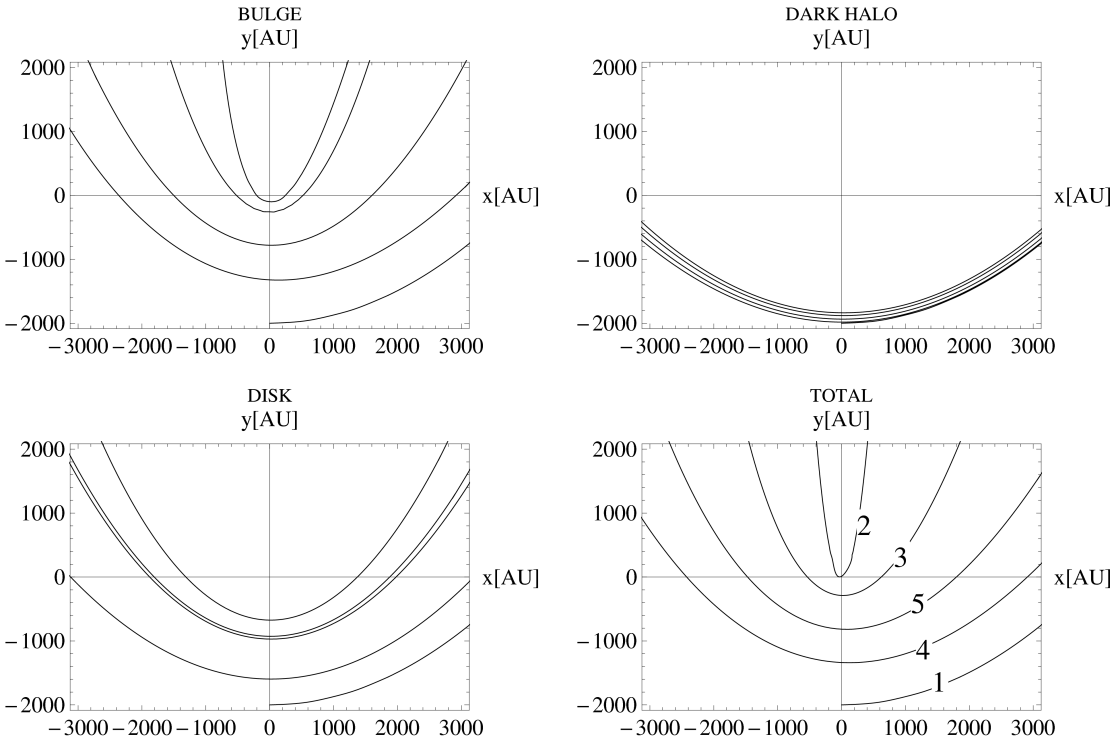

FIGURE 5.3: Zoom of the perihelion zone for the comet orbit at 4 kpc from the Galactic center (Hill's approximation). The different contributions from the Galaxy components to the perihelion variation are shown. The order of time-sequence is marked by numbers in the "'Total"' case, obtained by the sum of the contributions due to bulge, disk and dark halo.

At the distance of 4 kpc, the first factor due to the disk and DM halo are, in absolute value, < 1 (the velocity due to disk and DM halo are increasing), on the contrary the term due to the bulge is 1.5. So the bulge dominance is manifest even without considering the contribution due to its second factor $(v_{cBG})^2$.
Starting from this very basic example, we will add details to our model, introducing the spiral arms perturbation and consequently deserve the Hill's approximation. We will also build a random 3D sample of comets to integrate around a Sun in motion through the Galactic disk.

5.3 Integration in a non-axisymmetric potential

The introduction of the spiral arms in the galactic potential, breaks the cylindrical symmetry which usually holds for the cometary motion under the effect of the tidal field of the Galaxy (like the Hill's approximation, that we have seen in the previous paragraph, and other simplified expressions of the equations of motion suggested by Trumpler and Weaver (1953), Heisler and Tremaine (1986), Levison et al. (2001)). To probe the spiral arms perturbation on the comet orbits, the lack of symmetry forced us

to use a non-approximated expression for equations of motion in which a main keplerian motion around the Sun is perturbed by the action of the Galaxy. The surrounding galactic environment is introduced by a perturbative function. It may be useful, before proceed with applications on the comet motion, to draft the system of equations of motion by a theoretical point of view.

5.3.1 The relative form and the perturbative function $\mathcal{R}$

Following Danby (1962), we consider a generic system on N bodies and transfer the origin of the reference system to the N-th particle. The position vector of the i-th body with respect to N-th one may be expressed as:

$$\mathbf{r}_i = \mathbf{r'}_i + \mathbf{r}_N \tag{5.6}$$

Deriving twice with respect to the time we obtain:

$$\ddot{\mathbf{r}}'_i = \ddot{\mathbf{r}}_i - \ddot{\mathbf{r}}_\mathbf{N} \tag{5.7}$$

where the accelerations on the right side of the previous equation are calculated as follow:

$$m_i \frac{\mathrm{d}^2\mathbf{r}_i}{\mathrm{d}t^2} = G \sum_{\substack{j=1 \\ j\neq i}}^{N} \frac{m_i\, m_j}{r_{ij}^3} \mathbf{r}_{ij} \qquad (i = 1, 2, ..N). \tag{5.8}$$

In particular we have the expression of the accelerations due to all the N particles on the i-th:

$$\ddot{\mathbf{r}}_i = G \sum_{\substack{j=1 \\ j\neq i}}^{N} \frac{m_j}{r_{ij}^3} \mathbf{r}_{ij} \qquad (i = 1, 2, ...N) \tag{5.9}$$

and the acceleration due to all the $N-1$ particles on the N-th:

$$\ddot{\mathbf{r}}_N = G \sum_{j=1}^{N-1} \frac{m_j}{r_{Nj}^3}. \tag{5.10}$$

Then we can write the acceleration of the i-th particles in the reference system centered on N-th the body as:

$$\ddot{\mathbf{r}}'_i = G \sum_{\substack{j=1 \\ j\neq i}}^{N} \frac{m_j}{r_{ij}^3} \mathbf{r}_{ij} - G \sum_{j=1}^{N-1} \frac{m_j}{r_{Nj}^3} \mathbf{r}_{Nj} \qquad (i = 1, 2, ...N). \tag{5.11}$$

If we isolate the term relative to the mass of the N-th particle from the first summation

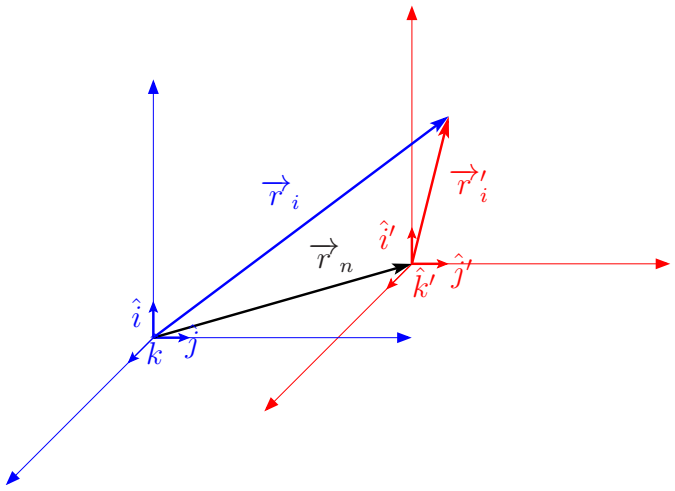

FIGURE 5.4: The transfer of the origin for the reference system to the N-th particle.

and the term that included the mass of the i-th particles from the second one, we have:

$$\begin{aligned}\ddot{\mathbf{r}}_i' =& G\frac{m_N}{r_{iN}^3}\mathbf{r}_{iN} + G\sum_{\substack{j=1\\ j\neq i}}^{N-1}\frac{m_j}{r_{ij}^3}\mathbf{r}_{ij} - G\frac{m_i}{r_{Ni}^3}\mathbf{r}_{Ni} - G\sum_{\substack{j=1\\ j\neq i}}^{N-1}\frac{m_j}{r_{Nj}^3}\mathbf{r}_{Nj} \\ =& -G(m_N+m_i)\frac{\mathbf{r}_{Ni}}{r_{Ni}^3} + G\sum_{\substack{j=1\\ j\neq i}}^{N-1} m_j\left(\frac{\mathbf{r}_{ij}}{r_{ij}^3} - \frac{\mathbf{r}_{Nj}}{r_{Nj}^3}\right) \qquad (i\neq N),\end{aligned} \tag{5.12}$$

pointing out that:

$$\mathbf{r}_{Ni} = \mathbf{r}_i - \mathbf{r}_N = \mathbf{r}_i', \tag{5.13}$$

$$\mathbf{r}_{ij} = \mathbf{r}_j - \mathbf{r}_i = \mathbf{r}_j' - \mathbf{r}_i', \tag{5.14}$$

we can obtain the ***relative form for the equations of motion***:

$$\ddot{\mathbf{r}}_i + G(m_N+m_i)\frac{\mathbf{r}_i}{r_i^3} = \underbrace{G\sum_{\substack{j=1\\ j\neq i}}^{N-1} m_j\left(\frac{\mathbf{r}_j-\mathbf{r}_i}{r_{ij}^3} - \frac{\mathbf{r}_j}{r_j^3}\right)}_{PERTURBATIVE\ COMPONENT}, \qquad (i\neq N) \tag{5.15}$$

where we have deleted the superscripts, considering that the vectors involved inside the last expression are all referred to the central body P_N, placed on the origin of the reference system.

We can underline that if the body number of the system is equal to $N = 2$, the term on the right side in the previous expression becomes identically null and the equation is reduced to the relative two-body motion equation, moving under the mutual gravitational forces. It means that the motion of each particle is regulated by the equation of motion of the two-body system, composed by the primary and the particle itself, under the perturbation force term due to the presence of the other particle.

If the primary body has the dominant mass in the system [3], then the member on the right side in Eq. 5.15 presents small terms with respect to the left one. If conversely, the central body does not correspond with the most massive one or with the main gravitational contribution, the treatise is still working, since it is not grounded on approximations due to the smallness of the perturbed component.

Inside the perturbation terms we can identify two different types of accelerations. The first, inversely proportional to the square distance between each couple of particles, is the *direct acceleration*. The second one, inversely proportional to the square distance of each particle to the origin on which the primary body lies, is the *indirect acceleration*. The last one represents the central body acceleration due to all the system particles and it is an expression of the fictitius forces associated to the non inertial reference system assumed.

The perturbed forces could be also deduced from the ***perturbative function*** $\mathcal{R}_i$, defined as

$$\mathcal{R}_i = \sum_{\substack{j=1 \\ j\neq i}}^{N-1} \mathcal{R}_{ij} = G \sum_{\substack{j=1 \\ j\neq i}}^{N-1} m_j \left(\frac{1}{r_{ij}} - \frac{\mathbf{r}_i \bullet \mathbf{r}_j}{r_j^3} \right), \tag{5.16}$$

and the equations of motion could be written:

$$\ddot{\mathbf{r}}_i + G(m_N + m_i)\frac{\mathbf{r}_i}{r_i^3} = \frac{\partial \mathcal{R}_i}{\partial \mathbf{r}_i} \qquad (i = 1, 2, ...N-1). \tag{5.17}$$

It is useful to underline that the system Eq. (5.17) contains $N-1$ different perturbative functions. Indeed, this function acquires different expressions varing the particle of the system for which the correspond equation of motion is written.

We considered the previous formalism to describe the cometary motion around the Sun, perturbed by the tidal field of the Galaxy. If the origin is taken coinciding with Sun position and introducing a general formulation for the potential of the Galactic components, we have:

$$\begin{cases} \ddot{\mathbf{r}}_C + G(m_S + m_C)\dfrac{\mathbf{r}_C}{r_C^3} = \nabla\Phi_G(\mathbf{r}_{CG}) - \nabla\Phi_G(\mathbf{r}_G) \\ \\ \ddot{\mathbf{r}}_G + Gm_S\dfrac{\mathbf{r}_G}{r_G^3} + \nabla\Phi_G(\mathbf{r}_G) = \nabla\Phi_G(\mathbf{r}_{GC}) - Gm_C\dfrac{\mathbf{r}_C}{r_C^3} \end{cases} \tag{5.18}$$

where the subscripts C, G and S are referred to the cometary, Galactic and solar quantity respectively.

To describe the cometary orbit we integrate the system of equations (Eq. 5.18): the first equation is about the heliocentric cometary motion around the Sun perturbed by the presence of the Galaxy, and the second one expressed the motion of the Galactic

[3] When this condition is verified, the condition $m_N >> \sum_{i=1}^{n-1} m_i$ is satisfied.

components around the Sun perturbed by the comets (absolutely negligible). The last one is the reflection of the solar motion, in other words, fixing the new origin of the reference frame at the Sun, we see the Galaxy moving around the solar position with the same path of the Sun but in the opposite direction.
The next calculations for the comet orbits will use the galactic potential that involve all the components already included in the study for the solar motion: the bulge, the disk, the dark halo and the 3D spiral arms (see § 2). Explicitly:

$$\Phi_G(R,\theta,z,t) = \Phi_{BG}(R,z) + \Phi_D(R,z) + \Phi_{DH}(R,z) + \Phi_s(R,\phi,z,t) \tag{5.19}$$

The integration of the cometary paths in the total potential $\Phi_G(R,\theta,z,t)$, with the non-approximated formulation of the equations of motion, is particularly challenging from a computational point of view, as we will see in the next paragraph.

5.3.1.1 Numerical problems

The tidal perturbation is contained in the difference between the gradient of the galactic potential at the comet place and the Sun position: $\nabla\Phi_G(\mathbf{r}_{CG}) - \nabla\Phi_G(\mathbf{r}_G)$. These two quantities are very close, entailing a loss of numerical accuracy during the integration of the cometary orbits. In order to remedy this loss of accuracy, that results particularly significant for cometary distance $r_C < 10^2$ AU (see blue line in Fig. 5.5), we have introduced a Taylor series expansion (TSE) of the gradient difference around zero. This substitution allow us to conserve enough digits (red line in Fig. 5.5) and improve the accuracy for the results obtained from the integration of the equations of motion.

r_C (AU)	Digits $(\nabla\Phi_{comet} - \nabla\Phi_{sun})$	Digits TS	Error (Exact vs TSE) 1st	2nd	3rd
10^0	4.63	13.25	10^{-12}	10^{-20}	10^{-29}
10^1	5.63	13.25	10^{-10}	10^{-17}	10^{-25}
10^2	6.63	13.25	10^{-8}	10^{-14}	10^{-21}
10^3	7.63	13.25	10^{-6}	10^{-11}	10^{-17}
10^4	8.63	13.25	10^{-4}	10^{-8}	10^{-13}
10^5	9.63	13.25	10^{-2}	10^{-5}	10^{-9}

TABLE 5.1: Evaluation for the numerical errors. Comparison between the number of digits provide by the exact tidal term and the TSE expression (columns 2 and 3). In columns 4, 5 and 6 are reported the errors due to the introduction of the approximation of the TSE itself, with respect the cometary position and the series order considered.

The use of a TSE to express the tidal perturbation, if from one side avoids the reduction

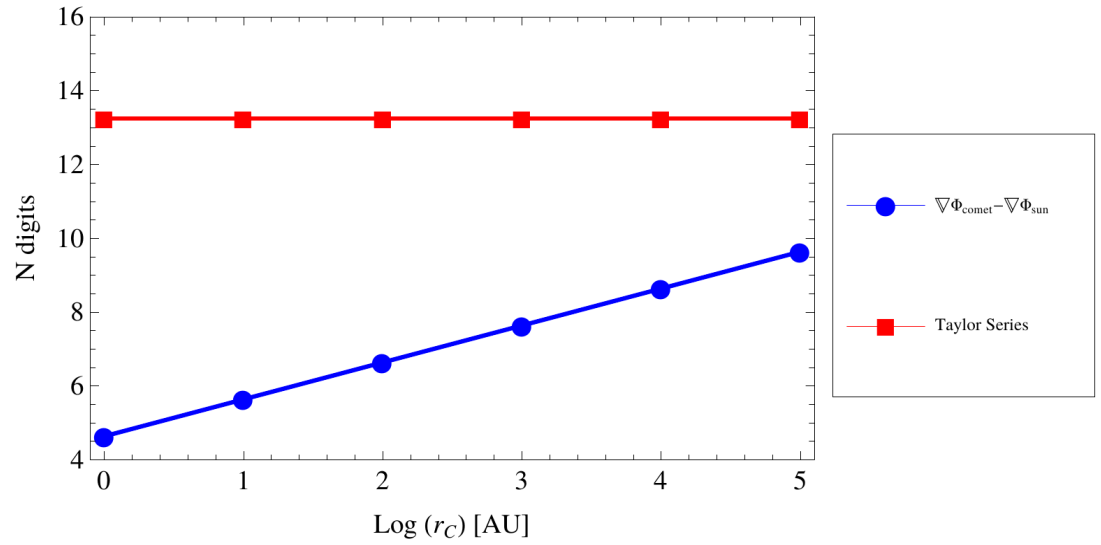

FIGURE 5.5: Loss of digits during the integration of the equations of motion. Comparison between the accuracy for the full expression and the Taylor series expansion

of digits, at the same time introduces an approximation in the tidal term itself. It is crucial to verify if the error due to the TSE approximation may be worse than that introduced by the loss of significant numerals. In other words we have to check the balance between accuracy and precision inside the integration process. As it is well known, higher is the order of the series, bigger is the agreement between TSE and the exact expression.

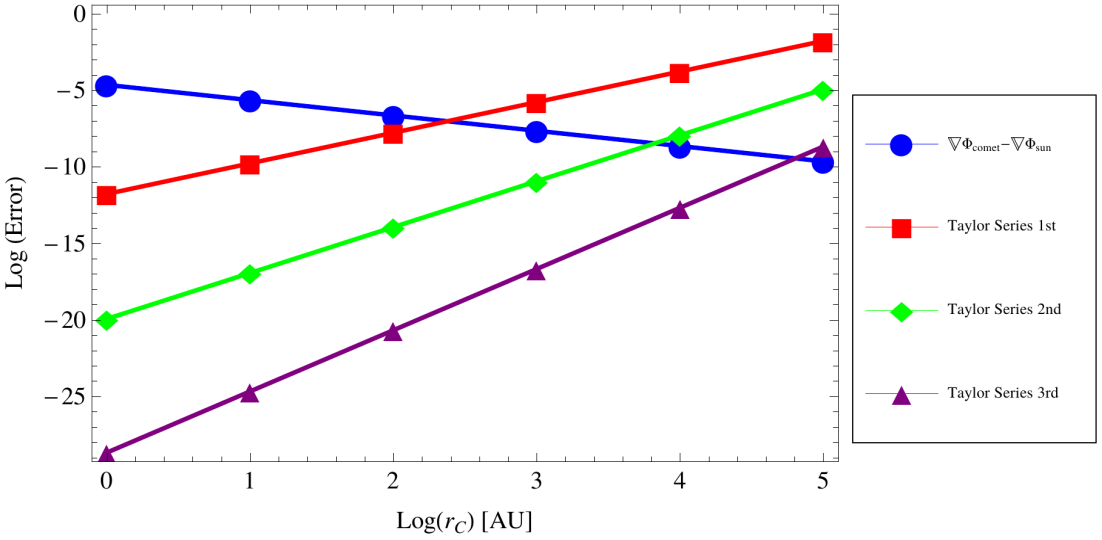

FIGURE 5.6: Comparison between errors in the integration process due to the loss of digits and the approximation introduced by the TSE for different series order (1st, 2dn and 3rd order).

In Fig. 5.6, we can see the comparison between the errors introduced by the loss of

digits and the TSE approximation (1st, 2dn and 3rd order). The TSE is more precise than the exact tidal terms for cometary distance $r_c < 10^3$ AU, no matter which order are considered. The situation gets worst increasing r_c: for distance of order 10^4 AU the first order TSE fails to give a enough precise description of the orbit, while for $r_c \sim 10^5$ AU only the 3rd order of the TSE could be used in order to obtain a consistent description. The semi-major axis of a typical object belongs to the Oort cloud is inside the range $10^3 - 10^5$ AU, but during its life, especially under the action of a perturbation, the comet may be achieved distance that can also differ in orders of magnitude. In addition, we have to take into account that the aphelion position, where comet meets the greatest distance with respect to the Sun, is the most sensitive to the Galactic tidal action, since in corresponding of the aphelion, the comet undergoes the gravitational "kick" due to the tide. From the previous considerations arise the need to adopt the better description in order to provide an accurate and precise calculation for the orbit on a wide range of distance. The 3rd order of the TSE is the most reasonable choice to combine computational efficiency and an accurate description. All the values of the numerical analysis are listed in Tab. 5.1.

5.3.2 Initial conditions for Sun and comets

5.3.2.1 The solar path

The main goal of this work is to understand the influence that a possible solar migration, induced by a non-axisymmetric structure like the spiral, may have on the Oort cloud dynamics. We have also seen in the previous paragraphs, that the introduction of a component that breaks the cylindrical symmetric is no longer compatible with a treatment that simplifies the equations of motions, like the Hill's approximation. We need to make a comparison between the behavior of a comet around a Sun with a position nearly fixed in the Galactic disk (the type of orbit that we obtain with an integration in the axisymmetric potential), and a comet that follows a Sun dragged in the disk by the action of the spiral arms perturbation. In addition we want to be sure that the difference that may be observed is not due to the features that deviate from the circular motion integrating the solar path in axisymmetric potential (i.e. the motion along the vertical direction of about 100 pc and along the radial direction of about 1 kpc), but really by the action of the spiral arms. In this framework, the choice to deserve the circular approximation for the solar orbit, appears obliged both for the integration with and without the spiral arms perturbation.

From the results of the study about the Sun, we select one solar path with an inner position with respect to the Galactic center ($R_{\odot i}$=6.2 kpc), that achieved the current

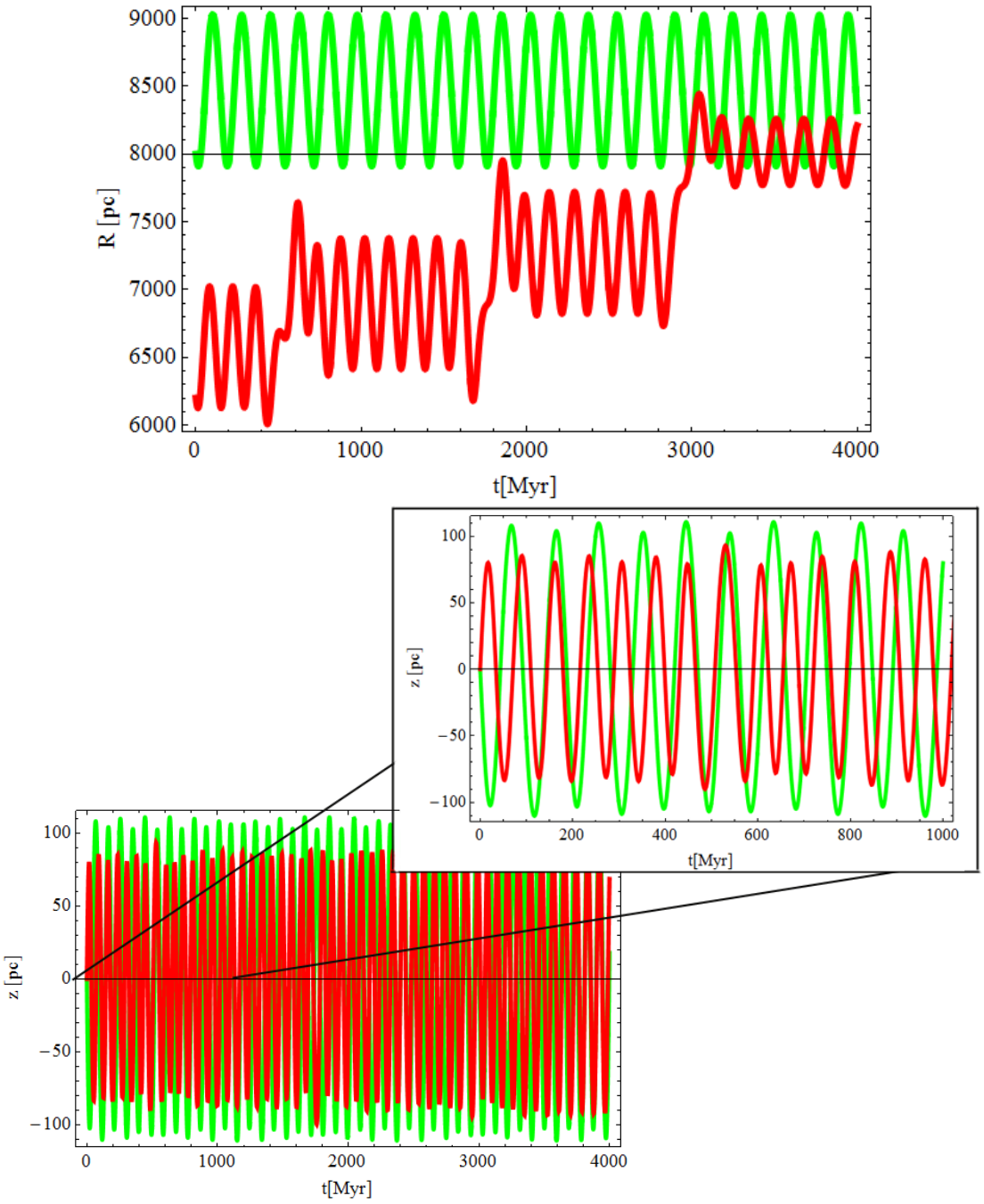

FIGURE 5.7: Comparison between the solar path with and without the spiral arm perturbation. The radial (top panel) and vertical (bottom panel) motion are shown: the green line is the usual motion of the Sun integrated in axisymmetric potential, while the red trend is the results of the perturbation provide by three transient spiral arms.

solar position with the current velocities, after 3 encounters with the spiral arms, for a total integration time T_{int} =4 Gyr. In Fig. 5.7 are shown the two different solar path used for the integration of the cometary orbits. The green line is the usual motion of the Sun calculated in an axisymmetric potential, while the red trend is the results of the integration in a Galactic potential perturbed by three consecutive transient spiral

arms (top panel), action of which is particularly evident in the radial direction. The perturbation of the solar path on the vertical direction is less important, as we expected by a structure strongly flatten as the spiral (bottom panel).

5.3.2.2 The 3D cometary samples

In order to investigate the effects of the loss of symmetry in the Galactic potential and the consequences of a not fixed solar position on the cometary behavior, we use different sample of comets, each of them composed by 30 objects. The choice to limit ourselves at a small number of body in this first survey, was imposed by the need to test different combination of cometary features and, of course, by the integration time requested for such type of calculations, especially those under the perturbation of the spiral arms. A sample of 10^4 - 10^5 comets will be provide a more realist sample for the Oort cloud, but our first aim is to probe if the spiral perturbation is relevant for the comet dynamics, as it seems to be for the solar one, and identify the way in which the perturbation acts on the cometary objects. The specific properties of each sample will be listed in detail in §5.4. Here we simply indicate the outlines about how building up the sample.
Following Fouchard et al. (2011), we obtain a random sample with a non flat distribution for all the initial orbital elements Fig. 5.8, in particular:

- the semi-major axis a is chosen between $3 \times 10^3 < a < 1 \times 10^5$ AU, with a density probability $\propto a_0^{-1.5}$;
- the eccentricity e follows a density probability $\propto e_0$ with the constraint $q_0 > 32$ AU, the limit below that comets may be undergone to the planetary effects, changing in a completely different way their motion, going out of our present aims;
- the argument of perihelion ω_0, the longitude of ascending node Ω_0, mean anomaly M_0 and the cosine of inclination $\cos i_0$ are chosen completely randomly with a flat density distribution in agreement with the spherical symmetry of the Oort Cloud.

Using the previous criteria we obtained samples completely random, or with only one elements that varies spreading on the initial conditions of the comets.

5.3.3 Results for the cometary integration in a 3D non-axisymmetric potential

We performed 5 simulations, using different cometary samples with initial conditions chosen as explained in the previous paragraph. Since we were mainly interested into the

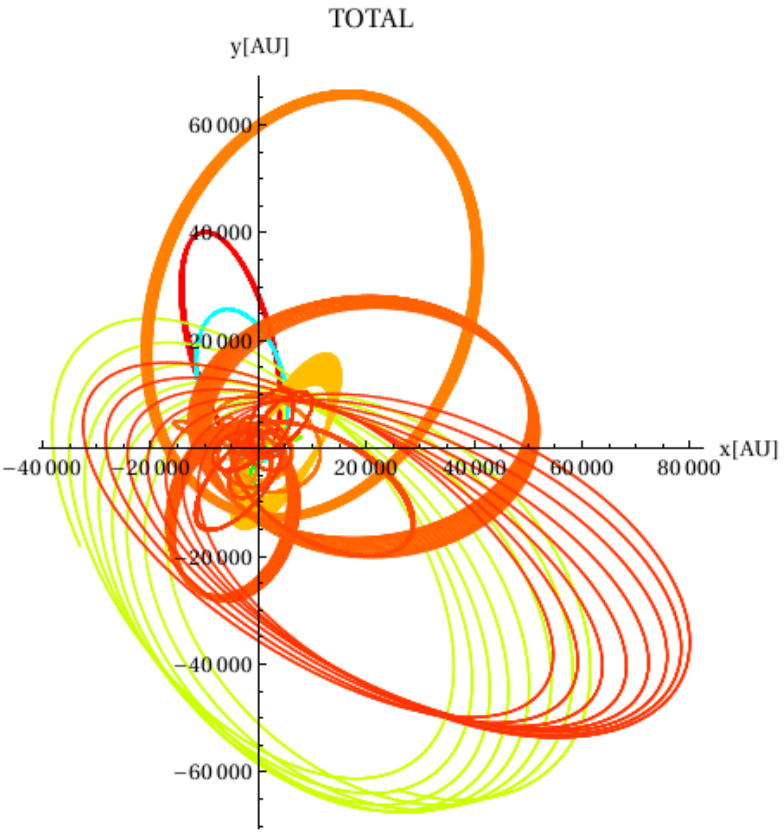

FIGURE 5.8: An example for a cometary random sample, built using a non flat distribution of the semi-major axis a and the eccentricity e, following Fouchard et al. (2011).

galactic field, our model do not include the stellar passages and the planetary action on the comets. We integrated the cometary path on a total time of 4 Gyr, making the assumption to have a well defined Oort cloud 500 Myr after the birth of the Sun.

5.3.3.1 Samples with only inclination varied

We started our investigation with several cases in which are fixed all the orbital elements but the inclination i. In these way it will possible to isolate the effect due to the variation of this parameter alone, that is particularly relevant in the understanding of the balance between the planar and the orthogonal components of the Galactic tide along the cometary path. For each sample was computed the number of objects that achieve the most internal planetary region, in order to underline also an effect of the spiral structure on the cometary injection rate, with some consequence also for habitability in the Galaxy. We fixed the threshold to the entry in the inner part of our planetary system equals to 32 AU, assuming the same criteria used building the initial conditions of the samples.

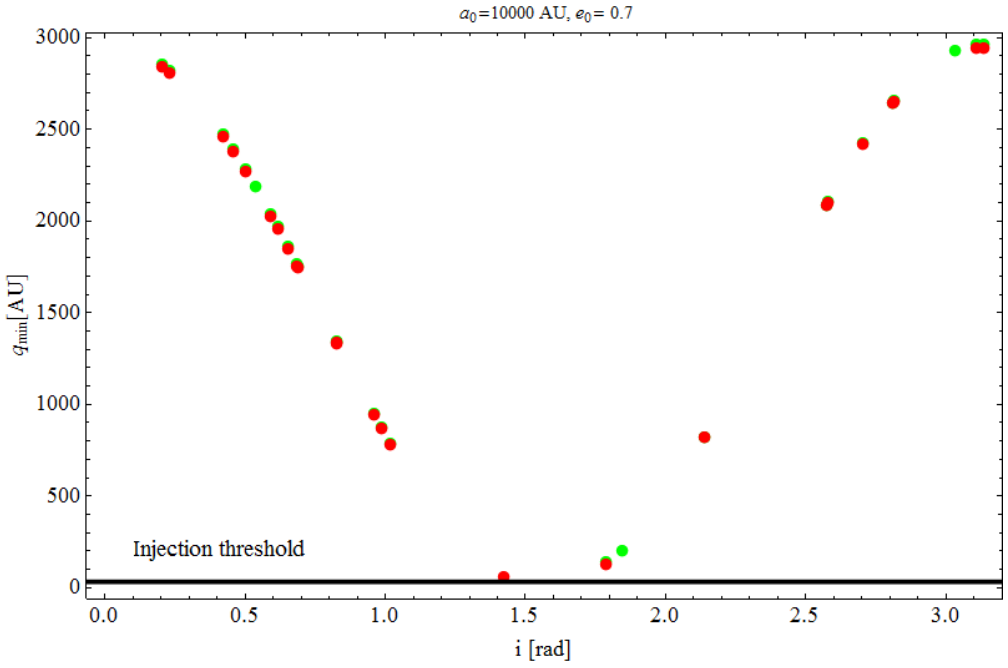

FIGURE 5.9: Minimum perihelion distance q_{min} vs inclination i for a cometary sample with fixed $a_0 = 10^4$ AU, $e_0 = 0.7$, $\omega_0 = 0.147$ rad, $\Omega_0 = 0.592$ rad, $M_0 = 3.846$ rad and i_0 randomly chosen. The red points are relative to comets integrated in a Galactic environment with a spiral arms structure, while the green points are referred to the motion of the same comets in axisymmetric potential. The black solid line highlights the threshold for the cometary injection in the inner part of Solar System. The values of q_{min} do not evidence relevant differences between the two Galactic environment considered

- **SAMPLE 1**

  The first sample considered has fixed semi-major axis $a = 10^4$ AU and fixed eccentricity $e = 0.7$. In Tab. 5.3 are listed the minimum perihelion values q_{min} and the maximum aphelion values Q_{max} that each comet achieved during the whole integration time, with an without the perturbation effect due the spiral arms. The comets that are indicated as "Null", are those objects that do not belong to the system at the end of the integration time due to the tidal action. In Fig. 5.9 are shown the cometary q_{min} vs the initial inclination i_0, the red points are relative to comets integrated in a Galactic environment with a spiral arms structure, while the green points are referred to the motion of the same comets in axisymmetric potential. The comets that undergone the stronger reduction of the perihelion distance present inclination close to $\pi/2$, where the orthogonal components of the tides are strongest. The comets of this samples appear enough bounded to the Sun, and not sufficiently sensitive to the tidal effects of the Galaxy, to highlight some difference in the comet behavior due to the addition of the spiral structure. Indeed

the minimum position with respect to the Sun shows a substantial agreement between the two approaches (with and without the spiral arms).

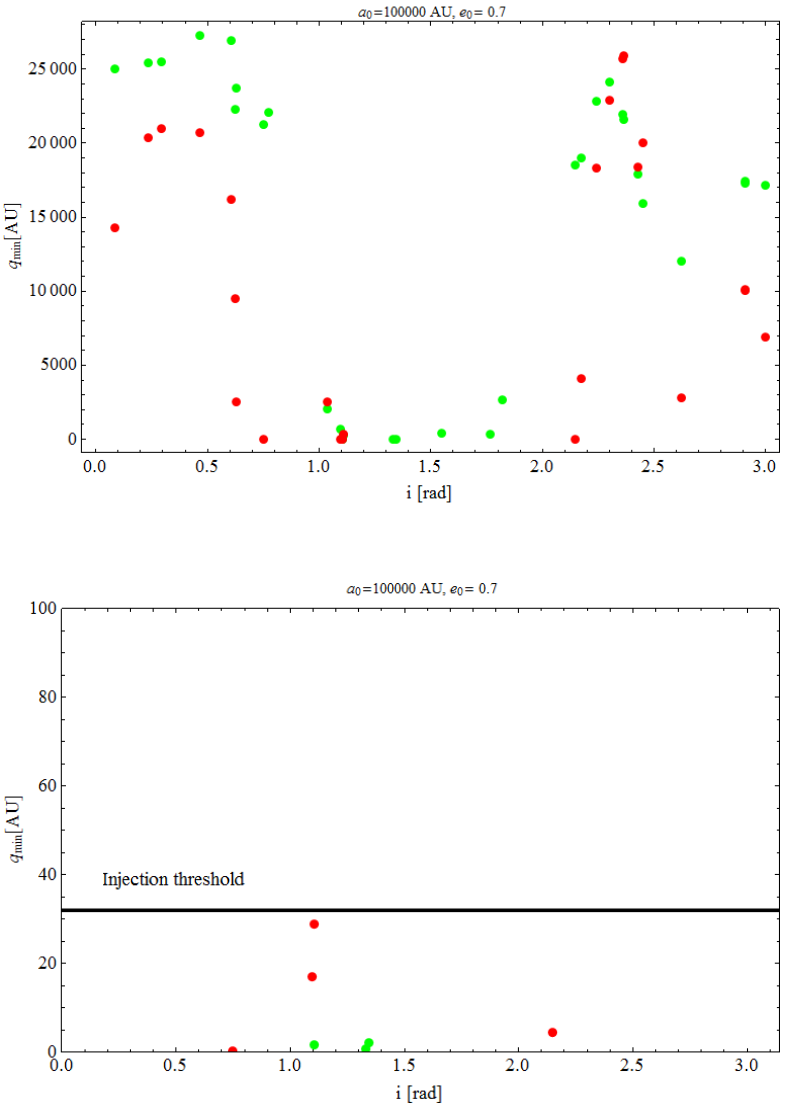

FIGURE 5.10: Minimum perihelion distance q_{min} vs inclination i for a cometary sample with fixed $a_0 = 10^5$ AU, $e_0 = 0.7$, $\omega_0 = -1.615$ rad,$\Omega_0 = 4.476$ rad, $M_0 = -2.011$ rad and i_0 randomly chosen. The red points are relative to comets integrated in a Galactic environment with a spiral arms structure, while the green points are referred to the motion of the same comets in axisymmetric potential. Some differences in q_{min} start to arise due to the spiral arms perturbation, in particular for orbits with small inclinations with respect to the Galactic plane. The bottom panel shows the details about the injection threshold for the comets in correspondence to $q = 32AU$.

- **SAMPLE 2**

  In the second sample we maintained the same choice for the eccentricity $e = 0.7$ and increases the semi-major axis $a = 10^5$ AU. We kept fixed these orbital elements on the sample, as Ω_0, ω_0 and M_0, varying the inclination as in the previous example

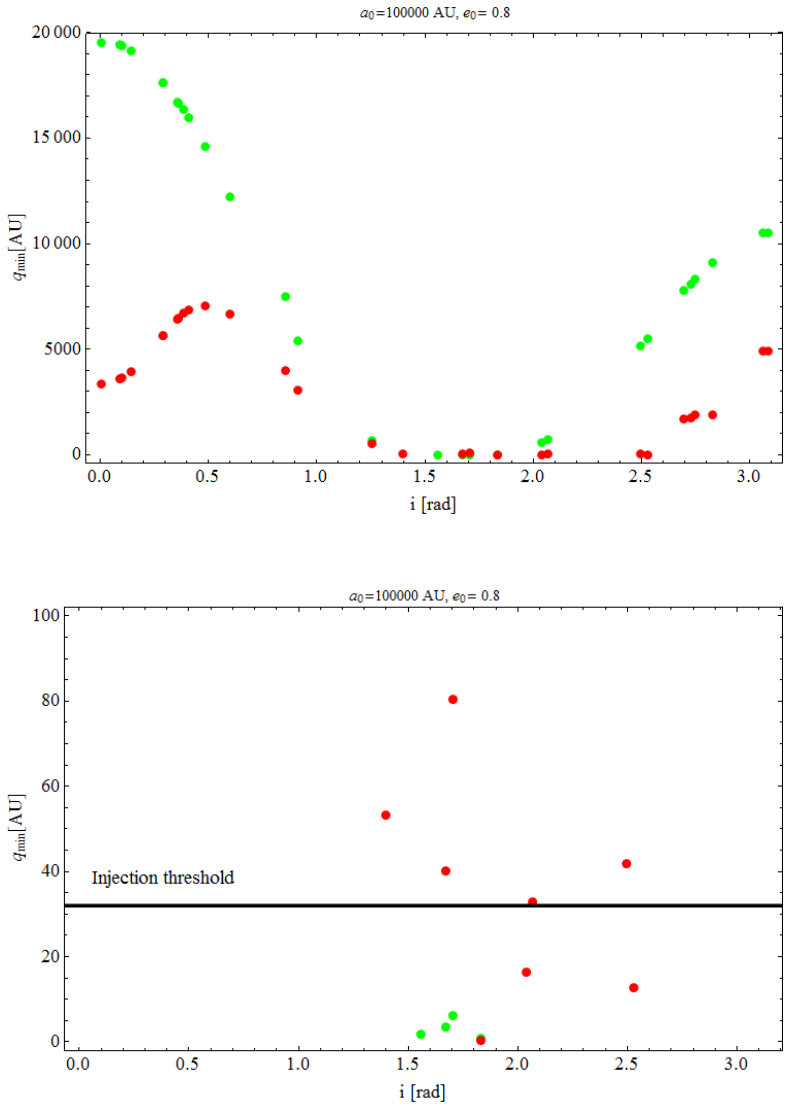

FIGURE 5.11: Minimum perihelion distance q_{min} vs inclination i for a cometary sample with fixed $a_0 = 10^5$ AU, $e_0 = 0.7$, $\omega_0 = -2.909$ rad,$\Omega_0 = 5.882$ rad, $M_0 = 0.873$ rad and i_0 randomly chosen. The red points are relative to comets integrated in a Galactic environment with a spiral arms structure, while the green points are referred to the motion of the same comets in axisymmetric potential. The gap in q_{min} increases: for cometary orbits with small inclinations the q_{min} obtained under the spiral arms perturbation are significantly smaller with respect to the values achieved without. Despite that the injection rates are substantially in agreement with the unperturbed case (bottom panel and Tab. 5.2)

(details and results for each comets listed in Tab. 5.4). The graph in Fig. 5.10 about the q_{min} vs the random inclination begins to manifest a gap between the perihelion position due to the spiral action, in particular the perturbation seems to reduce q for comets with a small inclination with respect the galactic plane.

- **SAMPLE 3**

  We widened in eccentricity the investigation around the maximum value of $a = 10^5$

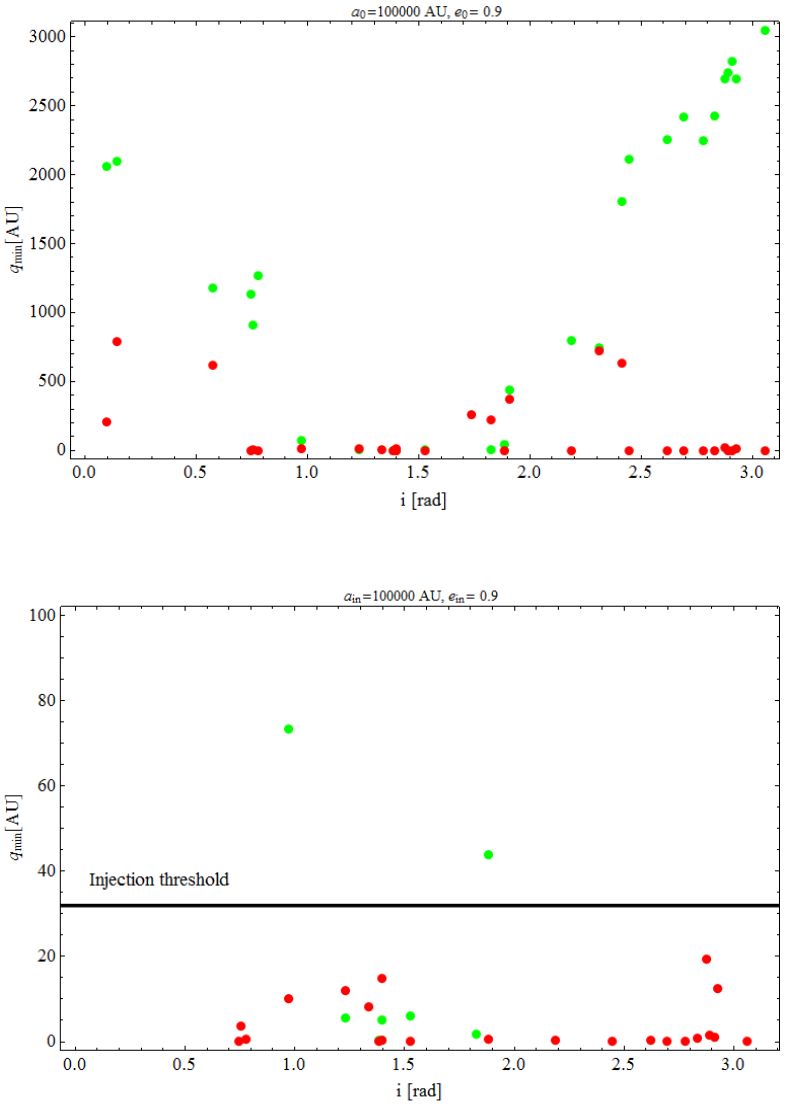

FIGURE 5.12: Minimum perihelion distance q_{min} vs inclination i for a cometary sample with fixed $a_0 = 10^5$ AU, $e_0 = 0.9$, $\omega_0 = 0.633$ rad, $\Omega_0 = 4.162$ rad, $M_0 = 0.744$ rad and i randomly chosen. The red points are relative to comets integrated in a Galactic environment with a spiral arms structure, while the green points are referred to the motion of the same comets in axisymmetric potential. The effects of the spiral becomes more evident, determining many injections in the inner part of the solar system, that will has not verified without the presence of the spiral (bottom panel and Tab. 5.2).

AU, that seems to be enough sensitive to the field of the Galactic tide to display the effects of the introduction of the spiral arms perturbation. In order to look to a more extreme cometary orbits we increase the eccentricity to the values of $e = 0.8$ (see Tab. 5.5). These most eccentric orbits emphasize the discrepancy between the Galactic perturbation with and without the break of the potential cylindrical symmetry. For small inclinations the q_{min} obtained under the spiral arms perturbation are significantly smaller than those without (see Fig. 5.11). The agreement

between the two set of results was recovered for the cometary orbits with high inclinations, where the orthogonal component of the tide is completely dominant in the injection process, as is possible to infer from the absolutely compatible injection rate obtained in the two different cases (see Tab. 5.2).

- **SAMPLE 4**
  The most extreme case is a sample with the maximum value for the semi-major axis $a = 10^5$ AU and the high eccentricity $e = 0.9$ (all details of the sample reported in Tab. 5.6). In Fig. 5.12 it is possible to see the stronger action of the spiral arm perturbation, that for comet orbits close to the plane, produces an accentuate reduction of the perihelion distance, determining several injections in the inner part of the planetary system, that will has not verified without the presence of the spiral structure.

The results obtained for the different samples considered highlight a growing influence of the spiral arms on cometary objects with wide and elongate orbits, and with a moderate inclination with respect the Galactic plane. In Tab. 5.2 has been summarized the injection efficiency for each sample, with an without the present of the spiral perturbation. The spiral structure perturbs in significant way every samples with $a = 10^5$ AU, but it is only for an extreme eccentricity $e = 0.9$ that becomes crucial for the injection rate, leading to the inner part of the planetary system the 73% of the objects, while the axisymmetric potential injects only the 20% of the sample in the regions close to the Sun. It is important to stress that in a real cometary cloud (i.e. with a non flat distribution in a and e) this huge rate may be not so exaggerated, since the numbers of cometary objects with a so wide and elongate orbits are non the major part of the cloud (as we will see in §5.3.3.2) . Despite that the perturbation due to the tide, in presence of the spiral perturbation, on the outer shell of the Oort cloud is not negligible. In particular, the spiral perturbation seems to bolster the action of the planar component of the tide, indeed this action becomes evident for small inclination, where the influence of the orthogonal component decreases. It easy to understand that this results is in agreement with the flatten geometry and the mass distribution of a structure like the spiral arms, that is concentrated on the plane, and exercises a small influence along the vertical direction. In other words, the planar component of the Galactic tide, may be not longer negligible in presence of a components that breaks the cylindrical symmetry of the potential.

Looking to the graphs (Figs. 5.9, 5.10, 5.11, 5.12) it is possible to notice that the symmetry with respect to the inclination central values $\pi/2$, decreases as the growing of the semi-major axis. This behavior may be explained as a consequence of the position

DIFFERENCE IN INJECTION RATE FOR EACH SAMPLE								
							Injection Rate (%)	
	a_0 (AU)	e_0	i_0 (rad)	Ω_0 (rad)	ω_0 (rad)	M_0 (rad)	With SP	Without SP
1	10^4	0.7	RC	0.592	0.147	3.846	0	0
2	10^5	0.7	RC	4.476	-1.615	-2.011	13.3	10
3	10^5	0.8	RC	5.882	-2.909	0.873	10	13.3
4	10^5	0.9	RC	4.162	0.633	0.744	73.3	20
R	RC	RC	RC	RC	RC	RC	6.7	6.7

TABLE 5.2: Difference in injection rate for each cometary sample. The orbital elements that are chosen randomly are indicate as RC.

of the Sun during its oscillation through the galactic plane during the integration of the cometary orbit. The solar oscillation period along the vertical direction is about $P_{z\odot} = 90$ Myr. The orbital period of a comets around the Sun (in a keplerian motion), may be calculated by the simple relation:

$$T = 2\pi\sqrt{\frac{a^3}{\mu}}, \tag{5.20}$$

where $\mu = GM_\odot$ as usual.

A comet with a semi-major axis of about 10^4 AU results to have an orbital period P_c equals to about 1 Myr, while an object with $a = 10^5$ AU completes its orbit in a period of 31 Myr. The tidal field is symmetric with respect to the i, that means that will have to register a completely symmetric trend around the maximum inclination $i = \pi/2$, if the Sun is in the same conditions during the integration of the comet motions. For comets with $a = 10^4$ AU, the cometary period is small compare to $P_{z\odot}$, makes the orbits not sensitive to the vertical motion of the Sun. Indeed, as it is possible to see in Fig. 5.13, where the black points represent the position of the Sun when the comets of the sample with $a = 10^4$ AU achieve the minimum perihelion distance. The minimum perihelion distance are registered in correspondence of symmetric solar distance from the galactic plane. In the same way we can explain the lack of a perfect symmetry for comet orbits with a wider a. The comet with $a = 10^5$ AU has a period of about a third of $P_{z\odot}$, that becomes compatible with the period of the solar oscillation along the vertical direction. In this way the Sun may be found in different distance along the z-axis during the integration of the cometary motions. This effects is clearly shown in Fig. 5.14, about the integration of the sample with $a = 10^5$ AU and maximum eccentricity $e = 0.9$. The q_{min} for each comets of the sample are in correspondence to very different solar distances from the Galactic plane. This analysis allow us to obtain some clues about the influence

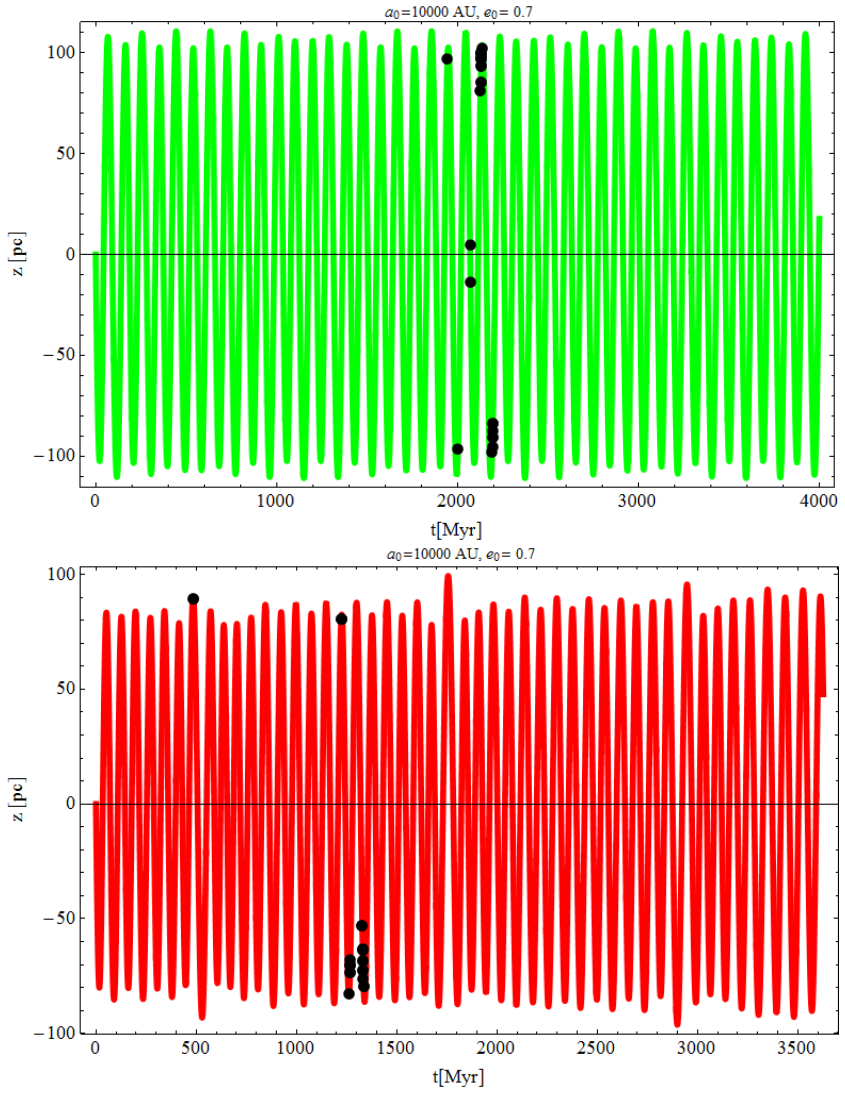

FIGURE 5.13: Solar position along the vertical motion during the integration of the cometary sample with $a_0 = 10^4$ AU in a potential without (green trend, top panel) and with the spiral arm perturbation (red trend, bottom panel). The black points represent the position of the Sun when the comets of the sample achieve the minimum perihelion distance q_{min}. The minimum perihelion values are registered in correspondence of symmetric solar distances from the galactic plane.

of the vertical motion of the Sun on the comets dynamics. The relative position of our star with respect the plane of the Milky Way, seems to have a specific weight on the comet dynamics, as some recent works already claimed, see Gardner et al. (2011). This may be another argument against the assumption of a circular approximation for the solar orbit in studied about the Oort cloud evolution.

The last issue about this first set of results, is to understand in which way the radial migration could influence the extreme large injection rate registered for the most elongate and eccentric cometary sample. The point is to clarify if the peak for the cometary injections occurs at some particular distance from the center of the Galaxy, entailing possible consequences for the GHZ's edges, or if the cometary entries are spread over

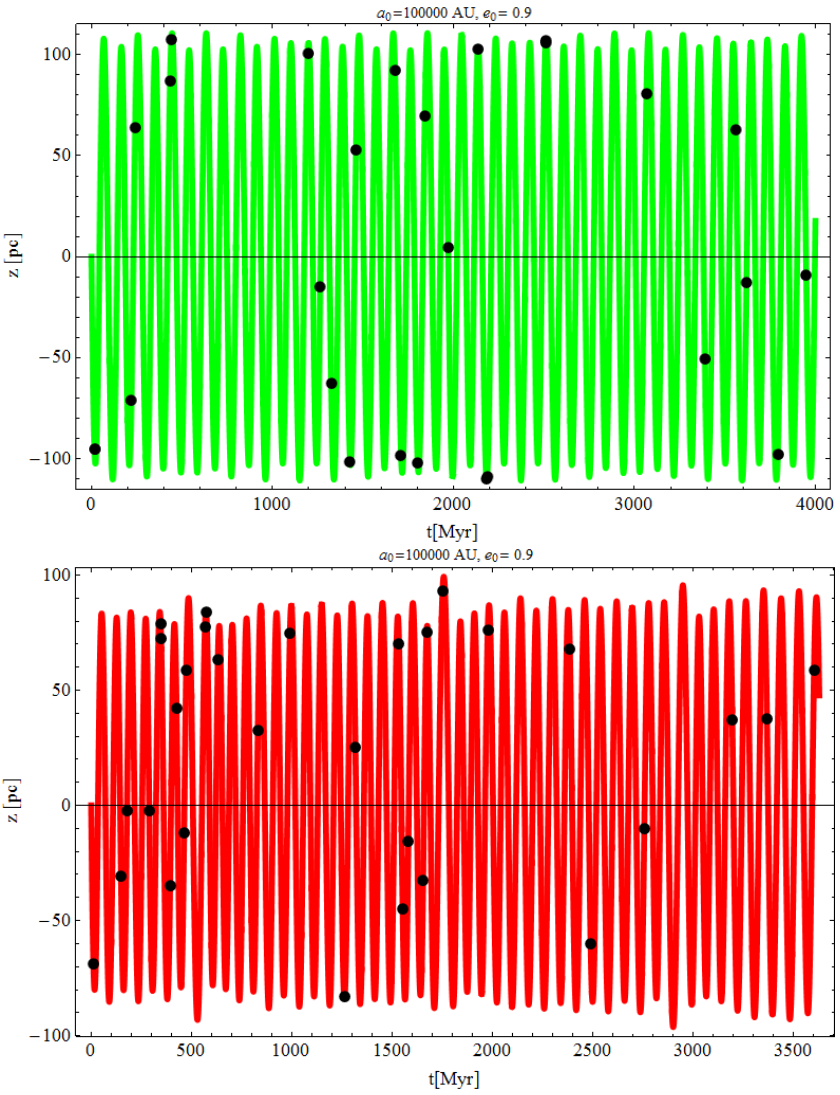

FIGURE 5.14: Solar position along the vertical motion during the integration of the cometary sample with $a_0 = 10^5$ AU in a potential without (green trend, top panel) and with the spiral arm perturbation (red trend, bottom panel). The black points represent the position of the Sun when the comets of the sample achieve the minimum perihelion distance q_{min}. The q_{min} for each comets of the sample are reached in correspondence to very different solar distances from the Galactic plane, as consequence of an orbital cometary period comparable with $P_{z\odot}$.

the whole the solar path, from the initial inner position of 6 kpc to the final one, in agreement with the current Sun collation of 8 kpc from the Galactic center. In Fig. 5.15, we marked with black points the position of the Sun along its migration motion at the moments in which the comets are injected in the inner part of the planetary system (i. e. the comets have $q \leq 32$ AU), for the sample that produces the greatest injection rate under the spiral perturbation ($a_0 = 10^5$ AU and $e_0 = 0.9$). It is possible to see that the major part of the comets are pulled inside the inner planetary region in the firsts 2 Gyr, for solar position between (6 and 7 kpc), while no comets has been sufficiently perturbed to entry in the Solar System during the last 1 Gyr of integration,

when the migrated Sun reaches a position in agreement with the current one. The evidence of a region in the Galactic disk with a so high injection rate, even if for the outer part of our cometary cloud, may involve a redefinition of the habitability edges in the Galaxy. In particular region not precluded to the formation of a planetary system, i. e. that satisfied the requirements of metallicity and presence of a suitable host star, may compromise the development of the life with a high cometary impact risk.

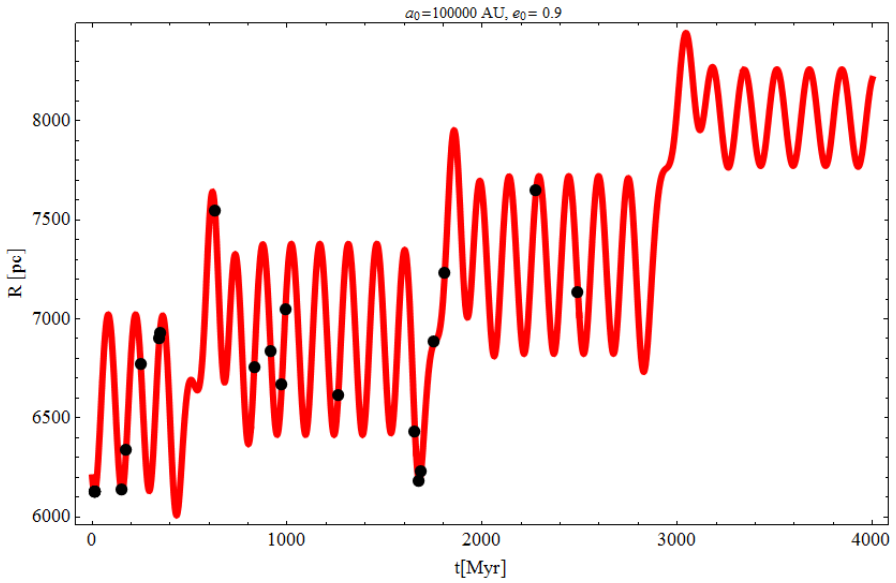

FIGURE 5.15: Solar position along the vertical motion during the integration of the cometary sample with $a_0 = 10^5$ AU and $e = 0.9$, in a potential perturbed by the spiral arms. The black points represent the position of the Sun when the comets of the sample reach the perihelion threshold of 32 AU, to enter in inner region of the planetary system. The injections are concentrated in solar position encompassed between 6 an 7 kpc.

5.3.3.2 Random Sample

The results provided by the cometary samples of the previous paragraph showed a significant perturbation of the outer shell of the Oort cloud, i.e. for those comets with the most elongate orbits. For this kind of comets the perihelion distance seems to be strongly affected by the present of the spiral arms, producing an extreme elevate rate of injection for the sample with the extreme conditions ($a_0 = 10^5$ AU, $e = 0.9$). In order to generalize the conclusions about the role played by the spiral arms in the cometary dynamics, we considered a small completely random sample of 30 objects (the details for the comets in the sample are listed in Tab. 5.7), and repeated the same study done for the previous samples.

Unfortunately the very small number of comets considered and the non flat distribution in the semi-major axis assumed for the Oort cloud, produced a sample imbalanced to tiny a, provided only two comets with an orbit enough large to highlight the presence of the

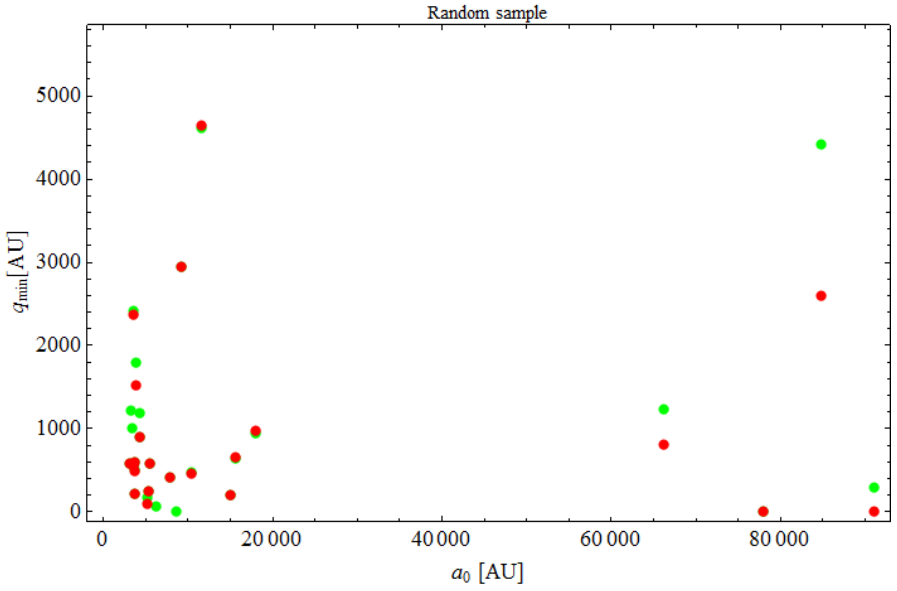

FIGURE 5.16: Minimum perihelion distance q_{min} vs semi-major axis a_0 for a cometary sample completely random. The red points are relative to comets integrated in a Galactic environment with a spiral arms structure, while the green points are referred to the motion of the same comets in axisymmetric potential. The sample appears unbalanced to tiny semi-major axis for which the action of the spiral arms is barely recognizable and produce a injection rate identical for axisymmetric and non-axisymmetric potential (see Tab. 5.2).

non-axisymmetric perturbation (see Fig. 5.16). We did not recognize a particular clue of the spiral perturbation, obtained also the same injection rate both for axisymmetric and non-axisymmetric potential (see the last line in Tab. 5.2).

We also built a graph about the distribution of the minimum perihelion q_{min} vs the eccentricity (Fig. 5.17) and the inclination (Fig. 5.18), that shown again a sample in which is difficult to identify a proof of the spiral presence for the comets represented by the red dots. In conclusion it was not possible to highlight a tangible action of the spiral arms perturbation for a sample closer to the real orbital distribution presents in the Oort Cloud. That is due both by the very limited number of comets considered, but also by the strong concentration around semi-major axis values of $a = 10^4$ AU for the real comets distribution (the Oort spike). Despite that, the elevate injection rate triggered by the presence of the non-axisymmetric structure, that involves a solar migration and seems to reinforce the influence of the planar component of the tide, producing an depletion effect that may entail a redefinition for the external bound of the cloud, and may be a significant importance in the past injection processes.

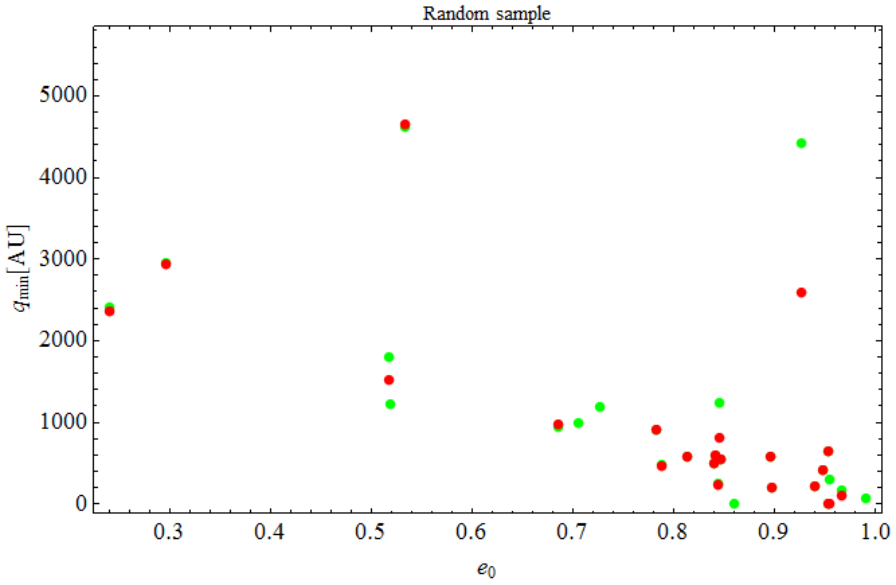

FIGURE 5.17: Minimum perihelion distance q_{min} vs eccentricity axis a_0 for a cometary sample completely random. The red points are relative to comets integrated in a Galactic environment with a spiral arms structure, while the green points are referred to the motion of the same comets in axisymmetric potential. In the sample appears difficult to identify the proof for the presence of the spiral arm perturbation.

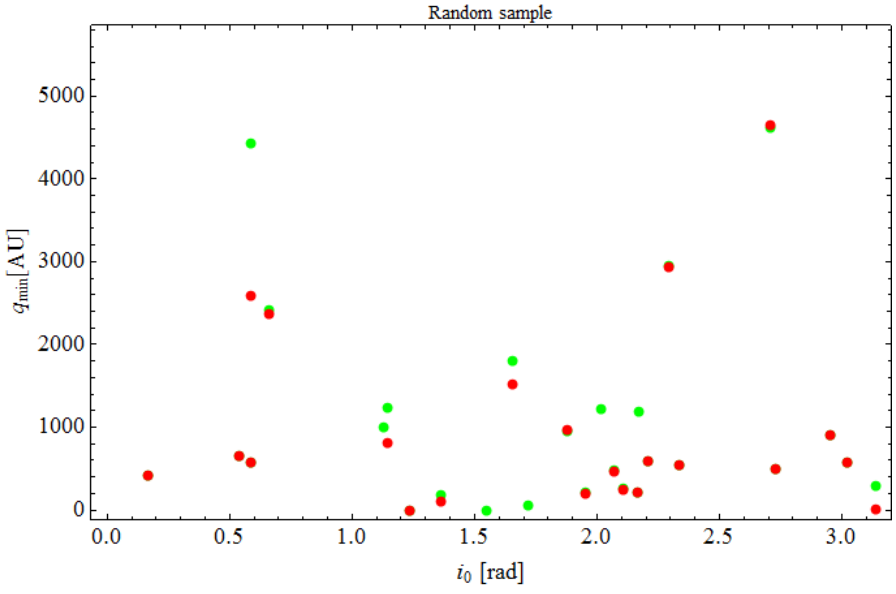

FIGURE 5.18: Minimum perihelion distance q_{min} vs inclination i_0 for a cometary sample completely random. The red points are relative to comets integrated in a Galactic environment with a spiral arms structure, while the green points are referred to the motion of the same comets in axisymmetric potential.

5.4 Data cometary sample

FIXED ORBITAL ELEMENTS: $a = 10^4$ AU, $e = 0.7$, $q_0 = 3000$ AU $\omega_0 = 0.147$ rad,$\Omega_0 = 0.592$ rad and $M_0 = 3.846$ rad					
		With spiral arms		Without spiral arms	
Comet	i_0 (rad)	q_{min} (AU)	Q_{max} (AU)	q_{min} (AU)	Q_{max} (AU)
1	2.578	2101.950	17895.0	2103.540	17891.0
2	2.814	2651.430	17345.7	2655.430	17339.8
3	2.703	2420.510	17575.8	2423.240	17570.3
4	0.456	2380.550	17611.1	2395.660	17590.8
5	2.573	2087.840	17909.1	2089.390	17904.8
6	2.137	819.424	19175.9	819.247	19172.0
7	1.787	130.235	19875.3	139.761	19863.1
8	0.500	2269.690	17720.8	2284.630	17700.1
9	0.590	2027.700	17961.1	2041.890	17940.8
10	0.616	1954.900	18034.3	1968.760	18013.1
11	0.986	870.996	19113.0	877.789	19094.6
12	1.019	782.285	19200.8	789.300	19181.7
13	1.644	Null	Null	Null	Null
14	3.031	Null	Null	2928.290	17064.2
15	0.537	Null	Null	2187.640	17795.4
16	2.809	2641.980	17354.7	2645.910	17348.7
17	0.688	1743.260	18244.5	1755.890	18224.3
18	3.107	2942.240	17056.1	2961.280	17033.7
19	0.421	2461.340	17531.2	2476.550	17510.9
20	1.420	58.515	19897.5	Null	Null
21	0.827	1328.280	18657.7	1336.970	18641.5
22	3.135	2943.650	17054.7	2963.350	17033.3
23	0.652	1849.720	18138.5	1863.030	18118.1
24	0.825	1334.810	18651.9	1343.580	18634.6
25	0.203	2843.100	17150.4	2857.940	17132.5
26	0.685	1751.850	18235.8	1764.540	18215.7
27	1.847	Null	Null	202.921	19797.8
28	1.643	Null	Null	Null	Null
29	0.958	946.810	19038.0	953.469	19019.0
30	0.231	2808.020	17185.2	2823.100	17166.7

TABLE 5.3: Data about the cometary sample with fixed $a_0 = 10^4$ AU, $e_0 = 0.7$, $\omega_0 = 0.147$, $\Omega_0 = 0.592$, $M_0 = 3.846$ and i_0 randomly chosen. The comets indicated as "Null" do not belong to the system at the end of the integration time for the tidal action

FIXED ORBITAL ELEMENTS: $a = 10^5$ AU, $e = 0.7$, $q_0 = 30000$ AU $\omega_0 = -1.615$ rad,$\Omega_0 = 4.476$ rad and $M_0 = -2.011$ rad					
		With spiral arms		Without spiral arms	
Comet	i_0 (rad)	q_{min} (AU)	Q_{max} (AU)	q_{min} (AU)	Q_{max} (AU)
1	2.300	22896.600	235721.0	24104.200	208992.0
2	2.363	25917.900	227237.0	21622.700	211410.0
3	1.822	Null	Null	2648.170	267396.0
4	2.357	25679.200	226300.0	21930.400	210697.0
5	0.293	21003.700	180289.0	25501.900	172480.0
6	0.630	2517.750	221963.0	23690.100	189192.0
7	2.623	2790.060	260104.0	12027.500	211800.0
8	0.622	9484.180	216028.0	22316.500	189817.0
9	1.765	Null	Null	346.307	283269.0
10	2.999	6933.340	203208.0	17152.600	187630.0
11	2.147	4.459	372451.0	18521.200	228384.0
12	0.750	0.333	267710.0	21262.300	196448.0
13	0.467	20713.000	193021.0	27303.400	175461.0
14	1.034	2502.200	271129.0	2047.980	244068.0
15	1.548	Null	Null	382.351	301024.0
16	2.910	10074.600	207262.0	17311.600	188784.0
17	0.232	20390.200	182913.0	25445.600	170811.0
18	2.242	18331.700	266965.0	22862.800	216696.0
19	2.173	4119.530	356916.0	18989.900	230352.0
20	1.097	16.939	314366.0	718.755	254041.0
21	0.607	16173.600	202712.0	26964.000	184614.0
22	1.110	325.029	316749.0	296.814	261042.0
23	1.104	28.786	317489.0	1.772	249779.0
24	1.345	Null	Null	2.200	270202.0
25	2.452	20027.100	232933.0	15925.200	217286.0
26	2.908	10110.100	207390.0	17450.300	188761.0
27	0.087	14268.900	197450.0	25040.500	171573.0
28	1.331	Null	Null	0.635	270831.0
29	0.771	Null	Null	22091.800	202647.0
30	2.429	18369.400	225314.0	17931.100	214580.0

TABLE 5.4: Data about the cometary sample with fixed $a_0 = 10^5$ AU, $e_0 = 0.7$, $\omega_0 = -1.615$, $\Omega_0 = 4.476$, $M_0 = -2.011$ and i_0 randomly chosen.

FIXED ORBITAL ELEMENTS: $a = 10^5$ AU, $e = 0.8$, $q_0 = 19999$ AU $\omega_0 = -2.909$ rad,$\Omega_0 = 5.882$ rad and $M_0 = 0.873$ rad					
		With spiral arms		Without spiral arms	
Comet	i_0 (rad)	q_{min} (AU)	Q_{max} (AU)	q_{min} (AU)	Q_{max} (AU)
1	0.005	3372.520	217199.0	19548.000	187815.0
2	2.069	32.933	223368.0	707.563	207006.0
3	3.086	4922.990	203790.0	10520.400	192476.0
4	0.142	3935.720	217112.0	19139.400	188046.0
5	1.706	80.332	222382.0	6.156	208805.0
6	1.833	0.417	222286.0	0.789	208619.0
7	0.089	3584.720	217557.0	19416.400	187866.0
8	0.410	6862.590	215398.0	15947.300	190526.0
9	1.673	40.094	222190.0	3.590	208707.0
10	1.560	Null	Null	1.819	207949.0
11	2.040	16.450	223314.0	577.201	207331.0
12	2.748	1895.470	211738.0	8299.070	195349.0
13	0.289	5650.130	215351.0	17608.400	189845.0
14	2.496	41.890	233197.0	5160.790	199716.0
15	0.482	7072.300	214187.0	14610.000	191803.0
16	0.099	3638.360	217509.0	19374.000	187894.0
17	0.363	6489.430	215438.0	16662.200	189785.0
18	0.289	5648.500	215355.0	17610.700	189843.0
19	1.399	53.301	221391.0	Null	Null
20	2.829	1886.990	216049.0	9122.850	194282.0
21	1.256	507.501	216234.0	653.696	204082.0
22	2.727	1754.080	214569.0	8086.770	195774.0
23	2.695	1716.920	217419.0	7766.820	196326.0
24	2.528	12.719	218781.0	5504.910	199101.0
25	0.386	6698.010	215462.0	16365.700	190146.0
26	0.354	6408.620	215415.0	16718.400	189667.0
27	3.062	4933.450	203873.0	10490.600	192476.0
28	0.855	3973.520	211252.0	7483.910	198007.0
29	0.597	6677.990	208815.0	12226.600	193938.0
30	0.913	3047.810	212278.0	5397.870	198770.0

TABLE 5.5: Data about the cometary sample with fixed $a_0 = 10^5$ AU, $e_0 = 0.8$, $\omega_0 = -2.909$, $\Omega_0 = 5.882$, $M_0 = 0.873$ and i_0 randomly chosen.

FIXED ORBITAL ELEMENTS: $a = 10^5$ AU, $e = 0.9$, $q_0 = 9999$ AU $\omega_0 = 0.633$ rad,$\Omega_0 = 4.162$ rad and $M_0 = 0.744$ rad					
		With spiral arms		Without spiral arms	
Comet	i_0 (rad)	q_{min} (AU)	Q_{max} (AU)	q_{min} (AU)	Q_{max} (AU)
1	1.399	0.356	213594.0	5.202	200194.0
2	0.971	10.112	199793.0	73.395	198466.0
3	0.096	210.273	219485.0	2059.360	197980.0
4	2.444	0.149	233982.0	2109.100	205472.0
5	1.527	0.068	206657.0	6.030	206617.0
6	2.889	1.483	228682.0	2738.740	207745.0
7	0.575	615.893	199595.0	1177.000	194749.0
8	1.824	223.776	204734.0	1.758	207127.0
9	2.779	0.055	219599.0	2244.360	206502.0
10	2.411	630.512	218192.0	1810.030	205279.0
11	1.398	14.779	201648.0	0.320	203114.0
12	2.831	0.896	225756.0	2429.510	207648.0
13	2.926	12.482	230721.0	2696.180	207533.0
14	0.744	0.134	202449.0	1131.140	197459.0
15	1.335	8.197	193595.0	Null	Null
16	1.383	0.098	198183.0	0.314	198345.0
17	1.735	259.409	213671.0	Null	Null
18	2.188	0.397	214907.0	796.962	207313.0
19	1.907	372.871	212004.0	440.882	200887.0
20	2.910	1.073	227102.0	2820.160	207635.0
21	2.875	19.347	227802.0	2693.620	207881.0
22	2.311	721.558	226186.0	748.959	206660.0
23	1.883	0.508	222442.0	43.941	205109.0
24	0.143	787.932	217488.0	2100.790	197767.0
25	2.694	0.187	221471.0	2417.740	209746.0
26	0.752	3.743	199572.0	906.070	196999.0
27	2.619	0.477	248534.0	2256.020	208396.0
28	3.058	0.102	226038.0	3047.670	207162.0
29	0.778	0.693	196744.0	1265.620	196501.0
30	1.232	12.084	200176.0	5.583	198812.0

TABLE 5.6: Data about the cometary sample with fixed $a_0 = 10^5$ AU, $e_0 = 0.9$, $\omega_0 = 0.633$, $\Omega_0 = 4.162$, $M_0 = 0.744$ and i_0 randomly chosen.

RANDOM COMETARY SAMPLE										
							With spiral arms		Without spiral arms	
Comet	a (AU)	e	i_0 (rad)	Ω_0 (rad)	Ω_0 (rad)	M_0 (rad)	q_{min} (AU)	Q_{max} (AU)	q_{min} (AU)	Q_{max} (AU)
1	15582.000	0.953	0.538	4.148	4.254	2.831	653.390	30525.7	646.802	30522.1
2	5151.780	0.966	1.364	0.440	1.680	3.060	101.896	10178.1	174.169	10130.0
3	5311.660	0.844	2.106	1.997	3.251	5.673	242.028	10386.9	254.028	10375.7
4	6260.300	0.990	1.717	3.806	4.960	1.572	Null	Null	62.786	12458.6
5	66201.500	0.844	1.146	3.815	0.394	4.751	803.672	137474.0	1236.870	134859.0
6	15032.300	0.897	1.952	0.964	3.320	3.935	200.556	29857.1	206.680	29829.2
7	3695.290	0.839	2.730	5.753	0.244	2.147	496.898	6816.8	502.210	6798.0
8	3811.500	0.517	1.656	2.662	2.110	0.195	1519.660	6093.0	1795.250	5817.8
9	5071.690	0.957	1.334	0.513	3.294	0.786	Null	Null	Null	Null
10	4330.040	0.726	2.172	5.166	5.958	5.003	Null	Null	1187.320	7472.7
11	4277.560	0.782	2.954	6.059	0.562	3.654	902.465	7633.8	902.240	7625.9
12	3177.590	0.987	2.421	3.831	4.411	5.852	Null	Null	Null	Null
13	3527.790	0.846	2.334	2.963	1.922	5.242	544.744	6510.8	544.744	6510.8
14	11615.200	0.533	2.705	1.051	2.588	4.843	4644.980	18579.1	4621.160	18600.2
15	3528.810	0.240	0.660	3.430	3.818	1.401	2363.690	4704.7	2417.410	4652.1
16	10353.200	0.788	2.070	5.876	6.122	1.278	465.681	20224.5	476.519	20203.7
17	3130.840	0.813	3.020	4.339	1.229	4.485	580.158	5678.5	580.787	5677.8
18	3392.240	0.705	1.129	0.040	2.509	3.349	Null	Null	1000.660	5783.8
19	84764.700	0.926	0.585	0.080	5.905	0.412	2596.160	179310.0	4423.580	169406.0
20	9239.340	0.295	2.294	3.372	1.662	2.877	2940.290	15536.2	2948.230	15525.3
21	83471.900	0.717	2.289	6.165	4.363	1.777	9610.090	177605.0	13929.300	161922.0
22	91061.100	0.955	3.136	2.736	5.862	4.682	2.809	193217.0	298.706	186863.0
23	3732.600	0.940	2.164	2.621	4.568	5.167	213.066	7240.2	213.264	7239.6
24	3746.670	0.840	2.206	5.349	5.024	0.828	598.769	6894.6	598.769	6894.6
25	77935.100	0.952	1.233	1.835	3.814	5.003	0.368	177358.0	0.391	168273.0
26	7904.290	0.947	0.165	5.510	4.481	4.410	414.330	15394.0	415.316	15392.9
27	8587.590	0.859	1.549	4.005	1.783	1.140	Null	Null	Null	Null
28	3226.630	0.518	2.018	2.043	1.658	0.577	Null	Null	1217.160	5206.6
29	5459.390	0.895	0.585	0.341	2.018	2.732	574.644	10344.3	574.644	10344.3
30	18003.200	0.685	1.877	0.940	1.389	3.062	968.863	35141.0	949.240	35114.8

TABLE 5.7: Data about the cometary sample with initial condition chosen randomly with a non flat distribution for the semi-major axis a and for the eccentricity e.

Conclusions

The Solar System is not a completely isolate structure with an independent dynamics, but it is immersed into a wider Galactic environment that may influence its evolution. The Galaxy is not only a silent observer, but it is directly involved in many processes that might modify the history of the Sun and its main cometary reservoir: the Oort cloud. The comets are the more ancient witnesses of the formation of the Solar System, these object conserve the marks of the primordial chemical and dynamical conditions in which the Sun was born. The spherical structure where the comets are stored, lies in the most peripheral region of the Solar System, constantly prone to the perturbations of the Galaxy, in particular due to the stellar passages and the Galactic tidal field, that are able to inject these fossils of the past, close the central star. The Oort cloud is frontier between out Solar System and the Milky Way, the point in which we have the contact between the planetary and the Galactic dynamics.

The idea of a solar migration is finding a growing consensus, supported by the exigence to explain some observative evidence, like the gap in metallicity between the Sun and its current local environment. The identification of the spiral arms structure as the principal responsible of the stellar migration through the disk was suggested by several authors (e. g. Roškar et al. (2008a), Sellwood and Binney (2002)). Despite that, the effects of the such type of non-axisymmetric perturbation, with the solar migration that seems to entail, is less considered in the past studies about the Oort cloud. Indeed, the inclusion of the spiral structure in the studies related to the Oort cloud dynamics is challenging essentially for two reasons: the strong uncertainties about the dynamical and morphological characterization of the spiral arms and the lack of symmetric that this structure originate in the potential of the Galaxy, making the integration of cometary orbits more heavy from a computation point of view.

The work done has the main aim to introduce a spiral structure that may produce a solar migration compatible with the constraints given by the solar history (current

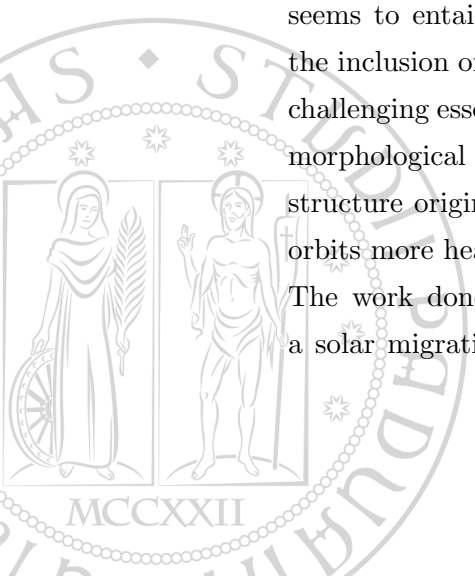

position, peculiar velocity and metallicity), in order to study the comet behavior around a Sun that experience different galactic environment over its evolution. We built our model using the observational data provided by Siebert et al. (2012), about the spiral structure in the current solar environment, and we extended the classical theory of Lin & Shu to a 3D-dimensional model for the spiral arms perturbation. The need to add the third dimension in the spiral model, was born by the requirement to not overestimate the perturbation on the plane, as may happen considering an infinitely thin structure. In order to take into account the wide range of uncertainties around the spiral arms structure and evolution, we performed a statistical investigation for the main parameters that characterize this structure, trying to identify which of these parameters may be crucial to obtain an efficient solar migration from an inner position in the disk, fixed by metallicity requirements, to the current one. We find that this type of non-axisymmetric perturbation is able to move the Sun from an closer initial position around 6 kpc up to the present solar collocation, if the pattern speed is higher with the respect the value obtained for the data concerning the solar environment.

The solar migration inside the galactic disk may become relevant also in the framework of the habitability. Indeed if the Sun is not in a fixed position from the beginning of its history, it could spend a significant fraction of its life outside the galactic region considered as the more suitable for life. For these reasons we have taken into account approaches to the Galactic habitability in order to insert our results in the framework of the Galactic Habitable Zone (GHZ), founding that the obtained solar path is compatible with the galactic conditions that allow the life to arise, at least according to the canonical model of Lineweaver et al. (2004).

We devoted the final part of our investigation to apply the spiral perturbation to the comets, introducing the solar migration and adding the direct presence producing the non-axisymmetric component in the galactic potential of the tidal field. We considered few cometary samples, each composed by 30 objects, integrated in a potential with and without the spiral perturbation modulating it by a transient regime. The results show a growing influence of the spiral arm on cometary objects with large and elongate orbits, and with moderate inclination with respect to the Galactic plane. The spiral structure perturbs in a significant way the comets belonged to the outer shell of the Oort cloud ($a = 10^5$ AU), and for extreme eccentricity provides a injection rate three times bigger than the integration performed without the spiral arms on the same objects. The introduction of the spiral perturbation seems to bolster the planar component of the tide, that may be not longer negligible in affecting the cometary perihelion. We also tried to understand in which way the radial migration could influence the extreme large injection rate registered for the most elongate and eccentric cometary sample. The point to clarify was if the peak for the cometary injections occured at some particular distance from the center of the Galaxy, entailing possible consequences for the GHZ's

edges, or if the cometary entries were spread over the whole solar path, without any preferential collocation for the Sun. It turned out that the major part of cometary injections were registered between 6 and 7 kpc. Looking to these very promising results for strong elongate orbit, we have to take into account that the major number of objects in the Oort Cloud is concentrated around $a = 10^4$ AU (the Oort spike), where the spiral arm perturbation seem to be not so effective. Indeed when we tried to build a more realistic cometary sample, with a non flat distribution for the semi-major axis and the eccentricity, we were not able to highlight a statistically significant action of the spiral arms perturbation due to the very limited number of comets considered in the sample. In conclusion it seems not possible at the moment to highlight a tangible action of the spiral arms perturbation for a sample closer to the present orbital distribution in the Oort Cloud. That might have a threefold meaning:

a) the result is due simply to the number of comet considered which is too much low;

b) the real comets distribution shows a spike around $a = 10^4$ AU and then the Galaxy tide (including that of spiral arms) plays a smaller role for more bound objects biasing our results found for larger semi axes;

c) the present distribution in the semi major axis is indeed the result of a strong depletion of larger semi axis values due to the past injection effect produced by all the components of Galactic tide during the Sun migration as addressed by our preliminary results.

In this frame work the very next improvement of this work will be the integration of number of comets at least comparable with the real Oort cloud ($10^4 - 10^5$objects), in order to provide more details about the three previous issues.

A

Tutorial of orbital dynamics

A.1 Fundamental Laws

Motions inside our Solar System could be explained and described, in first approximation, using the basic laws of the celestial mechanics as the Kepler's laws, the Newton's Universal law of gravitation, the formalism for two and (restricted) three-body problem. In following sections we will summarize the most important notions about these topics.

A.1.1 Kepler's Laws of planetary motion

Kepler derive his three laws of planetary motion between 1609 and 1619, using an empirical approach (Murray and Dermott, 1999). From observations, including those made by Thyco Brahe, Kepler deduced that:

1. The planets move in ellipses with the Sun at one focus.
2. A radius vector from the Sun to a planet sweeps out equal areas in equal times.
3. The time square of the orbital period of a planet is proportional to the cube of its semi-major axis.

The geometry implied by the first two laws is an ellipse has two foci and according to the first law the Sun occupies one focus while the other one is empty (Fig. A.1a). In Fig. A.1b each shaded region represents the area swept out by the radius from the Sun to an orbiting planet in equal time intervals, and the second law states that these areas are equal.
Half the length of the long axis of the ellipse is called the semi-major axis a. Kepler's

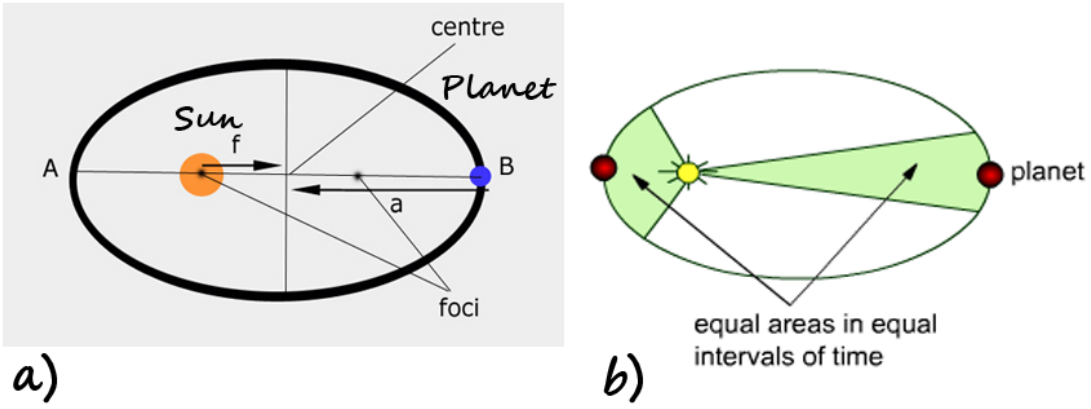

FIGURE A.1: The geometry implied by Kepler's first two laws of planetary motion

third law relates a to the planetary orbital period T. He deduced that

$$T^2 \propto a^3, \tag{A.1}$$

so that if two planets have semi-major axes a_1 and a_2 and periods T_1 and T_2 then $T_1/T_2 = (a_1/a_2)^{3/2}$, which is consisted with his original formulation of the law.
It is important to remember that Kepler's laws were purely empirical: he had no physical understanding of why the planets obeyed these law. The explanation will be provided by Newton about seventy years after, and in that way the Kepler laws could interest not only the planetary motion but a large sample of different celestial bodies.

A.1.2 Newton's Universal Law of Gravitation

In 1687 Isaac Newton proved that a simple, inverse square law of force gives rise to all motion in the Solar System (Murray and Dermott, 1999) . There is a good evidence that Robert Hooke, a contemporary and rival of Newton, had proposed the inverse square law of force before Newton (Westfall 1980) but Newton's great achievement was show that Kepler's laws of motion are a natural consequence of this force and the resulting motion is described by a conic section.
In scalar form, Newton proposed that the magnitude of the force F between any two masses in the universe, m_1 and m_2, separated by a distance d is given by

$$F = G\frac{m_1 m_2}{d^2}, \tag{A.2}$$

where $G = 6.672 \times 10^{-11}$ m^3 kg^{-1} s^{-2} is the universal costant of gravitation.
In his *Principia* Newton also propouned his three laws of motion:

1. Bodies remain in a state of rest or uniform motion in a straight line unless acted upon a force.

2. The force experienced by a body is equal to the rate of change of its momentum.

3. To every action there is an equal and opposite reaction.

The combination of these laws with the universal law of gravitation was to have a profound effect on our understanding of the universe. By extending Newtonian gravitation to more than two bodies it was shown that the mutual gravitational interaction result in ellipses that are no loger fixed. Indeed in our solar system, the orbits of the planets slowly rotate or *precess* in space over timescale of $\sim 10^5$ years.
We now know that Newton's universal law of gravitation is only an approximation, albeit a very good one, and that a better model of gravity is given by Eistein's general theory of relativity, but the classical gravitation approach fits well the purposes of the following chapters.

A.2 The two-body problem

The two-body problem is the simplest, integrable problem in Solar System dynamics (Murray and Dermott, 1999) . It concerns the interaction of two point masses moving under a mutual gravitational attraction described by Newton's universal law of gravitation Eq. (A.2).
Consider the motion of two masses m_1 and m_2 with position vectors $\mathbf{r}_1$ and $\mathbf{r}_2$ referred to some origin O fixed in inertial space (see Fig. A.2.

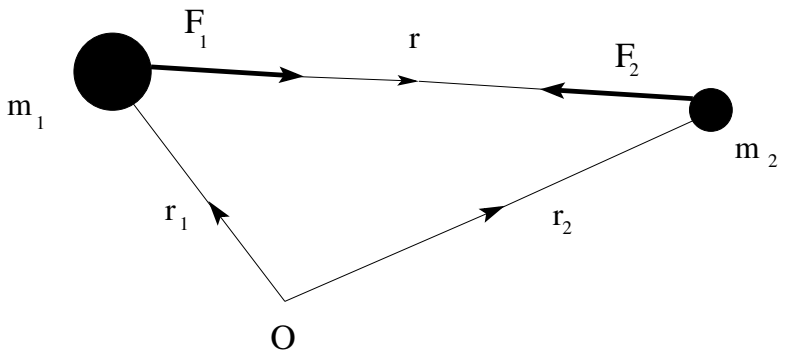

FIGURE A.2: A vector diagram for the forces acting on two masses m_1 and m_2, with position vectors $\mathbf{r}_1$ and $\mathbf{r}_2$

The vector $\mathbf{r} = \mathbf{r}_2 - \mathbf{r}_1$ denotes the relative position of the mass m_2 with respect to m_1. The gravitational forces and the consequent accelerations experienced by the two

masses are:

$$\mathbf{F}_1 = G\frac{m_1 m_2}{r^3}\mathbf{r} = m_1\ddot{\mathbf{r}}_1 \quad \text{and} \quad \mathbf{F}_2 = -G\frac{m_1 m_2}{r^3}\mathbf{r} = m_2\ddot{\mathbf{r}}_2 \tag{A.3}$$

respectively and where G is the universal gravitational constant. Thus

$$m_1\ddot{\mathbf{r}}_1 + m_2\ddot{\mathbf{r}}_2 = 0, \tag{A.4}$$

which can be integrated direcly twice to given

$$m_1\dot{\mathbf{r}}_1 + m_2\dot{\mathbf{r}}_2 = \mathbf{a} \quad \text{and} \quad m_1\mathbf{r}_1 + m_2\mathbf{r}_2 = \mathbf{a}t + \mathbf{b}, \tag{A.5}$$

where $\mathbf{a}$ and $\mathbf{b}$ are constant vectors. If $\mathbf{R} = (m_1\mathbf{r}_1 + m_2\mathbf{r}_2)/(m_1 + m_2)$ denotes the position vector of the center of mass, then Eqs. (A.5) can be written

$$\dot{\mathbf{R}} = \frac{\mathbf{a}}{m_1 + m_2} \quad \text{and} \quad \mathbf{R} = \frac{\mathbf{a}t + \mathbf{b}}{m_1 + m_2} \tag{A.6}$$

This implies that either the center of mass is stationary (if $\mathbf{a} = 0$) or it is moving with a constant velocity in a straight line with respect to the origin O.

Now consider the motion of m_2 with respect to m_1. This allow us to simplify the problem without losing any of its essential features. Writing $\ddot{\mathbf{r}} = \ddot{\mathbf{r}}_2 - \ddot{\mathbf{r}}_1$, and using Eq. (A.3), we obtain

$$\frac{\mathrm{d}^2\mathbf{r}}{\mathrm{d}t^2} + \mu\frac{\mathbf{r}}{r^3} = 0, \tag{A.7}$$

where $\mu = G(m_1 + m_2)$. This is the *equation of relative motion*. In order to solve it and find the path of m_2 relative to m_1 we must first derive several constans of the motion. Taking the vector product of $\mathbf{r}$ with Eq. (A.7) we have $\mathbf{r}\times\ddot{\mathbf{r}} = 0$ which can be integrated direcly to given

$$\mathbf{r}\times\dot{\mathbf{r}} = \mathbf{h}, \tag{A.8}$$

where $\mathbf{h}$ is a costant vector perpendicular to both $\mathbf{r}$ and $\dot{\mathbf{r}}$. Hence the motion of m_2 about m_1 lies in a plane perpendicular to the direction defined by $\mathbf{h}$. This also implies that the position and velocity vectors always lie in the same plane. Eq. (A.8) is commonly referred to as the *angular momentum integral*.

Since $\mathbf{r}$ and $\ddot{\mathbf{r}}$ always lie in the orbital plane we can restrict ourself to considering motion in that plane. We now transform to a polar coordinate system (r, θ), referred to an origin centred on the mass m_1 and an arbitrary reference line corresponding to $\theta = 0$. If we let $\hat{\mathbf{r}}$ and $\hat{\theta}$ denote unit vectors along and perpendicular to the radius vector respectively, then the position, velocity, and acceleration vectors can be rewritten in polar coordinates as

$$\mathbf{r} = r\hat{\mathbf{r}}, \qquad \dot{\mathbf{r}} = \dot{r}\hat{\mathbf{r}} + r\dot{\theta}\hat{\theta} \qquad \ddot{\mathbf{r}} = (\ddot{r} - r\dot{\theta}^2)\hat{\mathbf{r}} + \left[\frac{1}{r}\frac{\mathrm{d}}{\mathrm{d}r}(r^2\dot{\theta})\right]\hat{\theta}. \tag{A.9}$$

Substituting the expression for $\dot{\mathbf{r}}$ into Eq. (A.8) gives $\mathbf{h} = r^2\dot{\theta}\hat{\mathbf{z}}$, where $\hat{\mathbf{z}}$ is a unit vector perpendicular to the plane of the orbit forming a right-handed triad with $\hat{\mathbf{r}}$ and $\hat{\theta}$. Hence

$$h = r^2\dot{\theta}. \tag{A.10}$$

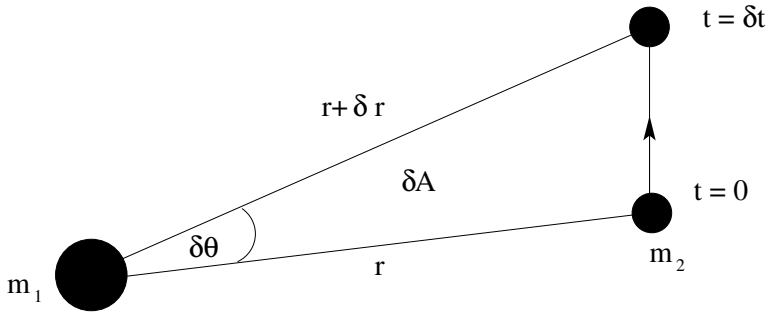

FIGURE A.3: The area δA swept out in a time δt as a position vector moves through an angle $\delta\theta$

Consider the motion of the mass m_2 during a time interval δt (see Fig. A.3). At time $t = 0$ it has polar coordinates (r, θ), while at time $t + \delta t$ its polar coordinates have changed to $(r + \delta r, \theta + \delta\theta)$. The area swept out by the radius vector in time δt is

$$\delta A \approx \frac{1}{2}r(r + \delta r)\sin\delta\theta \approx \frac{1}{2}r^2\delta\theta \tag{A.11}$$

neglecting second- and higher-order terms in the small quantities. By dividing each side by δt and taking the limit as $\delta t \to 0$ we have

$$\frac{\mathrm{d}A}{\mathrm{d}t} = \frac{1}{2}r^2\frac{\mathrm{d}\theta}{\mathrm{d}t} = \frac{1}{2}h. \tag{A.12}$$

Since h is a constant this implies that equal areas are swept out in equal times and hence Eq. (A.12) is the mathematical form of Kepler's second law of planetary motion. Note that this does not require an inverse square law of force, but only that the force is directed along the line joining the two masses.

We obtain a scalar equation for the relative motion by substituting the expression for $\ddot{\mathbf{r}}$ from Eq. (A.9) into Eq. (A.7); comparing the $\hat{\mathbf{r}}$ components gives

$$\ddot{r} - r\dot{\theta}^2 = -\frac{\mu}{r^2}. \tag{A.13}$$

To solve this equation and find r as a function of θ we need to make the substitution $u = 1/r$ (*Binet's transformation*) and to eliminate the time by making use of the constant

$h = r^2\dot{\theta}$. By differentiating r with respect to time, we obtain:

$$\dot{r} = -\frac{1}{u^2}\frac{\mathrm{d}u}{\mathrm{d}\theta}\dot{\theta} = -h\frac{\mathrm{d}u}{\mathrm{d}\theta} \quad \text{and} \quad \ddot{r} = -h\frac{\mathrm{d}^2u}{\mathrm{d}\theta^2}\dot{\theta} = -h^2u^2\frac{\mathrm{d}^2u}{\mathrm{d}\theta^2} \tag{A.14}$$

and Eq. (A.13) can be rewritten

$$\frac{\mathrm{d}^2u}{\mathrm{d}\theta^2} + u = \frac{\mu}{h^2}. \tag{A.15}$$

This is a second-order, linear differential equation with a general solution

$$u = \frac{\mu}{h^2}\left[1 + e\cos(\theta - \varpi)\right], \tag{A.16}$$

where e (an amplitude) and ϖ (a phase) are two constants of integration. Substituting back for r we have the final expression

$$r = \frac{p}{1 + e\cos(\theta - \varpi)}, \tag{A.17}$$

which is the general equation of a conic in polar coordinates where e is the *eccentricity* and p is the *semilatus rectum* given by

$$p = h^2/\mu. \tag{A.18}$$

The four possible conics are:

cicle:	$e = 0$	$p = a$
ellipse:	$0 < e < 1$	$p = a(1 - e^2)$
parabola:	$e = 1$	$p = 2q$
hyperbola:	$e > 1$	$p = a(e^2 - 1)$

where the costan a is the *semi-major axis* of the conic. In the special case of the parabola p is define in terms of q, the distance to the central mass at closest approach. The conic section curves derive their name from the curves formed by the intersection of various planes with the surface of a cone (Fig. A.4)

The type of conic is determined by the angle the plane makes with the horizontal. If the plane is horizontal, that is, perpendicular to the axis of symmetry of the cone, then the resulting curve is a circle. If the angle is less than the slope angle of the cone then an ellipse results, whereas if the plane is parallel to the slope of the cone a parabola results. A hyperbola result if the angle is anywhere between the slope angle of the cone and the vertical.

To conclude this very brief explanation about the two-body problem, we can derive another very important constant of the motion by taking the scalar product of $\dot{\mathbf{r}}$ with

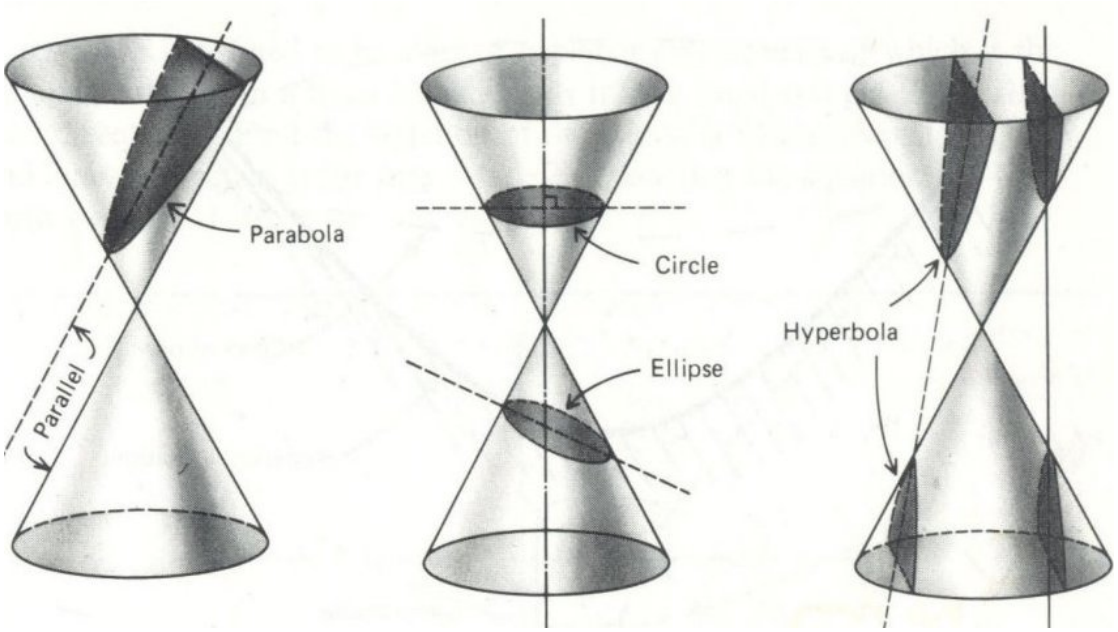

FIGURE A.4: The intersection of planes at different angles with the surface of a cone form the family of the conics section curves

Eq. (A.7).This gives the scalar equation

$$\dot{\mathbf{r}} \cdot \ddot{\mathbf{r}} + \mu \frac{\dot{r}}{r^2} = 0 \tag{A.19}$$

which can be integrated to give

$$\frac{1}{2}v^2 - \frac{\mu}{r} = C, \tag{A.20}$$

where $v^2 = \dot{\mathbf{r}} \cdot \dot{\mathbf{r}}$ is the square of the velocity and C is a constant of the motion. Equation (A.20), often called *vis viva integral*, shows that the orbital energy per unit mass is conserved. Thus the two-body problem has four constants of the motion: the energy integral C and the three components of the angular momentum integral, $\mathbf{h}$.

A.2.1 Orbital elements

We can extend the previous notions from the planets to the others objects presented in our planetary system, indeed neglecting mutual perturbations, all bodies in the Solar System move relative to the Sun in an elliptical orbit, the Sun being at one of the two foci of the ellipse (Morbidelli, 2005) . Since we are not interest about unbounded motions, we will concentrate on the elliptic case. Therefore, it is convenient to characterize the relative motion of a body by quantities that describe the geometrical properties of its orbital ellipse and its instantaneous position on the ellipse. These quantities are usually called *orbital elements*.

The shape of the ellipse can be completely determined by two orbital elements that we

have already met in the previous paragraph about the conics: the *semi-major axis* a and the *eccentricity* e (Fig. A.5). The eccentricity is the ratio between the distance of the focus from the center of the ellipse and the semi-major axis of the ellipse and describe the deviation from the circular orbit.

On an elliptic orbit, the closest point to the Sun is called the *perihelion*, and its

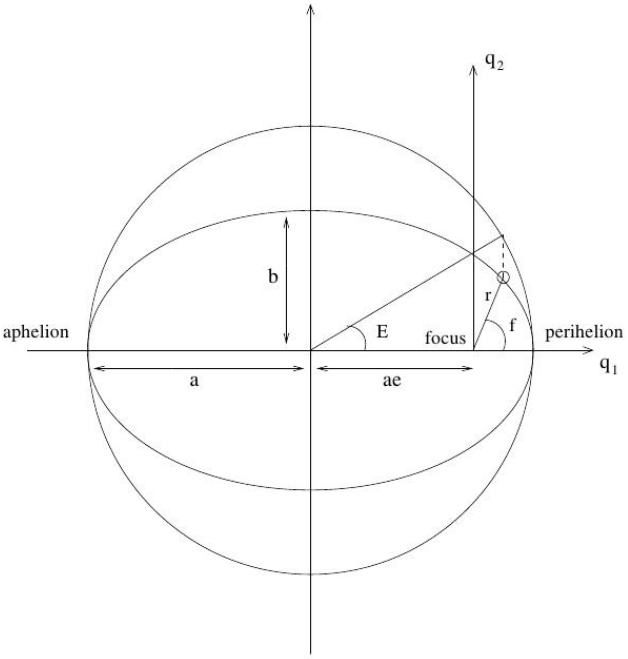

FIGURE A.5: The definition of orbital elements a, E and e (Morbidelli, 2005)

heliocentric distance q is equal to $a(1-e)$; the farthest point is called the *aphelion* and its distance Q is equal to $a(1+e)$. To denote the position of a body on its orbit, it is convenient to use an orthogonal reference frame q_1, q_2 with origin at the focus of the ellipse occupied by the Sun and q_1 axis oriented towards the perihelion of the orbit. Alternatively, polar coordinates r, f can be used. The angle f is usually called the *true anomaly* of the body. From Fig. A.5, with geometrical relationships we obtain:

$$q_1 = a(\cos E - e), \qquad q_2 = a\sqrt{1-e^2}\sin E \tag{A.21}$$

and we can rewritten the Eq. (A.17)

$$r = a(1 - e\cos E) \quad \text{with} \quad \cos f = \frac{\cos E - e}{1 - e\cos E} \tag{A.22}$$

where E, as Fig. A.5 shows, is the angle subtended at the center of the ellipse by the projection of the position of the body on the circle which is tangent to the ellipse at perihelion and aphelion, it is called *eccentric anomaly*. The quantities a, e and E are enough to characterize the position of a body in its orbit.

From Newton equations, it is possible to derive (Danby, 1962) the evolution law of E with respect to time, usually called the *Kepler equation*:

$$E - e\sin E = n(t - t_0) \tag{A.23}$$

where

$$n = \sqrt{G(m_0 + m_1)}a^{-3/2} \tag{A.24}$$

is the orbital frequency, or *mean motion*, of the body, m_0 and m_1 are the masses of the Sun and of the body respectively and t_0 is the time of passage at perihelion.

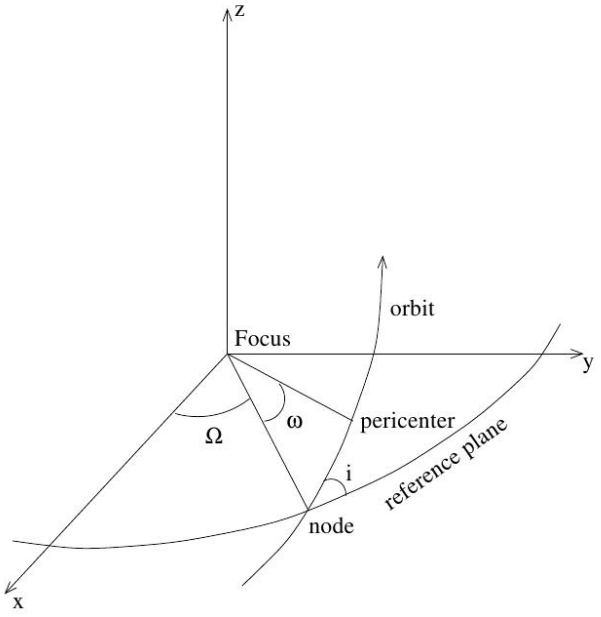

FIGURE A.6: The definition of orbital elements i, Ω and ω (Morbidelli, 2005)

It could be useful also introduce a new angle:

$$M = n(t - t_0) \tag{A.25}$$

called *mean anomaly*, as an orbital element that changes linearly with the the time.
To characterize the orientation of the ellipse in space, with respect to an arbitrary orthogonal reference frame (x, y, z) centered on the Sun, we have to introduce three new orbital elements, in particolar three angles (see Fig. A.6). The first one is the *inclination* i of the orbital plane with respect to the (x, y) reference plane. If the orbit has a nonzero inclination, it intersects the (x, y) plane in two points, called the *nodes* of the orbit. Astronomers distinguish between an *ascending* node, where the body passes from negative to positive z, and a *descending* node, where the body plunges towards negative z. The orientation of the orbital plane in space is then completely determined

when one gives the angular position of the ascending node from the x axis. This angle is traditionally called the *longitude of ascending node*, and is usually denoted by Ω. The last angle is the *argument of perihelion* ω defined as the angular position of the perihelion, measured in the orbital plane relative to the line connecting the central body to the ascending node; it characterizes the orientation of the ellipse in its plane.
In the definition of the orbital elements above, note that when the inclination is zero, ω and M are not defined, because the position of the ascending node is not determined. Moreover, M is not defined also when the eccentricity is zero, because the position of the perihelion is not determined. Therefore, it is convenient to introduce the *longitude of perihelion* $\varpi = \omega + \Omega$ and the *mean longitude* $\lambda = M + \omega + \Omega$. The first angle is well defined when $i = 0$, while the second one is well defined when $i = 0$ and/or $e = 0$.
In absence of external perturbations, the orbital motion is perfectly elliptic: the orbital elements a, e, i, ϖ, Ω, are fixed, and λ moves linearly with time, with frequency (A.24). When a small perturbation is introduced, two effects are produced:

1. the motion of λ is no longer perfectly linear. Correspondingly, the other orbital elements have short periodic oscillations with frequencies of order of the orbital frequencies;

2. the angles ϖ and Ω start to rotate slowly. As we have already mentioned this motion is called precession. Typical precession periods in the Solar System are of order of 10,000.100,000 years. Correspondingly, e and i have long periodic oscillations, with periods of order of the precession periods.

The regularity of these short periodic and long periodic oscillations is broken when one of the following two situations occur:

i. the perturbation becomes large, for instance when there are close approaches between the body and the perturbing planet, or when the mass of the perturber is comparable to that of the Sun;

ii. the perturbation becomes resonant[1].

In either of these cases the orbital elements a, e, i can have large non-periodic, irregular variations.

[1] A resonance occurs when the frequencies of $\lambda, \widetilde{\omega}$ or Ω of the body, or an integer combination of them, are in integer ratio with one of the time frequencies of the perturbation.

A.3 The restricted three-body problem

The last topis of this small tutorial is the three-body problem. Unlike the simple and integrable two-body problem the three-body problem has not an analytic solution. In this section we give only the most important notions about this wide and complex problem and refer to the references for more details (in particular (Murray and Dermott, 1999)).

(Binney and Tremaine, 2008) The restricted three body-problem is to find the trajectory of a massless test particle that orbits in the combined gravitational field of these two masses.

The two masses, m and M with $m < M$, travel in a circular orbit around their common center of mass with angular speed

$$\Omega_c = \sqrt{\frac{G(M+m)}{R_0^3}} \tag{A.26}$$

where R_0 is the separation between the two bodies; so the gravitational field is stationary when referred to a coordinate system centered on the center of mass that rotates at speed Ω_c. We orient this coordinate system so that two masses are centered at $\mathbf{r}_m = [MR_0/(M+m), 0, 0]]$ and $\mathbf{r}_M = [-mR0/(M+m), 0, 0]$ and the angular speed id $\mathbf{\Omega}_c = (0.0.\Omega)$. It is possible to show that on any orbit in such a system, the quantity called *Jacobi integral*

$$\begin{aligned} E_J &= \frac{1}{2}v^2 + \Phi(\mathbf{r}) - \frac{1}{2}|\mathbf{\Omega}_c \times \mathbf{r}|^2 \\ &= \frac{1}{2}v^2 + \Phi_{eff}(\mathbf{r}) \end{aligned} \tag{A.27}$$

is conserved. Since $v^2 \geq 0$, a particle with Jacobi integral E_J can never trepass into a region where $\Phi_{eff}(\mathbf{r}) > E_J$. Consequently, the surface $\Phi_{eff}(\mathbf{r}) = E_J$, the zero surface for stars of Jacobi integral E_J, forms an impenetrable wall for such particles. Fig. A.7 shows contours of constant Φ_{eff} in the equatorial plane of two orbiting point masses; the Lagrange points are the extrema (maxima and saddle points) of this surface.

From the figure we see that the zero-velocity surfaces near each body are centered on it, but farther out the zero-velocity surfaces surround both bodies. Hence, at the critical value of Φ_{eff} corresponding to the last zero-velocity surface surrounding a single body is called its *tidal* or *Roche surface*; since this surface touches the Lagrange point L_3 that lies between the two masses on the line connecting them[2], it is natural to identify the outermost radius of orbits bound to m as the distance r_J between m and L_3.

[2]Different authors use different conventions for numbering of the L_3

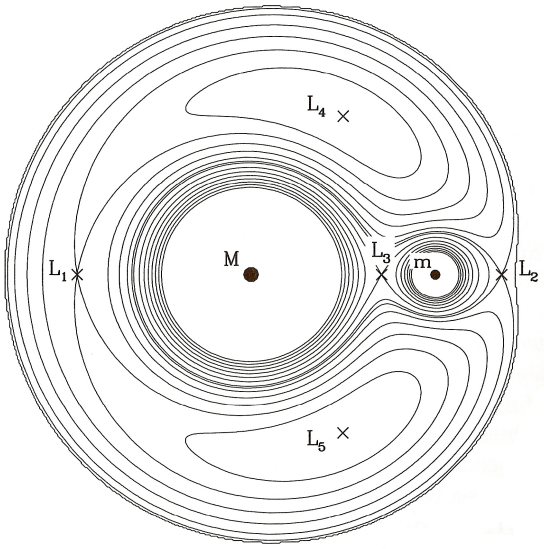

FIGURE A.7: Countours of equal effective potential Φ_{eff} for two point masses in a circular orbit (Binney and Tremaine, 2008)

We may evaluate r_J by noticing that at $(x_m - r_J, 0, 0)$ the effective potential has a saddle point, so

$$\left(\frac{\partial \Phi_{eff}}{\partial x}\right)_{(\mathbf{r}_m - \mathbf{r}_J, 0, 0)} = 0 \tag{A.28}$$

For two point masses a distance R_0 apart, Eq. (A.26) and Eq. (A.27) imply:

$$\Phi_{eff}(\mathbf{r}) = -G\left[\frac{M}{|\mathbf{r} - \mathbf{r}_M|} + \frac{m}{|\mathbf{r} - \mathbf{r}_m|} + \frac{M+m}{2R_0^3}(x^2 + y^2)\right]. \tag{A.29}$$

At a point between the two masses, Eq. (A.28) is satisfied if

$$0 = \frac{1}{G}\left(\frac{\partial \Phi_{eff}}{\partial x}\right)_{(x_m - r_j, 0, 0)} = \frac{M}{(R_0 - r_J)^2} - \frac{m}{r_J^2} - \frac{M+m}{R_0^3}\left(\frac{MR_0}{M+m} - r_J\right). \tag{A.30}$$

This equation leads to a fifth-order polynomial whose roots give r_J. In general these roots must be found numerically. However if $m << M$, then $r_J << R_0$, and we can expand $(R_0 - r_J)^{-2}$ in powers of r_J/R_0 to find

$$0 = \frac{M}{R_0^2}\left(1 + \frac{2r_J}{R_0} + \ldots\right) - \frac{m}{r_J^2} - \frac{M}{R_0^2} + \frac{M+m}{R_0^3} r_J \simeq \frac{3Mr_J}{R_0^3} - \frac{m}{r_j^2}. \tag{A.31}$$

Then to first order in r_J/R_0,

$$r_J = \left(\frac{m}{3M}\right)^{1/3} R_0. \tag{A.32}$$

We call the radius r_J the **Jacobi radius** of the mass m; alternative names are the **Roche** or **Hill radius**. The Jacobi radius of an orbiting mass is expected to correspond to its tidal radius.

B

Data from the RAVE survey

The RAVE survey Siebert et al. (2011b), Steinmetz et al. (2006), Zwitter et al. (2008) provides along the line-of-sight with a precision of 2 km s^{-1} for a large number of stars in the southern hemisphere with $9 < I < 12$. The targets have been selected randomly by RAVE within the I-band interval, in this way the properties of RAVE are similar to a magnitude limited survey. In order to provide additional information about the proper motions and magnitudes the RAVE catalogue is cross-matched with astrometric (PPMX, UCAC2, Tyncho-2) and photometric catalogues (2MASS, DENIS). In their work Siebert et al. (2012) use the internal version of the catalogue which contains data for 434 807 spectra, corresponding to 393 9.3 starts. In addition the star distances, necessary to compute the galactocentric velocity, are available for the 30% of the RAVE starts in three studies Breddels et al. (2010), Burnett et al. (2011), Zwitter et al. (2010). The final sample in Siebert et al. (2012) consists in 213 713 stars from the survey limit to a distances of 2 kpc from the Sun and to 1 kpc along the vertical direction above and below the plane.

C

Hill's approximation in 3D axisymmetric potential

C.1 Extension in 3D axisymmetric potential

Referring to Fig.5.1 (see Fig. 8.7 of Binney & Tremaine, 2008, Chapt. 8) we consider the general gravitational potential Φ due to the host system on the point $\boldsymbol{X} \equiv (\hat{\mathbf{X}} + \mathbf{x})$ of the satellite system which has the center of mass at $\hat{\mathbf{X}}$. By expansion in Taylor series we get:

$$\Phi(\hat{\mathbf{X}} + \mathbf{x}) \simeq \Phi(\hat{\mathbf{X}}) + \sum_{k=1}^{3} (\vec{x})_k \left(\frac{\partial \Phi}{\partial X_k} \right)_{\hat{\mathbf{X}}} \tag{C.1}$$

In the case of the Solar system inside the Galaxy it turns to be $\hat{\boldsymbol{X}} \equiv \boldsymbol{R_o} \equiv (X_o, Y_o, 0)$ the coordinate system (X, Y, Z) having the origin into the Galaxy center.

Taking into account the X_j (j=1,2,3) component of the gradient $\nabla\Phi$, Eq.(C.1) yields:

$$\frac{\partial \Phi}{\partial X_j} \simeq \left(\frac{\partial \Phi}{\partial X_j} \right)_{\boldsymbol{R_o}} + \sum_{k=1}^{3} (\vec{x})_k \left(\frac{\partial^2 \Phi}{\partial X_j \partial X_k} \right)_{\boldsymbol{R_o}} \tag{C.2}$$

According to Binney & Tremaine (2008, sect. 8.2.1) the first term of Taylor's expansion disappears as soon as we refer the movement of an object in the satellite system to the center of mass of the same Solar System, choosing it as origin of reference system $\boldsymbol{x} \equiv (x, y, z)$ (Fig.5.1). To understand it let us remember that the acceleration $\boldsymbol{a'}$ of the object considered, in respect to that of the center of mass $\boldsymbol{a_{cm}}$, becomes:

$$\boldsymbol{a} = \boldsymbol{a'} - \boldsymbol{a_{cm}} \tag{C.3}$$

The consequence is that the second term of (C.2) yields for $\boldsymbol{a_{cm}}$ into (C.3):

$$\frac{1}{M_S}\sum_{\beta} m_\beta \left(-\sum_{j,k}\Phi_{jk}(\vec{x})_k^\beta\right) = \frac{1}{M_S}\left(-\sum_{j,k}\Phi_{jk}\sum_{\beta} m_\beta(\vec{x})_k^\beta\right) \tag{C.4}$$

which becomes zero due to the definition of the center of mass for a system of β particles of total mass M_S once it is assumed as the origin of the reference system. Conversely the contribution of the first derivative, $\left(\frac{\partial\Phi}{\partial X_j}\right)_{\boldsymbol{R_o}} = \Phi_j$ into Eq.(C.2) due to the center of mass acceleration is:

$$-\frac{1}{M_S}\sum_{\beta}(m_\beta\Phi_j) = -\Phi_j \tag{C.5}$$

by definition of center of mass. Then Eq.(C.3) for the object considered transforms into:

$$\boldsymbol{a} = -\Phi_j - \sum_{j,k}\Phi_{jk}(\vec{x})_k + \Phi_j = -\sum_{j,k}\Phi_{jk}(\vec{x})_k \tag{C.6}$$

Considering then two new reference systems with the center on Sun: $\boldsymbol{X'}, \boldsymbol{x}$, which differ from the old reference one simply by a translation along $\boldsymbol{X}$, so that:

$$\begin{aligned} X' = X - R_o = x \\ Y' = Y = y \\ Z' = Z = x \end{aligned}$$

Due to the same differentials in the old and new systems we may calculate the force components of the host system, with the center located now at $\boldsymbol{X'_c} \equiv (-R_o, 0, 0)$, over the Solar system as follows:

$$\frac{\partial\Phi}{\partial X} \simeq x\left(\frac{\partial^2\Phi}{\partial X^2}\right)_{\boldsymbol{R_o}} + y\left(\frac{\partial^2\Phi}{\partial X\partial Y}\right)_{\boldsymbol{R_o}} + z\left(\frac{\partial^2\Phi}{\partial X\partial Z}\right)_{\boldsymbol{R_o}} \tag{C.7}$$

$$\frac{\partial\Phi}{\partial Y} \simeq y\left(\frac{\partial^2\Phi}{\partial Y^2}\right)_{\boldsymbol{R_o}} + z\left(\frac{\partial^2\Phi}{\partial Y\partial Z}\right)_{\boldsymbol{R_o}} + x\left(\frac{\partial^2\Phi}{\partial Y\partial X}\right)_{\boldsymbol{R_o}} \tag{C.8}$$

$$\frac{\partial\Phi}{\partial Z} \simeq z\left(\frac{\partial^2\Phi}{\partial Z^2}\right)_{\boldsymbol{R_o}} + x\left(\frac{\partial^2\Phi}{\partial Z\partial X}\right)_{\boldsymbol{R_o}} + y\left(\frac{\partial^2\Phi}{\partial Z\partial Y}\right)_{\boldsymbol{R_o}} \tag{C.9}$$

without distinguishing the derivatives respect to the system $\boldsymbol{X}$ from those respect to $\boldsymbol{X'}$.

We consider now the case of an axisymmetric potential:

- $\Phi = \Phi(R, Z);\ R = \sqrt{(X' + R_o)^2 + Y'^2};\ R_\odot = R_o$
- $\frac{\partial \Phi}{\partial R} = \Phi';\ \frac{\partial^2 \Phi}{\partial R^2} = \Phi'',$

then:

$$\frac{\partial \Phi}{\partial X'} = \frac{\partial \Phi}{\partial R}\frac{\partial R}{\partial X'} = \Phi' \frac{X' + R_o}{R} \tag{C.10}$$

$$\frac{\partial \Phi}{\partial Y'} = \frac{\partial \Phi}{\partial R}\frac{\partial R}{\partial Y'} = \Phi' \frac{Y'}{R} \tag{C.11}$$

$$\frac{\partial^2 \Phi}{\partial X'_i \partial X'_j} = \frac{\partial}{\partial X'_i}\left(\Phi' \frac{X'_j}{R}\right) = \left(\Phi'' - \frac{\Phi'}{R}\right)\frac{X'_i X'_j}{R^2} + \frac{\Phi'}{R}\delta_{ij}; \tag{C.12}$$
$$(i, j = 1, 2;\ X'_1 = X' + R_o, X'_2 = Y')$$

From the last relationships we obtain that on the equatorial plane:

$$(\Phi)_{xx} = \left(\frac{\partial^2 \Phi}{\partial X'^2}\right)_{R_\odot} = \Phi''(R_o) \tag{C.13}$$

$$(\Phi)_{yy} = \left(\frac{\partial^2 \Phi}{\partial Y'^2}\right)_{R_\odot} = \frac{\Phi'(R_o)}{R_o} \tag{C.14}$$

$$(\Phi)_{xy} = (\Phi)_{yz} = 0 \tag{C.15}$$

For the vertical z-component of gravitational force:

$$\frac{\partial^2 \Phi}{\partial Z \partial X'_j} = \frac{\partial}{\partial Z}\left(\Phi' \frac{X'_j}{R}\right) = \frac{X'_j}{R}\frac{\partial^2 \Phi}{\partial Z \partial R} \tag{C.16}$$

It means:

$$(\Phi)_{xz} = \left(\frac{X' + R_o}{R}\frac{\partial^2 \Phi}{\partial Z \partial R}\right)_{R_\odot} = \left(\frac{X' + R_o}{R}\frac{\partial \Phi'}{\partial Z}\right)_{R_\odot} \tag{C.17}$$

$$(\Phi)_{yz} = \left(\frac{Y'}{R}\frac{\partial^2 \Phi}{\partial Z \partial R}\right)_{R_\odot} = \left(\frac{Y'}{R}\frac{\partial \Phi'}{\partial Z}\right)_{R_\odot} \tag{C.18}$$

which are both equal zero due to the assumption of a circular motion of Sun on the Galactic plane around the Galactic center: $\Phi' = R\Omega^2$. That occurs also as a request of the symmetry of the system respect to the equatorial plane according to which the force component (C.9) on the plane (z=0) has to be zero.

Moreover, remembering Poisson's equation it follows:

$$(\Phi)_{zz} = \left(\frac{\partial^2 \Phi}{\partial Z^2}\right)_{R_\odot} \simeq 4\pi G\bar{\rho} \tag{C.19}$$

where $\bar{\rho}$ is the mean density in the Sun's neighborhood along z-direction. From the Eq.s (C.14, C.19) the breaking of spherical symmetry is manifest.

According to this result and taking into account that the comet orbits we are considering lie on the equatorial plane ($z = 0$) the two first equations of the system (5.3) follow. As soon as the 3D orbits are considered, the Eq. (C.19) yields the third equation to be added into the same equation system.

C.1.1 On tide contributions in Hill's approximation

Due to the additive contribution of each Galaxy component to the total gravitational potential (see Eq.2.1) and to the assumption of the Sun's circular motion it follows that the corresponding circular and angular velocity contribution of each dynamical component, v_{ci} and Ω_{oi}, respectively, turns to be:

$$\frac{v_{ci}^2}{R_o} = (-\nabla\Phi_i)_{R_o} = \Omega_{oi}^2 R_o;\ i = BG, D, DH \tag{C.20}$$

Then, in the first equation of the system (5.3), the following transformation holds for the term in square brackets as soon as it refers to a specific dynamical component:

$$\Omega_{oi}^2 - \Phi_i'' = \left(-2\Omega_i\Omega_i' R\right)_{R_o} = 2\frac{v_{ci}^2}{R_o^2}\left(1 - \frac{dln\ v_{ci}}{dln\ R}\right)_{R_o} \tag{C.21}$$

The x-component Galaxy tide with its partial compensation due to the variation of centrifugal force at x-coordinate turns then to be depending on the radial velocity contribution of each Galactic component.

From the other side the y-component Galaxy tide (see, second equation of system (5.3)), is fully compensated by the corresponding variation of centrifugal force at y-coordinate so that the term in brackets:

$$\Omega_{oi}^2 - \frac{\Phi_i'(R_0)}{R_0} \tag{C.22}$$

turns to be zero no matter what is the component considered.

Bibliography

L. H. Amaral and J. R. D. Lepine. A self-consistent model of the spiral structure of the Galaxy. *MNRAS*, 286:885–894, 1997.

V. S. Avedisova. Structure of the Sagittarius / Carina Spiral Arm and Parameters of the Spiral Pattern. *Astrophysics*, 30:83, 1989.

F. N. Bash. Does the Galaxy have four spiral arms. *ApJ*, 250:551–560, 1981.

D. Bindoni and L. Secco. Violent relaxation in phase-space. *New Astronomy Reviews*, 52:1–18, 2008.

J. Binney and S. Tremaine. *Galactic Dynamics: Second Edition*. Princeton University Press, 2008.

J. Binney, O. E. Gerhard, A. A. Stark, J. Bally, and K. I. Uchida. Understanding the kinematics of Galactic centre gas. *MNRAS*, 252:210–218, 1991.

J. Binney, O. Gerhard, and D. Spergel. The photometric structure of the inner Galaxy. *MNRAS*, 288:365–374, 1997.

J. J. Binney and N. W. Evans. Cuspy dark matter haloes and the Galaxy. *MNRAS*, 327:L27–L31, October 2001.

N. Bissantz, P. Englmaier, and O. Gerhard. Gas dynamics in the Milky Way: second pattern speed and large-scale morphology. *MNRAS*, 340:949–968, 2003.

L. Blitz, M. Fich, and S. Kulkarni. The new Milky Way. *Science*, 220:1233–1240, 1983. doi: 10.1126/science.220.4603.1233.

H. Boehnhardt. *Split comets*, pages 301–316. 2004.

J. Bovy, H.-W. Rix, and D. W. Hogg. The Milky Way Has No Distinct Thick Disk. *ApJ*, 751:131, 2012.

R. Brasser, A. Higuchi, and N. Kaib. Oort cloud formation at various Galactic distances. *A&A*, 516:A72, 2010.

M. A. Breddels, M. C. Smith, and et al. Helmi. Distance determination for RAVE stars using stellar models. *A&A*, 511:A90, 2010.

B. Burnett, J. Binney, and Sharma et al. Distance determination for RAVE stars using stellar models. III. The nature of the RAVE survey and Milky Way chemistry. *A&A*, 532:A113, 2011.

D. Burstein. Structure and origin of S0 galaxies. III - The luminosity distribution perpendicular to the plane of the disks in S0's. *ApJ*, 234:829–836, 1979.

C. Chiappini, F. Matteucci, and D. Romano. Abundance Gradients and the Formation of the Milky Way. *ApJ*, 554:1044–1058, 2001.

M. Creze and M. O. Mennessier. An Attempt to Interpret the Mean Properties of the Velocity Field of Young Stars in Terms of Lin's Theory of Spiral Waves. *A&A*, 27: 281, 1973.

J. Danby. *Fundamentals of celestial mechanics*. 1962.

W. Dehnen and J. J. Binney. Local stellar kinematics from HIPPARCOS data. *MNRAS*, 298:387–394, 1998.

L. Dones, P. R. Weissman, H. F. Levison, and M. J. Duncan. *Oort cloud formation and dynamics*, pages 153–174. 2004.

E. D'Onghia, M. Vogelsberger, and L. Hernquist. Self-perpetuating Spiral Arms in Disk Galaxies. *ApJ*, 766:34, 2013.

M. Duncan, T. Quinn, and S. Tremaine. The formation and extent of the solar system comet cloud. *AJ*, 94:1330–1338, 1987.

M. J. Duncan and H. F. Levison. A scattered comet disk and the origin of Jupiter family comets. *Science*, 276:1670–1672, 1997.

M. J. Duncan, H. F. Levison, and S. M. Budd. The Dynamical Structure of the Kuiper Belt. *AJ*, 110:3073, 1995.

P. A. Dybczyński, G. Leto, M. Jakubík, T. Paulech, and L. Neslušan. The simulation of the outer Oort cloud formation. The first giga-year of the evolution. *A&A*, 487: 345–355, 2008.

D. M. Elmegreen. Spiral structure of the Milky Way and external galaxies. In H. van Woerden, R. J. Allen, and W. B. Burton, editors, *The Milky Way Galaxy*, volume 106 of *IAU Symposium*, pages 255–270, 1985.

Y. Fenner and B. K. Gibson. Deriving the Metallicity Distribution Function of Galactic Systems. *Publ. Astron. Soc. Aust*, 20:189–195, 2003.

J. A. Fernandez. Mass removed by the outer planets in the early solar system. *Icarus*, 34:173–181, 1978.

J. A. Fernandez. On the existence of a comet belt beyond Neptune. *MNRAS*, 192: 481–491, 1980a.

J. A. Fernandez. Evolution of comet orbits under the perturbing influence of the giant planets and nearby stars. *Icarus*, 42:406–421, 1980b.

C. Flynn, J. Sommer-Larsen, and P. R. Christensen. Kinematics of the outer stellar halo. *MNRAS*, 281:1027–1032, 1996.

M. Fouchard, H. Rickman, C. Froeschlé, and G. B. Valsecchi. The last revolution of new comets: the role of stars and their detectability. *A&A*, 535:A86, 2011. doi: 10.1051/0004-6361/201116514.

K. C. Freeman. On the Disks of Spiral and so Galaxies. *ApJ*, 160:811, 1970.

J. García-Sánchez, P. R. Weissman, and Preston et al. Stellar encounters with the solar system. *A&A*, 379:634–659, 2001. doi: 10.1051/0004-6361:20011330.

E. Gardner, P. Nurmi, C. Flynn, and S. Mikkola. The effect of the solar motion on the flux of long-period comets. *MNRAS*, 411:947–954, 2011.

Y. M. Georgelin and Y. P. Georgelin. The spiral structure of our Galaxy determined from H II regions. *A&A*, 49:57–79, 1976a.

Y. M. Georgelin and Y. P. Georgelin. The spiral structure of our Galaxy determined from H II regions. *A&A*, 49:57–79, 1976b.

B. Gladman, M. Holman, T. Grav, J. Kavelaars, P. Nicholson, K. Aksnes, and J.-M. Petit. Evidence for an Extended Scattered Disk. *Icarus*, 157:269–279, 2002.

G. Gonzalez, D. Brownlee, and P. Ward. The Galactic Habitable Zone: Galactic Chemical Evolution. *Icarus*, 152:185–200, 2001.

M. A. Gordon. Determination of the spiral pattern speed of the galaxy. *ApJ*, 222: 100–102, 1978.

M. G. Gowanlock, D. R. Patton, and S. M. McConnell. A Model of Habitability Within the Milky Way Galaxy. *Astrobiology*, 11:855–873, 2011.

J. S. Greaves and M. C. Wyatt. Debris discs and comet populations around Sun-like stars: the Solar system in context. *MNRAS*, 404:1944–1951, 2010.

J. Heisler. Monte Carlo simulations of the Oort comet cloud. *Icarus*, 88:104–121, 1990.

J. Heisler and S. Tremaine. The influence of the galactic tidal field on the Oort comet cloud. *Icarus*, 65:13–26, 1986.

A. P. Henderson. A possible four-arm spiral pattern in the Galaxy. *A&A*, 58:189–196, 1977.

J. G. Hills. Comet showers and the steady-state infall of comets from the Oort cloud. *AJ*, 86:1730–1740, 1981.

N. A. Kaib, R. Roškar, and T. Quinn. Sedna and the Oort Cloud around a migrating Sun. *Icarus*, 215:491–507, 2011.

S. Kendall, R. C. Kennicutt, C. Clarke, and M. D. Thornley. Tracing spiral density waves in M81. *MNRAS*, 387:1007–1020, 2008.

A. Klypin, H. Zhao, and R. S. Somerville. ΛCDM-based Models for the Milky Way and M31. I. Dynamical Models. *ApJ*, 573:597–613, 2002.

M. J. Kuchner, M. E. Brown, and M. Holman. Long-Term Dynamics and the Orbital Inclinations of the Classical Kuiper Belt Objects. *AJ*, 124:1221–1230, 2002.

K. Kuijken and G. Gilmore. The galactic disk surface mass density and the Galactic force K(z) at Z = 1.1 kiloparsecs. *ApJ*, 367:L9–L13, 1991.

G. P. Kuiper. On the Origin of the Solar System. In J. A. Hynek, editor, *50th Anniversary of the Yerkes Observatory and Half a Century of Progress in Astrophysics*, page 357, 1951.

J. R. D. Lépine, A. Roman-Lopes, Z. Abraham, T. C. Junqueira, and Y. N. Mishurov. The spiral structure of the Galaxy revealed by CS sources and evidence for the 4:1 resonance. *MNRAS*, 414:1607–1616, 2011.

H. F. Levison. In T. Rettig and J. M. Hahn, editors, *Completing the Inventory of the Solar System*, volume 107 of *Astronomical Society of the Pacific Conference Series*, pages 173–191, 1996.

H. F. Levison and M. J. Duncan. From the Kuiper Belt to Jupiter-Family Comets: The Spatial Distribution of Ecliptic Comets. *Icarus*, 127:13–32, 1997.

H. F. Levison, L. Dones, and M. J. Duncan. The Origin of Halley-Type Comets: Probing the Inner Oort Cloud. *AJ*, 121:2253–2267, 2001.

H. F. Levison, M. J. Duncan, L. Dones, and B. Gladman. The Scattered Disk as a Source of Halley-Type Comets. In *AAS/Division for Planetary Sciences Meeting Abstracts #36*, volume 36 of *Bulletin of the American Astronomical Society*, page 1082, 2004.

J. R. Lewis and K. C. Freeman. Kinematics and chemical properties of the old disk of the Galaxy. *AJ*, 97:139–162, 1989.

C. C. Lin and G. Bertin. Formation and maintenance of spiral structure in galaxies. In H. van Woerden, R. J. Allen, and W. B. Burton, editors, *The Milky Way Galaxy*, volume 106 of *IAU Symposium*, pages 513–530, 1985.

C. C. Lin and F. H. Shu. On the Spiral Structure of Disk Galaxies. *ApJ*, 140:646, 1964.

C. C. Lin, C. Yuan, and F. H. Shu. On the Spiral Structure of Disk Galaxies. III. Comparison with Observations. *ApJ*, 155:721, 1969.

C. H. Lineweaver. An Estimate of the Age Distribution of Terrestrial Planets in the Universe: Quantifying Metallicity as a Selection Effect. *Icarus*, 151:307–313, 2001.

C. H. Lineweaver, Y. Fenner, and B. K. Gibson. The Galactic Habitable Zone and the Age Distribution of Complex Life in the Milky Way. *Science*, 303:59–62, 2004.

S. A. Lowe, W. W. Roberts, J. Yang, G. Bertin, and C. C. Lin. Modal approach to the morphology of spiral galaxies. 3: Application to the galaxy M81. *ApJ*, 427:184–201, 1994.

M. Masi, L. Secco, and G. Gonzalez. Effects of the Planar Galactic Tides and Stellar Mass on Comet Cloud Dynamics. *The Open Astronomy Journal*, 2009.

J. J. Matese, D. P. Whitmire, and J. J. Lissauer. A Widebinary Solar Companion as a Possible Origin of Sedna-like Objects. *Earth Moon and Planets*, 97:459–470, 2005.

M. Mayor and D. Queloz. A Jupiter-mass companion to a solar-type star. *Nature*, 378: 355–359, November 1995. doi: 10.1038/378355a0.

M. R. Merrifield. The Galactic Halo and CDM. In S. Ryder, D. Pisano, M. Walker, and K. Freeman, editors, *Dark Matter in Galaxies*, volume 220 of *IAU Symposium*, page 431, 2004.

I. Minchev. *The effect of spiral and bar structure on the Milky Way velocity distribution.* PhD thesis, University of Rochester, 2008.

Y. N. Mishurov and I. A. Zenina. Yes, the Sun is located near the corotation circle. *A&A*, 341:81–85, 1999.

M. Miyamoto and R. Nagai. Three-dimensional models for the distribution of mass in galaxies. *PASJ*, 27:533–543, 1975.

H. Mo, F. C. van den Bosch, and S. White. *Galaxy Formation and Evolution*. 2010.

A. Morbidelli. Origin and Dynamical Evolution of Comets and their Reservoirs. *arXiv:astro-ph/0512256*, 2005.

C. D. Murray and S. F. Dermott. *Solar system dynamics*. 1999.

T. Naab and J. P. Ostriker. A simple model for the evolution of disc galaxies: the Milky Way. *MNRAS*, 366:899–917, 2006.

J. F. Navarro, C. S. Frenk, and S. D. M. White. A Universal Density Profile from Hierarchical Clustering. *ApJ*, 490:493, 1997.

A. H. Nelson and T. Matsuda. On one-dimensional galactic spiral shocks. *MNRAS*, 179: 663–670, 1977.

B. Nordström, M. Mayor, J. Andersen, J. Holmberg, F. Pont, B. R. Jørgensen, E. H. Olsen, S. Udry, and N. Mowlavi. The Geneva-Copenhagen survey of the Solar neighbourhood. Ages, metallicities, and kinematic properties of $\sim$ 14 000 F and G dwarfs. *A&A*, 418:989–1019, 2004.

J. H. Oort. The structure of the cloud of comets surrounding the Solar System and a hypothesis concerning its origin. *Bull. Astron. Inst. Netherlands*, 11:91–110, 1950.

B. E. J. Pagel. *Nucleosynthesis and Chemical Evolution of Galaxies*. Cambridge University Press, 1997.

L. Piovan, C. Chiosi, E. Merlin, T. Grassi, R. Tantalo, U. Buonomo, and L. P. Cassarà. Formation and Evolution of the Dust in Galaxies. II. The Solar Neighbourhood. *ArXiv e-prints 1107.4561*, 2011.

L. Portinari and C. Chiosi. On star formation and chemical evolution in the Galactic disc. *A&A*, 350:827–839, 1999.

N. Prantzos. On the "Galactic Habitable Zone". *Space Sci. Rev.*, 135:313–322, 2008.

N. Prantzos and J. Silk. Star Formation and Chemical Evolution in the Milky Way: Cosmological Implications. *ApJ*, 507:229–240, 1998.

M. J. Reid, K. M. Menten, X. W. Zheng, A. Brunthaler, L. Moscadelli, Y. Xu, B. Zhang, M. Sato, M. Honma, T. Hirota, K. Hachisuka, Y. K. Choi, G. A. Moellenbrock, and A. Bartkiewicz. Trigonometric Parallaxes of Massive Star-Forming Regions. VI. Galactic Structure, Fundamental Parameters, and Noncircular Motions. *ApJ*, 700: 137–148, 2009.

R. Roškar, V. P. Debattista, T. R. Quinn, G. S. Stinson, and J. Wadsley. Riding the Spiral Waves: Implications of Stellar Migration for the Properties of Galactic Disks. *ApJ*, 684:L79–L82, 2008a.

R. Roškar, V. P. Debattista, G. S. Stinson, T. R. Quinn, T. Kaufmann, and J. Wadsley. Beyond Inside-Out Growth: Formation and Evolution of Disk Outskirts. *ApJ*, 675: L65–L68, 2008b.

R. Schönrich, J. Binney, and W. Dehnen. Local kinematics and the local standard of rest. *MNRAS*, 403:1829–1833, 2010.

J. A. Sellwood and J. J. Binney. Radial mixing in galactic discs. *MNRAS*, 336:785–796, 2002.

R. Shetty, S. N. Vogel, E. C. Ostriker, and P. J. Teuben. Kinematics of Spiral-Arm Streaming in M51. *ApJ*, 665:1138–1158, 2007.

A. Siebert, B. Famaey, and Minchev et al. Detection of a radial velocity gradient in the extended local disc with RAVE. *MNRAS*, 412:2026–2032, 2011a.

A. Siebert, M. E. K. Williams, and Siviero et al. The RAdial Velocity Experiment (RAVE): Third Data Release. *AJ*, 141, 2011b.

A. Siebert, B. Famaey, and Binney et al. The properties of the local spiral arms from RAVE data: two-dimensional density wave approach. *MNRAS*, 425:2335–2342, 2012.

S. C. Simonson, III. A density-wave map of the galactic spiral structure. *A&A*, 46: 261–268, 1976.

M. Spano, M. Marcelin, P. Amram, C. Carignan, B. Epinat, and O. Hernandez. GHASP: an Hα kinematic survey of spiral and irregular galaxies - V. Dark matter distribution in 36 nearby spiral galaxies. *MNRAS*, 383:297–316, 2008.

M. Steinmetz, T. Zwitter, and Siebert et al. The Radial Velocity Experiment (RAVE): First Data Release. *AJ*, 132, 2006.

S. A. Stern. On the Collisional Environment, Accretion Time Scales, and Architecture of the Massive, Primordial Kuiper Belt. *AJ*, 112:1203, 1996.

E. L. Stiefel and G. Scheifele. *Linear and regular celestial mechanics; perturbed two-body motion, numerical methods, canonical theory.* 1971.

C. Struck, C. L. Dobbs, and J.-S. Hwang. Slowly breaking waves: the longevity of tidally induced spiral structure. *MNRAS*, 414:2498–2510, 2011.

A. Toomre. On the gravitational stability of a disk of stars. *ApJ*, 139:1217–1238, 1964.

S. Tremaine. The distribution of comets around stars. In *Planets Around Pulsars*, volume 36 of *Astronomical Society of the Pacific Conference Series*, pages 335–344, 1993.

C. A. Trujillo, D. C. Jewitt, and J. X. Luu. Properties of the Trans-Neptunian Belt: Statistics from the Canada-France-Hawaii Telescope Survey. *AJ*, 122:457–473, 2001.

R. J. Trumpler and H. F. Weaver. *Statistical astronomy.* Dover Publications, 1953.

J. P. Vallée. New Velocimetry and Revised Cartography of the Spiral Arms in the Milky WAY - A Consistent Symbiosis. *AJ*, 135:1301–1310, 2008.

M. D. Weinberg, S. L. Shapiro, and I. Wasserman. The dynamical fate of wide binaries in the solar neighborhood. *ApJ*, 312:367–389, 1987.

P. R. Weissman. The Oort Cloud. In T. Rettig and J. M. Hahn, editors, *Completing the Inventory of the Solar System*, volume 107 of *Astronomical Society of the Pacific Conference Series*, pages 265–288, 1996.

F. L. Whipple. A comet model. I. The acceleration of Comet Encke. *ApJ*, 111:375–394, 1950.

P. Wiegert and S. Tremaine. The Evolution of Long-Period Comets. *Icarus*, 137:84–121, 1999.

R. Wielen, B. Fuchs, and C. Dettbarn. On the birth-place of the Sun and the places of formation of other nearby stars. *A&A*, 314:438, 1996.

C. Yuan. Application of the Density-Wave Theory to the Spiral Structure of the Milky way System. II. Migration of Stars. *ApJ*, 158:889, 1969a.

C. Yuan. Application of the Density-Wave Theory to the Spiral Structure of the Milky way System. I. Systematic Motion of Neutral Hydrogen. *ApJ*, 158:871, 1969b.

H. Zhao. Analytical models for galactic nuclei. *MNRAS*, 278:488–496, 1996.

T. Zwitter, A. Siebert, and Munari et al. The Radial Velocity Experiment (rave): Second Data Release. *AJ*, 136:421–451, 2008.

T. Zwitter, G. Matijevič, and Breddels et al. Distance determination for RAVE stars using stellar models . II. Most likely values assuming a standard stellar evolution scenario. *A&A*, 522, 2010.